THE UNIVERSITY *of* EDINBURGH

This thesis has been submitted in fulfilment of the requirements for a postgraduate degree (e.g. PhD, MPhil, DClinPsychol) at the University of Edinburgh. Please note the following terms and conditions of use:

This work is protected by copyright and other intellectual property rights, which are retained by the thesis author, unless otherwise stated.
A copy can be downloaded for personal non-commercial research or study, without prior permission or charge.
This thesis cannot be reproduced or quoted extensively from without first obtaining permission in writing from the author.
The content must not be changed in any way or sold commercially in any format or medium without the formal permission of the author.
When referring to this work, full bibliographic details including the author, title, awarding institution and date of the thesis must be given.

Constitutive models and finite elements for plasticity in generalised continuum theories

Fahad Gulib

THE UNIVERSITY *of* EDINBURGH
Institute for Infrastructure and Environment

Thesis submitted for the degree of

Doctor of Philosophy

October 2018

To my father Fazlur Rahman…

(06 Sept. 1956 – 29 Nov. 2017)

Declaration

I declare that this thesis was composed by myself, that the work contained herein is my own except where explicitly stated otherwise in the text, and that this work has not been submitted for any other degree or professional qualification except as specified. Part of this work has been presented in the following publications:

Peer review conference papers and abstracts:

F. Gulib, S.-A. Papanicolopulos. Finite element implementation and detailed comparisons of generalised plasticity models. 6th European Conference on Computational Mechanics (ECCM6). Jun. 2018. Glasgow, UK.

- F. Gulib, S.-A. Papanicolopulos. A comparison of finite element implementation of Cosserat and strain-gradient plasticity models for predicting localisation. XIV International Conference on Computational Plasticity (COMPLAS2017). Sept. 2017. Barcelona, Spain.
- F. Gulib, S.-A. Papanicolopulos. Review and comparison of numerical implementations for Cosserat plasticity. Bifurcation and Degradation of Geomaterials with Engineering Applications. Springer Series in Geomechanics and Geoengineering. Proc. of the 11th International Workshop on Bifurcation and Degradation in Geomaterials (IWBGD2017). May 2017, pp. 225-231. Limassol, Cyprus.
- F. Gulib, S.-A. Papanicolopulos. Finite element implementation of Cosserat elastoplastic models. 4th Infrastructure & Environment Scotland PGR conference. May 2017. Edinburgh, UK.

Fahad Gulib

October 2018

Acknowledgements

The journey of completing this thesis would not be possible without the help, encouragement, friendship, and guidance of so many people, to all of whom I wish to express my sincere thanks.

I would like to express my deep gratitude to my advisor for this thesis, Dr Stefanos Aldo Papanicolopulos for formulating the basis of my research, useful suggestions and patient guidance.

Special thanks to my co-adviser for this thesis, Professor Pankaj Pankaj, for guidance, constructive help and suggestions.

I am grateful to all my colleagues from the Institute for Infrastructure and Environment at the University of Edinburgh especially to Ofonime Harry, Dr Zeynep Karatza, Behzad Soltanbeigi, Dr Julien Sindt and Dr Rangarajan Radhakrishnan for their kind support and friendship.

I would like to thank my parents for their continuous support and my wife Earfath Ara Khan for countless reasons.

This Ph.D. thesis was supported by the full scholarship from the People Programme (Marie Curie Actions) of the European Union's Seventh Framework Programme (FP7/2007-2013) under REA grant agreement n^{o} 618096 and the University of Edinburgh.

Abstract

The mechanical behaviour of geomaterials (e.g. soils, rocks and concrete) under plastic deformation is highly complex due to that fact that they are granular materials consisting of discrete non-uniform particles. Failure of geomaterials is often related to localisation of deformation (strain-localisation) with excessive shearing inside the localised zones. The microstructure of the material then dominates the material behaviour in the localised zones. The formation of the localised zone (shear band) during plastic deformation decreases the material strength (softening) significantly and initiates the failure of the material.

There are two main approaches to the numerical modelling of localisation of deformation in geomaterials; discrete and continuum. The discrete approach can provide a more realistic material description. However, in the discrete approach, the modelling of all particles is complicated and computationally very expensive for a large number of particles. On the other hand, the continuum approach is more flexible, avoids modelling the interaction of individual particles and is computationally much cheaper.

However, classical continuum plasticity models fail to predict the localisation of deformation accurately due to loss of ellipticity of the governing equations, and spurious mesh-dependent results are obtained in the plastic regime. Generalised plasticity models are proposed to overcome the difficulties encountered by classical plasticity models, by relaxing the local assumptions and taking into account the microstructure-related length scale into the models. Among generalised plasticity models, Cosserat (micropolar) and stain-gradient models have shown significant usefulness in modelling localisation of deformation in granular materials in the last few decades.

Currently, several elastoplastic models are proposed based on Cosserat and strain-gradient theories in the literature. The individual formulation of the models has been examined almost always in isolation and are paired with specific materials in a mostly arbitrary fashion. Therefore, there is a lack of comparative studies between these

models both at the theory level and in their numerical behaviour, which hinders the use of these models in practical applications.

This research aims to enable broader adoption of generalised plasticity models in practical applications by providing both the necessary theoretical basis and appropriate numerical tools. A detailed comparison of some Cosserat and strain-gradient plasticity models is provided by highlighting their similarities and differences at the theory level. Two new Cosserat elastoplastic models are proposed based on von Mises and Drucker-Prager type yield function.

The finite element formulations of Cosserat and strain-gradient models are presented and compared to better understand their advantages and disadvantages regarding numerical implementation and computational cost. The finite elements and material models are implemented into the finite element program ABAQUS using the user element subroutine (UEL) and an embedded user material subroutine (UMAT) respectively. Cosserat finite elements are implemented with different Cosserat elastoplastic models. The numerical results show how the Cosserat elements behaviour in the plastic regime depends on the models, interpolation of displacement and rotation and the integration scheme.

The effect of Cosserat parameters and specific formulations on the numerical results based on the biaxial test is discussed. Two new mixed-type finite elements as well as existing ones (C^1, mixed-type and penalty formulation), are implemented with different strain-gradient plasticity models to determine the numerical behaviour of the elements in the plastic regime. A detailed comparison of the numerical results of Cosserat and strain-gradient elastoplastic models is provided considering specific strain-localisation problems. Finally, some example problems are simulated with both the Cosserat and strain-gradient models to identify their applicability.

Table of Contents

List of Figures

List of Tables

1 Introduction

1.1 Strain localisation in granular media

Granular media are one of the most extensive materials on earth and are very important to a countless variety of engineering and industrial branches. Failure of geomaterials (e.g. soils, rocks and concrete) is related to localisation of deformation (strain localisation) with excessive shearing inside the localised zones. Strain localisation is a phenomenon where part of the material undergoes significant deformation (and therefore degradation) compared to the rest of the material. It is evident from the triaxial and biaxial shear experiment that the localised zone has a finite thickness (Muhlhaus & Vardoulakis, 1987). The formation of the localised zone (shear band) during the deformation decreases the material strength (softening) significantly and initiates the failure of the material. The behaviour of geomaterials under confined or unconfined loading is very complicated. A realistic approach to modelling of the discrete nature of the materials within the continuum framework requires the incorporation of the characteristic length scale related to the microstructure of the materials.

Strain localisation and the mechanism of the formation of shear zones is very important since they act as a precursor to the failure of the materials. The localised shear zone leads to unstable behaviour of the entire structure, e.g. in the problem of foundation, slopes, piles and earth retaining walls. Localisation under shear occurs within the material either in the form of a spontaneous shear zone as a single, multiple or regular patterns of the localised shear zone (Han & Vardoulakis, 1991; Harris, Viggiani, Mooney, & Finno, 1995; Desrues, Chambon, Mokni, & Mazerolle, 1996). Significant grain rotations (Oda, Konishi, & Nemat-Nasser, 1982; Uesugi, Kishida, & Tsubakihara, 1988; Tejchman, 1989), large strain gradients (Vardoulakis, 1980), high void ratios with material softening (Desrues, Chambon, Mokni, & Mazerolle, 1996) and void fluctuations (Löffelmann, 1989) are observed within the shear zones. The

thickness of the shear zone is dependent on various factors such as the mean grain diameter (Vardoulakis, 1980; Tejchman, 1989), initial void ratio (Tejchman, 1989; Desrues & Hammad, 1989), grain roughness and grain size distribution (Tejchman, 1989; Desreues & Viggiani, 2004).

The experimental observation of strain localisation phenomena in geomaterials shows strong spatial density variation that characterises gradient dependency and the deformation of the material. The shear band formation and localised zone of finite thickness with increased porosity have been observed in the sand (Vardoulakis & Graf, 1985). Extensive experimental studies have been conducted to investigate the various aspects of the strain localisation such as shear resistance, localisation criteria, thickness of shear zone and distribution of void ratio (Vardoulakis, 1980; Tejchman, 1989; Desrues, Chambon, Mokni, & Mazerolle, 1996; Vardoulakis & Sulem, 1995; Alshibli & Sture, 2000; Lade, 2002).

Classical continuum plasticity models can only predict the load carrying capacity at the initial stage of strain localisation. Also, they fail to predict the finite thickness of the shear band when strain softening models are considered. Mathematical modelling of localisation problems using classical plasticity leads to loss of ellipticity for the governing equations and spurious mesh-dependency numerical solutions are obtained in the post-peak regime. Classical continuum theories do not take into account any information on nearby material points, due to their local assumptions and no internal length scales in the constitutive descriptions. The local assumption can no longer provide realistic solutions when the microscopic and macroscopic length scales are comparable. Generalised continuum theories are proposed to take into account the microstructural effect by relaxing some restrictions of classical continuum mechanics.

In the literature, a variety of generalised continuum theories have been proposed to overcome the difficulties encountered by classical methods and take into account the microstructures such as Cosserat (micropolar) continuum theory (Cosserat & Cosserat, 1909), micromorphic continua (Toupin, 1962; Mindlin R. , 1964; Germain, 1973), the nonlocal gradient plasticity (Aifantis, 1984; Aifantis, 1987; Zbib & Aifantis, 1988; Zbib & Aifantis, 1988) and the flow theory of gradient plasticity (Fleck & Hutchinson, 1993; Fleck & Hutchinson, 1997). The existing generalised continuum theories

include higher-order gradient terms with coefficients that represents the characteristic length scale in the constitutive equations.

1.2 Scale effects

The application of classical continuum theories is not suitable when the size of the structure and the internal length which is related to the size of the microstructure is comparable. The microstructural effect is noticeable when the size of the structure is a relatively small multiple of the internal length, greater than 1. The existence of characteristic length scale in generalised continuum theories not only consider the microstructural effects in predicting strain localisation but also capture the scale (size) effect phenomena observed experimentally on softening granular material (Tejchman, 2008). Consequently, generalised continuum theories are needed to consider the microstructural effects into the models.

Many microscale experiments on metals, bones and geomaterials have been carried out to determine scale effects in solids (Fleck, Muller, Ashby, & Hutchinson, 1994; Nix & Gao, 1998; Tsagrakis & Aifantis, 2002; Park & Lakes, 1986; Yang & Lakes, 1982; Atkinson, 1993; Wijk, 1989; Brace, 1961; Jaeger, 1967). In the recent years, small-scale experiments such as micro-indentation tests (or nano-indentation tests) have become a popular method of showing scale effects (Gane & Cox, 1970; Doerner & Nix, 1986; Atkins & Tabour, 1965). The indentation hardness has been shown to be size-dependent when the width of the impression is below about fifty microns (Begley & Hutchinson, 1998). Scale effects are also shown when the characteristic length scale related to the plastic deformation is on the order of microns. For example: twisting of thin copper wire (Fleck, Muller, Ashby, & Hutchinson, 1994) and bending of ultra-thin beams (Stolken & Evans, 1998).

The classical theories of plasticity cannot predict scale effects due to lack of internal length scale into their constitutive models. The prediction of material behaviour using classical plasticity is therefore unrealistic at the micron level. The current designing tools with classical continuum theories may not be suitable for analysing advanced industrial applications at the micron level. Therefore, generalised continuum theories with characteristic length scale that relate the microstructures with the macroscopic

material behaviour is necessary to predict realistic material behaviour. Among nonlocal approaches, Cosserat (micropolar) and strain gradient models have received significant interest in recent years in modelling scale effects and strain localisation phenomena.

1.3 Related work and possible solutions

1.3.1 Traditional finite element method

The numerical finite element results based on classical continuum mechanics are controlled by the size and orientation of the mesh and therefore predict unrealistic results when strain-softening models are considered. The load-displacement curves in the post-failure regime and the width of the shear zone change considerably upon mesh refinement. Therefore, the numerical finite element solutions based on classical approach are sensitive to mesh density. Currently, for geomaterials advanced and realistic local constitutive models are available. However, strain localisation in the post-failure regime requires a model to take into account the information related to microstructure which is not possible with a local constitutive model.

A simple example of a classical plasticity model with strain softening material in plane-strain condition, biaxial compression test is carried out to demonstrate the mesh dependency numerical solution in the post-peak regime. Finite element analysis (FEA) is carried out using the classical von Mises plasticity model with the strain-softening material. The rectangular specimen has width $\mathrm{B}=60\mathrm{mm}$ and height $\mathrm{H}=120\mathrm{mm}$. The specimen is subjected to 4.0 mm vertically downwards displacement (the load is a displacement control one) from the top and the bottom left is fixed. The boundary conditions along the vertical sided are traction-free, and the vertical displacement (i.e. $\mathrm{u_y}=0$) is restricted at the bottom. To trigger localisation, a material imperfection (weak zone) is assumed in at the bottom left element of the specimen. The material parameters used are Young's modulus $E=4000\mathrm{MPa}$, Poisson's ratio $v=0.49$, hardening/softening modulus $\mathrm{h_p}=-400\mathrm{MPa}$, yield stress $\sigma_{y0}=100\mathrm{MPa}$ and yield stress of the weak zone $\sigma_{w0}=98\mathrm{MPa}$. The discretisation used is 8x16, 10x20 and 12x24-mesh.

Figure 1.1 shows that the load-displacement curve in the plastic regime decreases significantly upon mesh refinement. Figure 1.2 shows the equivalent plastic strain increases and the shear band width (SBW) decreases with increasing mesh density. The numerical finite element solutions based on classical continuum theory are mesh dependent and therefore unrealistic.

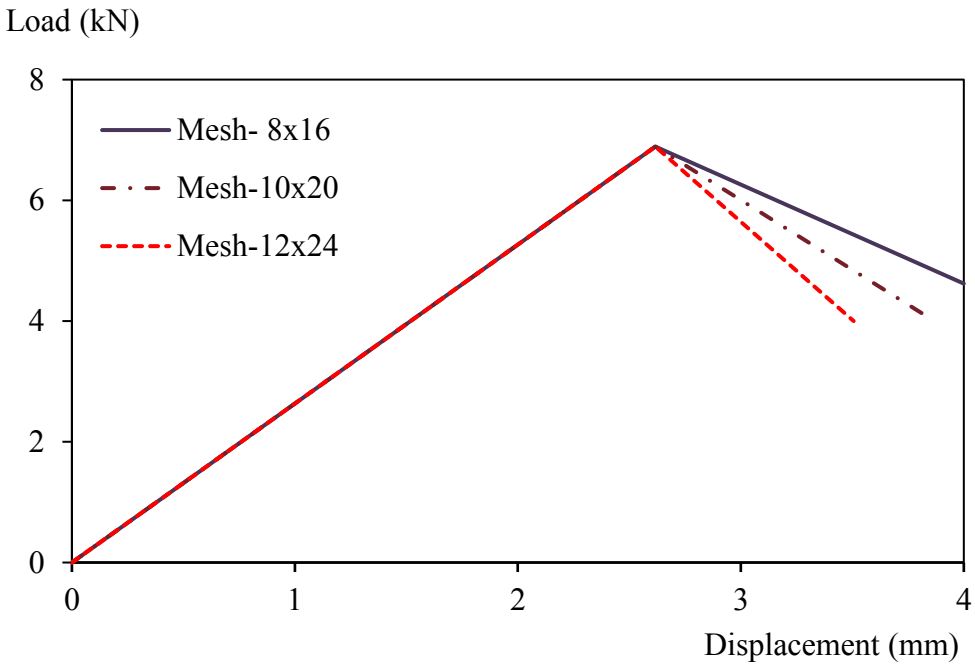

Figure 1.1 Load-displacement curve for Classical von Mises plasticity model.

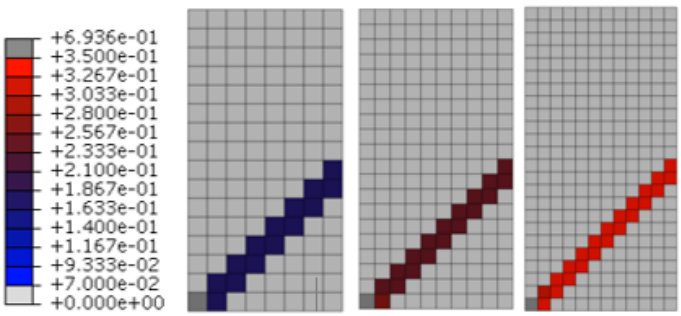

Figure 1.2 Undeformed mesh with the contour of the equivalent plastic strain from left to right: 8x16, 10x20 and 12x24.

In the last few decades, various techniques have been developing to overcome the deficiencies of classical continuum models when strain-softening material are considered. One of the most prominent techniques is so-called strong discontinuity

approach that allows a finite element with a displacement discontinuity (Larsson & Larsson, 2000; Regueiro & Borja, 2001; Lai, Borja, Duvernay, & Meehan, 2003) and capable of predicting mesh-independent results. However, strong discontinuity approach does not take into account any internal length scale related to the microstructure. Discrete element models have been used to investigate the formation of the shear zone inside of granular materials (Oda & Kazama, 1998; Oda & Iwashita, 2000; Thornton, 2003). To better describe the shear localisation, additional techniques have been used such as remeshing (Pastor & Peraire, 1989; Ehlers & Volk, 1998), multi-scaling (Gitman, 2006) which are very useful for large geotechnical problems, and element-free Galerkin concept (Beltyschko, Krongauz, Organ, Fleming, & Krysl, 1996; Pamin, Askes, & de Borst, 2003).

The granular material consists of voids and grains in contact. The micromechanical behaviour of geomaterials (e.g. rocks, soils) is radically discontinuous, heterogeneous and non-linear. Although geomaterials are of discrete nature, their micromechanical behaviour can be captured with reasonable accuracy using generalised continuum theories that take into account the microstructural related length scale into the models.

1.3.2 Cosserat 'Micropolar' theory

The Cosserat theory was first developed and presented as Cosserat theory of elasticity (Cosserat & Cosserat, 1909). The theory was further developed and shown that classical theory of elasticity and the couple stress theory are the special cases of the Cosserat elasticity theory (Mindline & Tiersten, 1962). Rework of the Cosserat theory by many authors have established the kinematics and statics of Cosserat continuum in a suitable format for applied mechanics problems (Kuvshinskii & Aero, 1964; Mindlin R. , 1965; Eringen A. , 1966). According to Germain's terminology, Cosserat is a special case of a micromorphic continuum of the first order (Germain, 1973).

In Cosserat continuum, a material point has, besides the three translational degrees of freedom (DOF) as in classical continuum, three additional independent rotational DOF. The material point is considered as a rigid particle. One of the essential and distinct features of Cosserat continua is that the stress tensor may not be symmetric as

in the classical case and the balance of angular moment equation has to be modified accordingly. The addition of couple-stress due to curvature (rotation-gradient) introduces a characteristic length scale into the constitutive equations.

Granular materials undergo high rotational and translational deformation at failure. The classical strain tensor fails to capture the real kinematics of the granular material such as micro-rotation. Other alternative tensors need to be used instead (Vardoulakis & Sulem, 1995; Oda & Iwashita, 1999). Since grain undergoes rotational and translational deformation in the three dimensional (3D) space, a single grain might have six DOF (three translational and three rotation). The Cosserat point has been found very useful to represent average grains regarding kinematics (Kanatani, 1979; Muhlhaus & Vardoulakis, 1987; Vardoulakis & Sulem, 1995; Oda & Iwashita, 2000)

In two dimensional (2D) problems, many researchers have utilised Cosserat von-Mises and pressure dependent Drucker-Prager type plasticity models as the regularisation approach to analyse strain localisation problems (de Borst, 1991; Sharbati & Naghdabadi, 2006; Tejchman & Wu, 1993; Khoei, Yadegari, & Anahid, 2006; de Borst, 1993; Arslan & Sture, 2008; Li & Tang, 2005).

Recently, adaptive FEA within the Cosserat continuum is used to simulate localisation phenomena (Khoei, Gharehbaghi, & and Tabarraie, 2007). Elastoplastic Cosserat continuum is used to simulate the shear localisation along the interface between cohesionless granular soil and bounding structure (Ebrahimian, Noorzad, & Alsaleh, 2011). The Cosserat (micropolar) continuum has been used in many research areas, such as crystal plasticity, composite and biomechanics. The Cosserat viscoelastic continuum model is used to describe the spinal dislocations and disclamations (Ivancevic, 2009). The micropolar single crystal plasticity model can qualitatively capture the same range of behaviours as slip gradient-based models (Casolo, 2006).

The researchers mentioned above mostly focused on 2D plane stain problems. The actual engineering structures are usually in 3D. Recently, numerical analysis of shell structures, cantilevers and plates based on 3D Cosserat continuum has been carried out (Rubin, 2005; Liu & Rosing, 2007; Riahi & Curran, 2009; Riahi, Curran, & Bidhendi, 2009).

Currently, there is a lack of comparative studies between Cosserat plasticity models based on von-Mises and Drucker-Prager yield criterion. All the Cosserat plasticity models are capable of predicting localised deformation (de Borst, 1991; Sharbati & Naghdabadi, 2006; Tejchman & Wu, 1993; Khoei, Yadegari, & Anahid, 2006; de Borst, 1993; Arslan & Sture, 2008; Li & Tang, 2005). The derivation of different formulations and the use of different values for the Cosserat parameters makes it difficult to understand the differences in the numerical behaviour of the models. Also, the effect of the Cosserat parameters in plasticity calculations on the numerical results is not presented.

An essential aspect of numerical finite element analysis is the type of elements employed. Different researchers have used different elements without giving details of the integration scheme, and no comparisons of the numerical behaviour of the elements in the plastic regime are available. All the above factors hinder the use of generalised plasticity models by engineers and researchers in practical applications where classical continuum models fail to predict a realistic solution especially when the microstructural behaviour dominates the overall deformation of the structure.

1.3.3 Couple-stress theory

The existence of couple-stress in materials was initially postulated by Voigt (1887). However, Cosserat and Cosserat (1909) were the first to develop a mathematical model to analyse materials with couple stress. In a simplified micropolar theory, the so-called couple-stress theory, the rotation is not independent of displacement, but are related to it in the same as in classical continuum mechanics. In other words, in couple-stress theory the rotation is subjected to constraint as in classical continuum, i.e. the rotation is defined as the skew-symmetric part of the displacement gradient (Aero & Kuvshinskii, 1961; Mindline & Tiersten, 1962; Koiter, 1964). Therefore, the couple-stress theory is regarded as ‘constrained’ Cosserat (micropolar) theory in which the micro-rotation become equal to the macro-rotation. As a result, the displacement field determines the rotation field as well.

The main reasons behind the extension of the classical to micropolar and couple-stress theory were that classical theory was unable to predict the size effect phenomena

observed experimentally in problems where the structural length scale is comparable to a material microstructural length such as grain size in polycrystalline or granular aggregate. The couple-stress and related nonlocal theories of elastic and inelastic material response are of interest to describe the deformation mechanism and manufacturing of micro and nanostructured material and devices as well as inelastic localisation phenomena.

The elastic couple-stress theory has been extended to an elastoplastic model based on von-Mises yield criterion where shear band formation is considered, and the numerical finite element solutions turn out to be independent of mesh spacing (Ristinmaa & Vecchi, 1996). However, the couple-stress theory does not represent a realistic description of granular media where the micro-rotation may not be equal to the macro-rotation. The rotation of individual particles differs from that of the neighbouring particles observed experimentally (Andò, et al., 2017).

1.3.4 Strain-gradient theory

The second or higher gradient continua can be found in a paper by Cauchy (1851) as mentioned by Biot (1967). About a century later the theory of second-gradient (or strain-gradient) elasticity was thoroughly formulated (Toupin, 1962; Mindlin R. , 1964; Mindlin & Eshel, 1968). Since then, a large number of work has been carried out on strain gradient theories.

Gradient elasticity formulation can be based on the second gradient of displacement, strain-gradients or the rotation gradients and the symmetric part of the strain-gradient. All three forms (I, II and III) of gradient elasticity are equivalent. Recently, strain-gradient theories have been used to solve problems in elasticity (Shu, King, & Fleck, 1999; Askes & Aifantis, 2002; Zervos, Papanicolopulos, & Vardoulakis, 2009; Papanicolopulos, Zervos, & Vardoulakis, 2009), plasticity (Fleck & Hutchinson, 1993; Chambon, Caillerie, & Matsuchima, 2001; Zervos, Papanastasiou, & Vardoulakis, 2001; Qiu, Huang, Wei, Gao, & Hwang, 2003) and fracture mechanics (Amanatidou & Aravas, 2002; Askes & Gutiérrez, 2006; Papanicolopulos & Zervos, 2009) where size effects or localised deformation plays an important role.

Strain gradient plasticity models (Fleck & Hutchinson, 1997; Chambon, Caillerie, & Matsuchima, 2001; Qiu, Huang, Wei, Gao, & Hwang, 2003) have shown to predict size effect or localised deformation when strain softening materials are considered. At present, there is a lack of comparative studies between the strain gradient plasticity models in 2D, and no numerical comparisons are available between the models in the plastic regime. Although the essential properties of some strain gradient plasticity models in small-strain and one-dimensional setting are presented (Jirásek & Rolshoven, 2009), the real behaviour in 2D or 3D material involves intense shearing within the localised deformation zone which cannot be captured in the 1D analysis.

An essential feature of the strain-gradient models is that if traditional finite elements are used for the numerical solutions, then C^1 displacement continuity is required. Alternatively, mixed-type (Shu, King, & Fleck, 1999; Matsushima, Chambon, & Caillerie, 2002), meshless methods (Askes & Aifantis, 2002) , penalty method (Zervos, Papanicolopulos, & Vardoulakis, 2009) and other specialised numerical approaches (Askes & Gutiérrez, 2006) can be employed to avoid the C^1 requirement. However, not all the mixed-type elements perform well (Shu, King, & Fleck, 1999). In most cases, the elements have been used in elasticity problems or paired with specific plasticity models only.

At present, there is a lack of understanding of the numerical behaviour of various elements in different strain gradient plasticity models, especially in the post-peak regime. Also, no detailed guidance is available on which elements to be used in strain gradient plasticity models that predict satisfactory numerical solutions, are easier to implement and are computationally cheapest. All the above issues restrict the use of strain gradient plasticity models in general by researchers and engineers.

1.3.5 Micromorphic theory

Micromorphic theory (Eringen & Suhubi, 1964; Eringen A. , 1999) treats a material body as a continuous collection of a large number of deformable particles, with each particle possessing finite size microstructure. In micromorphic continuum, in addition to the three translational degrees of freedom (DOF), there are nine DOF associated

with the unsymmetric micro-deformation tensor which includes micro-rotation, micro-stretch and micro-shear.

The Cosserat (micropolar), 'constrained' Cosserat or couples-stress and second gradient theory are the different special cases of first-order micromorphic theory (Germain, 1973). Micromorphic theory can be reduced to Mindlin's Microstructure theory (1964) assuming infinitesimal deformation and slow motion. When the microstructure of the material is considered rigid, it becomes a micropolar theory (Eringen & Suhubi, 1964). The micropolar theory is identical to Cosserat theory (Cosserat & Cosserat, 1909) assuming constant microinertia. Couple-stress theory is obtained by restraining the particle to rotate as a continuum. In second gradient (strain-gradient) the microstructure deforms as the continuum. When the particle reduced to the mass point, all the theories reduced to classical continuum mechanics.

Recently, a finite strain micromorphic elastoplasticity model is presented assuming J_2 flow plasticity (Regueiro, 2010). A finite strain micromorphic pressure-dependent Drucker-Prager plasticity model is formulated by Regueiro (2009). A 3D finite element is formulated for micromorphic material and tested on linear isotropic elasticity problem to demonstrate the elastic length scale effects on the numerical results (Regueiro & Isbuga, 2011). A micromorphic model on finite inelasticity has been developed and applied to metals (Sansour, Skatulla, & Zbib, 2010). Numerous works on micromorphic elastic and inelastic material modelling are still on-going for predicting scale effects and localised deformation phenomena. However, a large number of elastic parameters appears in the constitutive equations. The real physical meaning of the parameters is not clear and how to determine the parameters remains an open issue.

1.3.6 Nonlocal theory

The main idea of the non-local theory is to establish a relationship between the macro and the micro quantities of the material with microstructure. In this theory, the nonlocal stress at a material point is a function of weighted values of the entire strain field. The concept of nonlocal elasticity has been established by Kröner (1967), Edelen

(1976) and others. The constitutive theory of nonlocal elasticity can be found in detail in Edelen (1976).

Recently, many application of nonlocal elasticity theory has been made to fields such as fracture mechanics (Aifantis, 1992; Bazant & Pijaudier-Cabot, 1988) and dislocation theory (Pan & Fang, 1994). A nonlocal coupled damage-plasticity model has been proposed recently for the analysis of ductile failure (Nguyen, Korsunsky, & Belnoue, 2015). Although the nonlocal theory is capable of predicting localised deformation the theory needs much improvement in terms if constitutive modelling and determination and utilisation of a length scale (Nguyen, Korsunsky, & Belnoue, 2015).

The progress of the nonlocal integral formulation of plasticity and damage has been carried out by Bazant and Jirásek (2002) and concluded that nonlocality is now generally accepted as the proper approach for regularizing the boundary problems of continuum damage mechanics, for capturing the size effect, and for avoiding spurious localization, giving rise to pathological mesh sensitivity.

1.4 Objectives of the thesis

The use of specific generalised plasticity models in the literature is based on quite arbitrary pairing (e.g. the use of Cosserat plasticity for soil or nonlocal plasticity for concrete) due to lack of an overall understanding of the different available models and their properties. Indeed, the lack of clarity on the properties of different generalised models and the differences in the numerical solutions often deter the use of such models by researchers in various disciplines, even in cases where it is clear that classical continuum is unable to provide correct (or even physically sound) results. Another essential aspect of numerical simulations is the use of appropriate elements for the plasticity models which can influence the solutions in the plastic regime.

The overall research goal is to enable wider adoption of generalised (specifically Cosserat and strain gradient) plasticity models in practical applications by providing both the theoretical basis and appropriate numerical tools.

The research goal is attained by six distinct (though interrelated) objectives. These objectives are:

(i) Study and compare the existing and proposed generalised plasticity (Cosserat and strain gradient) models to highlight the similarities and differences of the models regarding the underlying properties, formulations and the parameters used.

(ii) Study and compare the existing and new finite elements for Cosserat and strain gradient models concerning different formulations and ease of numerical implementation.

(iii) Numerical implementation of the finite elements with different Cosserat and strain gradient plasticity models: to compare the numerical behaviour of the elements in the post-peak regime. Provide a recommendation of the appropriate elements for plasticity (Cosserat and strain gradient) models regarding satisfactory numerical solutions and the computational cost.

(iv) Provide a numerical comparison between the existing and proposed Cosserat plasticity models. Investigate the effect of Cosserat parameters on the numerical solutions.

(v) Provide a numerical comparison and the evolution of the shear band formation for Cosserat and strain gradient plasticity models.

(vi) Consider specific applications to showcase the numerical behaviour and the applicability of the models, thus encouraging their wider adoption.

1.5 Outline of the thesis

In Chapter 2, a detailed comparison of different Cosserat and strain-gradient plasticity models is presented regarding their fundamental properties, formulations and the parameters used. New Cosserat von Mises and Drucker Prager type plasticity models are proposed by reducing the number of parameters to simplify the models.

In Chapter 3, a detailed literature review of different finite elements for Cosserat and strain gradient models have been carried out. The existing and new finite elements for Cosserat and strain gradient models presented and compared regarding the element formulations and ease of numerical implementation.

In Chapter 4, ten and thirteen different elements are implemented with different Cosserat and strain gradient plasticity models respectively. Numerical finite element simulations are then carried out to compare the numerical behaviour of the elements for in the plastic regime. A recommendation of the appropriate elements for plasticity (Cosserat and strain gradient) models is provided.

In Chapter 5, the existing and new Cosserat plasticity models are implemented with the recommended elements from Chapter 2 to compare the numerical behaviour of the models in the post-peak regime. Attention is focused on determining how the Cosserat parameters and the different formulations affect the numerical results.

In Chapter 6, the numerical solutions of Cosserat and strain gradient plasticity models are compared using the same material parameters. The evolution of the shear band formation and any changes in the shear band width (SBW) is investigated. The effect of internal length on numerical results for Cosserat and strain gradient models are examined. The SBW is equalised for the models by changing the internal length only.

In Chapter 7, some engineering applications related to geotechnical problems are simulated using different internal length for the Cosserat and strain gradient model from Chapter 6 so that the SBW remains the same. Also, the numerical solution of the models is compared regarding load-displacement curves and the numerical stability in the plastic regime.

Chapter 8, summarises the conclusions from the results obtained with some recommendation for future work.

1.6 The novelty of the thesis

This thesis presents a number of new results. Since these are not always intensely pointed out within the text, to obtain a more uniform presentation of the topic, a summary of the key points presenting new results is provided here. These are:

- A detailed comparison of the Cosserat and strain gradient plasticity models are presented regarding formulations and the parameters considered in small stain, plane stain case.

- A new Cosserat von Mises (VM5) and Drucker-Prager (DP5) plasticity model is proposed by reducing the number of Cosserat parameters so that the plasticity part is essentially the same as classical.
- A detailed comparison of ten and thirteen finite elements for Cosserat and strain gradient models respectively are provided concerning different formulations, DOF at nodes, shape functions, integration scheme, ease of numerical implementation and the computational cost.
- A new penalty method and two mixed-type Lagrange multiplier element formulations with full and reduced integration scheme for strain gradient models are presented that are easier to implement and computationally less expensive compared to the existing ones.
- A numerical comparison of ten and thirteen different finite elements in three different Cosserat and four different strain gradient plasticity models respectively are provided. Therefore, detailed guidance concerning the numerical behaviour of different finite elements in different Cosserat and strain gradient plasticity models are provided.
- Cosserat elements COS8(4)R (and COS6(3)G3) and the new mixed-type element QU30L3 are recommended for Cosserat and strain gradient plasticity models respectively that are easy to implement, computationally cheaper and predicts satisfactory numerical solutions (i.e. no significant numerical issues such as volumetric locking and spurious hourglass deformation modes).
- The numerical solutions of the proposed Cosserat model VM5 hold all the essential features of the existing Cosserat models (VM1…VM4).
- An equivalent SBW for Drucker-Prager (CCMDP, FHDP and DP1) plasticity models can be obtained by changing the internal length only. However, the load-displacement curves diverge from one another significantly during the softening stages of the plastic deformation.

2 A comparison of Cosserat and strain-gradient plasticity models

The classical plasticity models do not have any internal length scale in their constitutive equations that would relate to the microstructure of the material. Therefore, they are unable to predict the localised plastic domain accurately when strain-softening models are considered, and their numerical finite element solutions are mesh-dependent. In the literature, generalised plasticity models are proposed to overcome the drawbacks of classical plasticity, by incorporating at least one material parameter of the dimension of length into the model.

Generalised plasticity models such as Cosserat and strain-gradient are developed by relaxing some restrictions of classical continuum models. Cosserat media allows the material point to rotate independently, and an internal length enters the constitutive equation. In strain gradient models the material point deforms the same way as a classical continuum. However, the consideration of the neighbouring particle by taking into account the gradient of the strain (or second gradient of the displacement) in strain-gradient models introduce internal length scales into the constitutive equations.

In this chapter a detailed comparison of some Cosserat and strain-gradient plasticity models are presented regarding the necessary properties, formulations and the parameters used to evaluate different quantities. This chapter also introduces two new Cosserat plasticity models. The main assumptions considered are the static, rate independent, small-strain deformation in a 2D setting.

2.1 Cosserat plasticity basic equations

In a nonlinear, small-strain deformation study, the decomposition of the total strain rate $\dot{\boldsymbol{\varepsilon}}$ can be written into elastic and plastic strain rate as

$$\dot{\boldsymbol{\varepsilon}} = \dot{\boldsymbol{\varepsilon}}^{\mathrm{e}} + \dot{\boldsymbol{\varepsilon}}^{\mathrm{p}} \tag{2.1}$$

The stress rate must satisfy

$$\dot{\boldsymbol{\sigma}} = \mathbf{D}^{\mathrm{e}}\dot{\boldsymbol{\varepsilon}}^{\mathrm{e}} \tag{2.2}$$

where $\mathbf{D}^{\mathrm{e}}$ is the elastic stiffness material matrix. Re-arranging and substituting equation (2.1) into (2.2) gives

$$\dot{\boldsymbol{\sigma}} = \mathbf{D}^{\mathrm{e}}(\dot{\boldsymbol{\varepsilon}} - \dot{\boldsymbol{\varepsilon}}^{\mathrm{p}}) \tag{2.3}$$

As in classical plasticity, the plastic strain rate for Cosserat is given by

$$\dot{\boldsymbol{\varepsilon}}^{\mathrm{p}} = \dot{\gamma}\mathbf{g} \tag{2.4}$$

with loading-unloading conditions

$$\dot{\gamma} \geq 0, \quad f \leq 0, \quad \dot{\gamma} f = 0 \tag{2.5}$$

where $\dot{\gamma}$ is the plastic multiplier, $\mathbf{g}$ is the plastic flow potential vector and f is the yield function. In a 2D Cosserat continuum under plane strain conditions ($\dot{\varepsilon}_{zz} = 0$), the strain vector can be written as

$$\dot{\boldsymbol{\varepsilon}} = \left[\dot{\varepsilon}_{xx} \quad \dot{\varepsilon}_{yy} \quad \dot{\varepsilon}_{zz} \quad \dot{\varepsilon}_{xy} \quad \dot{\varepsilon}_{yx} \quad l\dot{\kappa}_{xz} \quad l\dot{\kappa}_{yz}\right]^{\mathrm{T}} \tag{2.6}$$

The strain rate components are

$$\begin{aligned} &\dot{\varepsilon}_{xx} = \frac{\partial \dot{u}_x}{\partial x}, \quad \dot{\varepsilon}_{yy} = \frac{\partial \dot{u}_y}{\partial y}, \quad \dot{\varepsilon}_{zz} = \frac{\partial \dot{u}_z}{\partial z} \\ &\dot{\varepsilon}_{xy} = \frac{\partial \dot{u}_y}{\partial x} - \dot{\omega}_z, \quad \dot{\varepsilon}_{yx} = \frac{\partial \dot{u}_x}{\partial y} + \dot{\omega}_z \end{aligned} \tag{2.7}$$

where $\dot{\omega}_z$ is the relative rotation rate. The micro-curvatures (rotation gradient) rate is

$$\dot{\kappa}_{xz} = \frac{\partial \dot{\omega}_z}{\partial x}, \quad \dot{\kappa}_{yz} = \frac{\partial \dot{\omega}_z}{\partial y} \tag{2.8}$$

Similarly, we assemble the stress rate components in the stress rate vector as

$$\dot{\boldsymbol{\sigma}} = \left[\dot{\sigma}_{xx} \quad \dot{\sigma}_{yy} \quad \dot{\sigma}_{zz} \quad \dot{\sigma}_{xy} \quad \dot{\sigma}_{yx} \quad \dot{m}_{xz}/l \quad \dot{m}_{yz}/l\right]^{\mathrm{T}} \tag{2.9}$$

where l is the internal length scale and $\dot{m}_{xz}$ (and $\dot{m}_{yz}$) are the couple-stress components.

The effect of the internal length scale is considered by several researchers (de Borst, 1991; Sharbati & Naghdabadi, 2006; Khoei, Yadegari, & Anahid, 2006). Increasing the internal length the maximum effective plastic strain decreases and predicts a stiffer load-displacement curve. Unlike classical continuum, the SBW and plastic zone remain unchanged for Cosserat media when discretisation refines (i.e. increasing the mesh density). For Cosserat continuum, the internal length may control the plastic zone. Increasing the internal length the SBW and the plastic zone increases (Sharbati & Naghdabadi, 2006). The internal length l and the size of the element l_e must satisfy $l/l_e \geq 0.15$ (Sharbati & Naghdabadi, 2006) otherwise one might predict mesh dependent solutions.

The Cosserat elastic stiffness matrix under plane strain condition (de Borst, 1991; Tejchman & Wu, 1993; Sharbati & Naghdabadi, 2006) is defined as

$$\mathbf{D}^{\mathrm{e}} = \begin{bmatrix} \lambda+2\mu & \lambda & \lambda & 0 & 0 & 0 & 0 \\ \lambda & \lambda+2\mu & \lambda & 0 & 0 & 0 & 0 \\ \lambda & \lambda & \lambda+2\mu & 0 & 0 & 0 & 0 \\ 0 & 0 & 0 & \mu+a\mu & \mu-a\mu & 0 & 0 \\ 0 & 0 & 0 & \mu-a\mu & \mu+a\mu & 0 & 0 \\ 0 & 0 & 0 & 0 & 0 & b\mu & 0 \\ 0 & 0 & 0 & 0 & 0 & 0 & b\mu \end{bmatrix} \tag{2.10}$$

In the Cosserat elastic stiffness matrix in equation (2.10), two dimensionless parameters (a and b) appear in addition to Lamé parameters (λ and μ) as in classical continuum. The Cosserat shear modulus is defined as

$$\mu_c = a\mu \tag{2.11}$$

The effect of Cosserat parameter a was investigated by Sharbati et al. (2006). Increasing the value (0.5 – 3.7) of a the equivalent plastic strain decreased slightly and predicted a marginally stiffer behaviour in the load-displacement curve. However, this increase in the load-displacement graph is too small. Therefore the value of the parameter a has a minimal effect on the Cosserat theory. However, if $a = 0$ (i.e. Cosserat shear modulus equal to zero) then classical plasticity is recovered (Iordache & Willam, 1998).

The elastic stiffness matrix in equation (2.10) has appeared with a different multiplier (i.e. the parameter *b*) in the couple stress–curvature relation. For instance, de Borst (1991) considered *b* equals to 2 whereas Sharbati et al. (2006) and Tejchman et al. (1993) considered *b* equal to 4 and 1 respectively. This multiplier differs from the definitions of the length scale *l* used (Sharbati & Naghdabadi, 2006).

The Lamé parameters are given by

$$\mu = \frac{E}{2(1-v)} \tag{2.12}$$

$$\lambda = \frac{2\mu v}{1-2v} \tag{2.13}$$

where E and v are Young's modulus and the Poisson's ratio respectively having classical meaning.

2.2 Cosserat plasticity models

2.2.1 Von Mises

The value of the Cosserat parameters a and b used to evaluate $\mathbf{D}^e$ in different Cosserat von Mises type plasticity models are shown in Table 2.1. All the models consider the parameter $a = 0.5$ except model VM4. The parameter b varies between one and four for the models VM1…VM4.

Table 2.1 Cosserat parameters *a* and *b* to evaluate $\mathbf{D}^e$.

Cosserat plasticity model	Reference	*a*	*b*
VM1	(de Borst, 1991)	0.5	2
VM2	(Sharbati & Naghdabadi, 2006)	0.5	4
VM3	(Khoei, Yadegari, & Anahid, 2006)	0.5	2
VM4	(Tejchman & Wu, 1993)	2	1

The yield function of the models (VM1…VM4) depends on the stress $\boldsymbol{\sigma}$, couple-stress $\mathbf{m}$ and the hardening-softening parameter $\bar{\varepsilon}^p$ and is given by

$$f\left(\boldsymbol{\sigma},\mathbf{m},\bar{\varepsilon}^p\right)=\bar{\sigma}\left(\boldsymbol{\sigma},\mathbf{m}\right)-\sigma_y\left(\bar{\varepsilon}^p\right) \tag{2.14}$$

The effective stress can be written as

$$\bar{\sigma}=\left[3J_2\right]^{1/2} \tag{2.15}$$

To generalise the effect of couple stress and the non-symmetric nature of the stress tensor in Cosserat J_2 is defined (Sulem & Vardoulakis, 1990) as

$$J_2 = a_1\, s_{ij}s_{ij} + a_2\, s_{ij}s_{ji} + \frac{1}{l^2}\left(a_3\, m_{ij}m_{ij} + a_4\, m_{ij}m_{ji}\right) \tag{2.16}$$

where s_{ij} and m_{ij} are the components of the deviatoric part of the stress and couple-stress tensor respectively and implies that the constraint

$$a_1 + a_2 = \frac{1}{2} \tag{2.17}$$

so that the classical expression of J_2 can be obtained when $m_{ij} = 0$ and $s_{ij} = s_{ji}$.

In the literature, no investigation has been carried out to determine the effect of the Cosserat parameters $a_1 \ldots a_4$ to compute J_2 on the numerical results (Ebrahimian, Noorzad, & Alsaleh, 2011). Different authors have used different values of $a_1 \ldots a_4$ as shown in Table 2.2. All the authors have considered the parameter $a_4 = 0$ except for Sulem and Vardoulakis (1990). The standard set of parameters are adopted (de Borst, 1991) mainly for the simple numerical algorithm. The proposed model VM5 consider classical plasticity where $a_1 = 1/2$ and do not require additional parameters $a_2 \ldots a_4$. As a result, the model is straightforward to implement.

In 2D Cosserat continuum J_2 can be written in a compact matrix-vector notation as

$$J_2 = \frac{1}{2}\boldsymbol{\sigma}^{\mathrm{T}}\mathbf{P}\boldsymbol{\sigma} \tag{2.18}$$

The plastic potential matrix $\mathbf{P}$ for plane-strain problems (assuming $a_4 = 0$) can be written as

$$\mathbf{P} = \begin{bmatrix} 2/3 & -1/3 & -1/3 & 0 & 0 & 0 & 0 \\ -1/3 & 2/3 & -1/3 & 0 & 0 & 0 & 0 \\ -1/3 & -1/3 & 2/3 & 0 & 0 & 0 & 0 \\ 0 & 0 & 0 & 2a_1 & 2a_2 & 0 & 0 \\ 0 & 0 & 0 & 2a_2 & 2a_1 & 0 & 0 \\ 0 & 0 & 0 & 0 & 0 & 2a_3 & 0 \\ 0 & 0 & 0 & 0 & 0 & 0 & 2a_3 \end{bmatrix} \tag{2.19}$$

Table 2.2 Cosserat parameters $a_1 \ldots a_4$ for the calculation of J_2.

Model	Set	a_1	a_2	a_3	a_4
VM1…VM3	Standard	1/4	1/4	1/2	0
VM4	TW1993	3/8	1/8	1	0
(Muhlhaus & Vardoulakis, 1987)	Micro-mechanical	3/4	-1/4	1/8	0
(Muhlhaus, Vardoulakis, & Tejchman, 1987)	MVT1987	3/4	-1/4	4	0
(Sulem & Vardoulakis, 1990)	SV1990	2/3	-1/6	2/3	-1/6
(Vardoulakis & Sulem, 1995)	Kinematic	3/8	1/8	1/4	0
	Static	3/4	-1/4	1	0

The current yield stress σ_y is a function of the $\bar{\varepsilon}^p$ such that

$$\sigma_y = \sigma_y\left(\bar{\varepsilon}^p\right) = \sigma_{y0} + h_p \bar{\varepsilon}^p \tag{2.20}$$

where $\bar{\varepsilon}^p$ is the hardening-softening parameter (equivalent plastic strain) and h_p is the plastic modulus (positive for hardening and negative for softening).

All the models in Table 2.1 assumed associated flow rule. Therefore, the plastic potential vector can be written as

$$\mathbf{g} = \mathbf{f} = \frac{\partial f}{\partial \boldsymbol{\sigma}} \tag{2.21}$$

Using equations (2.4), (2.21) and (2.14) and noting that for a plastic state $f = 0$, the flow vector can be written as

$$f = \frac{3}{2\sigma_y}\mathbf{P}\boldsymbol{\sigma} \tag{2.22}$$

The plastic multipliers derived for the models (VM1…VM4) are shown in Table 2.3. The models VM1 and VM3 derived an explicit formulation for the plastic multiplier in a truncated Taylor series around $\left(\boldsymbol{\sigma}_t, \bar{\varepsilon}_0^p\right)$.

Table 2.3 Plastic multiplier for the Cosserat von Mises plasticity models.

Model	Plastic multiplier, $\dot{\gamma}$
VM1 and VM4	$\dfrac{f\left(\boldsymbol{\sigma}_t, \bar{\varepsilon}_0^p\right)}{\mathbf{f}^T\mathbf{D}^e\mathbf{g} + h_p}$
VM2	$\dfrac{\mathbf{f}\mathbf{D}^e\dot{\boldsymbol{\varepsilon}}}{\mathbf{f}^T\mathbf{D}^e\mathbf{g} + h_p}$
VM3	$\dfrac{f\left(\boldsymbol{\sigma}_t, \bar{\varepsilon}_0^p\right)}{3\mu + h_p}$

The definition of the equivalent plastic strain rate can be generalised for Cosserat media (Muhlhaus & Vardoulakis, 1987; de Borst, 1991) as

$$\dot{\bar{\varepsilon}}^p = \left[b_1\,\dot{e}_{ij}^p\dot{e}_{ij}^p + b_2\,\dot{e}_{ij}^p\dot{e}_{ji}^p + b_3\,l^2(\dot{\kappa}_{ij}^p\dot{\kappa}_{ij}^p)\right]^{1/2} \tag{2.23}$$

where $\dot{e}_{ij}^p$ and $\dot{\kappa}_{ij}^p$ are the deviatoric plastic strain and the plastic rotation-gradient rate respectively and implies that the constraint

$$b_1 + b_2 = \frac{2}{3} \tag{2.24}$$

so that the classical strain-hardening hypothesis can be retrieved if $\dot{\kappa}_{ij}^{p} = 0$ and $\dot{e}_{ij}^{p} = \dot{e}_{ji}^{p}$ as

$$\dot{\bar{\varepsilon}}^{p} = \left[\frac{2}{3}\dot{e}_{ij}^{p}\dot{e}_{ij}^{p}\right]^{1/2} \tag{2.25}$$

The equivalent plastic strain rate in equation (2.23) can be written in compact matrix notation as

$$\dot{\bar{\varepsilon}}^{p} = \left[\frac{2}{3}(\dot{\boldsymbol{\varepsilon}}^{p})^{T}\mathbf{Q}\dot{\boldsymbol{\varepsilon}}^{p}\right]^{1/2} \tag{2.26}$$

where

$$\mathbf{Q} = \begin{bmatrix} 2/3 & -1/3 & -1/3 & 0 & 0 & 0 & 0 \\ -1/3 & 2/3 & -1/3 & 0 & 0 & 0 & 0 \\ -1/3 & -1/3 & 2/3 & 0 & 0 & 0 & 0 \\ 0 & 0 & 0 & 1.5b_1 & 1.5b_2 & 0 & 0 \\ 0 & 0 & 0 & 1.5b_2 & 1.5b_1 & 0 & 0 \\ 0 & 0 & 0 & 0 & 0 & 1.5b_3 & 0 \\ 0 & 0 & 0 & 0 & 0 & 0 & 1.5b_3 \end{bmatrix} \tag{2.27}$$

Different authors have used different sets of Cosserat parameters $b_1 \ldots b_3$ to compute the effective plastic strain rate $\dot{\bar{\varepsilon}}^{p}$ as shown in Table 2.4 without presenting the effect of these parameters on the numerical results. The model VM4 derived an expression for $\dot{\bar{\varepsilon}}^{p}$ by considering slip and rotation in a random assembly of circular rods. The models VM1…VM3 use a standard set of parameters $b_1 \ldots b_3$ based on ease of numerical implementation and algorithm point of view.

Table 2.4 Cosserat parameters $b_1 \ldots b_3$ used for the calculation of $\dot{\bar{\varepsilon}}^p$.

Model	Set	b_1	b_2	b_3
VM1…VM3	Standard	1/3	1/3	2/3
VM4	TW1993	3	-1	1
(Muhlhaus, Vardoulakis, & Tejchman, 1987)	MVT1987	3	-1	4
(Sulem & Vardoulakis, 1990)	SV1990	8/5	2/5	8/5

The pseudo-elastic stiffness operator and the consistent elastoplastic modulus derived for different models are given in Table 2.5. The consistent elastoplastic modulus proposed by VM2 is simplest due to no inverse calculation required for the pseudo-elastic stiffness operator. The models VM1 and VM4 derived the same expression for the consistent elastoplastic modulus. However, the model VM3 derived a slightly different formulation for the pseudo-elastic stiffness operator.

Table 2.5 Consistent elastoplastic modulus for Cosserat von Mises plasticity models.

Model	Consistent elastoplastic modulus $\mathbf{D}^{ep}$	Pseudo-elastic stiffness operator $\mathbf{D}$
VM1 & VM4	$\mathbf{D}-\dfrac{\mathbf{D}\mathbf{g}\mathbf{f}^{T}\mathbf{D}}{\mathbf{f}^{T}\mathbf{D}\mathbf{g}+\left(\dfrac{h_p\sigma_y}{\sigma_y-\dot{\gamma}h_p}\right)}$	$\left[\left[\mathbf{D}^{e}\right]^{-1}+\dot{\gamma}\dfrac{3}{2\sigma_y}\mathbf{P}\right]^{-1}$
VM2	$\mathbf{D}-\dfrac{\mathbf{D}\mathbf{g}\mathbf{f}^{T}\mathbf{D}}{\mathbf{f}^{T}\mathbf{D}\mathbf{g}+h_p}$	$\mathbf{D}^{e}$
VM3	$\mathbf{D}-\dfrac{\mathbf{D}\mathbf{g}\mathbf{f}^{T}\mathbf{D}}{\mathbf{f}^{T}\mathbf{D}\mathbf{g}+h_p}$	$\left[\left[\mathbf{D}^{e}\right]^{-1}+\dfrac{\dot{\gamma}}{4}\left(\dfrac{3}{(J_2)^3}\right)^{\frac{1}{2}}\left(2J_2\mathbf{P}-\mathbf{P}\boldsymbol{\sigma}\boldsymbol{\sigma}^{T}\mathbf{P}\right)\right]^{-1}$

In Cosserat plasticity models, usually, ten additional parameters are required other than the Lamé parameters λ and μ as in classical plasticity. Two Cosserat parameters (*a, b*) are required to evaluate the elasticity material matrix in equation (2.10), which depends on the microstructure and the type of materials. The internal length scale l enters the constitutive equation (2.3). Four Cosserat parameters $a_1 \ldots a_4$ are required to calculate J_2. Three parameters $b_1 \ldots b_3$ are required to calculate the effective plastic strain rate $\dot{\bar{\varepsilon}}^{p}$. The choice of the parameters $a_1 \ldots a_4$ and $b_1 \ldots b_3$ depends on the ease of numerical implementation or algorithm (de Borst, 1991) or they can act solely as tuning values for different models.

2.2.2 Drucker-Prager

In this section, pressure-dependent Cosserat Drucker-Prager (DP) type plasticity models are compared in detail. The Cosserat parameter b used in Cosserat DP models

to evaluate $\mathbf{D}^{e}$ are given in Table 2.6. All the DP models use $a = 0.5$ and $b = 2$ (except DP2, $b = 4$).

The yield and plastic potential function takes the form

$$f\left(\boldsymbol{\sigma},\mathbf{m},\bar{\varepsilon}^{p}\right) = \bar{\sigma}\left(\boldsymbol{\sigma},\mathbf{m}\right) + \alpha_1 p\left(\boldsymbol{\sigma}\right) - \beta_1 c\left(\bar{\varepsilon}^{p}\right) \tag{2.28}$$

$$g\left(\boldsymbol{\sigma},\mathbf{m}\right) = \bar{\sigma}\left(\boldsymbol{\sigma},\mathbf{m}\right) + \alpha_2 p\left(\boldsymbol{\sigma}\right) \tag{2.29}$$

Table 2.6 Cosserat parameter *b* used to evaluate $\mathbf{D}^{e}$ for the DP models.

Model	Reference	b
DP1	(de Borst, 1993)	2
DP2	(Peng, Kong, & Xu, 2011)	4
DP3	(Arslan & Sture, 2008)	2
DP4	(Li & Tang, 2005)	2

The material parameters, α_1 and β_1 can be expressed regarding internal friction angle ϕ as

$$\alpha_1 = \frac{6\sin\phi}{3-\sin\phi} \tag{2.30}$$

$$\beta_1 = \frac{6\cos\phi}{3-\sin\phi} \tag{2.31}$$

The material parameters, α_2 and β_2 can be expressed by replacing the internal friction angle ϕ with the dilatancy angle ψ. Note that the yield surface of the Drucker-Prager and Mohr-Coulomb criteria coincident at the outer edges of the Mohr-Coulomb surface. As a result, the Drucker-Prager models will predict much higher stresses at failure as well as higher friction angle.

The models DP1…DP4 uses a standard set of parameters ($a_1 \ldots a_4$) to compute J_2 as shown in Table 2.2. The mean (hydrostatic) stress can be written as

$$\mathrm{p} = \boldsymbol{\sigma}^{\mathrm{T}} \boldsymbol{\pi} \tag{2.32}$$

where

$$\boldsymbol{\pi} = \begin{bmatrix} 1/3 & 1/3 & 1/3 & 0 & 0 & 0 & 0 \end{bmatrix}^{\mathrm{T}} \tag{2.33}$$

The cohesion c is the function of the hardening-softening parameter, in this case, equivalent plastic strain $\bar{\varepsilon}^{\mathrm{p}}$ such that

$$c = c(\bar{\varepsilon}^{\mathrm{p}}) = c_0 + \mathrm{h}_{\mathrm{p}} \bar{\varepsilon}^{\mathrm{p}} \tag{2.34}$$

where c_0 is the initial cohesion.

The flow and plastic potential vectors take the form

$$\mathbf{f} = \frac{3}{2\bar{\sigma}} \mathbf{P}\boldsymbol{\sigma} + \alpha_1 \boldsymbol{\pi} \tag{2.35}$$

$$\mathbf{g} = \frac{3}{2\bar{\sigma}} \mathbf{P}\boldsymbol{\sigma} + \alpha_2 \boldsymbol{\pi} \tag{2.36}$$

The formulation derived for the equivalent plastic strain rate $\dot{\bar{\varepsilon}}^{\mathrm{p}}$ and the methods used to determine plastic multiplier rate $\dot{\gamma}$ for isotropic hardening are given in Table 2.7. The models DP1 and DP4 derived an expression for *f* which is a function of $\dot{\gamma}$ and is solved using Regula-Falsi and Newton-Raphson method respectively. The models DP1 use a standard set of parameters ($b_1 \ldots b_3$) to compute $\dot{\bar{\varepsilon}}^{\mathrm{p}}$ from Table 2.4 using equation (2.23). The model DP3 uses classical continuum expression to calculate the plastic multiplier.

Table 2.7 Equivalent plastic strain and plastic multiplier for DP models.

Model	Equivalent plastic strain rate, $\dot{\bar{\varepsilon}}^{p}$	Plastic multiplier, $\dot{\gamma}$
DP1	Equation (2.23)	$f(\dot{\gamma})=0$ Regula-Falsi Method
DP2	$[\dot{\boldsymbol{\varepsilon}}^{p}:\dot{\boldsymbol{\varepsilon}}^{p}+l^{2}(\dot{\boldsymbol{\kappa}}^{p}:\dot{\boldsymbol{\kappa}}^{p})]^{1/2}$	Stress Integration algorithm, 4^{th}-order Runge-Kutta Method
DP3	$[\dot{\boldsymbol{\varepsilon}}^{p}:\dot{\boldsymbol{\varepsilon}}^{p}+l^{2}(\dot{\boldsymbol{\kappa}}^{p}:\dot{\boldsymbol{\kappa}}^{p})]^{1/2}$	$\dfrac{\mathbf{f}\mathbf{D}^{e}\dot{\boldsymbol{\varepsilon}}}{\mathbf{f}^{T}\mathbf{D}^{e}\mathbf{g}+h_{p}}$
DP4	$\dot{\gamma}\left(1+\text{sign}(p)\dfrac{\alpha_{2}}{\sqrt{3}}\right)$	$f(\dot{\gamma})=0$ Newton-Raphson Method

The formulation for pseudo-elastic stiffness operator $\mathbf{D}$ and the consistent elastoplastic modulus $\mathbf{D}^{ep}$ for the DP models are given in Table 2.8. Models DP1 require inverse computation to evaluate $\mathbf{D}$. Although model DP4 does not require any inverse matrix computation, the expression of $\mathbf{D}^{ep}$ is complicated (see equation (2.37)).

Table 2.8 Consistent elastoplastic modulus for the Cosserat DP models.

Model	Consistent elastoplastic modulus $\mathbf{D}^{ep}$	Pseudo-elastic stiffness operator $\mathbf{D}$
DP1	$\mathbf{D}-\frac{\mathbf{D}\mathbf{g}\mathbf{f}^{T}\mathbf{D}}{\mathbf{f}^{T}\mathbf{D}\mathbf{g}+h_{p}}$	$\left[\left[\mathbf{D}^{e}\right]^{-1}+\dot{\gamma}\frac{3}{2\bar{\sigma}}\left(2J_{2}\mathbf{P}-\mathbf{P}\boldsymbol{\sigma}\boldsymbol{\sigma}^{T}\mathbf{P}\right)\right]^{-1}$
DP2 & DP3	$\mathbf{D}-\frac{\mathbf{D}\mathbf{g}\mathbf{f}^{T}\mathbf{D}}{\mathbf{f}^{T}\mathbf{D}\mathbf{g}+h_{p}}$	$\mathbf{D}^{e}$
DP4	Equation (2.37)	Not required

The consistent elastoplastic modulus for DP4 is written as

$$\begin{aligned}\mathbf{D}^{ep}=\mathbf{P}^{*}&\left[\frac{3\left(1-\alpha+c_{\lambda}\right)}{2\bar{\sigma}^{2}}\mathbf{P}\boldsymbol{\sigma}\left(\mathbf{P}\boldsymbol{\sigma}\right)^{T}+\mathbf{C}_{\alpha}\right]\mathbf{D}^{ed}\mathbf{P}^{*}+\\ K&\left(1+\frac{K\alpha_{1}\alpha_{2}c_{\lambda}}{\mu}\right)\mathbf{m}\mathbf{m}^{T}+\frac{\sqrt{3}}{\bar{\sigma}}c_{\lambda}K\left[\alpha_{1}\mathbf{P}^{*}\left(\mathbf{P}\boldsymbol{\sigma}\right)\mathbf{m}^{T}+3\alpha_{2}\mathbf{m}\left(\mathbf{P}\boldsymbol{\sigma}\right)^{T}\mathbf{P}^{*}\right]\end{aligned} \tag{2.37}$$

where K is the elastic bulk modulus. The formulation of K, $\mathbf{P}^{*}$, α, c_{λ} and $\mathbf{C}_{\alpha}$ is given in Appendix 1.

2.2.3 New von Mises and Drucker-Prager models

In this section new Cosserat von Mises (VM5) and Drucker-Prager (DP5) type plasticity models are developed and presented in details. The main features of the new plasticity models are that the micro-rotation (rotation-gradient) is not considered in plasticity formulations. As a result, the plasticity formulations remain the same as classical. The new plasticity models reduce the number of Cosserat parameters, making it simpler to implement.

The new plasticity model VM5 and DP5 follow the same basic formulations in section 2.1. The stress-strain relation is given by equation (2.2). The Cosserat elastic stiffness matrix under the plane-strain condition is given by equation (2.10). The two dimensionless parameters ($a = 0.5$ and $b = 2$) appear in addition to Lamé parameters (λ and μ) as in classical continuum. The Cosserat shear modulus is defined by equation (2.11). Therefore, the basic plasticity formulation is the same as the existing Cosserat models.

The proposed models VM5 and DP5 are developed by considering the plasticity formulations same as classical. The classical expression of $J_2 = (1/2)s_{ij}s_{ij}$, which is obtained by assuming $m_{ij} = 0$, $s_{ij} = s_{ji}$ and $a_1 = a_2 = 1/4$ in equation (2.16). The proposed models ignore additional Cosserat parameters a_3 and a_4 which makes the computation simpler. The classical strain-hardening hypothesis in equation (2.25) can be retrieved if $\dot{\kappa}^p_{ij} = 0$ and $\dot{e}^p_{ij} = \dot{e}^p_{ji}$ from equation (2.23) and implies the constraint in equation (2.24). The newly developed plasticity models assume classical strain-hardening hypothesis by ignoring the additional Cosserat parameter b_3 due to micro-rotation.

The plastic multiplier and the consistent elastoplastic modulus formulation for the new VM5 model are the same as model VM1 and VM2 respectively. The plastic multiplier and the consistent elastoplastic modulus formulation for the new DP5 model are the same as model DP1 as shown in Table 2.7 and Table 2.8 respectively.

The main advantage of the proposed model VM5 and DP5 is that it requires only three additional Cosserat parameters (a, b and l) compared to classical and therefore more straightforward to implement. On the other hand, the existing Cosserat plasticity models require ten additional parameters.

2.3 Strain-gradient general framework

2.3.1 Strain-gradient (Form-I)

The strain energy density function $\widetilde{W}(\varepsilon_{ij}, \widetilde{\kappa}_{ijk})$ for isotropic linear gradient elasticity (Form-I) can be expressed (Mindlin R. , 1964) as

$$\widetilde{W} = \frac{1}{2}\widetilde{\lambda}\varepsilon_{ii}\varepsilon_{jj} + \widetilde{\mu}\varepsilon_{ij}\varepsilon_{ij} + \widetilde{a}_1\widetilde{\kappa}_{ijj}\widetilde{\kappa}_{ikk} + \widetilde{a}_2\widetilde{\kappa}_{iik}\widetilde{\kappa}_{kjj} + \widetilde{a}_3\widetilde{\kappa}_{iik}\widetilde{\kappa}_{jjk} + \widetilde{a}_4\widetilde{\kappa}_{ijk}\widetilde{\kappa}_{ijk} + \widetilde{a}_5\widetilde{\kappa}_{ijk}\widetilde{\kappa}_{kji} \tag{2.38}$$

where $\widetilde{W}$ is a function of both the conventional strain

$$\varepsilon_{ij} = \varepsilon_{ji} = \frac{1}{2}\left(u_{i,j} + u_{j,i}\right) \tag{2.39}$$

and the second-order displacement gradients (or the gradient of the strain)

$$\widetilde{\kappa}_{ijk} = \widetilde{\kappa}_{jik} = u_{k,ij} = \varepsilon_{ki,j} + \varepsilon_{kj,i} - \varepsilon_{ij,k} \tag{2.40}$$

and depends on five independent material parameters $\widetilde{a}_1 \ldots \widetilde{a}_5$ of dimension stress times length squared. The work conjugate quantities of the strains and the second order displacement gradients are the stresses σ_{ij} and the higher-order stresses $\widetilde{\mu}_{ijk}$ respectively, which are defined as

$$\sigma_{ij} = \frac{\partial \widetilde{W}(\varepsilon_{ij}, \widetilde{\kappa}_{ijk})}{\partial \varepsilon_{ij}} \tag{2.41}$$

$$\widetilde{\mu}_{ijk} = \frac{\partial \widetilde{W}(\varepsilon_{ij}, \widetilde{\kappa}_{ijk})}{\partial \widetilde{\kappa}_{ijk}} \tag{2.42}$$

Then

$$\sigma_{ij} = \widetilde{\lambda}\delta_{ij}\varepsilon_{kk} + 2\widetilde{\mu}\varepsilon_{ij} \tag{2.43}$$

$$\begin{aligned}\tilde{\mu}_{ijk} &= \frac{1}{2}\tilde{a}_1\left(\delta_{jk}\tilde{\kappa}_{ppi} + 2\delta_{ij}\tilde{\kappa}_{kpp} + \delta_{ik}\tilde{\kappa}_{ppj}\right) + \tilde{a}_2\left(\delta_{jk}\tilde{\kappa}_{ipp} + \delta_{ik}\tilde{\kappa}_{jpp}\right) \\ &+ 2\tilde{a}_3\delta_{ij}\tilde{\kappa}_{ppk} + 2\tilde{a}_4\tilde{\kappa}_{ijk} + \tilde{a}_5\left(\tilde{\kappa}_{kji} + \tilde{\kappa}_{kij}\right)\end{aligned} \tag{2.44}$$

2.3.2 Strain-gradient (Form-II)

The strain energy density function $\hat{W}(\varepsilon_{ij}, \hat{\kappa}_{ijk})$ for isotropic linear gradient elasticity (Form-II) can be expressed (Mindlin R. , 1964) as

$$\begin{aligned}\hat{W} &= \frac{1}{2}\tilde{\lambda}\varepsilon_{ii}\varepsilon_{jj} + \tilde{\mu}\varepsilon_{ij}\varepsilon_{ij} + \\ &\hat{a}_1\hat{\kappa}_{iik}\hat{\kappa}_{kjj} + \hat{a}_2\hat{\kappa}_{ijj}\hat{\kappa}_{ikk} + \hat{a}_3\hat{\kappa}_{iik}\hat{\kappa}_{jjk} + \hat{a}_4\hat{\kappa}_{ijk}\hat{\kappa}_{ijk} + \hat{a}_5\hat{\kappa}_{ijk}\hat{\kappa}_{kji}\end{aligned} \tag{2.45}$$

where $\hat{W}$ is a function of both the conventional strains in equation (2.39) and the strain gradients

$$\hat{\kappa}_{ijk} = \hat{\kappa}_{ikj} = \varepsilon_{jk,i} = \varepsilon_{kj,i} \tag{2.46}$$

and depends on five independent material parameters $\hat{a}_1 \ldots \hat{a}_5$ of dimension stress times length squared. The work conjugate quantities of the strains and the strain gradients are the stresses σ_{ij} and the higher-order stresses $\hat{\mu}_{ijk}$ respectively, which are defined as

$$\sigma_{ij} = \frac{\partial \hat{W}(\varepsilon_{ij}, \hat{\kappa}_{ijk})}{\partial \varepsilon_{ij}} \tag{2.47}$$

$$\hat{\mu}_{ijk} = \frac{\partial \hat{W}(\varepsilon_{ij}, \hat{\kappa}_{ijk})}{\partial \hat{\kappa}_{ijk}} \tag{2.48}$$

Hence,

$$\sigma_{ij} = \tilde{\lambda}\delta_{ij}\varepsilon_{kk} + 2\tilde{\mu}\varepsilon_{ij} \tag{2.49}$$

$$\begin{aligned}\hat{\mu}_{ijk} &= \frac{1}{2}\hat{a}_1\left(\delta_{ij}\hat{\kappa}_{kpp} + 2\delta_{jk}\hat{\kappa}_{ppi} + \delta_{ik}\hat{\kappa}_{jpp}\right) + 2\hat{a}_2\delta_{jk}\hat{\kappa}_{ipp} \\ &+ \hat{a}_3\left(\delta_{ij}\hat{\kappa}_{ppk} + \delta_{ik}\hat{\kappa}_{ppj}\right) + 2\hat{a}_4\hat{\kappa}_{ijk} + \hat{a}_5\left(\hat{\kappa}_{kji} + \hat{\kappa}_{jki}\right)\end{aligned} \tag{2.50}$$

where

$$\begin{aligned}&\hat{a}_1 = 2\tilde{a}_1 - 4\tilde{a}_3, \qquad \hat{a}_2 = -\tilde{a}_1 + \tilde{a}_2 + \tilde{a}_3 \\ &\hat{a}_3 = 4\tilde{a}_3, \qquad \hat{a}_4 = 3\tilde{a}_4 - \tilde{a}_5, \qquad \hat{a}_5 = -2\tilde{a}_4 + \tilde{a}_5\end{aligned} \tag{2.51}$$

Note that Mindlin (1964) presented three different forms of gradient elasticity depending on how the components of the second gradient of the displacement are grouped together, all forms are completely equivalent. Only Form-I and Form-II are presented in this chapter.

2.4 Fleck-Hutchinson strain-gradient model

The strain energy density $W(\varepsilon_{ij}, \eta'^{(I)}_{ijk})$ for a purely elastic isotropic, compressible solid (Fleck & Hutchinson, 1997) can be written as

$$\begin{aligned}W &= \frac{1}{2}\lambda\varepsilon_{ii}\varepsilon_{jj} + \mu\varepsilon_{ij}\varepsilon_{ij} + \\ &E\left(L_1^2\kappa'^{(1)}_{ijk}\kappa'^{(1)}_{ijk} + L_2^2\kappa'^{(2)}_{ijk}\kappa'^{(2)}_{ijk} + L_3^2\kappa'^{(3)}_{ijk}\kappa'^{(3)}_{ijk} + \right. \\ &\left. L_4^2\kappa^{H}_{ijk}\kappa^{H}_{ijk} + L_5^2\kappa^{H}_{ijk}\kappa'^{(3)}_{ijk}\right)\end{aligned} \tag{2.52}$$

The five elastic length scales $L_1 \ldots L_5$ have no physical significance in the equation (2.52). The strain energy density $W(\varepsilon_{ij}, \kappa'^{(I)}_{ijk})$ is a function of both the conventional strains ε_{ij} and orthogonal decomposition of the deviatoric strain-gradient $\boldsymbol{\kappa}'$

$$\kappa'_{ijk} = \kappa'^{(1)}_{ijk} + \kappa'^{(2)}_{ijk} + \kappa'^{(3)}_{ijk} \tag{2.53}$$

into three tensors $\boldsymbol{\kappa}'^{(I)}$

$$\kappa'^{(1)}_{ijk} = \kappa'^{S}_{ijk} - \frac{1}{5}\left(\delta_{ij}\kappa'^{S}_{kpp} + \delta_{jk}\kappa'^{S}_{ipp} + \delta_{ki}\kappa'^{S}_{jpp}\right)$$

$$\kappa'^{(2)}_{ijk} = \frac{1}{6}\left(e_{ikp}e_{jlm}\kappa'_{lpm} + e_{jkp}e_{ilm}\kappa'_{lpm} + 2\kappa'_{ijk} - \kappa'_{jki} - \kappa'_{kij}\right) \tag{2.54}$$

$$\kappa'^{(3)}_{ijk} = \frac{1}{6}\left(-e_{ikp}e_{jlm}\kappa'_{lpm} - e_{jkp}e_{ilm}\kappa'_{lpm} + 2\kappa'_{ijk} - \kappa'_{jki} - \kappa'_{kij}\right)$$
$$+ \frac{1}{5}\left(\delta_{ij}\kappa'^{S}_{kpp} + \delta_{jk}\kappa'^{S}_{ipp} + \delta_{ki}\kappa'^{S}_{jpp}\right)$$

The symmetric part of the deviatoric strain-gradients can be written as

$$\kappa'^{S}_{ijk} = \frac{1}{3}\left(\kappa'_{ijk} + \kappa'_{jki} + \kappa'_{kij}\right) \tag{2.55}$$

Note that $\boldsymbol{\kappa}'^{S}$ has the symmetries $\kappa'^{S}_{ijk} = \kappa'^{S}_{jki} = \kappa'^{S}_{kij} = \kappa'^{S}_{jik}$. The deviatoric strain-gradient

$$\kappa'_{ijk} = \kappa_{ijk} - \kappa^{H}_{ijk} \tag{2.56}$$

where $\boldsymbol{\kappa}^{H}$ is the hydrostatic part of the strain-gradient and is given by

$$\kappa^{H}_{ijk} = \frac{1}{4}\left(\delta_{ik}\kappa_{jpp} + \delta_{jk}\kappa_{ipp}\right) \tag{2.57}$$

The work conjugate quantities of orthogonal decomposition of the deviatoric strain gradient are higher-order stresses $m'^{(I)}_{ijk}$ as

$$\mu'^{(1)}_{ijk} = \frac{\partial W(\varepsilon_{ij}, \kappa'^{(1)}_{ijk})}{\partial \kappa'^{(1)}_{ijk}} = EL_1^2\kappa'^{(1)}_{ijk}$$

$$\mu'^{(2)}_{ijk} = \frac{\partial W(\varepsilon_{ij}, \kappa'^{(1)}_{ijk})}{\partial \kappa'^{(2)}_{ijk}} = EL_2^2\kappa'^{(2)}_{ijk} \tag{2.58}$$

$$\mu'^{(3)}_{ijk} = \frac{\partial W(\varepsilon_{ij}, \kappa'^{(I)}_{ijk})}{\partial \kappa'^{(3)}_{ijk}} = EL_3^2 \kappa'^{(3)}_{ijk} + EL_5^2 \kappa^H_{ijk}$$

2.5 Mechanism based strain-gradient plasticity model

The classical continuum plasticity models do not possess any internal length scales, therefore cannot predict size-dependent material behaviour at micron and submicron scales. There are many dislocations at the micron scale such that their collective behaviour should be taken into account by a continuum (but not classical) plasticity models. The strain gradient plasticity theories proposed (Fleck & Hutchinson, 1993; Fleck & Hutchinson, 1997; Huang, Gao, Nix, & Hutchinson, 2000; Shu & Fleck, 1999) based on the notation of geometrically necessary dislocations (Nye, 1953; Cottrell, 1964; Ashby, 1970; Arsenlis & Parks, 1999; Gurtin, 2000) are intended for applications to materials and structures whose dimension controlling plastic deformation falls into the range of micros or sub-microns. The applications of the above theories can be found in micro-components, microelectronic packages, micro-machining, thin films and composite materials.

The micromechanically motivated strain-gradient model for the flow stress of the materials, derived from the Taylor hardening model by Nix and Gao (1998) gives the foundation of the mechanism-based strain-gradient (MSG) plasticity models. The original MSG model (Gao, Huang, Nix, & Hutchinson, 1999; Huang, Gao, Nix, & Hutchinson, 2000) was developed from Toupin-Mindlin theory, interpreted as MSG deformation theory of plasticity. The flow theory of MSG plasticity (Qiu, Huang, Wei, Gao, & Hwang, 2003) is developed following the same multiscale, hierarchical framework for the MSG deformation theory of plasticity. The conventional theory of MSG (CMSG) plasticity is developed (Huang, Qu, Hwang, Li, & Gao, 2004) based on the Taylor dislocation model, but does not involve the higher-order stress and therefore is more straightforward to implement. The main advantage of using CMSG is that common isoparametric elements can be used (Martínez-Pañeda & Betegón, 2015) and therefore the boundary conditions are same as the classical models.

The constitutive relation for the MSG model (Qiu, Huang, Wei, Gao, & Hwang, 2003) is given by

$$\begin{aligned}\dot{\mu}_{ijk} &= c\left[\dot{\kappa}_{ijk}+\frac{1}{2}\left(\dot{\kappa}_{kij}+\dot{\kappa}_{kji}\right)+\left(\frac{2K}{\mu}-\frac{4}{3}\right)\dot{\kappa}^{H}_{ijk}\right]\\ &-\alpha'\left[\frac{3}{2\sigma^2}\frac{c}{1+a}\sigma'_{mn}\left(\sigma'_{ki}\dot{\kappa}_{jmn}+\sigma'_{kj}\dot{\kappa}_{imn}\right)\right]\\ &-\alpha'\left[\frac{3}{4\sigma^2}\frac{1}{1+a}\begin{bmatrix}\sigma'_{ki}\left(\mu_{jmn}+\mu_{jnm}-\mu_{mnj}\right)+\\ \sigma'_{kj}\left(\mu_{imn}+\mu_{inm}-\mu_{mni}\right)\end{bmatrix}\dot{\sigma}'_{mn}\right]\\ &+\alpha'\left[\frac{3}{4\sigma^2}\left(\frac{3\mu}{\sigma}+\frac{e}{1+a}\right)\left(\sigma'_{ki}g_j+\sigma'_{kj}g_i\right)\dot{\bar{\varepsilon}}^{p}\right]\\ &-\alpha'\left[\frac{3\mu}{\sigma}\left(\mu_{ijk}-\frac{K l_{\epsilon}^2}{6}\dot{\kappa}^{H}_{ijk}\right)\dot{\bar{\varepsilon}}^{p}\right]\end{aligned} \tag{2.59}$$

where

$$\alpha'=\begin{cases}0 & \text{if, } f\le 0 \text{ and } \dot{\bar{\varepsilon}}^{p}=0\\ 1 & \text{if, } f=0 \text{ and } \dot{\bar{\varepsilon}}^{p}>0\end{cases} \tag{2.60}$$

and

$$\begin{aligned}c&=\frac{\mu l_{\epsilon}^2}{12}, e=\frac{f_p'\left(\bar{\varepsilon}^{p}\right)}{f_p\left(\bar{\varepsilon}^{p}\right)}+\frac{f_p''\left(\bar{\varepsilon}^{p}\right)}{f_p'\left(\bar{\varepsilon}^{p}\right)}\\ g_k&=\sigma'_{ij}\left(\mu'_{kij}+\mu'_{kji}-\mu'_{ijk}\right)\\ \dot{\bar{\varepsilon}}^{p}&=\dot{\gamma}, \ \sigma=\sigma_y\\ l_{\epsilon}&=\beta\frac{\mu}{\sigma_y}b\end{aligned} \tag{2.61}$$

The material parameter K is the elastic bulk modulus, σ_y is the current yield stress, b is the magnitude of the Burger vector, l_{ϵ} is the mesoscale cell size, and the coefficient β is on the order of ten.

2.6 Strain-gradient plasticity basic equations

In a small strain, nonlinear deformation, the decomposition of the total strain rate $\dot{\boldsymbol{\varepsilon}}$ into elastic and plastic strain rate is given by equation (2.1). Similarly, the strain-gradient rate is decomposed into the elastic and plastic part as

$$\dot{\boldsymbol{\kappa}} = \dot{\boldsymbol{\kappa}}^{e} + \dot{\boldsymbol{\kappa}}^{p} \tag{2.62}$$

The stress rate must satisfy according to equation (2.2). Re-arranging and substituting equation (2.1) into (2.2) gives the stress rate in terms of strain rate and the plastic strain rate in equation (2.3). As in classical plasticity, the plastic strain rate is given by equation (2.4). Similarly, the higher-order stress must satisfy

$$\dot{\boldsymbol{\mu}} = \mathbf{C}^{e}\dot{\boldsymbol{\kappa}}^{e} \tag{2.63}$$

A simplified isotropic elastic material matrix $\mathbf{C}^{e}$ of Form-II (Papanicolopulos & Zervos, 2010) is obtained by setting

$$\begin{gathered} \hat{a}_1 = \hat{a}_3 = \hat{a}_5 = 0 \\ \hat{a}_2 = \frac{1}{2}\lambda l^2 \text{ , } \hat{a}_4 = \mu l^2 \end{gathered} \tag{2.64}$$

An equivalent isotropic elastic material matrix $\mathbf{C}^{e}$ of Form-I can be obtained using equations (2.51) as

$$\begin{gathered} \tilde{a}_1 = \tilde{a}_3 = 0 \\ \tilde{a}_2 = \frac{1}{2}\lambda l^2 \text{ , } \tilde{a}_4 = \mu l^2 \\ \tilde{a}_5 = 2\mu l^2 \end{gathered} \tag{2.65}$$

Although the material model is straightforward, the physical interpretation of the parameter choice in equation (2.64) is not defined. Substituting equation (2.62) into (2.63) gives

$$\dot{\boldsymbol{\mu}} = \mathbf{C}^{\mathrm{e}}\left(\dot{\boldsymbol{\kappa}} - \dot{\boldsymbol{\kappa}}^{\mathrm{p}}\right) \tag{2.66}$$

The derived formulation of the plastic strain-gradient rate $\dot{\boldsymbol{\kappa}}^{\mathrm{p}}$ for different strain-gradient plasticity models is given in Table 2.9. The FH and MSG models derived different formulation of $\dot{\boldsymbol{\kappa}}^{\mathrm{p}}\left(\dot{\boldsymbol{\varepsilon}}, \dot{\boldsymbol{\kappa}}\right)$ which is a function of both the strain and the strain-gradient. When the plastic length scales l_{I} in FH model approaches infinity, the plastic strain-gradient becomes zero. Therefore, CCM model is a unique (limit) case of FH model.

Table 2.9 Plastic strain-gradient rate $\dot{\boldsymbol{\kappa}}^{\mathrm{p}}$ for different models.

Model	References	$\dot{\boldsymbol{\kappa}}^{\mathrm{p}}$
FH	(Fleck & Hutchinson, 1997)	$\dot{\gamma}\frac{1}{\bar{\sigma}}\sum_{\mathrm{I}=1}^{3}\left[l_{\mathrm{I}}^{-2}\boldsymbol{\mu}'^{(\mathrm{I})}\right]$
CCM	(Chambon, Caillerie, & Matsuchima, 2001)	0
MSG	(Qiu, Huang, Wei, Gao, & Hwang, 2003)	$\dot{\boldsymbol{\kappa}}^{\mathrm{p}}\left(\dot{\boldsymbol{\varepsilon}}, \dot{\boldsymbol{\kappa}}\right)$

The orthogonal decomposition of the deviatoric higher order stress vectors can be written as

$$\begin{aligned}
\boldsymbol{\mu}'^{(1)} &= \mathrm{EL}_1^2\boldsymbol{\kappa}'^{(1)} \\
\boldsymbol{\mu}'^{(2)} &= \mathrm{EL}_2^2\boldsymbol{\kappa}'^{(2)} \\
\boldsymbol{\mu}'^{(3)} &= \mathrm{EL}_3^2\boldsymbol{\kappa}'^{(3)} + \mathrm{EL}_5^2\boldsymbol{\kappa}^{\mathrm{H}}
\end{aligned} \tag{2.67}$$

where

$$\boldsymbol{\kappa}'^{(1)} = \mathbf{A}^{(1)}\boldsymbol{\kappa}'$$
$$\boldsymbol{\kappa}'^{(2)} = \mathbf{A}^{(2)}\boldsymbol{\kappa}' \qquad (2.68)$$
$$\boldsymbol{\kappa}'^{(3)} = \mathbf{A}^{(3)}\boldsymbol{\kappa}'$$

The deviatoric and hydrostatic part of the strain gradient is given by

$$\boldsymbol{\kappa}' = \boldsymbol{\kappa} - \boldsymbol{\kappa}^{\mathrm{H}} \qquad (2.69)$$

$$\boldsymbol{\kappa}^{\mathrm{H}} = \mathbf{A}^{\mathrm{H}}\boldsymbol{\kappa}' \qquad (2.70)$$

The matrices $\mathbf{A}^{(1)} \cdots \mathbf{A}^{(3)}$ and $\mathbf{A}^{\mathrm{H}}$ can be computed using equations (2.54) and (2.57) respectively. It should be noted that the current formulation of the FH model predicts that higher order stress remains present in the case of purely elastic response with vanishing plastic strain-gradients. A sensible strategy is to take $\mathrm{L_I} << l_{\mathrm{I}}$, this is purely for mathematical convenience, and is given no physical significance (Fleck & Hutchinson, 1997).

2.7 Strain-gradient plasticity models

2.7.1 Von Mises

In this section, pressure independent von Mises type strain-gradient plasticity models are compared in detail. Three different strain-gradient plasticity models are considered as shown in Table 2.9. The yield function for the models is given in Table 2.10.

Table 2.10 Yield function for the strain-gradient plasticity models.

Model	Yield function
FH	$f\left(\boldsymbol{\sigma},\boldsymbol{\mu}'^{(\mathrm{I})},\bar{\varepsilon}^{\mathrm{p}}\right)=\bar{\sigma}\left(\boldsymbol{\sigma},\boldsymbol{\mu}'^{(\mathrm{I})}\right)-\sigma_{\mathrm{y}}\left(\bar{\varepsilon}^{\mathrm{p}}\right)$
CCM	$f\left(\boldsymbol{\sigma},\bar{\varepsilon}^{\mathrm{p}}\right)=\bar{\sigma}\left(\boldsymbol{\sigma}\right)-\sigma_{\mathrm{y}}\left(\bar{\varepsilon}^{\mathrm{p}}\right)$
MSG	$f\left(\boldsymbol{\sigma},\bar{\varepsilon}^{\mathrm{p}},\bar{\kappa}\right)=\bar{\sigma}\left(\boldsymbol{\sigma}\right)-\sigma_{\mathrm{y}}\left(\bar{\varepsilon}^{\mathrm{p}},\bar{\kappa}\right)$

The effective and current yield stress formulations for different models is given in Table 2.11. The effective stress of the FH model depends on both the stress and the orthogonal decompositions of the higher order stresses whereas for CCM and MSG model effective stress depends only on stresses. For the FH and CCM models, the current yield stress σ_{y} is a function of $\bar{\varepsilon}^{\mathrm{p}}$ as in the classical models, whereas for the MSG model σ_{y} is a function of both $\bar{\varepsilon}^{\mathrm{p}}$ and $\bar{\kappa}$.

Table 2.11 Effective and current yield stress.

Model	Effective stress, $\bar{\sigma}$	Current yield stress, σ_{y}
FH	$\left[\frac{3}{2}\mathbf{s}.\mathbf{s}+\sum_{\mathrm{I}=1}^{3}\left[l_{\mathrm{I}}^{-2}\boldsymbol{\mu}'^{(\mathrm{I})}.\boldsymbol{\mu}'^{(\mathrm{I})}\right]\right]^{\frac{1}{2}}$	$\sigma_{\mathrm{y}}\left(\bar{\varepsilon}^{p}\right)=\sigma_{\mathrm{y0}}+\mathrm{h}_{\mathrm{p}}\bar{\varepsilon}^{p}$
CCM	$\left[\frac{3}{2}\mathbf{s}.\mathbf{s}\right]^{\frac{1}{2}}$	$\sigma_{\mathrm{y}}\left(\bar{\varepsilon}^{p}\right)=\sigma_{\mathrm{y0}}+\mathrm{h}_{\mathrm{p}}\bar{\varepsilon}^{p}$
MSG	$\left[\frac{3}{2}\mathbf{s}.\mathbf{s}\right]^{\frac{1}{2}}$	$\sigma_{\mathrm{y}}\left(\bar{\varepsilon}^{\mathrm{p}},\bar{\kappa}\right)=\sigma_{\mathrm{ref}}\left[f_{\mathrm{p}}^{2}(\bar{\varepsilon}^{\mathrm{p}})+l\,\bar{\kappa}\right]^{\frac{1}{2}}$

The deviatoric stress is given by

$$s_{ij} = \sigma_{ij} - \frac{1}{3}\delta_{ij}\sigma_{kk} \tag{2.71}$$

The internal length scale for the MSG model is defined as

$$l = 18\alpha^2\left(\frac{\mu}{\sigma_{ref}}\right)^2 b \tag{2.72}$$

The uniaxial stress-strain relation for the MSG model gives

$$\sigma_{ref}\, f_p(\bar{\varepsilon}^p) = \sigma_{ref}\left[\frac{\sigma_{y0}}{E} + \bar{\varepsilon}^p\right]^N \tag{2.73}$$

where α is the Taylor coefficient, σ_{y0} is the initial yield stress in uniaxial tension and N is the plastic work-hardening exponent ($0 \leq N < 1$). The effective strain-gradient is given by

$$\bar{\kappa} = \left[\frac{1}{4}\boldsymbol{\kappa}'\boldsymbol{\kappa}'\right]^{1/2} \tag{2.74}$$

The plastic multiplier formulation for different strain-gradient plasticity models is given in Table 2.12. The plastic multiplier of FH (and MSG) model depends on both the strain and strain-gradient whereas CCM model depends only on strain (as in classical).

Table 2.12 Plastic multiplier of the strain-gradient plasticity models.

Model	Plastic multiplier, $\dot{\gamma}$
FH	$\dfrac{\dot{\bar{\sigma}}}{h_p}$
CCM	$\dfrac{\mathbf{f}\mathbf{D}^e\dot{\boldsymbol{\varepsilon}}}{\mathbf{f}^T\mathbf{D}^e\mathbf{g}+h_p}$
MSG	$\dfrac{1}{\sigma_y(1+a)}\left(\mathbf{s}.\dot{\boldsymbol{\varepsilon}}-3\alpha^2\mu b\dot{\kappa}\right)$

The overall effective stress and the strain-gradient rate is given by

$$\dot{\bar{\sigma}}=\left[\frac{3}{2\bar{\sigma}}\mathbf{s}.\dot{\mathbf{s}}+\frac{1}{\bar{\sigma}}\sum_{I=1}^{3}\left[l_I^{-2}\dot{\boldsymbol{\mu}}'^{(I)}.\dot{\boldsymbol{\mu}}'^{(I)}\right]\right]^{1/2} \tag{2.75}$$

$$\dot{\kappa}=\frac{1}{4\bar{\kappa}}\boldsymbol{\kappa}'.\dot{\boldsymbol{\kappa}} \tag{2.76}$$

All the models assumed associated flow rule in equation (2.21). The flow vector (as in classical) is given by equation (2.22). The elastoplastic modulus is given by

$$\mathbf{D}^{ep}=\mathbf{D}^e-\frac{\mathbf{D}^e\mathbf{g}\mathbf{f}^T\mathbf{D}^e}{\mathbf{f}^T\mathbf{D}^e\mathbf{g}+h_p} \tag{2.77}$$

All the strain-gradient plasticity models (FH, CCM and MSG) requires five additional parameters ($\tilde{a}_1\ldots\tilde{a}_5$ and $\hat{a}_1\ldots\hat{a}_5$ for Form-I and Form-II respectively) to evaluate $\mathbf{C}^e$.

2.7.2 Drucker-Prager

In this section, pressure-dependent Drucker-Prager strain-gradient plasticity models are compared in details. Three different strain-gradient Drucker-Prager models are

developed based on FH, CCM and MSG models in the previous section. The yield function for the strain-gradient Drucker-Prager models is given in Table 2.13.

Table 2.13 Yield function for strain-gradient Drucker-Prager models.

Model	Yield function
FHDP	$f\left(\boldsymbol{\sigma},\boldsymbol{\mu}'^{(\mathrm{I})},\bar{\varepsilon}^{\mathrm{p}}\right)=\bar{\sigma}\left(\boldsymbol{\sigma},\boldsymbol{\mu}'^{(\mathrm{I})}\right)+\alpha_{\mathrm{I}}\sigma_{\mathrm{m}}\left(\boldsymbol{\sigma}\right)-\beta_{\mathrm{I}}\sigma_{\mathrm{y}}\left(\bar{\varepsilon}^{\mathrm{p}}\right)$
CCMDP	$f\left(\boldsymbol{\sigma},\bar{\varepsilon}^{\mathrm{p}}\right)=\bar{\sigma}\left(\boldsymbol{\sigma}\right)+\alpha_{\mathrm{I}}\sigma_{\mathrm{m}}\left(\boldsymbol{\sigma}\right)-\beta_{\mathrm{I}}\sigma_{\mathrm{y}}\left(\bar{\varepsilon}^{\mathrm{p}}\right)$
MSGDP	$f\left(\boldsymbol{\sigma},\bar{\varepsilon}^{\mathrm{p}},\bar{\kappa}\right)=\bar{\sigma}\left(\boldsymbol{\sigma}\right)+\alpha_{\mathrm{I}}\sigma_{\mathrm{m}}\left(\boldsymbol{\sigma}\right)-\beta_{\mathrm{I}}\sigma_{\mathrm{y}}\left(\bar{\varepsilon}^{\mathrm{p}},\bar{\kappa}\right)$

The potential function for the Drucker-Prager models is given in Table 2.14. The material parameters α_1 , α_2 and β_1 which enters the plasticity calculations can be evaluated using equations (2.30) and (**2.31**).

Table 2.14 Plastic potential function for strain-gradient Drucker-Prager models.

Model	Plastic potential function
FHDP	$g\left(\boldsymbol{\sigma},\boldsymbol{\mu}'^{(\mathrm{I})}\right)=\bar{\sigma}\left(\boldsymbol{\sigma},\boldsymbol{\mu}'^{(\mathrm{I})}\right)+\alpha_{2}\sigma_{\mathrm{m}}\left(\boldsymbol{\sigma}\right)$
CCMDP	$g\left(\boldsymbol{\sigma}\right)=\bar{\sigma}\left(\boldsymbol{\sigma}\right)+\alpha_{2}\sigma_{\mathrm{m}}\left(\boldsymbol{\sigma}\right)$
MSGDP	$g\left(\boldsymbol{\sigma}\right)=\bar{\sigma}\left(\boldsymbol{\sigma}\right)+\alpha_{2}\sigma_{\mathrm{m}}\left(\boldsymbol{\sigma}\right)$

The effective stress $\bar{\sigma}$ and the cohesion $c=\sigma_{\mathrm{y}}$ are computed in a similar manager to that of von Mises plasticity models as shown in Table 2.11. The flow and plastic potential vectors can be evaluated using equation (2.35) and (**2.36**) respectively. The mean stress is given by

$$\sigma_m = \frac{1}{3}\mathrm{tr}(\boldsymbol{\sigma}) \tag{2.78}$$

The plastic multiplier for the Drucker-Prager models can be evaluated from Table 2.12. The continuum elastoplastic modulus is given by equation (2.77).

2.8 Conclusions

In Cosserat von Mises type plasticity models, different researchers have derived different formulation for the plastic multiplier and consistent elastoplastic modulus. Also, the value of the Cosserat parameters used to evaluate the elastic stiffness matrix, J_2 and the equivalent plastic strain rate are different which make it difficult to understand differences in the numerical behaviour of the models. The model VM5 is proposed in this chapter, which requires the lowest number of Cosserat parameters and therefore the plasticity formulation is the same as the classical one. The idea of reducing the number of parameter in Cosserat plasticity model VM5 came from CCM model where the plastic part of the strain-gradient is zero. As a result the plasticity calculations remain same as the classical plasticity. In Cosserat Drucker-Prager, type plasticity models, the formulation derived for the equivalent plastic strain rate and the consistent elastoplastic modulus are different. The models also use different methods to compute the plastic multiplier. The model DP5 is proposed in this chapter by reducing the number of Cosserat parameters so that the plasticity part is essentially the same as classical.

In strain-gradient von Mises and Drucker-Prager type plasticity models, the yield function can be dependent on a combination of stress, orthogonal decomposition of the deviatoric higher order stress, equivalent plastic strain and the effective strain-gradient. The formulation of the plastic multipliers is different for the strain-gradient plasticity models. Therefore the models are entirely different and expected to predict different numerical behaviour. The model CCM is relatively straightforward to implement compared to FH and MSG models since plastic strain-gradient do not enter the higher order stress calculations.

An overview of the main features of the Cosserat and strain-gradient plasticity models are summarised in Table 2.15. It should be noted that for Cosserat and strain-gradient models $\dot{\boldsymbol{\kappa}}$ is the rotation-gradient and strain-gradient respectively. The Cosserat and strain-gradient (FH, CCM and MSG) plasticity formulation for the higher order stresses and the yield functions are different. Therefore their numerical solutions are expected to be different.

Table 2.15 Overview of the Cosserat and strain-gradient plasticity models.

Model	Stress-strain	Higher order stress	Yield function
Cosserat	$\dot{\boldsymbol{\sigma}} = \mathbf{D}^{\mathrm{e}}(\dot{\boldsymbol{\varepsilon}} - \dot{\boldsymbol{\varepsilon}}^{\mathrm{p}})$	$\dot{\mathbf{m}} = \mathbf{C}^{\mathrm{e(cos)}}\left(\dot{\boldsymbol{\kappa}} - \dot{\boldsymbol{\kappa}}^{\mathrm{p}}\right)$	$f\left(\boldsymbol{\sigma}, \mathbf{m}, \bar{\varepsilon}^{\mathrm{p}}\right)$
FH	$\dot{\boldsymbol{\sigma}} = \mathbf{D}^{\mathrm{e}}(\dot{\boldsymbol{\varepsilon}} - \dot{\boldsymbol{\varepsilon}}^{\mathrm{p}})$	$\dot{\boldsymbol{\mu}} = \mathbf{C}^{\mathrm{e}}\left(\dot{\boldsymbol{\kappa}} - \dot{\boldsymbol{\kappa}}^{\mathrm{p}}\left(\dot{\boldsymbol{\varepsilon}}, \dot{\boldsymbol{\kappa}}\right)\right)$	$f\left(\boldsymbol{\sigma}, \boldsymbol{\mu}'^{(\mathrm{I})}, \bar{\varepsilon}^{\mathrm{p}}\right)$
CCM	$\dot{\boldsymbol{\sigma}} = \mathbf{D}^{\mathrm{e}}(\dot{\boldsymbol{\varepsilon}} - \dot{\boldsymbol{\varepsilon}}^{\mathrm{p}})$	$\dot{\boldsymbol{\mu}} = \mathbf{C}^{\mathrm{e}}\dot{\boldsymbol{\kappa}}$	$f\left(\boldsymbol{\sigma}, \bar{\varepsilon}^{\mathrm{p}}\right)$
MSG	$\dot{\boldsymbol{\sigma}} = \mathbf{D}^{\mathrm{e}}(\dot{\boldsymbol{\varepsilon}} - \dot{\boldsymbol{\varepsilon}}^{\mathrm{p}})$	$\dot{\boldsymbol{\mu}} = \mathbf{C}^{\mathrm{e}}\left(\dot{\boldsymbol{\kappa}} - \dot{\boldsymbol{\kappa}}^{\mathrm{p}}\left(\dot{\boldsymbol{\varepsilon}}, \dot{\boldsymbol{\kappa}}\right)\right)$	$f\left(\boldsymbol{\sigma}, \bar{\varepsilon}^{\mathrm{p}}, \bar{\kappa}\right)$

3 Finite elements for Cosserat and strain-gradient models

In this chapter, a literature review of the Cosserat finite elements proposed or used in different models are presented. A detailed comparison of different Cosserat element formulations are presented concerning the number of DOF at nodes, interpolation shape function for displacement (and rotation) and the integration scheme employed.

This chapter also contains a literature review of the existing elements for strain-gradient models. A detailed formulation of the existing and new elements for strain-gradient models are presented and compared regarding formulatrions, ease of numerical implementation and the computational cost.

3.1 A review of Cosserat finite elements

In this section, ten types of isoparametric Cosserat finite elements are presented including a detailed literature review of the elements. Figure 3.1 shows the sketch of ten types of Cosserat elements. In 2D Cosserat elements, two translational (u_x, u_y) and an independent rotational (ω_z) DOF are considered at nodes.

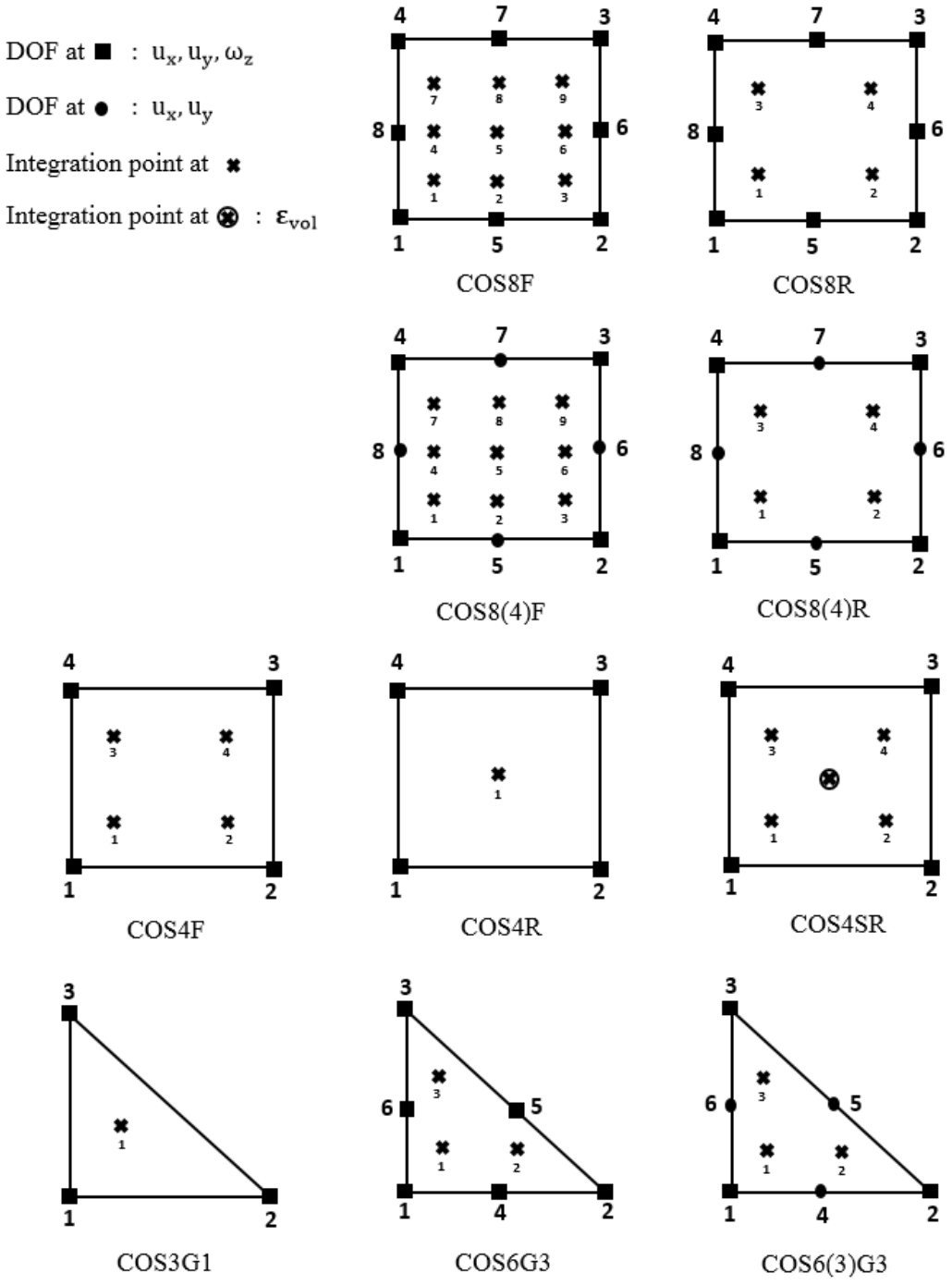

Figure 3.1 Sketch of ten types of Cosserat 2D element.

The code used for the quadrilateral element to label the type of elements, for example, COS8(4)F, is as follows: COS designates Cosserat elements; the number 8 represents the number of nodes with two translational DOF, the number within the bracket (.) represents the number of nodes with an independent rotational DOF and the

letter F indicates a full (quintic) integration scheme. The code employed for triangular elements to label the types of element: for example COS6(3)G3. COS designates Cosserat elements; the number 6 represents the number of nodes with two translational DOF, the number within the bracket (.) represents the number of nodes with an independent rotational DOF and letter with number G3 indicates the use three Gauss point.

The interpolation of displacement/rotation for a triangular element can be linear/linear, quadratic/linear or quadratic/quadratic, resulting in the COS3, COS6(3) and COS6 element. The triangular elements with one Gauss point rule give COS3G1, and with three-point Gauss rule gives COS6(3)G3 or COS6G3 elements. Similarly, the interpolation of displacement/rotation for quadrilateral elements can be linear/linear, quadratic/linear or quadratic/quadratic, resulting in the COS4, COS8(4) and COS8 element. The 4-node quadrilateral elements with full (cubic, 2x2) and reduced (linear, 1x1) integration scheme give COS4F and COS4R respectively. The 8-node quadrilateral elements with full (quintic, 3x3) and reduced (cubic, 2x2) integration scheme gives COS8(4)F (or COS8F) and COS8(4)R (or COS8R) elements respectively. The 4-node quadrilateral selective reduced (SR) integration element COS4SR uses full and reduced integration for the deviatoric and volumetric strains respectively. The combination of different DOF at nodes, interpolation of displacement/rotation and the integration scheme gives a total of ten Cosserat elements as shown in Table 3.1.

Finite elements for Cosserat continua must separately discretise and interpolate the displacement and the rotational field. For a given shape (e.g. triangle or quadrilateral in two dimensions) it is, therefore, necessary to select the appropriate interpolation for the displacement/rotation. The numerical solution of triangular or quadrilateral elements can be different for different integration scheme. Additionally, there is a need to select the appropriate spatial integration scheme to be used. While this can be chosen based solely on the displacement field, using a scheme that avoids locking and hourglassing, the way integration applies to the two different fields should also be taken into account in determining the appropriate integration scheme.

Table 3.1 Cosserat element with different integration scheme and DOF at nodes.

Element	Integration scheme	DOF at each corner node	DOF at each mid-edge node	Total DOF
COS8F	Quintic	u_x, u_y, ω_z	u_x, u_y, ω_z	24
COS8R	Cubic			
COS8(4)F	Quintic		u_x, u_y	20
COS8(4)R	Cubic			
COS4F			Not applicable	12
COS4R	Linear			
COS4SR	Cubic			
COS6G3	3 point Gauss rule		u_x, u_y, ω_z	18
COS6(3)G3			u_x, u_y	15
COS3G1	1 point Gauss rule		Not applicable	9

A significant amount of work has been carried out on numerical finite element implementation of Cosserat elastoplastic models such as those proposed by De Borst (1991), Papanastasiou et al. (1992) and Manzari (2004). In these models, authors have used different Cosserat elements, which make it unclear to select the appropriate element since there are no detailed comparisons available between the elements in elastoplastic problems. For Cosserat elasticity, the comparisons presented by Providas and Kattis (2002) for triangles and Zhang et al. (2005) for quadrilaterals both showed that all elements pass the patch test. The elements with quadratic/linear interpolation of displacement/rotation give a slightly more accurate result for triangular elements while for quadrilateral elements quadratic/quadratic interpolation of displacement/rotation perform marginally better than quadratic/linear elements. Providas and Kattis (2002) and Zhang et al. (2005) has shown that elements with linear/linear interpolation of displacement/rotation for both triangular and quadrilateral elements give poor performance compared to quadratic/linear or

quadratic/quadratic element. We are not, however, aware of any Cosserat plasticity results available in the literature with quadratic/linear elements.

Sulem and Cerrolaza (2002) suggest quadratic/linear elements but uses linear/linear interpolation, while Adhikary et al. (1999) used the quadratic/quadratic element. De Borst (1991) mentions numerical experimentation for the 6-node triangular quadratic/linear element, but only shows results for the 6-node triangular quadratic/quadratic element. Iordache and Willam (1998) present results for 3-node triangular linear/linear element only, though they also mentioned quadratic/linear and quadratic/quadratic elements. Papanastasiou and Vardoulakis (1992) stated a comparison that shows 9-node Lagrangian quadrilateral element is slightly better than the 8-node quadrilateral element, but the difference is negligible and therefore used the computationally cheaper 8-node quadrilateral element.

De Borst (1991) mentions that 6-node triangular element would require a quartic integration scheme to eliminate the possibility of zero-energy modes, but uses a cubic scheme, and also mentioned a triangular 6-node quadratic/linear interpolation element without showing the detailed results. Some authors (Alsaleh, 2004; Arslan & Sture, 2008) have used 4-node, selective reduced (SR) integration element. The selective reduced elements use a full (cubic, 2x2) integration for all the state variables and only a reduced (linear, 1x1) integration for the volumetric strains. A discussion on 8-node quadratic/quadratic reduced integration elements is given by Godio et al. (2015) for elastic Cosserat plates.

The elements proposed or used in the literature for Cosserat elasticity and plasticity models, and the spatial integration scheme employed are shown in Table 3.2. It is evident from Table 3.2 that different authors have used different Cosserat elements without giving enough information regarding the spatial integration scheme used. Also, no detailed comparisons are presented for the various integration schemes employed. From Table 3.2 it is also apparent that there are no results available for plasticity models using quadratic/linear elements. The quadratic/linear elements are computationally cheaper having a lower number of DOF than quadratic/quadratic elements.

Table 3.2 Summary of surveyed literature on Cosserat finite element analysis.

Reference	Constitutive Model	Element	Integration Scheme
(Nakamura, Benedict, & Lakes, 1984)	Elasticity	COS3	Not stated
(Nakamura & Lakes, 1988)	Elasticity	COS4	Not stated
(Providas & Kattis, 2002)	Elasticity	COS3/6/6(3)	Analytical
(Zhang, Wang, & Liu, 2005)	Elasticity	COS4/8/8(4)	Not stated
(de Borst, 1991)	Von Mises	COS6	Cubic
(de Borst & Sluys, 1991)	Von Mises	COS6	Quartic
(Tejchman & Wu, 1993)	Von Mises	COS3	3 point rule
(Sharbati & Naghdabadi, 2006)	Von Mises	COS4	Not stated
(de Borst, 1993)	Drucker-Prager	COS6	Not stated
(Iordache & Willam, 1998)	Drucker-Prager	COS3	Unclear
(Arslan & Sture, 2008)	Drucker-Prager	COS4	Cubic (SR)
(Peng, Kong, & Xu, 2011)	Drucker-Prager	COS8	Quintic
(Papanastasiou & Vardoulakis, 1992)	Mohr-Coulomb	COS8	Quintic
(Sulem & Cerrolaza, 2002)	Mohr-Coulomb	COS4	Not stated
(Adhikary, Mühlhaus, & Dyskin, 1999)	Mohr-Coulomb	COS8	Quintic
(Manzari, 2004)	Mohr-Coulomb	COS4	Not stated
(Adhikary & Dyskin, 2007)	Mohr-Coulomb	COS8	Not stated
(Papamichos, 2010)	Mohr-Coulomb	COS8	Not stated
(Alsaleh, 2004)	Lade-Kim	COS4	Cubic (SR)

The ten types of Cosserat elements described above can be categorised into three groups of elements:

(i) Quadratic/quadratic and linear/linear - Quadrilateral or triangular elements with the same order of shape function to achieve a higher order interpolation for the rotation than displacement.

(ii) Quadratic/linear - Quadrilateral or triangular elements with shape function one order lower for the rotation than displacement to obtain a same order of interpolation for both rotation and displacement.

(iii) Quadrilateral element with selective reduced integration scheme.

3.2 Cosserat finite element formulation

The equilibrium equation without acceleration in matrix-vector form can be written as

$$\mathbf{L}^{\mathrm{T}}\boldsymbol{\sigma}+\mathbf{b}=0 \tag{3.1}$$

In which $\mathbf{L}$ is the differential operator, $\boldsymbol{\sigma}$ is the stress vector and $\mathbf{b}$ is the body force vector. In the finite element method, the strain vector can be defined as

$$\boldsymbol{\varepsilon}=\mathbf{L}\mathbf{u}=\left[\varepsilon_{xx}\quad \varepsilon_{yy}\quad \varepsilon_{zz}\quad \varepsilon_{xy}\quad \varepsilon_{yx}\quad l\kappa_{xz}\quad l\kappa_{yz}\right]^{\mathrm{T}} \tag{3.2}$$

The displacement and rotation vector $\mathbf{u}$ at any point within the element can be written as

$$\mathbf{u}=\mathbf{N}\hat{\mathbf{u}}=[u_x\ u_y\ \omega_z]^{\mathrm{T}} \tag{3.3}$$

where $\hat{\mathbf{u}}$ is the nodal displacement and rotation vector and $\mathbf{N}$ is the shape function matrix. The strain-displacement matrix is given by

$$\mathbf{B}=\mathbf{L}\mathbf{N} \tag{3.4}$$

The strain vector can now be written as

$$\begin{gathered}\boldsymbol{\varepsilon}=\mathbf{B}\hat{\mathbf{u}}\\ \{\delta\boldsymbol{\varepsilon}\}=\mathbf{B}\{\delta\hat{\mathbf{u}}\}\end{gathered} \tag{3.5}$$

The principle of virtual work equation ignoring the body force gives

$$\int_V \{\delta\boldsymbol{\varepsilon}\}\boldsymbol{\sigma}\mathrm{d}V = \int_S \{\delta\hat{\mathbf{u}}\}\mathbf{t}\mathrm{d}S \tag{3.6}$$

The surface traction (force) vector can be written as

$$\mathbf{t} = [\mathrm{t}_x \quad \mathrm{t}_y \quad \mathrm{t}_c]^T \tag{3.7}$$

where t_x and t_y are the surface traction in the x- and y-direction respectively and t_c is the surface couple. Substituting equation (3.5) into (3.6) the governing equation is obtained as

$$\int_V \mathbf{B}^T\boldsymbol{\sigma}\mathrm{d}V = \mathrm{f}_{ext} \tag{3.8}$$

where f_{ext} is the equivalent external force vector on the nodal points and is given by

$$\mathrm{f}_{ext} = \int_S \mathbf{N}^T\mathbf{t}\mathrm{d}S \tag{3.9}$$

In the elastoplastic analysis, to solve the governing equation (3.8) incremental and Newton-Raphson iterative methods are used.

$$\int_V \mathbf{B}^T\{\delta\boldsymbol{\sigma}\}\mathrm{d}V = \mathbf{f}_{ext} - \int_V \mathbf{B}^T\{\boldsymbol{\sigma}\}\mathrm{d}V \tag{3.10}$$

Re-writing the above equation (3.10) as

$$\mathbf{K}^e\{\delta\hat{\mathbf{u}}\} = \mathbf{f}_{ext} - \int_V \mathbf{B}^T\{\boldsymbol{\sigma}\}\mathrm{d}V \tag{3.11}$$

The element stiffness matrix is given by

$$\mathbf{K}^e = \int_V \mathbf{B}^T\mathbf{D}^{ep}\mathbf{B}\mathrm{d}V \tag{3.12}$$

The shape functions are:

(i) 8-node isoparametric quadrilateral element

$$N_i = (1+\xi_i\xi)(1+\eta_i\eta)(\xi_i\xi+\eta_i\eta)/4,\ i=1,2,3,4$$

$$N_i = (1-\xi^2)(1+\eta_i\eta)/2,\ i=5,7 \qquad (3.13)$$

$$N_i = (1-\eta^2)(1+\xi_i\xi)/2,\ i=6,8$$

(ii) 4-node isoparametric quadrilateral element

$$N_i = (1+\xi_i\xi)(1+\eta_i\eta)/4,\ i=1,2,3,4 \qquad (3.14)$$

(iii) 3-node isoparametric triangular element

$$\sum_1^3 N_i = 1 \qquad (3.15)$$

$$N_1 = 1-\xi-\eta,\ N_2 = \xi,\ N_3 = \eta$$

(iv) 6-node isoparametric triangular element

$$N_1 = (1-\xi-\eta)(1-2\xi-2\eta)$$

$$N_2 = \xi(2\xi-1),\ N_3 = \eta(2\eta-1),\ N_4 = 4\xi(1-\xi-\eta) \qquad (3.16)$$

$$N_5 = 4\xi\eta,\ N_6 = 4\eta(1-\xi-\eta)$$

The natural coordinates (ξ, η) and the weighting for

(i) Quadrilateral with full (quintic, 3x3) integration scheme

$$[\mathbf{I}_9] = \begin{bmatrix} \xi_1 & \dots & \xi_9 \\ \eta_1 & \dots & \eta_9 \end{bmatrix} = \sqrt{\frac{3}{5}} \begin{bmatrix} -1 & 0 & 1 & -1 & 0 & 1 & -1 & 0 & 1 \\ -1 & -1 & -1 & 0 & 0 & 0 & 1 & 1 & 1 \end{bmatrix} \qquad (3.17)$$

$$\{\mathbf{W}_9\} = \frac{1}{81}\begin{bmatrix} 25 & 40 & 25 & 40 & 64 & 40 & 25 & 40 & 25 \end{bmatrix} \qquad (3.18)$$

(ii) Quadrilateral with reduced (cubic, 2x2) integration scheme

$$[\mathbf{I}_4]=\begin{bmatrix}\xi_1 & \xi_2 & \xi_3 & \xi_4\\ \eta_1 & \eta_2 & \eta_3 & \eta_4\end{bmatrix}=\frac{1}{\sqrt{3}}\begin{bmatrix}-1 & 1 & -1 & 1\\ -1 & -1 & 1 & 1\end{bmatrix} \tag{3.19}$$

$$\{\mathbf{W}_4\}=\{1 \quad 1 \quad 1 \quad 1\} \tag{3.20}$$

(iii) Quadrilateral with reduce (linear, 1x1) integration scheme

$$[\mathbf{I}_1]=\begin{bmatrix}\xi_1\\ \eta_1\end{bmatrix}=\begin{bmatrix}0\\ 0\end{bmatrix} \tag{3.21}$$

$$\mathbf{W}_1=4 \tag{3.22}$$

(iv) Triangular with 3-point integration scheme

$$[\mathbf{I}_{G3}]=\begin{bmatrix}\xi_1 & \xi_2 & \xi_3\\ \eta_1 & \eta_2 & \eta_3\end{bmatrix}=\begin{bmatrix}\frac{1}{6} & \frac{2}{3} & \frac{1}{6}\\ \frac{1}{6} & \frac{1}{6} & \frac{2}{3}\end{bmatrix} \tag{3.23}$$

$$\{\mathbf{W}_{G3}\}=\left\{\frac{1}{3} \quad \frac{1}{3} \quad \frac{1}{3}\right\} \tag{3.24}$$

(v) Triangular with 1-point integration scheme

$$[\mathbf{I}_{G1}]=\begin{bmatrix}\xi_1\\ \eta_1\end{bmatrix}=\begin{bmatrix}1/3\\ 1/3\end{bmatrix} \tag{3.25}$$

$$\mathrm{W}_{G1}=0.5 \tag{3.26}$$

The shape function derivatives with respect to natural coordinates (ξ, η)

$$[\mathbf{S}]=\begin{bmatrix}\frac{\partial \mathrm{N}_1}{\partial \xi} & \cdots & \frac{\partial \mathrm{N}_i}{\partial \xi}\\ \frac{\partial \mathrm{N}_1}{\partial \eta} & \cdots & \frac{\partial \mathrm{N}_i}{\partial \eta}\end{bmatrix} \tag{3.27}$$

where $\mathrm{i}=$ Number of nodes

The global coordinates (x, y) at the nodes

$$[\mathbf{X}]=\begin{bmatrix} x_1 & \dots & x_i \\ y_1 & \dots & y_i \end{bmatrix} \tag{3.28}$$

The Jacobian operator

$$[\mathbf{J}]=[\mathbf{S}]\ [\mathbf{X}]^{T}=\begin{bmatrix} J_{11} & J_{12} \\ J_{21} & J_{22} \end{bmatrix} \tag{3.29}$$

The Jacobian determinant

$$J_D = J_{11}J_{22} - J_{12}J_{21} \tag{3.30}$$

The Jacobin inverse

$$[\mathbf{J}_{(I)}]=[\mathbf{J}]^{-1}=\frac{1}{J_D}\begin{bmatrix} J_{22} & -J_{12} \\ -J_{21} & J_{11} \end{bmatrix} \tag{3.31}$$

The shape function derivatives with respect to global coordinates (x, y)

$$[\mathbf{S}_{(X)}]=[\mathbf{J}_{(I)}]\ [\mathbf{S}]=\begin{bmatrix} \frac{\partial N_1}{\partial x} & \dots & \frac{\partial N_i}{\partial x} \\ \frac{\partial N_1}{\partial y} & \dots & \frac{\partial N_i}{\partial y} \end{bmatrix} \tag{3.32}$$

3.2.1 Quadratic/quadratic and linear/linear

The strain-displacement matrix for quadratic/quadratic and linear/linear elements is given by equation (3.4). The shape function and the identity matrix can be written as

$$\mathbf{N}=[N_1\mathbf{I}\quad \dots \quad N_i\mathbf{I}] \tag{3.33}$$

$$\mathbf{I}=\begin{bmatrix} 1 & 0 & 0 \\ 0 & 1 & 0 \\ 0 & 0 & 1 \end{bmatrix} \tag{3.34}$$

The differential operator is given by

$$\mathbf{L}=\begin{bmatrix} \frac{\partial}{\partial x} & 0 & 0 \\ 0 & \frac{\partial}{\partial y} & 0 \\ 0 & 0 & 0 \\ 0 & \frac{\partial}{\partial x} & -1 \\ \frac{\partial}{\partial y} & 0 & 1 \\ 0 & 0 & l\frac{\partial}{\partial x} \\ 0 & 0 & l\frac{\partial}{\partial y} \end{bmatrix} \tag{3.35}$$

3.2.2 Quadratic/linear

The strain-displacement matrix for quadratic/linear elements is given by equation (3.4). The shape function matrix for quadratic/linear elements can be written as

$$\mathbf{N}=\begin{bmatrix} N_1 & 0 & 0 & \cdots & N_i & 0 & 0 & N_{i+1} & 0 & 0 & \cdots & N_{2i} & 0 & 0 \\ 0 & N_1 & 0 & \cdots & 0 & N_i & 0 & 0 & N_{i+1} & 0 & \cdots & 0 & N_{2i} & 0 \\ 0 & 0 & N_{1(L)} & \cdots & 0 & 0 & N_{i(L)} & 0 & 0 & 0 & \cdots & 0 & 0 & 0 \end{bmatrix} \tag{3.36}$$

In quadratic/linear elements the bi-linear shape function $N_{i(L)}$ is one order lower than the bi-quadratic shape functions N_i.

3.2.3 Selective reduced integration

The 4-node quadrilateral selective reduced integration element COS4SR is used (Alsaleh, 2004; Arslan & Sture, 2008) to avoid any possible volumetric locking. In selective reduced integration, the volumetric strains are evaluated in the element midpoint only. The decomposition of the strain vector into the deviatoric and volumetric part can be written as

$$\boldsymbol{\varepsilon} = \boldsymbol{\varepsilon}_{\text{dev}} + \boldsymbol{\varepsilon}_{\text{vol}} \tag{3.37}$$

where

$$\boldsymbol{\varepsilon}_{\text{dev}} = \boldsymbol{\varepsilon}_{\text{F}} - \boldsymbol{\varepsilon}_{\text{Fvol}} \tag{3.38}$$

$$\boldsymbol{\varepsilon}_{\text{vol}} = \boldsymbol{\varepsilon}_{\text{Rvol}} \tag{3.39}$$

The strain and its volumetric part are evaluated using 4 point gauss rule and is given by $\boldsymbol{\varepsilon}_{\text{F}}$ and $\boldsymbol{\varepsilon}_{\text{Fvol}}$ respectively. The volumetric part of the strain vector evaluated in the element midpoint only and is given by $\boldsymbol{\varepsilon}_{\text{Rvol}}$. The strain vector can now be written as

$$\boldsymbol{\varepsilon} = \overline{\mathbf{B}}\hat{\mathbf{u}} \tag{3.40}$$

where

$$\overline{\mathbf{B}} = \mathbf{B}_{\text{F}} - \mathbf{B}_{\text{Fvol}} + \mathbf{B}_{\text{Rvol}} \tag{3.41}$$

The strain-displacement matrix evaluated using 4 point gauss rule is given by $\mathbf{B}_{\text{F}}$ in equation (3.4) and its volumetric part

$$\mathbf{B}_{\text{Fvol}} = \mathbf{I}_{\text{vol}}\mathbf{B}_{\text{F}} \tag{3.42}$$

The strain-displacement matrix is evaluated in the element midpoint and is given by $\mathbf{B}_{\text{R}}$ in equation (3.4) and its volumetric part

$$\mathbf{B}_{\text{Rvol}} = \mathbf{I}_{\text{vol}}\mathbf{B}_{\text{R}} \tag{3.43}$$

where

$$\mathbf{I}_{\text{vol}} = \frac{1}{3}\mathbf{n}\mathbf{n}^{\text{T}} \tag{3.44}$$

and the vector

$$\mathbf{n} = [1 \quad 1 \quad 1 \quad 0 \quad 0 \quad 0 \quad 0]^T \tag{3.45}$$

This method is similar to a B-bar method, which modifies the definition of the strain in the element, therefore modifies the element stiffness matrix as well. The implementation of the element is not straightforward. However, the element is computationally cheaper and avoids any volumetric locking.

3.3 A review of finite elements for strain-gradient models

In this section, a total of thirteen 2D finite elements for the strain-gradient models are presented, including both existing and new ones. The sketch of thirteen 2D elements for the strain-gradient models is shown in Figure 3.2. Also, a detailed literature review is carried out for the existing elements such as C^1 triangular, mixed-type with Lagrange multiplier and penalty method. The detailed finite element formulations of the existing and the new ones are given in the next section.

The code is used to label each type of elements, for example, TU36C1. The letter T designates triangular, the total number of DOF is labelled with U36 which means the total number of DOF is 36 and C1 represents the type of element, i.e. C^1 continuity. The code used for the quadrilateral Lagrange multiplier element to label the type of elements: for example QU34L4 elements. The letter Q designate quadrilateral, the total number of DOF is labelled with U34 which means the total number of DOF is 34 and the Lagrange multipliers are designated as L4 which means the total number of Lagrange multiplier is 4. The code used for the quadrilateral penalty method element to label the type of elements: for example QU32P elements. The letter Q and U32 have the usual meaning as described above. The letter P stands for penalty method. The quadrilateral with reduced (cubic, 2x2) integration is labelled with R otherwise the element employed a full (quintic, 3x3) integration scheme (except TU36C1 element). The details of the interpolation and total DOF for the existing and new elements are given in Table 3.3.

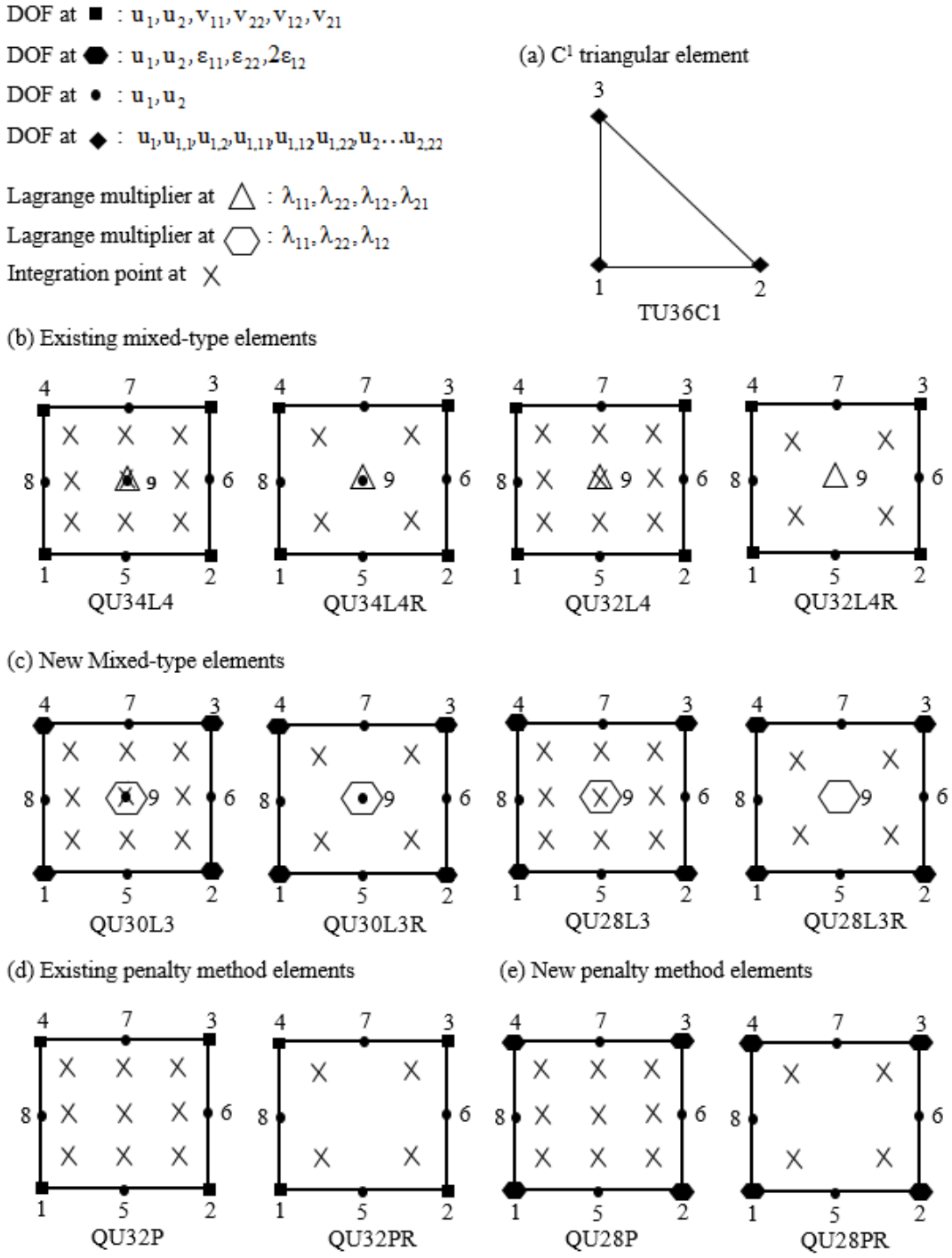

Figure 3.2 Sketch of thirteen finite elements for strain-gradient models.

Table 3.3 Existing and new finite elements for strain-gradient models.

Element	Interpolation	Total DOF	Comments
TU36C1	Displacement function of fifth-order polynomial	36	Existing elements
QU34L4 QU34L4R	u_1, u_2: Bi-quadratic Lagrangian $v_{11}, v_{22}, v_{12}, v_{21}$: Bi-linear $\lambda_{11}, \lambda_{22}, \lambda_{12}, \lambda_{21}$ - Constant	34	
QU32L4 QU32L4R	u_1, u_2: Bi-quadratic $v_{11}, v_{22}, v_{12}, v_{21}$: Bi-linear $\lambda_{11}, \lambda_{22}, \lambda_{12}, \lambda_{21}$: Constant	32	
QU32P QU32PR	u_1, u_2: Bi-quadratic $v_{11}, v_{22}, v_{12}, v_{21}$: Bi-linear		
QU30L3 QU30L3R	u_1, u_2: Bi-quadratic Lagrangian $\varepsilon_{11}, \varepsilon_{22}, 2\varepsilon_{12}$: Bi-linear $\lambda_{11}, \lambda_{22}, \lambda_{12}$: Constant	30	New elements
QU28L3 QU28L3R	u_1, u_2: Bi-quadratic $\varepsilon_{11}, \varepsilon_{22}, 2\varepsilon_{12}$: Bi-linear $\lambda_{11}, \lambda_{22}, \lambda_{12}$: Constant	28	
QU28P QU28PR	u_1, u_2: Bi-quadratic $\varepsilon_{11}, \varepsilon_{22}, 2\varepsilon_{12}$: Bi-linear		

The strain-gradient models require special treatment for the finite element formulation due to C^1 continuity requirement. It is this requirement, lack of understanding and complexities in the numerical implementation hinder the use of strain-gradient plasticity models in general. Argyris et al. (1968) and Dasgupta et al.

(1990) presented one such C^1 triangular element where only the displacement field is discretised.

The displacement field of C^1 (3-node) triangular element TU36C1 (Zervos, Papanastasiou, & Vardoulakis, 2001) varies as a complete quintic inside the element, but its normal derivatives along the element edges are constrained to be cubic. The displacement functions are taken as the complete fifth-order polynomial in area coordinates (Dasgupta & Sengupta, 1990). To achieve the highest possible accuracy 13 Gauss point integration is used. Each node contains 12 DOF, which includes the displacement, and the first and second derivatives of the displacement.

A range of methods has been developed such as mixed-type with Lagrange multiplier and penalty method elements to avoid the C^1 requirement where multiple fields are discretised. The mixed-type elements QU34L4 (Shu, King, & Fleck, 1999) developed based on Lagrange multipliers using standard C^0-continuous shape functions with full integration scheme achieved the same convergence as a C^1 element. In the mixed-type element, additional DOF so-called relaxed-stains are introduced. However, only a few mixed-type elements (TU24L4 and QU34L4) satisfies the stability conditions and work well for both compressible and incompressible solid (Shu, King, & Fleck, Finite elements for materials with strain gradient effects, 1999).

The mixed-type quadrilateral element QU32L4R based on Lagrange multipliers with reduced integration scheme (Matsushima, Chambon, & Caillerie, 2002), is similar to that of QU34L4 but differs in the number of nodal DOF, shape function and the integration scheme employed. The penalty method element with full integration scheme (Zervos, Papanicolopulos, & Vardoulakis, 2009) is much simpler to implement compared to Lagrange multiplier or C^1 elements. However, to minimise the additional error in the penalty method an appropriate value of the penalty parameter is required.

Amanatidou and Aravas (2002) developed several mixed-type quadrilateral elements for Form-I (and II) gradient elasticity. Askes and Gutierrez (2006) presented a mixed-type formulation based on a reformulation of gradient elasticity as an implicit gradient elasticity. Zervos (2008) presented 2D (triangular and quadrilateral) and 3D

(tetrahedron and hexahedron) elements discretising the theory of elasticity with microstructure (Mindlin R. , 1964).

The C^1 triangular (3-node) element TU36C1 has been used for problems of gradient elastoplasticity (Zervos, Papanastasiou, & Vardoulakis, 2001) without any numerical issues. The C^1 triangle (Specht, 1988), mixed-type Lagrange multiplier (Shu, King, & Fleck, 1999), higher-order (Wei & Hutchinson, 1997) and penalty method elements have been used for size effect problems in indentation test with MSG plasticity, all the elements give consistent results (Huang, Xue, Gao, Nix, & Xia, 2000). The higher-order element is only suitable for solids with zero higher-order stress tractions on the surface, which performed well in the fracture analysis of strain gradient plasticity (Wei & Hutchinson, 1997).

The existing strain-gradient elements are usually computationally expensive due to the large number of DOF, and the element formulations are presented differently which does not allow to make a basic comparison between the elements. Therefore, in this thesis, we have developed a new family of mixed-type Lagrangian elements which follows a general element formulation layout and allows comparison of the existing elements (Shu, King, & Fleck, 1999; Matsushima, Chambon, & Caillerie, 2002). However, the new elements differ by having few DOF and Lagrange multipliers with no additional field such as relaxed-strain. The new mixed-type Lagrangian elements are not only simpler but also computationally cheaper. The new penalty method elements are developed in a straightforward way making it simpler than the existing with few DOF. As a result, the new elements are relatively easy to implement and computationally less expensive compared to the existing ones.

Currently, there is a lack of C^1 elements that is based on displacement-only discretisation. Such elements are usually more complex, challenging to implement and increases the computational cost significantly. Papanicolopulos et al. (2010) attempt to compare between C^1, mixed-type and penalty method elements considering various weakness and strength of each approach. The advantage of using mixed-type element is that it gives the flexibility of developing diverse elements due to its relaxed-strains fields. However, not all mixed-type elements perform well (Shu, King, & Fleck, 1999; Amanatidou & Aravas, 2002).

Some of the existing finite elements which performed well are C^1 triangular TU36C1 (Dasgupta & Sengupta, 1990; Zervos, Papanastasiou, & Vardoulakis, 2001), mixed-type quadrilateral with Lagrange multiplier QU34L4 (Shu, King, & Fleck, 1999) and QU32L4R (Matsushima, Chambon, & Caillerie, 2002) and penalty method element QU32P (Zervos, Papanicolopulos, & Vardoulakis, 2009). However, there is a lack of numerical comparisons between the elements in different strain-gradient plasticity models. Also, the numerical behaviour of the elements in the plastic regime is not available to recommend suitable elements for elastoplastic problems regarding ease of numerical implementation, predicts satisfactory numerical solutions and computational cheaper.

3.4 Finite element formulations for strain-gradient models

3.4.1 C^1 triangular

In this section, Form-II formulation of C^1 triangular (3-node) element TU36C1 is presented (Dasgupta & Sengupta, 1990; Zervos, Papanastasiou, & Vardoulakis, 2001) The principle of virtual work is used to obtain the equilibrium equation. The work done due to internal forces

$$\delta\dot{W}_{int} = \int_V \left(\sigma_{ij}^{(0)}\delta\dot{\varepsilon}_{ij} + m_{kij}\delta c_{kij}\right)dV \tag{3.46}$$

where $\sigma_{ij}^{(0)} = \sigma_{ij}$. In the absence of body forces, the external work

$$\delta\dot{W}_{ext} = \int_{S_\sigma} \left(t_i\delta\dot{v}_i + \mu_i n_k \delta\dot{v}_{i,k}\right)dS \tag{3.47}$$

where t_i is the applied traction vector, m_i is the applied double force vector, n_i is the unit normal to S_σ and $\delta\dot{v}_i$ is the virtual displacement rate vector on S_σ. The principle of virtual work can then be written as

$$\delta\dot{W}_{int} = \delta\dot{W}_{ext} \tag{3.48}$$

Regarding the boundary condition, it can be shown (Vardoulakis & Sulem, 1995) that $\mathbf{t}_i$ and m_i are related to the Cauchy stress and the double stress as

$$t_i = n_j\sigma_{ij}^{(0)} - n_j n_k n_l \mu_{kij,l} - \left(n_j D_k + n_k D_j\right)\mu_{kij} + \left(n_j n_k D_l n_l + D_j n_k\right)\mu_{kij} \tag{3.49}$$

$$m_i = n_j n_k \mu_{kij} \tag{3.50}$$

with

$$D_k = \left(\delta_{kl} - n_k n_l\right)\frac{\partial}{\partial x_l} \tag{3.51}$$

The displacements within an element can be written in matrix form as

$$\mathbf{u} = \mathbf{N}\hat{\mathbf{u}} = \begin{bmatrix} u_1 & u_2 \end{bmatrix}^T \tag{3.52}$$

where u_1 and u_2 are the displacement field in the x and y-direction respectively. The shape function matrix

$$\mathbf{N} = \begin{bmatrix} N_1 \ldots N_6 & 0 \ldots 0 & N_7 \ldots N_{12} & 0 \ldots 0 & N_{13} \ldots N_{18} & 0 \ldots 0 \\ 0 \ldots 0 & N_1 \ldots N_6 & 0 \ldots 0 & N_7 \ldots N_{12} & 0 \ldots 0 & N_{13} \ldots N_{18} \end{bmatrix} \tag{3.53}$$

and the nodal DOF

$$\hat{\mathbf{u}} = \begin{bmatrix} u_1^{n1} & u_{1,1}^{n1} & u_{1,2}^{n1} & u_{1,11}^{n1} & u_{1,12}^{n1} & u_{1,22}^{n1} & u_2^{n1} \ldots u_{2,22}^{n1} & u_1^{n2} \ldots u_{2,22}^{n2} & u_1^{n3} \ldots u_{2,22}^{n3} \end{bmatrix}^T \tag{3.54}$$

The superscripts $n1 \ldots n3$ refer to the node number (1 to 3). A comma followed by a combination of 1 and 2 in the subscript denotes differentiation along x and y-direction respectively. The shape function used for this element was derived in analytical form by Dasgupta and Sengupta (1990). To obtain the highest possible accuracy, a 13-Gauss point scheme is used. The stress, higher-order stress, strain and strain-gradients are given by

$$\boldsymbol{\sigma} = \mathbf{D}^{e}\boldsymbol{\varepsilon} = \begin{bmatrix}\sigma_{11} & \sigma_{22} & \sigma_{12}\end{bmatrix}^{T} \tag{3.55}$$

$$\boldsymbol{\mu}_{x} = \mathbf{C}^{e}\boldsymbol{\varepsilon}_{x} = \begin{bmatrix}\mu_{111} & \mu_{122} & \mu_{112}\end{bmatrix}^{T} \tag{3.56}$$

$$\boldsymbol{\mu}_{y} = \mathbf{C}^{e}\boldsymbol{\varepsilon}_{y} = \begin{bmatrix}\mu_{211} & \mu_{222} & \mu_{212}\end{bmatrix}^{T} \tag{3.57}$$

$$\boldsymbol{\varepsilon} = \mathbf{L}_{1}\mathbf{N}\hat{\mathbf{u}} = \mathbf{B}_{1}\hat{\mathbf{u}} = \begin{bmatrix}\varepsilon_{11} & \varepsilon_{22} & \gamma_{12}\end{bmatrix}^{T} \tag{3.58}$$

$$\boldsymbol{\varepsilon}_{x} = \frac{\partial}{\partial x}\boldsymbol{\varepsilon} = \mathbf{L}_{2x}\mathbf{N}\hat{\mathbf{u}} = \mathbf{B}_{2x}\hat{\mathbf{u}} \tag{3.59}$$

$$\boldsymbol{\varepsilon}_{y} = \frac{\partial}{\partial y}\boldsymbol{\varepsilon} = \mathbf{L}_{2y}\mathbf{N}\hat{\mathbf{u}} = \mathbf{B}_{2y}\hat{\mathbf{u}} \tag{3.60}$$

The differential operators

$$\mathbf{L}_{1} = \begin{bmatrix}\frac{\partial}{\partial x} & 0 \\ 0 & \frac{\partial}{\partial y} \\ \frac{\partial}{\partial y} & \frac{\partial}{\partial x}\end{bmatrix},\ \mathbf{L}_{2x} = \frac{\partial}{\partial x}\mathbf{L}_{1},\ \mathbf{L}_{2y} = \frac{\partial}{\partial y}\mathbf{L}_{1} \tag{3.61}$$

The principle of virtual work equation gives the following system of equations for the nodal DOF

$$\begin{aligned}&\int_{V}\left(\mathbf{B}_{1}^{T}\mathbf{D}^{ep}\mathbf{B}_{1} + \mathbf{B}_{2x}^{T}\mathbf{C}^{e}\mathbf{B}_{2x} + \mathbf{B}_{2y}^{T}\mathbf{C}^{e}\mathbf{B}_{2y}\right)dV\,\hat{\mathbf{u}} \\ &= \int_{S_{\sigma}}\left[\mathbf{N}^{T}\hat{\mathbf{t}} + \left(n_{x}\frac{\partial \mathbf{N}^{T}}{\partial x} + n_{y}\frac{\partial \mathbf{N}^{T}}{\partial y}\right)\hat{\mathbf{m}}\right]dS\end{aligned} \tag{3.62}$$

where $\hat{\mathbf{t}}$ is the boundary traction vector, $\hat{\mathbf{m}}$ is the boundary double traction vector and $\mathbf{n} = \begin{bmatrix}n_{x} & n_{y}\end{bmatrix}$ is the outward unit normal to the boundary. The equation (3.62) can be re-written in a compact form as

$$\mathbf{K}^{e}\,\hat{\mathbf{u}} = \mathbf{f}_{e} \tag{3.63}$$

where $\mathbf{K}^{e}$ is the element stiffness matrix and $\mathbf{f}_{e}$ is the load vector. The Newton-Raphson iterative method is used to solve the equation (3.63) and the residual forces at the end of each iteration as

$$\mathbf{R} = \int_{V} \left(\mathbf{B}_{1}^{T} \boldsymbol{\sigma}^{(0)} + \mathbf{B}_{2x}^{T} \boldsymbol{\mu}_{x} + \mathbf{B}_{2y}^{T} \boldsymbol{\mu}_{y} \right) dV - \mathbf{f}_{e} \tag{3.64}$$

3.4.2 Existing mixed-type quadrilateral

In this section, Form-I formulation of the existing mixed-type elements is presented. Within this type of formulation, additional DOF v_{ij} the so-called relaxed displacement gradient is introduced, and equality with the displacement gradients is postulated in an approximate manner (Zybell, Mühlich, Kuna, & Zhang, 2012)

$$v_{ij} - u_{j,i} \approx 0_{ij} \tag{3.65}$$

The relaxed strain-gradients are defined by

$$\kappa_{ijk} = \frac{1}{2}\left(v_{jk,i} + v_{ik,j} \right) \tag{3.66}$$

The principle of virtual work equation ignoring body forces can be written as

$$\int_{V} \left(\delta\boldsymbol{\varepsilon}^{T} \boldsymbol{\sigma} - \nabla\delta\mathbf{u}^{T} \boldsymbol{\lambda} \right) dV = \int_{\partial At} \delta\mathbf{u}^{T} \mathbf{t}\, dA \tag{3.67}$$

$$\int_{V} \left(\delta\boldsymbol{\kappa}^{T} \boldsymbol{\mu} - \delta\mathbf{v}^{T} \boldsymbol{\lambda} \right) dV = \int_{\partial As} \delta\mathbf{v}^{T} \mathbf{s}\, dA \tag{3.68}$$

$$\int_{V} \delta\boldsymbol{\lambda}^{T} \left(\mathbf{v} - \nabla\mathbf{u} \right) dV = 0 \tag{3.69}$$

where $\mathbf{t}$ and $\mathbf{s}$ are the know boundary tractions and higher-order boundary tractions respectively. The displacements $\mathbf{u}$, the relaxed displacement gradient ν and the Lagrange multiplier λ within an element is given by

$$\mathbf{u} = \mathbf{N}^{u}\hat{\mathbf{u}} = \begin{bmatrix} u_1 & u_2 \end{bmatrix}^{T} \tag{3.70}$$

$$\mathbf{v} = \mathbf{N}^{v}\hat{\mathbf{v}} = \begin{bmatrix} v_{11} & v_{22} & v_{12} & v_{21} \end{bmatrix}^{T} = \begin{bmatrix} u_{1,1} & u_{2,2} & u_{1,2} & u_{2,1} \end{bmatrix}^{T} \tag{3.71}$$

$$\boldsymbol{\lambda} = \mathbf{N}^{\lambda}\hat{\boldsymbol{\lambda}} = \begin{bmatrix} \lambda_{11} & \lambda_{22} & \lambda_{12} & \lambda_{21} \end{bmatrix}^{T} \tag{3.72}$$

The shape function matrices

$$\mathbf{N}^{u} = \begin{bmatrix} N_1 & & \dots & N_i & \\ & N_1 & \dots & & N_i \end{bmatrix} \tag{3.73}$$

where, $i = \begin{cases} 9 & \text{for QU34L4, QU34L4R} \\ 8 & \text{for QU32L4, QU32L4R} \end{cases}$

$$\mathbf{N}^{v} = \begin{bmatrix} N_1 & & & \dots & N_4 & & & \\ & N_1 & & \dots & & N_4 & & \\ & & N_1 & \dots & & & N_4 & \\ & & & N_1 \ \dots & & & & N_4 \end{bmatrix} \tag{3.74}$$

$$\mathbf{N}^{\lambda} = \begin{bmatrix} 1 & & & \\ & 1 & & \\ & & 1 & \\ & & & 1 \end{bmatrix} \tag{3.75}$$

The nodal quantities

$$\hat{\mathbf{u}} = \begin{bmatrix} u_1^{n1} & u_2^{n1} & \dots & u_1^{ni} & u_2^{ni} \end{bmatrix}^{T} \tag{3.76}$$

$$\hat{\mathbf{v}} = \begin{bmatrix} v_{11}^{n1} & v_{22}^{n1} & v_{12}^{n1} & v_{21}^{n1} & \dots & v_{11}^{n4} & v_{22}^{n4} & v_{12}^{n4} & v_{21}^{n4} \end{bmatrix}^{T} \tag{3.77}$$

$$\hat{\boldsymbol{\lambda}} = \begin{bmatrix} \lambda_{11}^{n9} & \lambda_{22}^{n9} & \lambda_{12}^{n9} & \lambda_{21}^{n9} \end{bmatrix}^T \tag{3.78}$$

The relevant quantities can be written as

$$\boldsymbol{\sigma} = \mathbf{D}^e \boldsymbol{\varepsilon} = \begin{bmatrix} \sigma_{11} & \sigma_{22} & \sigma_{12} \end{bmatrix}^T \tag{3.79}$$

$$\boldsymbol{\varepsilon} = \mathbf{B}^{\varepsilon} \hat{\mathbf{u}} = \begin{bmatrix} \varepsilon_{11} & \varepsilon_{22} & \gamma_{12} \end{bmatrix}^T \tag{3.80}$$

$$\boldsymbol{\mu} = \mathbf{C}^e \tilde{\boldsymbol{\kappa}} = \begin{bmatrix} \tilde{\mu}_{111} & \tilde{\mu}_{221} & \tilde{\mu}_{122} & \tilde{\mu}_{222} & \tilde{\mu}_{112} & \tilde{\mu}_{211} \end{bmatrix}^T \tag{3.81}$$

$$\boldsymbol{\kappa} = \mathbf{B}^{\kappa} \hat{\mathbf{v}} = \begin{bmatrix} \tilde{\kappa}_{111} & \tilde{\kappa}_{221} & 2\tilde{\kappa}_{122} & \tilde{\kappa}_{222} & \tilde{\kappa}_{112} & 2\tilde{\kappa}_{211} \end{bmatrix}^T \tag{3.82}$$

$$\nabla \mathbf{u} = \mathbf{B}^{v} \hat{\mathbf{u}} \tag{3.83}$$

The matrices $\mathbf{B}^{v}$, $\mathbf{B}^{\varepsilon}$ and $\mathbf{B}^{\kappa}$ are given by

$$\mathbf{B}^{v} = \mathbf{L}^{v} \mathbf{N}^{u}, \quad \mathbf{B}^{\varepsilon} = \mathbf{L}^{\varepsilon} \mathbf{N}^{u}, \quad \mathbf{B}^{\kappa} = \mathbf{L}^{\kappa} \mathbf{N}^{v} \tag{3.84}$$

The differential operators are

$$\mathbf{L}^{v} = \begin{bmatrix} \partial_1 & . \\ . & \partial_2 \\ \partial_2 & . \\ . & \partial_1 \end{bmatrix}, \quad \mathbf{L}^{\varepsilon} = \begin{bmatrix} \partial_1 & . \\ . & \partial_2 \\ \partial_2 & \partial_1 \end{bmatrix}$$

$$\mathbf{L}^{\kappa} = \begin{bmatrix} \partial_1 & . & . & . \\ . & . & \partial_2 & . \\ . & \partial_1 & . & \partial_2 \\ . & \partial_2 & . & . \\ . & . & . & \partial_1 \\ \partial_2 & . & \partial_1 & . \end{bmatrix} \tag{3.85}$$

where $\partial_i = \partial / \partial u_i$

After some algebraic manipulation, the equation (3.67) to (**3.69**) can be written as

$$\delta\hat{\mathbf{u}}^{T}\left(\int_{V}\left(\left[\mathbf{B}^{\varepsilon}\right]^{T}\boldsymbol{\sigma}-\left[\mathbf{B}^{v}\right]^{T}\mathbf{N}^{\lambda}\hat{\boldsymbol{\lambda}}\right)dV-\int_{\partial At}\left[\mathbf{N}^{u}\right]^{T}\mathbf{t}\,dA\right)=0 \tag{3.86}$$

$$\delta\hat{\mathbf{v}}^{T}\left(\int_{V}\left(\left[\mathbf{B}^{\kappa}\right]^{T}\boldsymbol{\mu}-\left[\mathbf{N}^{v}\right]^{T}\mathbf{N}^{\lambda}\hat{\boldsymbol{\lambda}}\right)dV-\int_{\partial As}\left[\mathbf{N}^{v}\right]^{T}\mathbf{s}\,dA\right)=0 \tag{3.87}$$

$$\delta\hat{\boldsymbol{\lambda}}^{T}\int_{V}\left[\mathbf{N}^{\lambda}\right]^{T}\left(\mathbf{N}^{v}\hat{\mathbf{v}}-\left[\mathbf{B}^{v}\right]^{T}\hat{\mathbf{u}}\right)dV=0 \tag{3.88}$$

Because $\delta\hat{\mathbf{u}}$, $\delta\hat{\mathbf{v}}$ and $\delta\hat{\boldsymbol{\lambda}}$ are independent variations, equations (3.86) to (**3.88**) can be transformed into the following system of equations:

$$\begin{bmatrix}\left[\mathbf{K}^{uu}\right] & [0] & -\left[\mathbf{K}^{u\lambda}\right]\\ [0] & \left[\mathbf{K}^{vv}\right] & \left[\mathbf{K}^{v\lambda}\right]\\ -\left[\mathbf{K}^{u\lambda}\right]^{T} & \left[\mathbf{K}^{v\lambda}\right]^{T} & [0]\end{bmatrix}\begin{bmatrix}d\hat{\mathbf{u}}\\ d\hat{\mathbf{v}}\\ d\hat{\boldsymbol{\lambda}}\end{bmatrix}=\begin{bmatrix}\mathbf{F}_{0}^{u}\\ \mathbf{F}_{0}^{v}\\ 0\end{bmatrix}-\int_{V}\begin{bmatrix}\mathbf{F}^{u}\\ \mathbf{F}^{v}\\ 0\end{bmatrix}dV \tag{3.89}$$

where the stiffness matrices are

$$\begin{aligned}\left[\mathbf{K}^{uu}\right]&=\int_{V}\left[\mathbf{B}^{u}\right]^{T}\left[\mathbf{D}^{ep}\right]\left[\mathbf{B}^{u}\right]dV\\ \left[\mathbf{K}^{vv}\right]&=\int_{V}\left[\mathbf{B}^{\kappa}\right]^{T}\left[\mathbf{C}^{e}\right]\left[\mathbf{B}^{\kappa}\right]dV\end{aligned}, \tag{3.90}$$

$$\left[\mathbf{K}^{u\lambda}\right]=\int_{V}\left[\mathbf{B}^{v}\right]^{T}\left[\mathbf{N}^{\lambda}\right]dV\ ,\ \left[\mathbf{K}^{v\lambda}\right]=\int\left[\mathbf{N}^{v}\right]^{T}\left[\mathbf{N}^{\lambda}\right]dV$$

and the right-hand side vectors read

$$\begin{bmatrix}\mathbf{F}^{u}\\ \mathbf{F}^{v}\\ 0\end{bmatrix}=\begin{bmatrix}\left[\mathbf{B}^{\varepsilon}\right]^{T}\boldsymbol{\sigma}\\ \left[\mathbf{B}^{\kappa}\right]^{T}\boldsymbol{\mu}\\ 0\end{bmatrix}+\begin{bmatrix}[0] & [0] & -\left[\mathbf{B}^{\varepsilon}\right]^{T}\mathbf{N}^{\lambda}\\ [0] & [0] & \left[\mathbf{N}^{v}\right]^{T}\mathbf{N}^{\lambda}\\ -\left[\mathbf{N}^{\lambda}\right]^{T}\mathbf{B}^{\varepsilon} & \left[\mathbf{N}^{\lambda}\right]^{T}\mathbf{N}^{v} & [0]\end{bmatrix}\begin{bmatrix}\hat{\mathbf{u}}\\ \hat{\mathbf{v}}\\ \hat{\boldsymbol{\lambda}}\end{bmatrix} \tag{3.91}$$

3.4.3 New mixed-type quadrilateral

In this section, Form-II formulation of the new mixed-type elements based on Lagrange multiplier is presented. Within this new formulation, additional DOF v_{ij} the so-called relaxed displacement gradient are replaced by using the common strain field. Therefore, discretising the strain instead of the displacement gradient. As a result, the new mixed-type elements have fewer DOF and Lagrange multipliers. Another advantage of new elements is that they are relatively easy to implement and computationally less expensive compared to the existing ones.

The displacement $\mathbf{u}$ is given by equation (3.70), the strain field $\mathbf{v}$ and the Lagrange multiplier $\boldsymbol{\lambda}$ within an element is given by

$$\mathbf{v} = \mathbf{N}^{v}\hat{\mathbf{v}} = \begin{bmatrix} \varepsilon_{11} & \varepsilon_{22} & 2\varepsilon_{12} \end{bmatrix}^{T} = \boldsymbol{\varepsilon} \tag{3.92}$$

$$\boldsymbol{\lambda} = \mathbf{N}^{\lambda}\hat{\boldsymbol{\lambda}} = \begin{bmatrix} \lambda_{11} & \lambda_{22} & \lambda_{12} \end{bmatrix}^{T} \tag{3.93}$$

Note that the number of Lagrange multipliers decreases in the new mixed-type element. The shape function matrices are

$$\mathbf{N}^{u} = \begin{bmatrix} N_1 & & \dots & N_i & \\ & N_1 & \dots & & N_i \end{bmatrix}$$
$$i = \begin{cases} 9 & \text{for QU30L3, QU30L3R} \\ 8 & \text{for QU28L3, QU28L3R} \end{cases} \tag{3.94}$$

$$\mathbf{N}^{v} = \begin{bmatrix} N_1 & & & \dots & N_4 & & \\ & N_1 & & \dots & & N_4 & \\ & & N_1 & \dots & & & N_4 \end{bmatrix} \tag{3.95}$$

$$\mathbf{N}^{\lambda} = \begin{bmatrix} 1 & & \\ & 1 & \\ & & 1 \end{bmatrix} \tag{3.96}$$

The nodal quantity $\hat{\mathbf{u}}$ is given by equation (3.76) and the other two nodal quantities

$$\hat{\mathbf{v}} = \begin{bmatrix} \varepsilon_{11}^{n1} & \varepsilon_{22}^{n1} & 2\varepsilon_{12}^{n1} & \dots & \varepsilon_{11}^{n4} & \varepsilon_{22}^{n4} & 2\varepsilon_{12}^{n4} \end{bmatrix}^{T} \tag{3.97}$$

$$\hat{\boldsymbol{\lambda}} = \begin{bmatrix} \lambda_{11}^{n9} & \lambda_{22}^{n9} & \lambda_{12}^{n9} \end{bmatrix}^{T} \tag{3.98}$$

The stress and strain quantities are given by equation (3.79) and (**3.80**) respectively. The other relevant quantities can be written as

$$\boldsymbol{\mu} = \mathbf{C}^{e}\hat{\boldsymbol{\kappa}} = \begin{bmatrix} \hat{\mu}_{111} & \hat{\mu}_{122} & \hat{\mu}_{212} & \hat{\mu}_{222} & \hat{\mu}_{211} & \hat{\mu}_{112} \end{bmatrix}^{T} \tag{3.99}$$

$$\boldsymbol{\kappa} = \mathbf{B}^{\kappa}\hat{\mathbf{v}} = \begin{bmatrix} \hat{\kappa}_{111} & \hat{\kappa}_{221} & 2\hat{\kappa}_{122} & \hat{\kappa}_{222} & \hat{\kappa}_{112} & 2\hat{\kappa}_{211} \end{bmatrix}^{T} \tag{3.100}$$

$$\nabla \mathbf{u} = \mathbf{B}^{v}\hat{\mathbf{u}} = \boldsymbol{\varepsilon} \tag{3.101}$$

The matrices $\mathbf{B}^{v}$, $\mathbf{B}^{\varepsilon}$ and $\mathbf{B}^{\kappa}$ are given by equation (3.84) and the differential operators are

$$\mathbf{L}^{v} = \mathbf{L}^{\varepsilon} = \begin{bmatrix} \partial_1 & . \\ . & \partial_2 \\ \partial_2 & \partial_1 \end{bmatrix}, \quad \mathbf{L}^{\kappa} = \begin{bmatrix} \partial_1 & . & . \\ . & \partial_1 & . \\ . & . & \partial_2 \\ \partial_2 & . & . \\ . & \partial_2 & . \\ . & . & \partial_1 \end{bmatrix} \tag{3.102}$$

The system of equations, the stiffness matrices and the right-hand vectors are given by equation (3.89) to (3.91).

3.4.4 Existing and new penalty method quadrilateral

To avoid the zeros diagonal block in equation (3.89), the zero matrix is replaced with the invertible matrix $-\gamma^{-1}\mathbf{G}$ to obtain

$$\begin{bmatrix} [\mathbf{K}^{e}] & [\mathbf{K}^{c}]^{T} \\ [\mathbf{K}^{c}] & -\gamma^{-1}[\mathbf{G}] \end{bmatrix} \begin{bmatrix} d\hat{\mathbf{u}}^{e} \\ d\hat{\boldsymbol{\lambda}} \end{bmatrix} = \begin{bmatrix} \mathbf{r}^{e} \\ 0 \end{bmatrix} - \begin{bmatrix} [0] & [\mathbf{K}^{c}]^{T} \\ [\mathbf{K}^{c}] & -\gamma^{-1}[\mathbf{G}] \end{bmatrix} \begin{bmatrix} \hat{\mathbf{u}}^{e} \\ \hat{\boldsymbol{\lambda}} \end{bmatrix} \tag{3.103}$$

where

$$[\mathbf{K}^{e}] = \begin{bmatrix} [\mathbf{K}^{uu}] & [0] \\ [0] & [\mathbf{K}^{vv}] \end{bmatrix}, \quad [\mathbf{K}^{c}] = \begin{bmatrix} -[\mathbf{K}^{u\lambda}] & [\mathbf{K}^{v\lambda}] \end{bmatrix} \tag{3.104}$$

$$\hat{\mathbf{u}}^{e} = [\hat{\mathbf{u}} \quad \hat{\mathbf{v}}]^{T}, \quad \mathbf{r}^{e} = [\mathbf{F}^{u} \quad \mathbf{F}^{v}]^{T}$$

As $\gamma \to \infty$ the original equation (3.89) is recovered. This equation can be written as

$$[\mathbf{K}^{e}] d\hat{\mathbf{u}}^{e} + [\mathbf{K}^{c}]^{T} d\hat{\boldsymbol{\lambda}} = \mathbf{r}^{e} - [\mathbf{K}^{c}]^{T} \hat{\boldsymbol{\lambda}} \tag{3.105}$$

$$[\mathbf{K}^{c}] d\hat{\mathbf{u}}^{e} - \gamma^{-1}[\mathbf{G}]^{T} d\hat{\boldsymbol{\lambda}} = -[\mathbf{K}^{c}] \hat{\mathbf{u}}^{e} + \gamma^{-1}[\mathbf{G}] \hat{\boldsymbol{\lambda}} \tag{3.106}$$

Solving equation (**3.106**) for $d\hat{\boldsymbol{\lambda}}$ and substituting in (3.105) we obtain

$$\left([\mathbf{K}^{e}] - \gamma^{-1}[\mathbf{K}^{c}]^{T}[\mathbf{G}^{-1}][\mathbf{K}^{c}]\right) d\hat{\mathbf{u}}^{e} = \mathbf{r}^{e} - \gamma[\mathbf{K}^{c}]^{T}[\mathbf{G}^{-1}][\mathbf{K}^{c}] \hat{\mathbf{u}}^{e} \tag{3.107}$$

The penalty method formulation is more comfortable to implement than mixed-type with Lagrange multipliers and C^1 elements. However, to minimise the additional numerical error an appropriate value of the penalty parameter γ is required in equation (3.107).

Note that for $\mathbf{G} = \mathbf{I}$, which is the simplest case, the resulting penalty formulation is similar (but not identical) as the one proposed by Zervos et al. (2009), QU32P. Similarly, the new penalty method element, QU28P (and QU28PR) can be formulated based on the new mixed-type elements in the previous section.

3.5 Conclusions

The quadratic/linear elements which are computationally cheaper than quadratic/quadratic elements have not been tested with Cosserat plasticity models, and no results are available in the literature. Selective reduced integration (COS4SR) element can be the cheapest element possible without any numerical issues such as locking or spurious deformation hourglass modes due to the reduced integration of the volumetric part of the strain. Different authors have used different Cosserat elements in both elasticity and plasticity models without giving enough information regarding the spatial integration scheme employed which can lead to confusions. In general, the finite element formulation of Cosserat is same as Classical with some differences in the elastic stiffness moduli and the strain-displacement matrix. Therefore, any Cosserat elements and plasticity models can be easily implemented into any standard finite element code by considering additional independent rotational DOF at nodes. Currently, there is a lack of numerical comparisons between the Cosserat elements in plasticity models especially in the post-peak regime where localised deformation occurs.

The C^1 (TU36C1), mixed-type based on Lagrange multipliers (QU34L4 and QU32L4R) and penalty method (QU32P) elements have performed reasonably well in strain-gradient models without any numerical issues. All the elements for strain-gradient models are computationally more expensive compared to Cosserat elements. The most and the least expensive elements are C^1 (TU36C1) and new penalty method (QU28PR) respectively. Although the total DOF in the C^1 triangular element is higher and use higher-order displacement shape function, the element only needs the displacement field to be discretised. The mixed-type Lagrange multiplier and penalty method elements are relatively straightforward to implement, and common shape functions can be used. However, Lagrange multiplier elements have non-positive stiffness matrices to take into account, and the penalty elements have the penalty parameter value to be defined. Currently, there is a lack of numerical comparison between the elements in strain-gradient plasticity models to recommend the appropriate elements regarding ease of numerical implementation that predicts satisfactory numerical solutions in the plastic regime and computationally cheaper.

4 Finite element benchmark tests

In this chapter, a total of ten Cosserat elements as shown in chapter 2 are implemented with three different Cosserat plasticity models (von Mises and Drucker-Prager). Numerical finite element simulation is carried out based on shear layer and biaxial compression test for the 2D plane strain case to compare the numerical behaviour of the elements in different plasticity models, especially in the plastic regime. The elements which predict satisfactory numerical solutions and computationally cheaper are recommended for elastoplastic analysis.

The existing and new elements for strain-gradient models are implemented with different strain-gradient plasticity models based on von Mises and Drucker-Prager yield criterion. Finite element analysis is carried out based on biaxial compression test to compare the numerical behaviour of the elements in different strain-gradient plasticity models, especially in the post-peak regime. Finally, appropriate elements for strain-gradient plasticity models are recommended that perform well without any numerical issues, easier to implement and computationally cheaper.

This chapter focus on the numerical behaviour of the elements for Cosserat and strain-gradient plasticity models. Therefore providing guidance for selecting suitable elements for elastoplastic analysis. The biaxial compression tests are carried out by introducing a material imperfection in the specimen by considering a weaker element with lower yield stress to trigger localised deformation and formation of the shear band.

All the elements for Cosserat and strain-gradient models are implemented using the user element subroutine (UEL) and the plasticity models embedded user material subroutine (UMAT) into the finite element program ABAQUS.

4.1 Cosserat elements

4.1.1 Shear layer tests

In this section a total of ten Cosserat elements as shown in chapter 3, Figure 3.1 is implemented with two different Cosserat von Mises (VM1 and VM2) and one pressure-dependent Drucker-Prager (DP1) model in chapter 2. A finite element simulation is then carried out to test the numerical behaviour of the elements in the plastic regime under pure shear.

The shear layer is assumed infinitely long in the third direction (z-axis) as a one-dimensional (1D) plane strain problem in finite element analysis using 2D Cosserat elements (de Borst, 1991). The height of the shear layer, H=100mm and the width, B=1mm. For both the quadrilateral and triangular elements, discretisation used namely for 20x1-mesh. For the triangular elements, each quadrilateral is composed of two triangular elements.

All nodal displacement in the y-axis (vertical) is restricted. The bottom of the shear layer is fixed, and every two nodes with the same y-coordinate are enforced to have equal displacement in the x-direction (horizontal) and rotation. Horizontal displacements on the right (positive x-direction) are prescribed at the top boundary. The rotational DOF on the top and the bottom nodes of the shear layer is fixed to trigger the shear band formation. The geometry, loading and boundary conditions for the shear layer test (8-node quadrilateral and 6-node triangular elements) are shown in Figure 4.1. Similarly, the boundary conditions for the 4-node quadrilateral and 3-node triangular elements can be applied as shown in Figure 4.1.

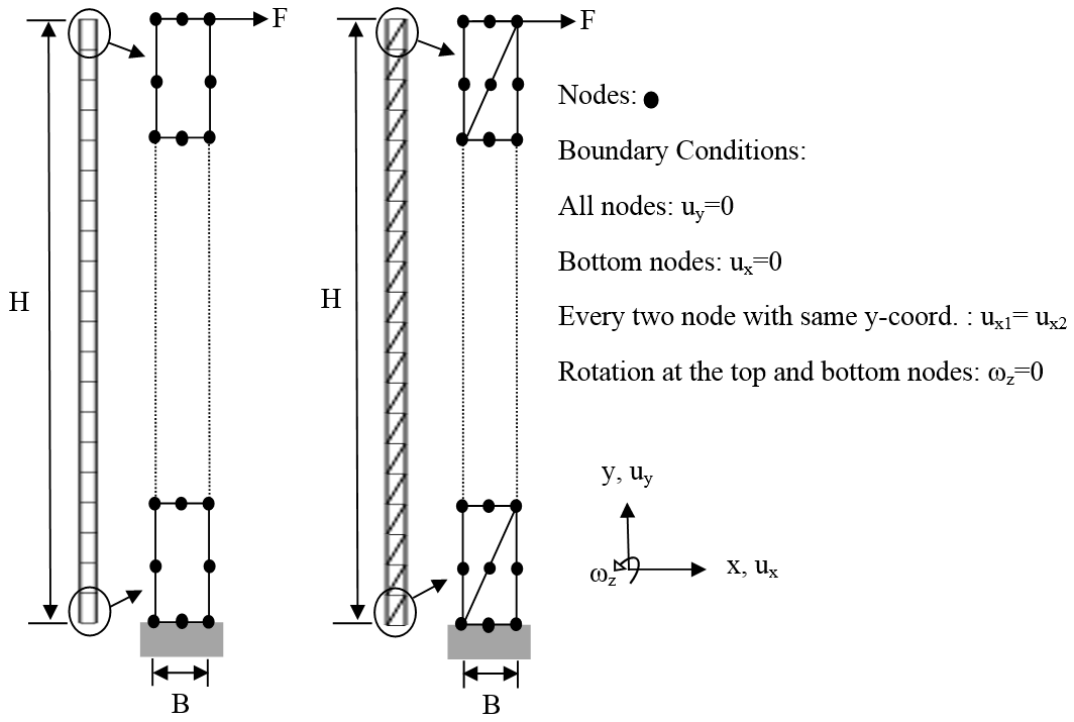

Figure 4.1 Shear layer geometry, loading and boundary condition (left: 8-node quadrilateral and right: 6-node triangular elements).

The material parameters used for all the models are: $E = 10000\text{MPa}$, $\nu = 0.25$, $\mu_c = 2000\text{MPa}$, $h_p = -500\text{MPa}$, $\sigma_{y0} = 100\text{MPa}$, $l = 12\text{mm}$. Note that the material parameters and model geometry remains same as de Borst (1991) shear layer test to compare with the existing results. Associated flow rule is assumed for the Drucker-Prager model, the friction and dilatancy angles are equal to zero.

A mesh refinement study is carried out for the shear layer test to evaluate an acceptable discretisation for which the solution converges and becomes mesh-independent. Four different discretisations have been used namely 4x1, 8x1, 20x1 and 30x-mesh using COS8R/F, COS8(4)R/F and COS4R elements with Cosserat VM1 model by de Borst (1991). Figure 4.2 shows the load-displacement curves for different discretisation. The 4x1-mesh gives a slightly stiffer response in the post-peak regime, while 8x1-mesh is only slightly stiffer during the sharp decrease in load carrying capacity at the later stage of localisation compared to 20x1 (and 30x1) mesh. The 20x1 and 30x1-mesh predict equivalent load-displacement curve which shows that mesh-

independent results are obtained by using 20x1-mesh. Figure 4.3 shows the deformed meshes and contour of equivalent plastic strain for different discretisation.

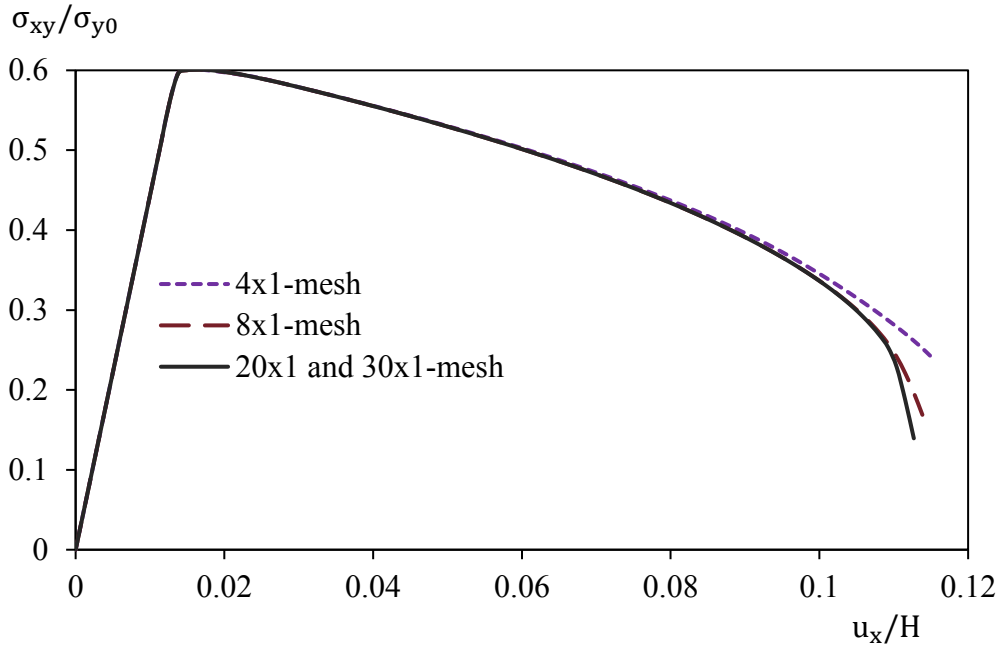

Figure 4.2 Load-displacement curves for shear layer using COS8R/F, COS8(4)R/F and COS4R elements with Cosserat VM1 model by de Borst (1991).

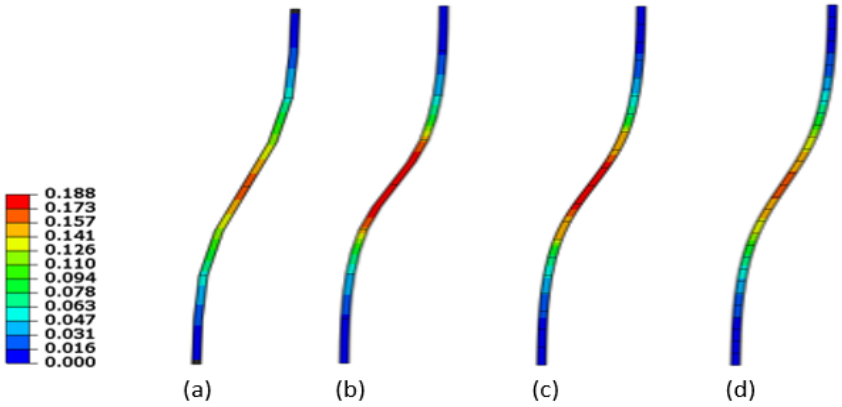

Figure 4.3 Deformed meshes and contour of equivalent plastic strain for shear layer: (a) 4 elements, (b) 8 elements, (c) 20 elements and (d) 30 elements

The first test for the elements is carried out with the Cosserat VM1 model by de Borst (1991). Figure 4.4 shows the load-displacement curve for the elements with VM1 model. The first group of elements includes quadratic/quadratic, quadratic/linear

and COS4R elements all give an equivalent load-displacement curve. The first group of elements are in good agreement with de Borst (1991) result. The element used by Borst (1991) is a 6-node triangular with four-point Gauss rule. The second group of elements includes COS4F and COS4R elements, which predict identical load-displacement curve but are slightly stiffer than the first group at the later stages of the plastic deformation. The third group of elements include only COSG1, which is stiffer than others at the later stages of the post-peak regime. Figure 4.5 shows the deformed meshes, and contour of the equivalent plastic strain of one element from each group for VM1 model as the elements within the group predicts the equivalent result.

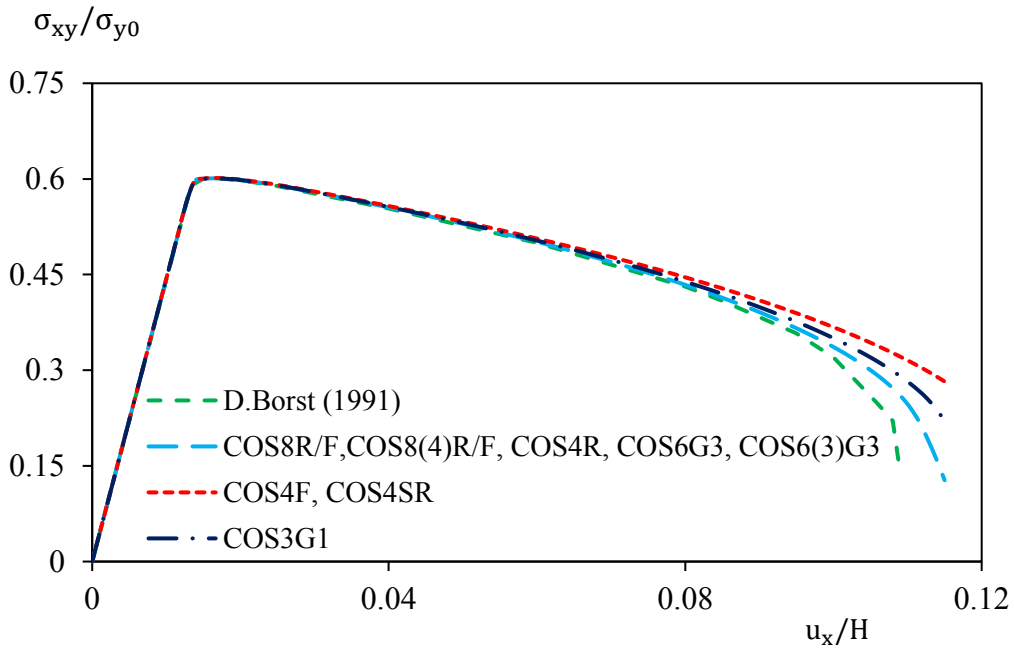

Figure 4.4 Load-displacement curve for the elements with VM1 model.

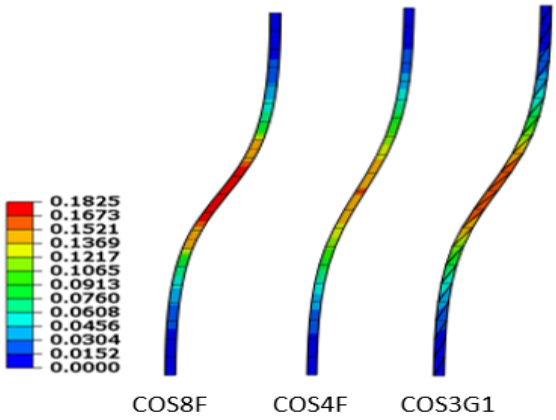

Figure 4.5 Deformed meshes and contour of the equivalent plastic strain of the elements with the VM1 model at the end of the simulation.

The second test for the elements is carried out with the Cosserat VM2 model by Sharbati and Naghdabadi (2006). Again, the second group of elements as described in the first test give slight stiffer response than the first group while the third group of elements are much stiffer at the later stages of the plastic deformation as shown in Figure 4.6. The elements behaviour in VM2 model is similar to that of VM1 model. Figure 4.7 shows the deformed meshes and contour of the equivalent plastic strain of one element from each group for VM2 model as the elements behaviour within the group are same.

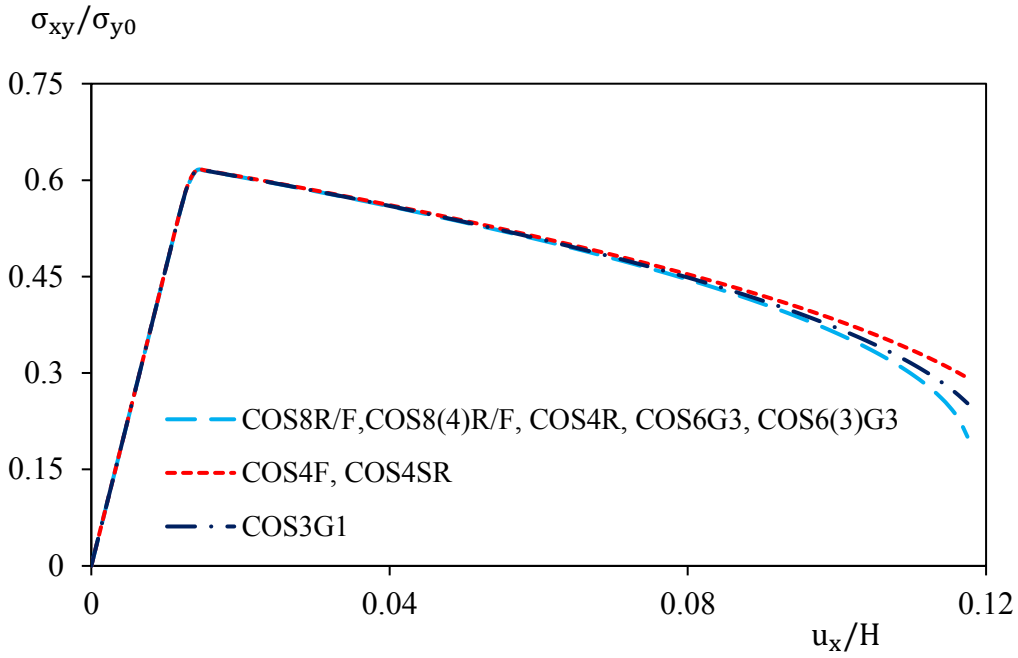

Figure 4.6 Load-displacement curve for the elements with VM2 model.

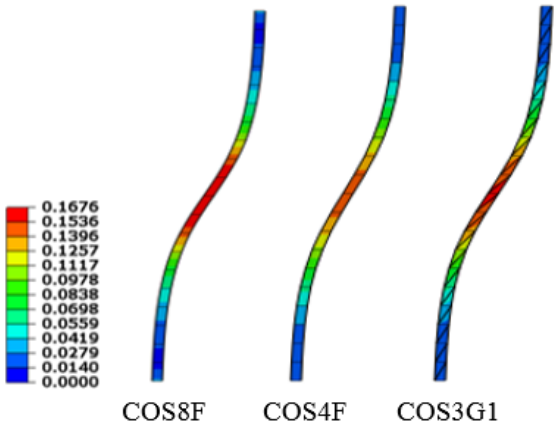

Figure 4.7 Deformed meshes and contour of the equivalent plastic strain of the elements with VM2 model at the end of the simulation.

The third test for the elements is carried out with the Cosserat DP1 model by de Borst (1993). Once again, the second group of elements as described in the first test give slight stiffer response than the first group while the third group of elements are stiffer at the later stages of softening as shown in Figure 4.8. Note that the numerical results for all the elements are very close to that of de Borst (1993) where he used a 6-node quadratic/quadratic element (integration scheme not mentioned). However, in the

latter case (biaxial test) we will see that there is a discrepancy between his and our numerical results. The deformed meshes and contour of the equivalent plastic strain of one element from each group for the DP1 model are shown in Figure 4.9 as the elements behaviour within the group is same.

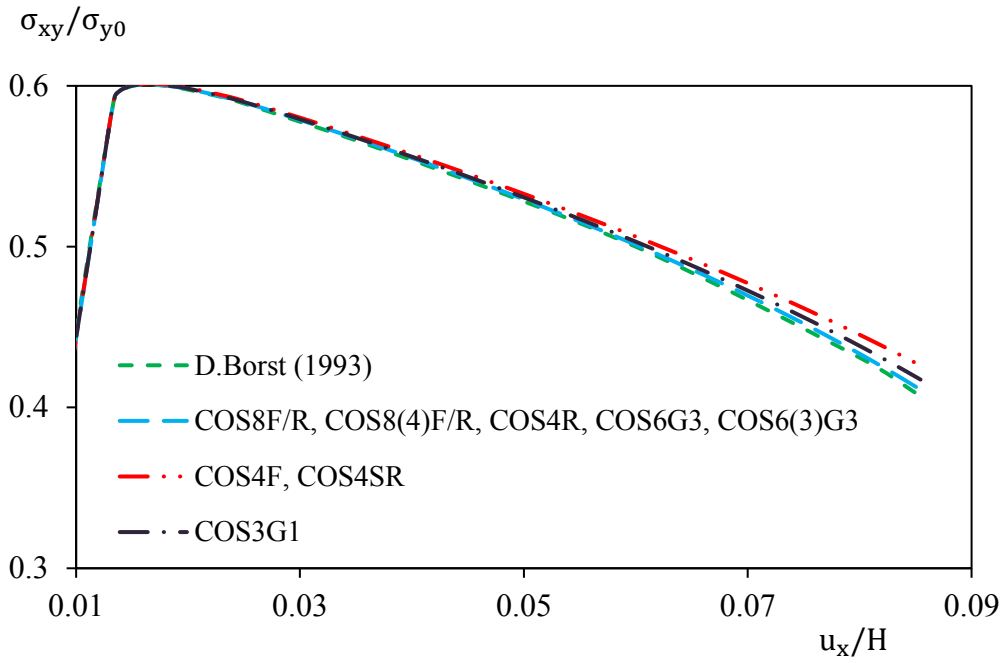

Figure 4.8 Load-displacement curve for the elements with the DP1 model.

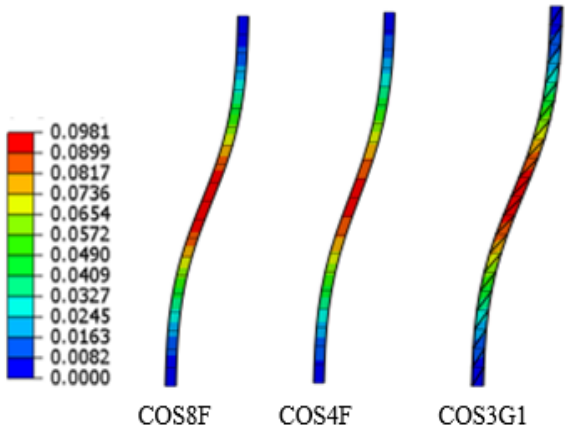

Figure 4.9 Deformed meshes and contour of the equivalent plastic strain of the elements with the DP1 model at the end of the simulation.

All the Cosserat elements in von Mises (VM1 and VM2) and pressure-dependent Drucker-Prager (DP1) model predicts acceptable results in the shear layer (1D)

problem without any numerical issues. Therefore, computationally least expensive 2D Cosserat element COS4R can be used for shear layer (1D) problem without any numerical issue. However, the shear layer test is more restricted regarding deformation since many DOF is set to zero. Therefore, shear layer test acts as an initial benchmark test for localised deformation analysis (de Borst, 1991) which is essentially a 1D problem simulated using the 2D elements. As a result, any volumetric locking or spurious hourglass deformation mode cannot be predicted from shear layer test.

4.1.2 Biaxial tests

A total of ten Cosserat elements as shown in chapter 3, Figure 3.1 is implemented with two different Cosserat von Mises (VM1 and VM2) and one pressure-dependent Drucker-Prager (DP1) plasticity model as shown in chapter 2. Finite element simulation is then carried out to test the numerical behaviour of the elements in the plastic regime considering the biaxial compression test in plane strain condition.

The rectangular specimen has width B=60mm and height H=120mm (for von Mises models) or H=180mm (for Drucker-Prager model). The specimen is subjected to 4.2 mm vertically downwards displacement (negative y-direction). The load (F) is a displacement control one from the top and the bottom left is fixed. Also, assuming natural boundary for the rotations on all sides (i.e. ω_z free). The boundary conditions along the vertical sided (y-direction) are traction-free, and the vertical displacement (i.e. $u_y = 0$) is restricted at the bottom. The geometry, loading and boundary conditions for the biaxial specimen are shown in Figure 4.10.

For the quadrilateral elements, discretisation used for the von Mises and Drucker-Prager models are 12x24-mesh and 12x36-mesh respectively. For the triangular elements, discretisation used for the von Mises and Drucker-Prager models are 6x12-mesh, and 6x18-mesh respectively, where each quadrilateral is composed of four crossed triangular elements. This element layout has been used because of the satisfaction of the incompressibility constraint in isochoric plasticity and the alignment of the element boundaries with expected direction of the shear band on the basis of analytical expressions (Rudnicki & Rice, 1975) so that intrinsically bias of the element

mesh is minimised. The mesh 3x6 has been tested with VM1 model (de Borst, 1991) using a 6-node triangular element with four-point Gauss rule. The mesh 3x6 predicts a slightly stiffer load-displacement response than 6x12 mesh while 6x12 and 12x24 mesh gives the equivalent result. Similar, mesh dependency for Cosserat VM2 model (Sharbati & Naghdabadi, 2006) was obtained using 4-node quadrilateral element, where mesh-independency is obtained if $l/e \geq 0.15$ where e is the size of the element. Therefore, we have considered mesh density such that $l/e \geq 0.2$ throughout the thesis for Cosserat models so that no mesh-dependency results are obtained.

A material imperfection (weak zone) is introduced to trigger localisation in one element at the bottom left of the specimen for von Mises models and at the left boundary near the horizontal centre line for the Drucker Prager model with a lower value of the initial yield stress σ_{w0}. For the von Mises models intentionally a shear band formation is triggered from the bottom left element. While for the Drucker-Prager model to avoid any possible buckling mode since H=3B, a weak element at the left boundary near the horizontal centre line is introduced.

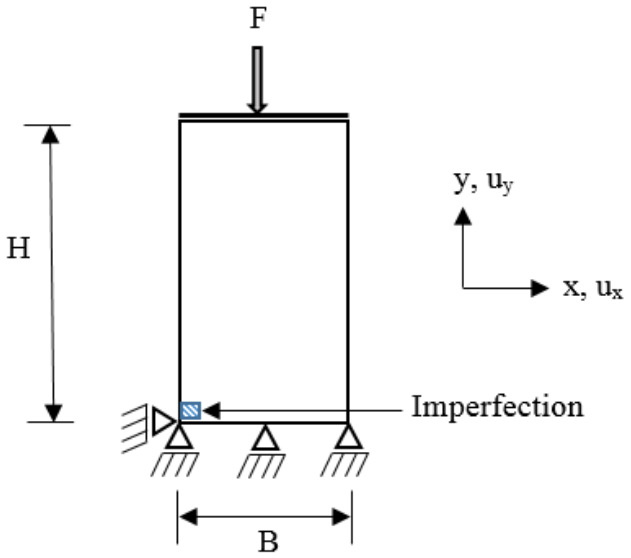

Figure 4.10 Biaxial geometry, loading and boundary conditions.

For all three sets of test for the Cosserat elements, the same material parameters and the biaxial geometry is used as the previous researchers to compare the results with the existing ones.

The first set of results for the Cosserat elements are obtained with VM1 model by de Borst (1991). The material parameters used are: $E = 11920\text{MPa}$, $\nu = 0.49$, $\mu_c = 2000\text{MPa}$, $h_p = -400\text{MPa}$, $\sigma_{y0} = 100\text{MPa}$, $\sigma_{w0} = 95\text{MPa}$ and $l = 9.996\text{mm}$.

The load-displacement curve for the elements with VM1 model by de Borst (1991) is shown in Figure 4.11. Note that de Borst (1991) have used a 6-node triangular element with four-point Gauss rule. The quadratic/quadratic and quadratic/linear elements give practically the same results, all very slightly stiffer than the ones reported by de Borst (1991) at the later stages of plasticity. COS4SR element gives a slightly stiffer but very similar result to quadratic/quadratic and quadratic/linear elements, while COS3G1 gives a much stiffer response at the later stages of plastic deformation. COS4F gives an overly stiff response. COS4R element gives a similar response to quadratic/quadratic or quadratic/linear elements, but the solution is spoiled by spurious hourglass deformation modes as shown in Figure 4.12. Only Cosserat COS8F element is shown in Figure 4.12 as the quadratic/quadratic and quadratic/linear elements all give the equivalent result.

The numerical simulation predicts a diffused deformation and the equivalent plastic strain spreads at the bottom of the specimen as shown in Figure 4.12. Numerical experimentation shows that a shear band is achieved with a smaller internal length. Note that the load-displacement curve is same during elastic deformation for all the elements. During the simulation, it was observed that the rotation field is almost inactive (zero) during elastic deformation. However, as soon as the deformation reaches plasticity, there is a sudden increase in rotation near the weak zone. Increasing the plastic deformation, the maximum rotation increases and its position changes within the plastic zone.

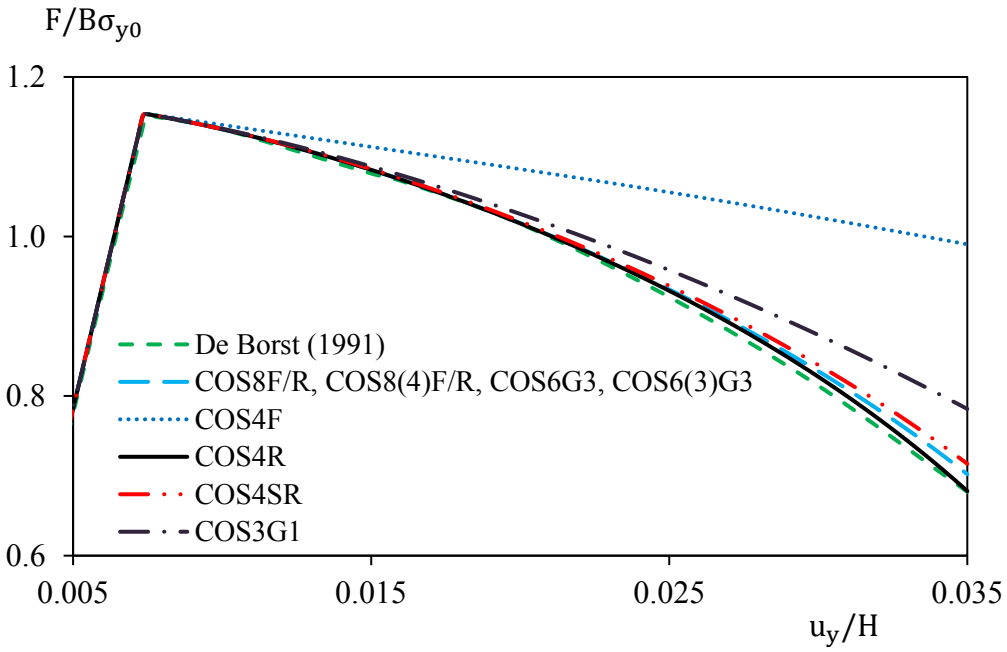

Figure 4.11 Load-displacement curve for the elements with VM1 model.

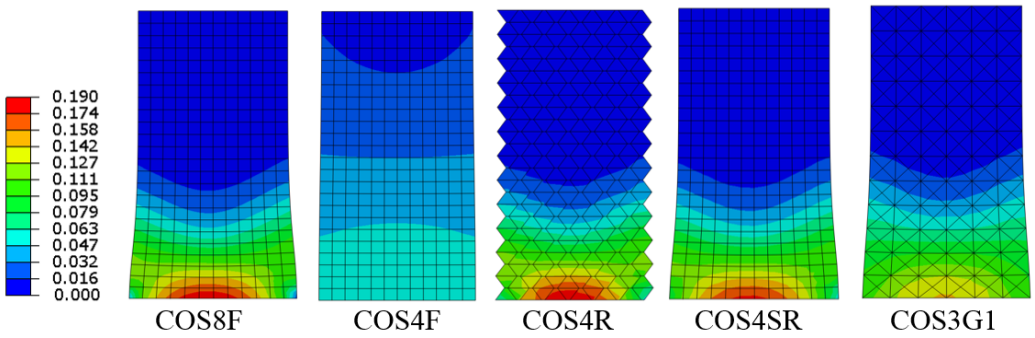

Figure 4.12 Deformed meshes and contour of the equivalent plastic strain of the elements with the VM1 model at $u_y/H = 0.035$.

The second set of results for the Cosserat elements are obtained with VM2 model by Sharbati and Naghdabadi (2006). The material parameters used are: $E = 4000\text{MPa}$, $\nu = 0.49$, $h_p = -120\text{MPa}$, $\sigma_{y0} = 100\text{MPa}$, $\sigma_{w0} = 98\text{MPa}$ and $l = 2\text{mm}$.

The load-displacement curve for all the elements with VM2 by Sharbati and Naghdabadi (2006) are shown in Figure 4.13. Note that Sharbati and Naghdabadi (2006) have used 4-node quadrilateral elements without mentioning the integration scheme employed. Again, with model VM2, COS4F is overly stiff, while COS4R

predicts a reasonable load-displacement curve but suffers from hourglassing. The quadrilateral quadratic/linear elements predict an almost identical load-displacement curve to quadrilateral quadratic/quadratic and triangular quadratic/quadratic and quadratic/linear elements, while COS4SR and COS3G1 elements are stiffer, more visibly than in the previous case. In Figure 4.14 only Cosserat COS8F element is shown as the quadratic/quadratic and quadratic/linear elements give an almost equivalent result.

The overall numerical behaviour of the elements in Sharbati and Naghdabadi (2006) and in de Borst (1991) models are very similar. All the elements predict reasonable results without any numerical issues except for COS4F and COS4R elements which predicts stiffer locking behaviour and hourglassing respectively. The element COS3G1predicts stiffer and very different results from the majority of the elements for both the model VM1 and VM2. While COS4SR element diverges more from the quadratic/quadratic and quadratic/linear elements than the first test with VM1 model which is not acceptable as the element shows different behaviour with different plasticity models. In general, the stiffer elements predict a more extensive plastic zone and SBW as shown in Figure 4.14.

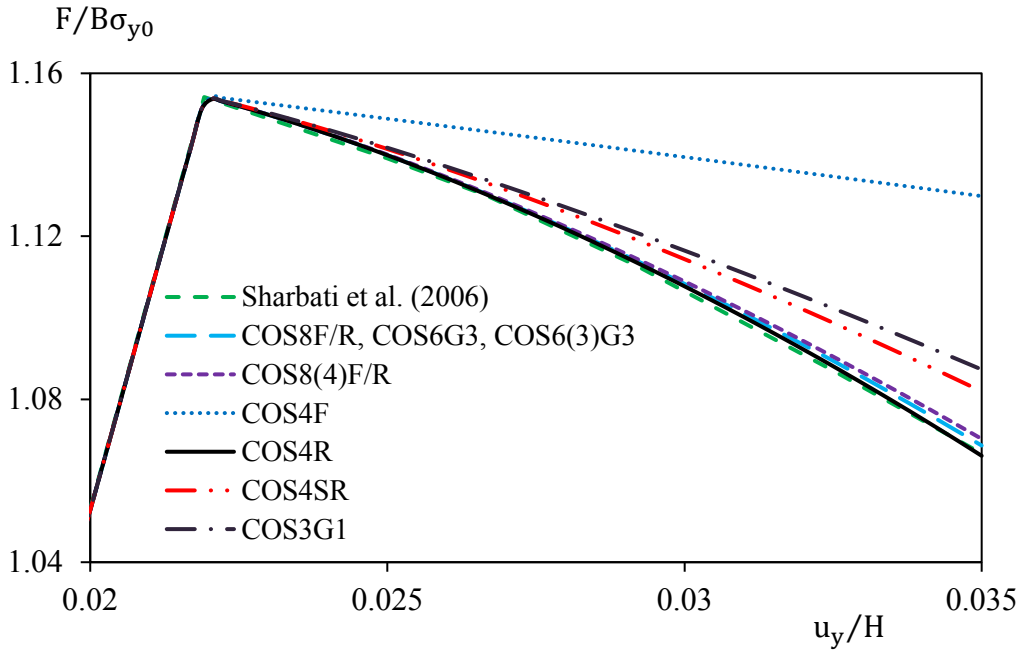

Figure 4.13 Load-displacement curve for the elements with VM2 model.

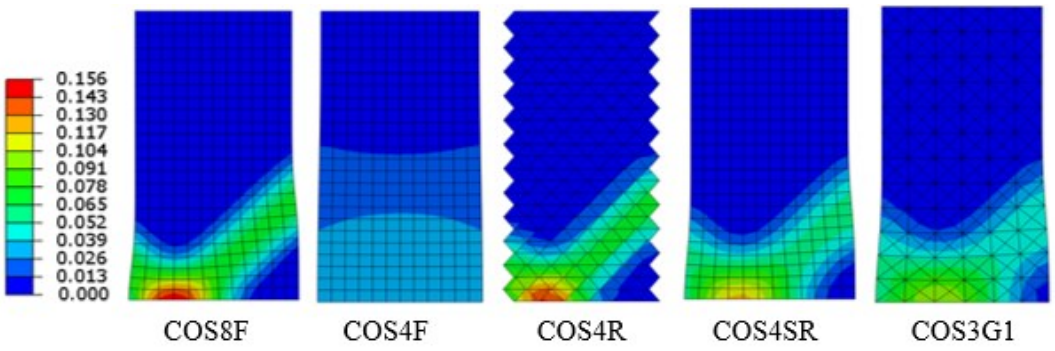

Figure 4.14 Deformed meshes and contour of the equivalent plastic strain of the elements with VM2 model at $u_y/H = 0.035$.

The deformed shape predicted by COS4F and COS4R elements with VM2 model in this work as shown in Figure 4.14 disagree with the deformed shaped (without any hourglass modes) predicted by Sharbati and Naghdabadi (2006) with an internal length of 1 mm for 4-node quadrilateral elements (integration scheme employed are not mentioned). Only COS4SR elements are capable of predicting the deformed shape obtained by Sharbati and Naghdabadi (2006). However, the element COS4SR predicts stiffer load-displacement curve as shown in Figure 4.13. Therefore, it is vital to mention the integration scheme employed as the integration scheme plays a vital role during plastic deformation.

The third set of results for the Cosserat elements are obtained with the pressure-dependent Drucker-Prager DP1 model. The material parameters used are: $E = 2400\text{MPa}$, $v = 0.2$, $\mu_c = 500\text{MPa}$, $h_p = -51.96\text{MPa}$, $c_0 = 2.078\text{MPa}$, $c_{w0} = 1.97\text{MPa}$ and $l = 6\text{mm}$. Non-associated plasticity is assumed with $\alpha_1 = 1.2$ and $\alpha_2 = 0$. Note that the material parameters used are precisely the same as de Borst (1993) biaxial test to enable comparison.

The load-displacement curve for the elements with the DP1 model is shown in Figure 4.15. The quadratic/quadratic, quadratic/linear and COS4R gives equal load-displacement curve, all are much softer than the ones reported by de Borst (1993) using 6-node triangular element (integration scheme not mentioned). Although COS4R gives satisfactory load-displacement curve, the element suffers from spurious hourglass deformation mode. The COS4SR element is stiffer compared to quadratic

displacement elements, while COS4F once again is overly stiff. The COS3G1 element gives a reasonable load-displacement curve but diverges at the later stages of plastic deformation. Figure 4.16 shows diffused localised deformation for all the elements at the bottom of the specimen. Numerical experimentation shows that a shear band formation can be predicted with a smaller internal length.

The numerical experimentation shows that, if we use the internal length as we did earlier for the shear layer test, i.e. $l = 12\text{mm}$ with the DP1 model, our biaxial results are very close de Borst (1993). This lead to conclusions that possibly he has used the same internal length as shear layer test or it might be that in his code a factor of two has been introduced somewhere. As we do not have the details of his coding, it is quite difficult to point out the exact reason for this differences in the biaxial results.

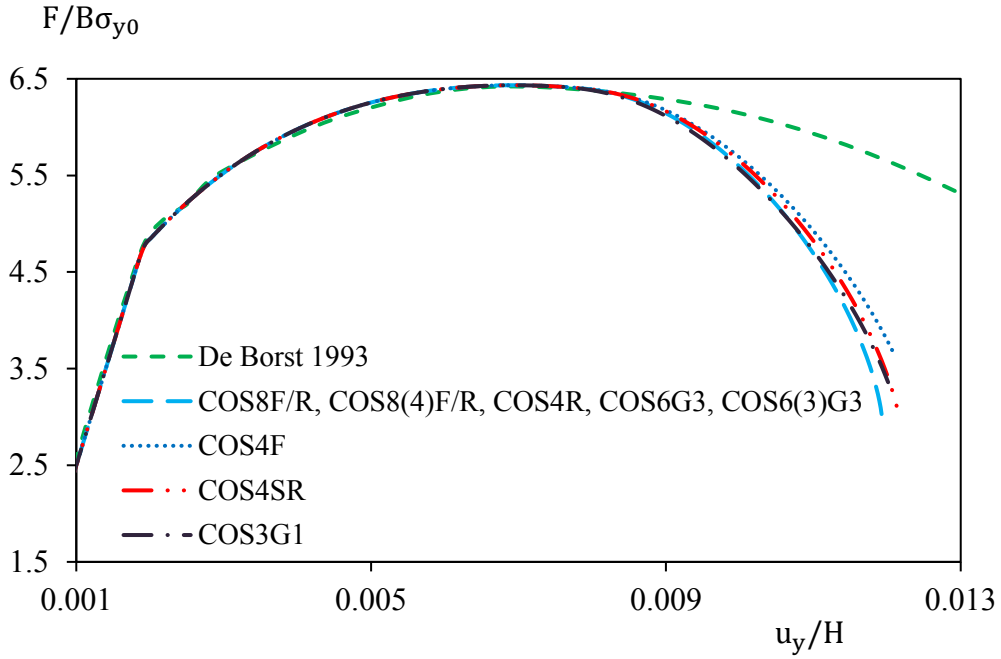

Figure 4.15 Load-displacement curve for the elements with the DP1 model.

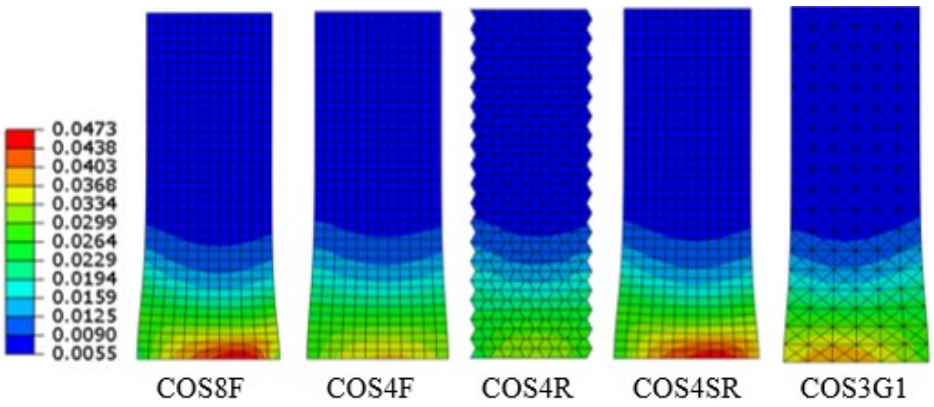

Figure 4.16 Deformed meshes and contour of the equivalent plastic strain of the elements with the DP1 model at the end of the simulation.

4.2 Finite elements for strain-gradient models: Biaxial tests

A total of thirteen elements as shown in chapter 3, Figure 3.1 is implemented with two different von Mises (CCM and FH) and two different Drucker-Prager (CCMDP and FHDP) strain-gradient plasticity models as shown in chapter 2. Numerical finite element simulations are then carried out to test the numerical behaviour of the elements in the post-peak regime.

The rectangular specimen has width B=60mm and height H=120mm. The biaxial geometry, loading and boundary conditions of the specimen for the tests remain the same as shown in Figure 4.10. The material parameters adopted for the CCM and FH strain-gradient plasticity models are: $E = 4000\text{MPa}$, $v = 0.49$, $\mathrm{h_p} = -40\text{MPa}$, $\sigma_{y0} = 100\text{MPa}$, $\sigma_{w0} = 98\text{MPa}$ and $l = 0.6\text{mm}$. Note that for FH model $l = \mathrm{L_I} = l_{\mathrm{I}}$ (i.e. all the elastic and plastic length scales are equal).

4.2.1 Mesh refinement studies

Mesh refinement studies are carried out for the elements to determine the effect of mesh density on the numerical solutions. Three different dicretisation is used for all the quadrilateral elements namely 8x16, 12x24 and 20x40-mesh. For the triangular C^1 elements, discretisation used namely 4x8, 6x12 and 12x24-mesh, where each quadrilateral is composed of four crossed triangular elements. The mesh refinement

study is carried out using the CCM model. During numerical experimentation, QU30L3R and QU34L4R elements showed spurious hourglass deformation modes. Therefore, no mesh refinement studies have been carried out for QU30L3R and QU34L4R elements.

(a) Penalty method elements

The numerical experimentation of the penalty parameter from $\gamma = 10^8$ to $\gamma = 10^{10}$ with the CCM plasticity model shows no difference in the numerical results. Therefore, the penalty parameter $\gamma = 10^8$ is used for all the simulations.

The load-displacement curves of the penalty elements QU28P (and QU32P) and QU28PR (and QU32PR) with different discretisations are shown in Figure 4.17 and Figure 4.18 respectively. The penalty method elements predict pathologically mesh dependent results. This indicates that the penalty parameter is not constant during the simulation and requires reformulation of the penalty method such that penalty parameter is determined at each increment instead of using a constant value of the penalty parameter. Figure 4.19 shows the deformed meshes and contour of equivalent plastic strain for the penalty method elements with different meshes at the end of the simulation. The SBW decreases with increasing mesh density. Although, the penalty method elements are computationally cheaper the elements give pathologically mesh dependent solutions.

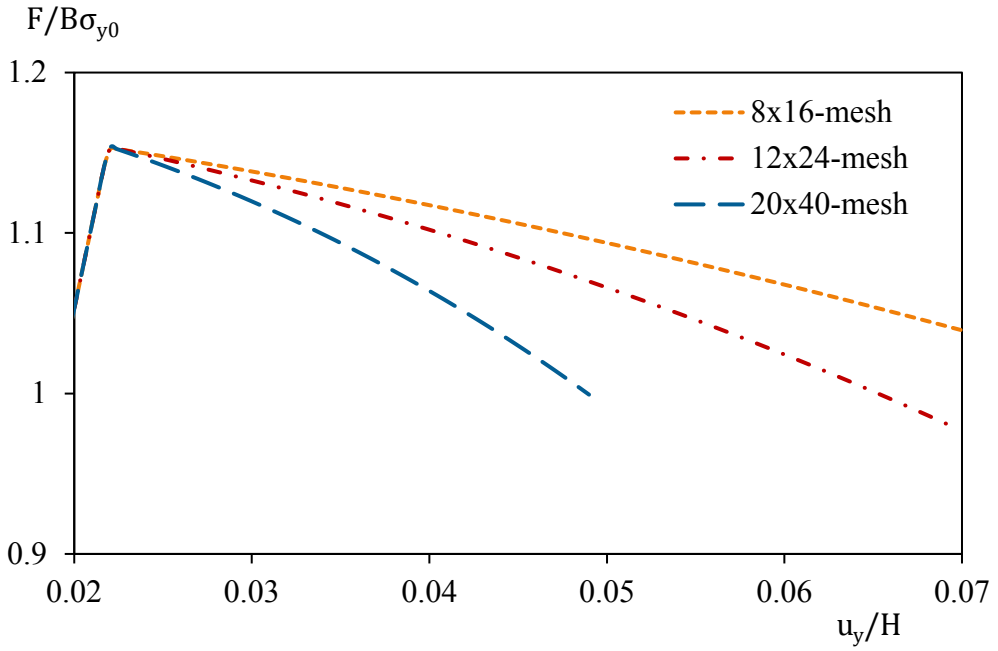

Figure 4.17 Load-displacement curves for the element QU28P and QU32P.

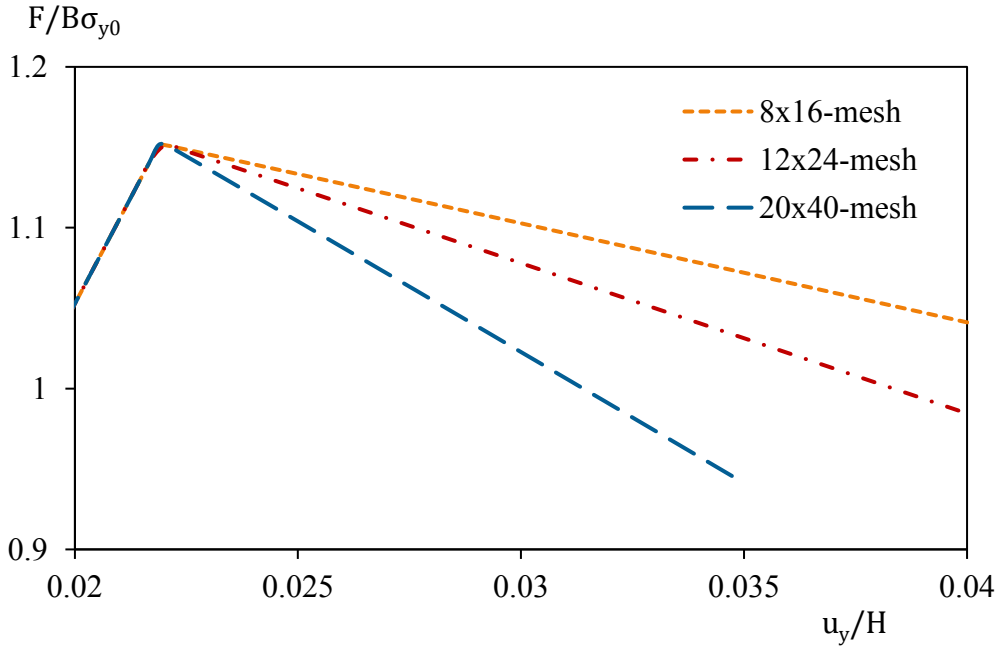

Figure 4.18 Load-displacement curves for the element QU28PR and QU32PR.

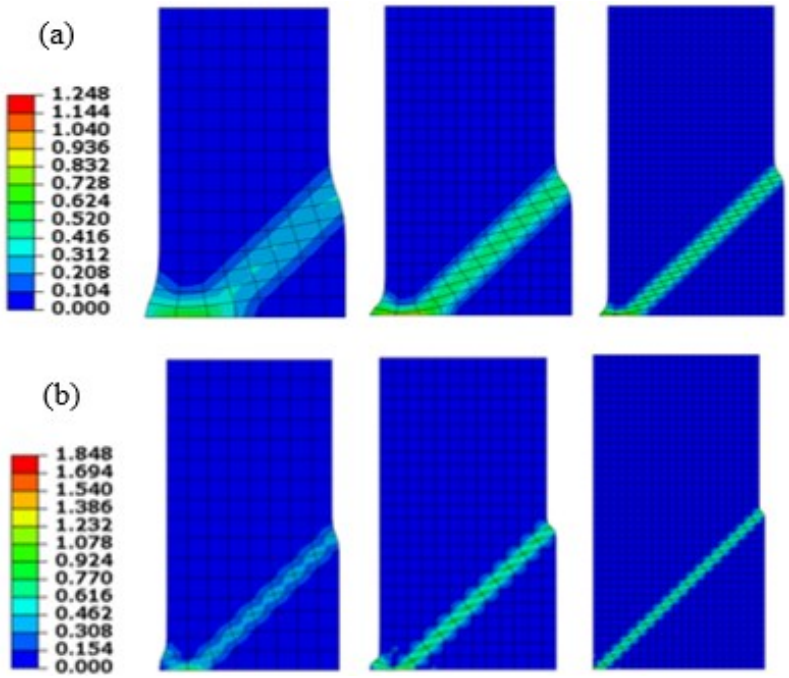

Figure 4.19 Deformed meshes and contour of the equivalent plastic strain for the elements at the end of the simulation: (a) QU28P and QU32P, (b) QU28PR and QU32PR.

(b) Quadrilateral mixed-type Lagrangian and triangular C^1 elements

The load-displacement curves for mixed-type Lagrangian elements: QU28L3, QU28L3R, QU30L3, QU32L4, QU32L4R and QU34L4 with different discretisation are shown from Figure 4.20 to Figure 4.25 respectively. The load-displacement curves for triangular C^1 element with different discretisation are shown in Figure 4.26. The elements QU28L3, QU30L3, QU32L4, QU32L4R and QU34L4, predicts a slightly stiffer load-displacement curve for 8x16-mesh. While the elements QU28L3 and TU36C1 shows no differences in the load-displacement curve even with the 8x16 and 4x8-mesh respectively. The mixed-type Lagrangian elements show equivalent load-displacement curve for 12x24 and 20x40-mesh. While the triangular C^1 element shows equivalent load-displacement for 4x24, 6x12 and 8x16-mesh. Therefore both the mixed-type Lagrangian and triangular C^1 element shows mesh-independent results with reasonable mesh refinement.

The deformed meshes and contour of the equivalent plastic strain at the end of the simulation for the elements: QU28L3 (and QU28L3R, QU30L3 QU32L4) and

QU32L4R (and QU34L4, TU36C1) are shown in Figure 4.27 and Figure 4.28 respectively. The SBW for the quadrilateral elements remains constant for 12x24 and 20x450-mesh while the SBW for triangular C^1 element are equal for all the meshes. The triangular C^1 element with higher order integration scheme allows mesh independent solutions with fewer meshes. The mixed-type Lagrangian elements also predict mesh independent solutions with reasonable mesh refinement (i.e.12x24). Therefore, any mixed-type and triangular C^1 element can be used with strain-gradient plasticity models with reasonable mesh refinement. However, considering the difficulties in numerical implementation and the computational cost the mixed-type Lagrangian elements are recommended.

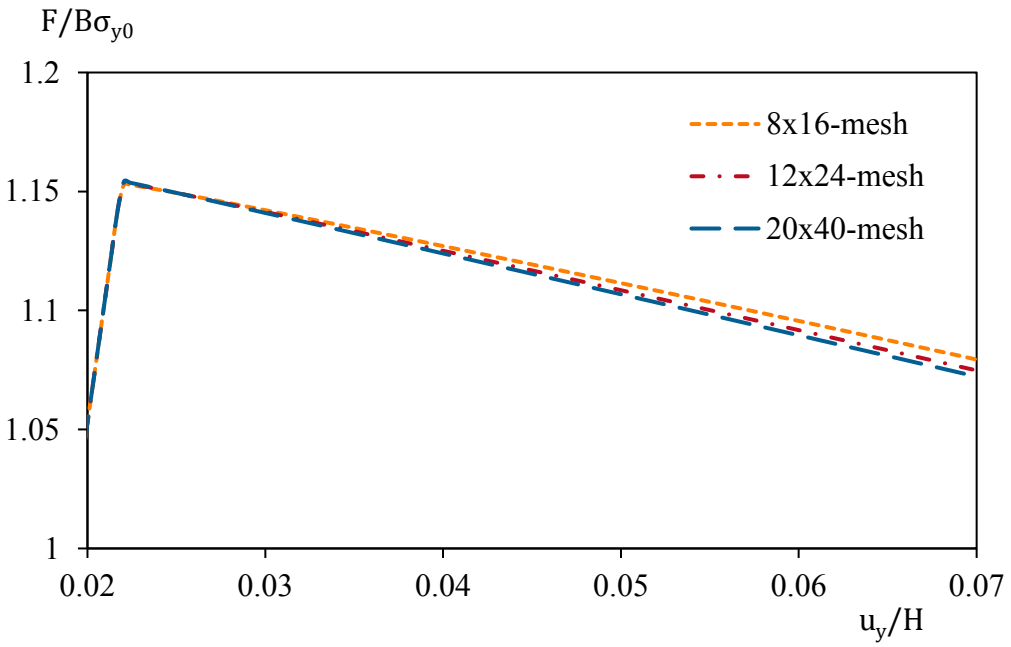

Figure 4.20 Load-displacement curves for the element QU28L3.

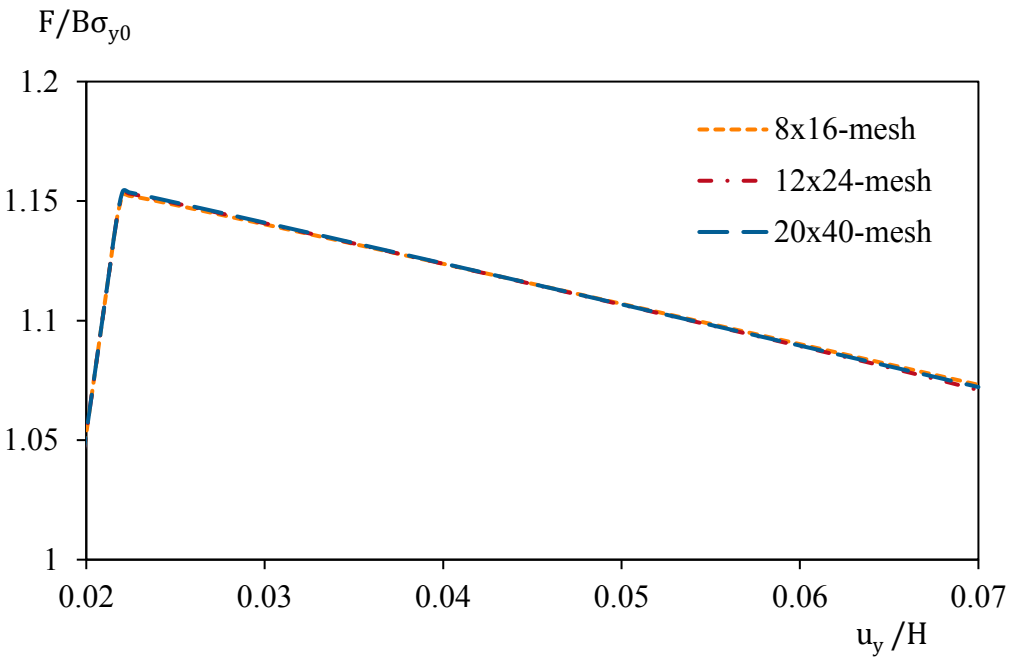

Figure 4.21 Load-displacement curves for the element QU28L3R.

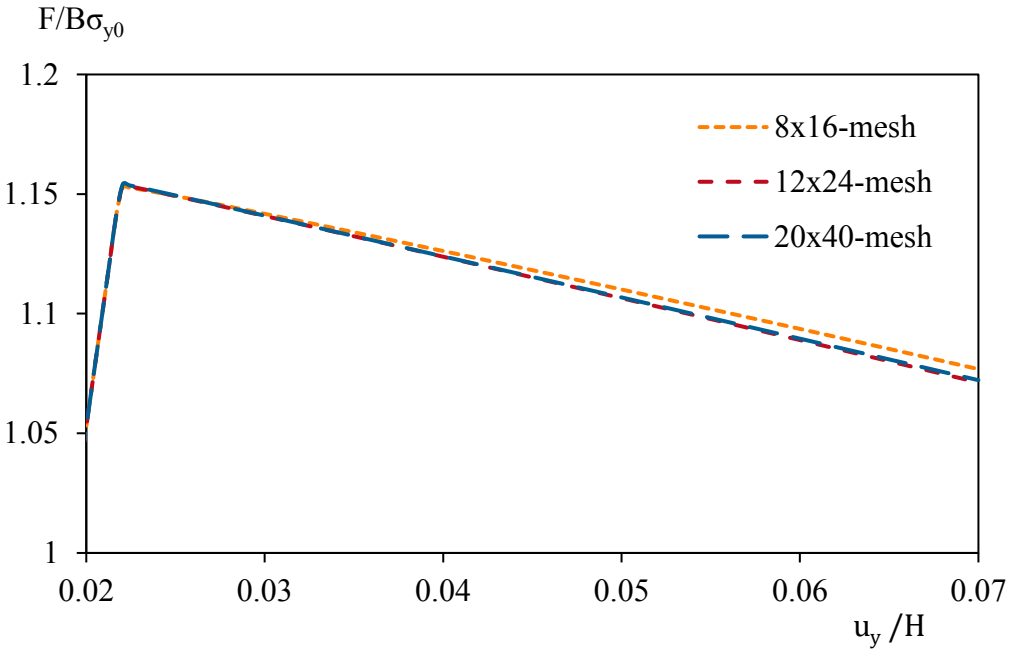

Figure 4.22 Load-displacement curves for the element QU30L3.

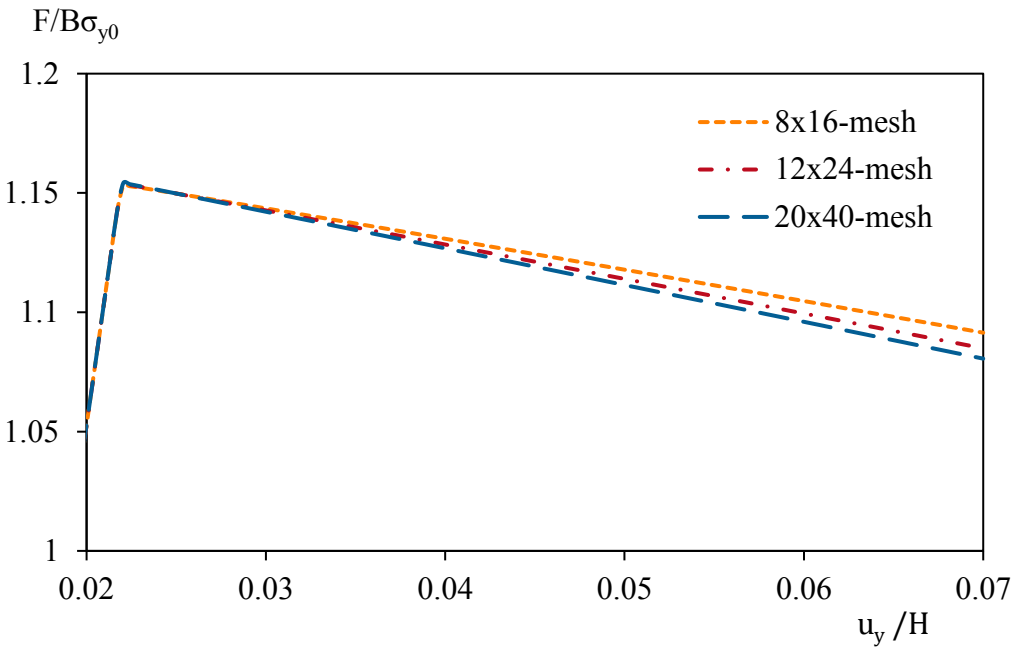

Figure 4.23 Load-displacement curves for the element QU32L4.

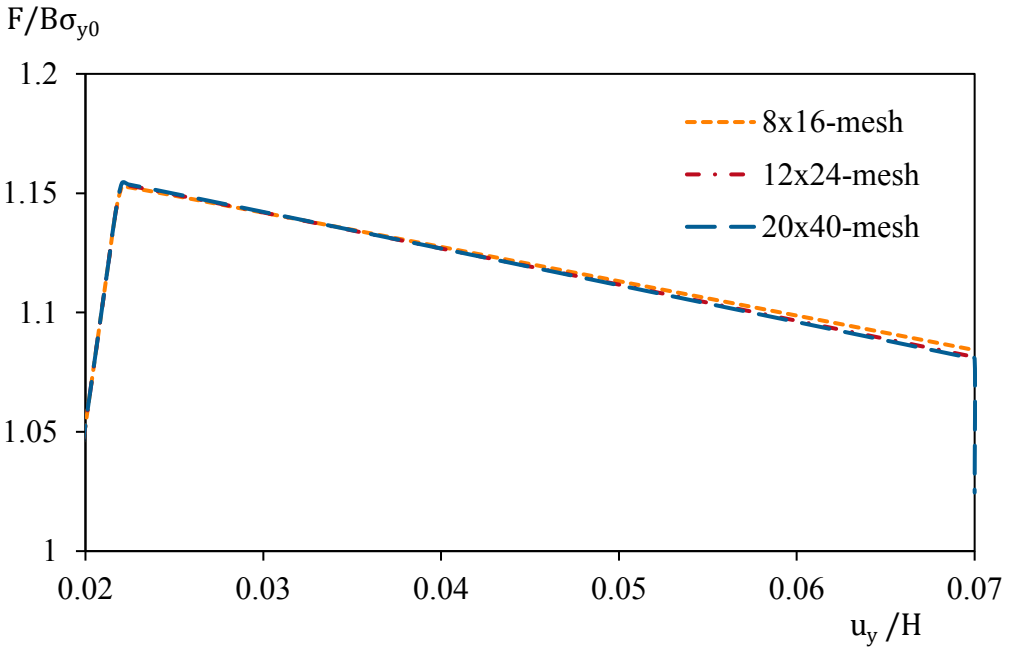

Figure 4.24 Load-displacement curves for the element QU32L4R.

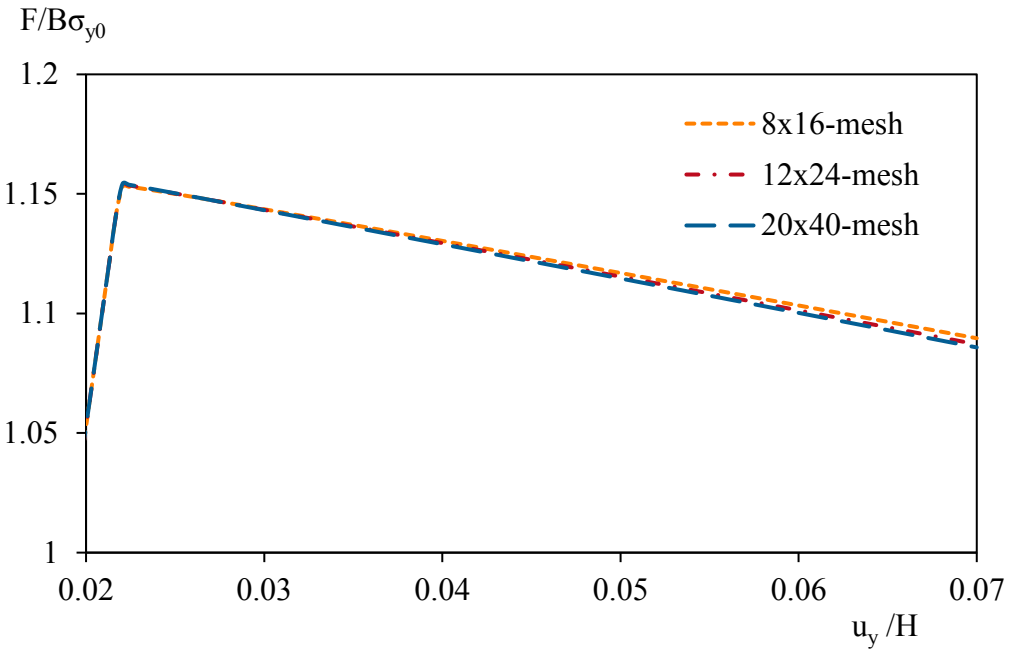

Figure 4.25 Load-displacement curves for the element QU34L4.

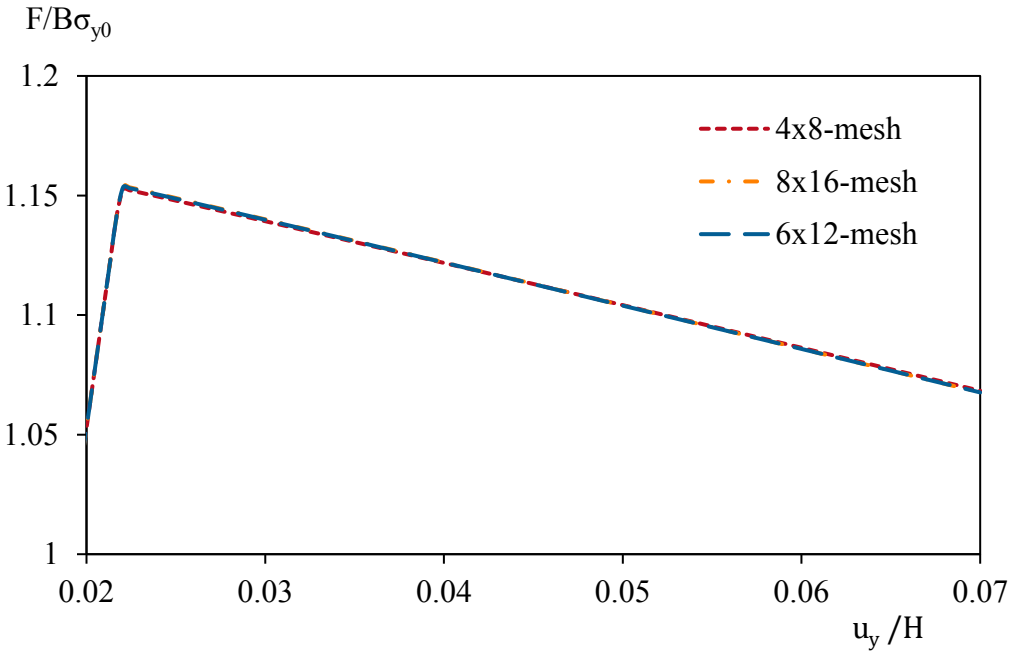

Figure 4.26 Load-displacement curves for the element TU36C1.

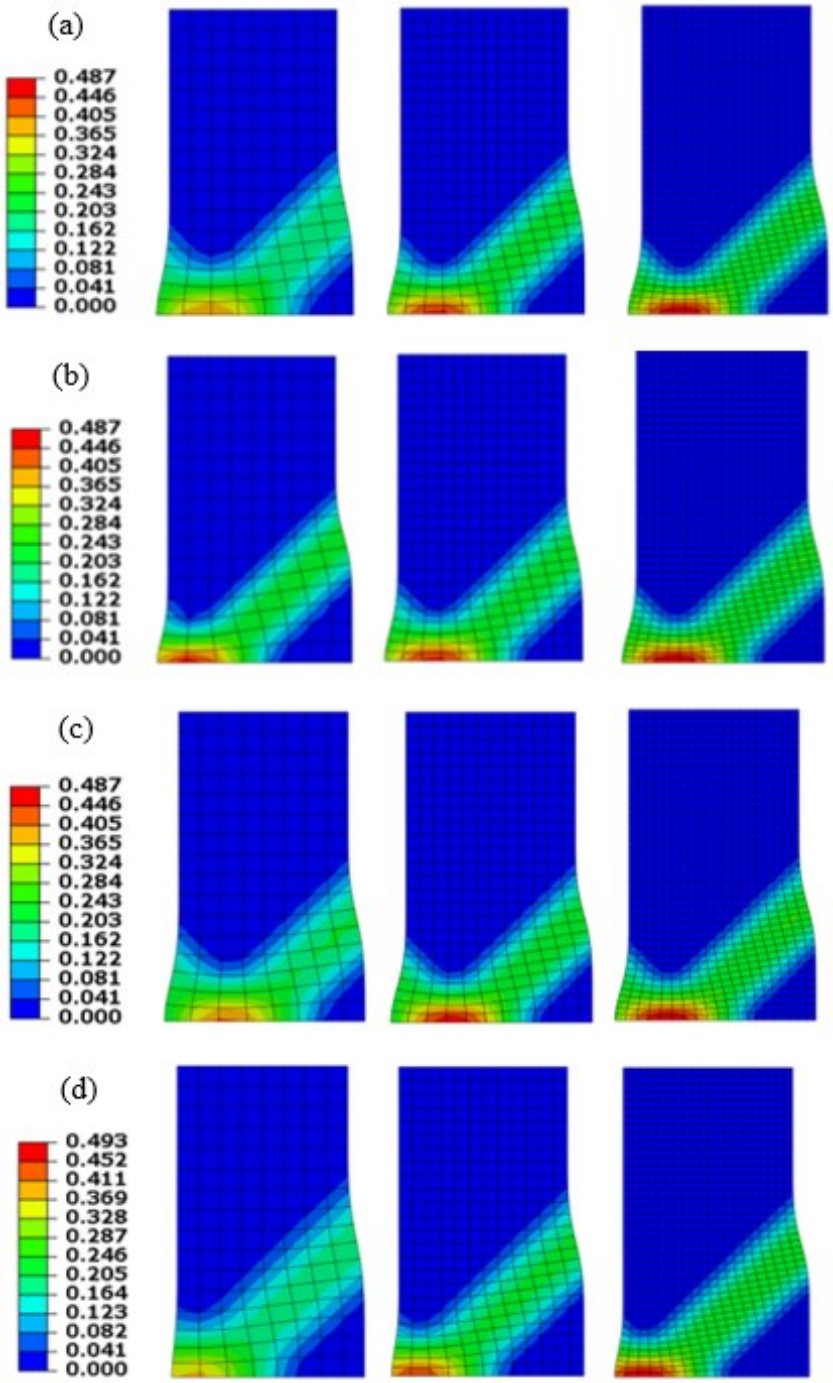

Figure 4.27 Deformed meshes and contour of the equivalent plastic strain for the elements at the end of the simulation: (a) QU28L3, (b) QU28L3R, (c) QU30L3 and (d) QU32L4.

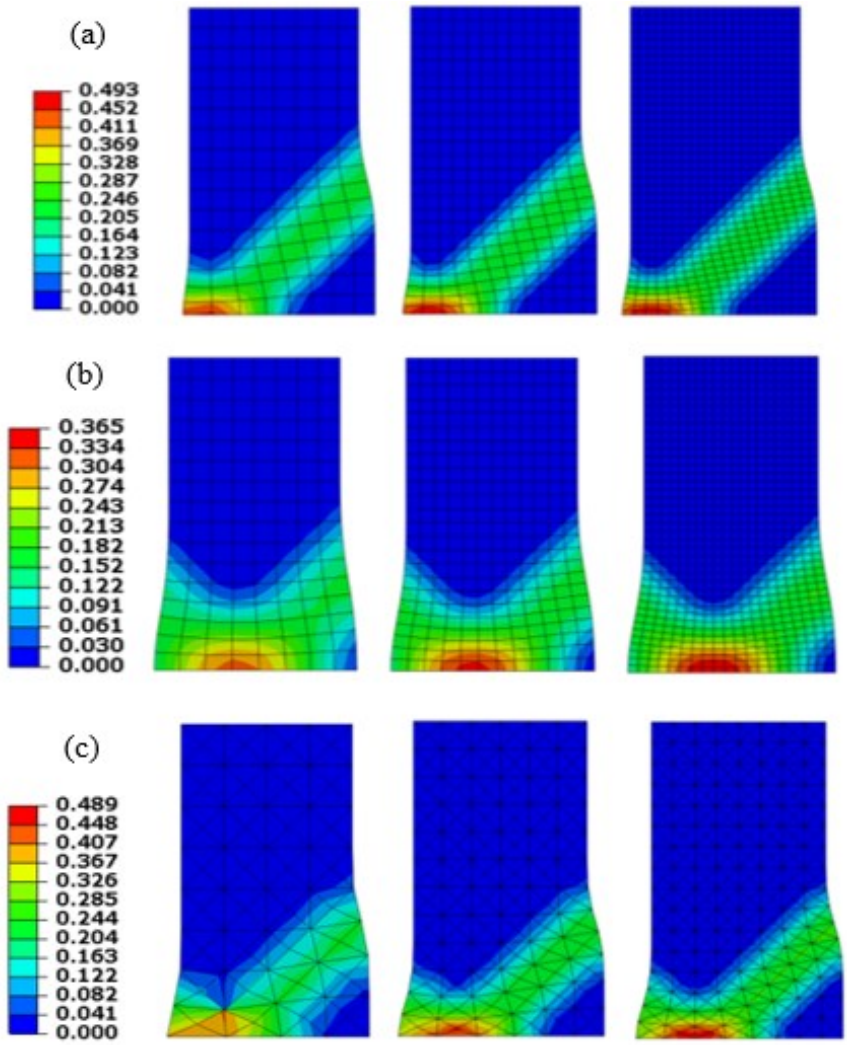

Figure 4.28 Deformed meshes and contour of the equivalent plastic strain for the elements at the end of the simulation: (a) QU32L4R, (b) QU34L4 and (c) TU36C1.

4.2.2 Finite elements and strain-gradient plasticity models

The mesh refinement studies in the previous section showed that the quadrilateral mixed-type Lagrangian elements predict a slightly stiffer load-displacement response with 8x16-mesh in the post-peak regime than 12x24-mesh whereas 12x24 and 20x40-mesh give the equivalent result. For triangular C^1 element, all meshes predict equivalent numerical solutions. Based on the numerical results obtained in the previous section the finite elements for strain-gradient models may predict mesh-dependency

results if $l/e < 0.1$ where $_e$ is the size of the element. From this point onwards we have used mesh density such that $l/e \geq 0.1$ so that mesh-independent results are obtained for the mixed-type Lagrangian and triangular C^1 elements. The penalty method elements show pathologically mesh dependent solutions. Therefore, we have considered the same mesh for the penalty method and mixed-type Lagrangian elements to make a comparison with different strain-gradient plasticity models.

The load-displacement curve for the elements with the CCM model is shown in Figure 4.29. The deformed meshes and contour of the equivalent plastic strain for the elements with the CCM model are shown in Figure 4.30. All the mixed-type and penalty elements with full (quintic, 3x3) integration and triangular C^1 element predict acceptable numerical results. Among quadrilateral full integration elements QU34L4 and QU28P (and QU32P) predict the most and the least stiff load-displacement curve respectively. The quadrilateral full integration elements are close to QU34L4 while QU28P (and QU32P) elements are much softer and further away. The numerical finite element solution of QU34L4R does not converge at the later stages of plasticity, and spurious deformation hourglass modes are predicted as shown in Figure 4.30. The numerical finite element solution of QU30L3R does not converge when reaches plasticity and also suffers from hourglassing. The penalty reduced integration elements QU28PR (and QU32PR) are overly soft. All the elements with reduced (cubic, 2x2) integration scheme show some numerical issues with CCM model expect QU28L3R and QU32L4R elements. The elements with stiffer load-displacement curve predict broader plastic zone at the bottom of the specimen and a larger SBW as shown in Figure 4.30.

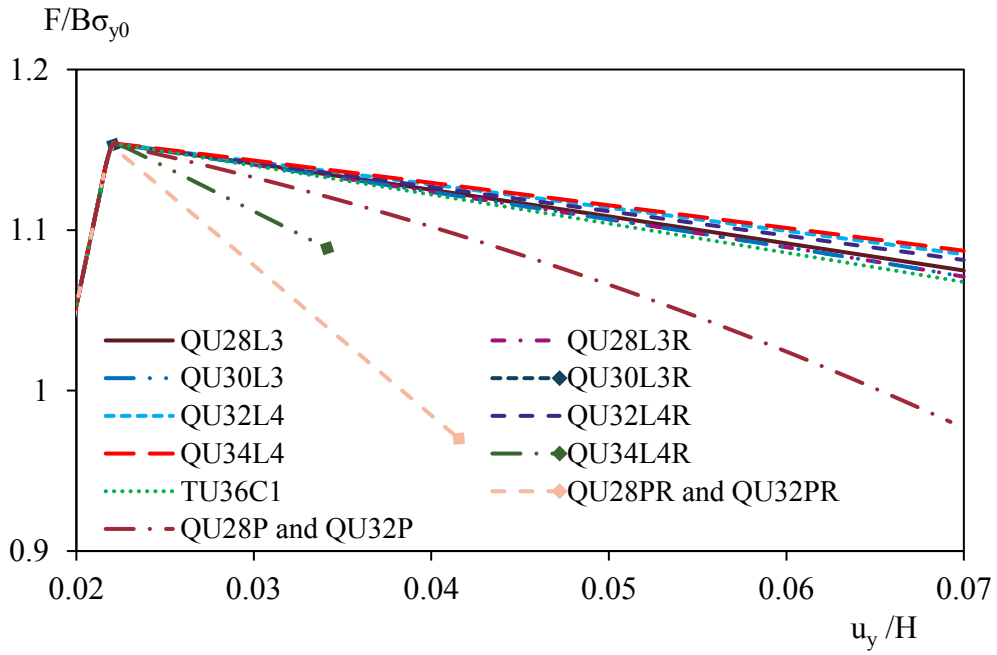

Figure 4.29 Load-displacement curve for the elements with CCM model.

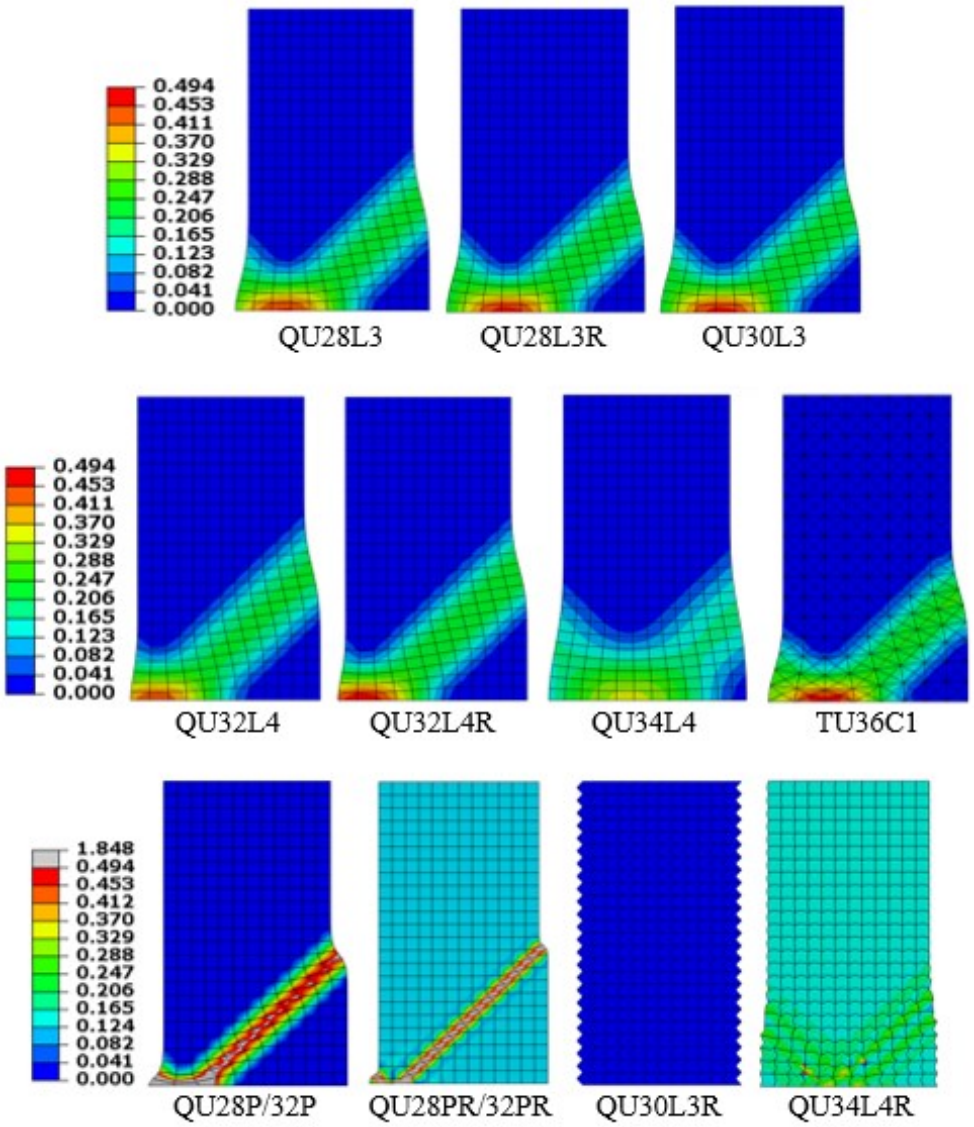

Figure 4.30 Deformed meshes and contour of the equivalent plastic strain for the elements with CCM model at the end of the simulation.

The load-displacement curve for the elements with FH model is shown in Figure 4.31. The deformed meshes and contour of the equivalent plastic strain for the elements with FH model are shown in Figure 4.32. All the mixed-type and penalty elements with full (quintic, 3x3) integration and triangular C^1 elements predict satisfactory numerical results. Among full integration elements, QU34L4 predicts the stiffest load-displacement curve. The numerical finite element solutions of QU28L3R and QU34L4R does not converge at the later stages of plasticity while QU28PR (and QU32PR) is overly soft. The numerical finite element solution of QU30L3R fails to

converge at plasticity. Both the elements QU30L3R and QU34L4R suffers from hourglass modes. All elements with reduced (cubic, 2x2) integration scheme show some numerical issues with FH model expect QU32L4R.

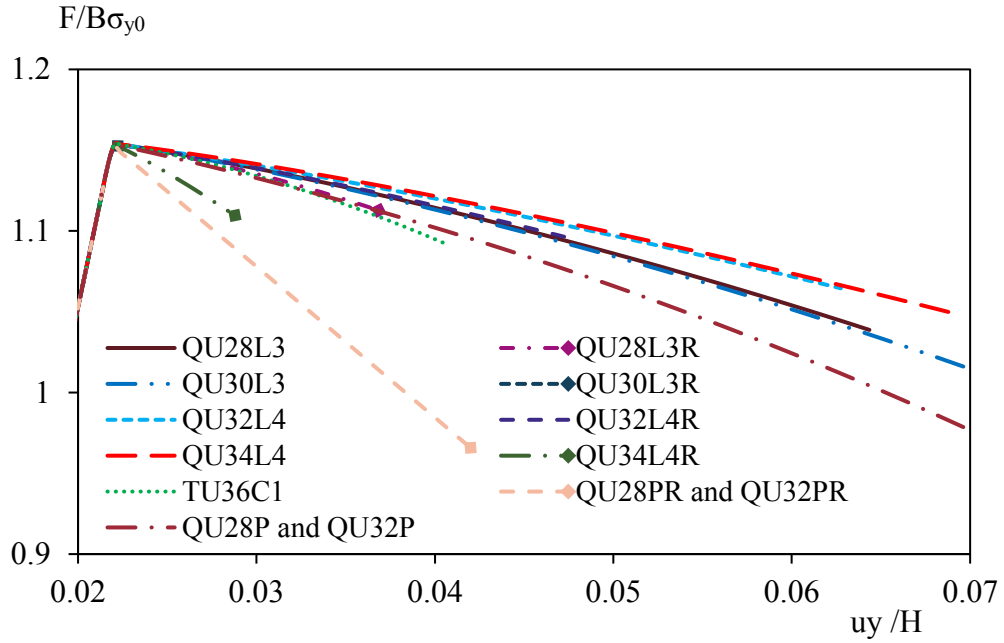

Figure 4.31 Load-displacement curve for the elements with FH model.

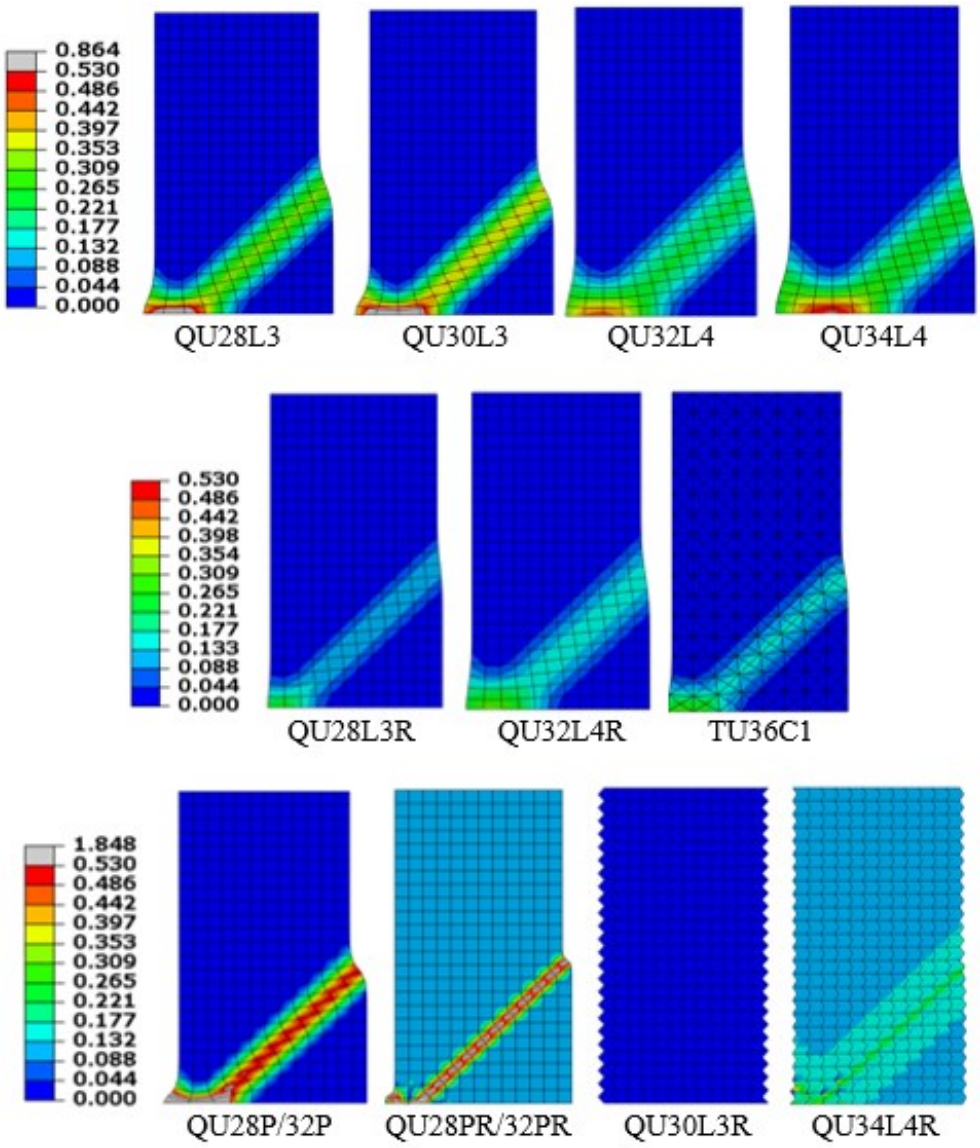

Figure 4.32 Deformed meshes and contour of the equivalent plastic strain for the elements with FH model at the end of the simulation.

The material parameters used for the pressure-dependent Drucker-Prager (CCMDP and FHDP) plasticity models are: $E = 11920\text{MPa}$, $v = 0.49$, $\mathrm{h_p} = -120\text{MPa}$, $c_0 = 50\text{MPa}$, $c_{w0} = 45\text{MPa}$ and $l = 0.6\text{mm}$. Note that for FHDP model $l = \mathrm{L_I} = l_{\mathrm{I}}$ (i.e. all the elastic and plastic length scales are equal). Associated plasticity is assumed with the friction and dilatancy angle such, that $\sin\phi = \sin\psi = 0.3.$

The load-displacement curve for the elements with CCMDP model is shown in Figure 4.33. The deformed meshes and contour of the equivalent plastic strain for the

elements with CCMDP model are shown in Figure 4.34. All the mixed-type and penalty elements with full (quintic, 3x3) integration and triangular C^1 elements predict acceptable numerical results (i.e. no significant numerical issues such as locking or hourglass deformation modes) except QU28L3 element. The numerical finite element solution of QU28L3 does not converge when the deformation reaches plasticity. Among full integration elements, QU34L4 and QU28P (and QU32P) predict the most and the least stiff load-displacement curve respectively. The elements QU28PR (and QU32PR) are overly soft. The elements QU30L3R and QU34L4R predict reasonable load-displacement curves but suffer from hourglass modes as shown in Figure 4.34. All the reduced (cubic, 2x2) integration elements show some numerical issues with CCMDP model except QU28L3R and QU32L4R elements.

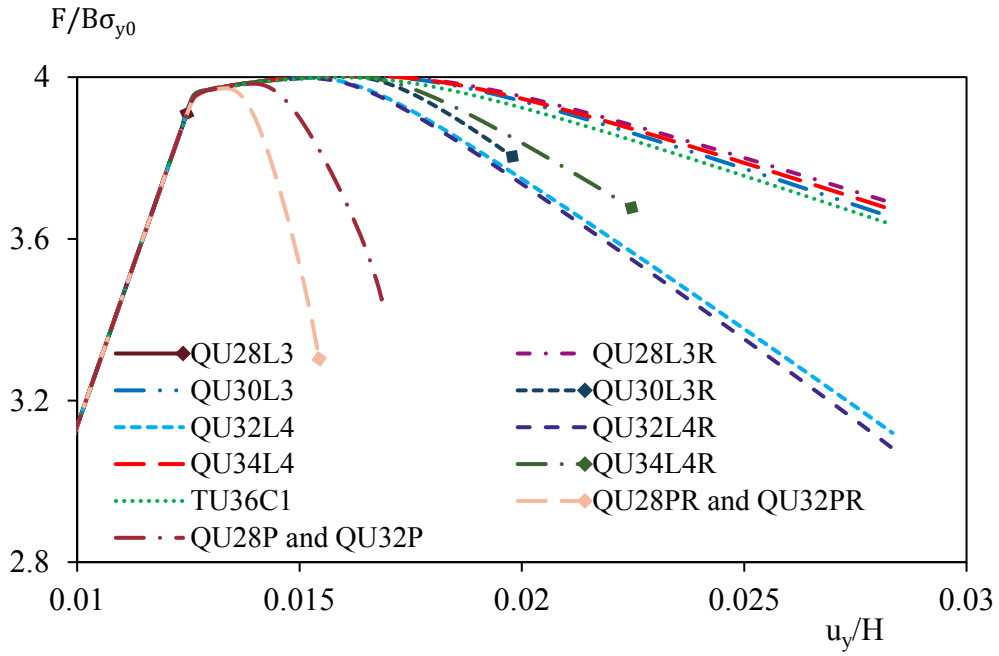

Figure 4.33 Load-displacement curve for the elements with CCMDP model.

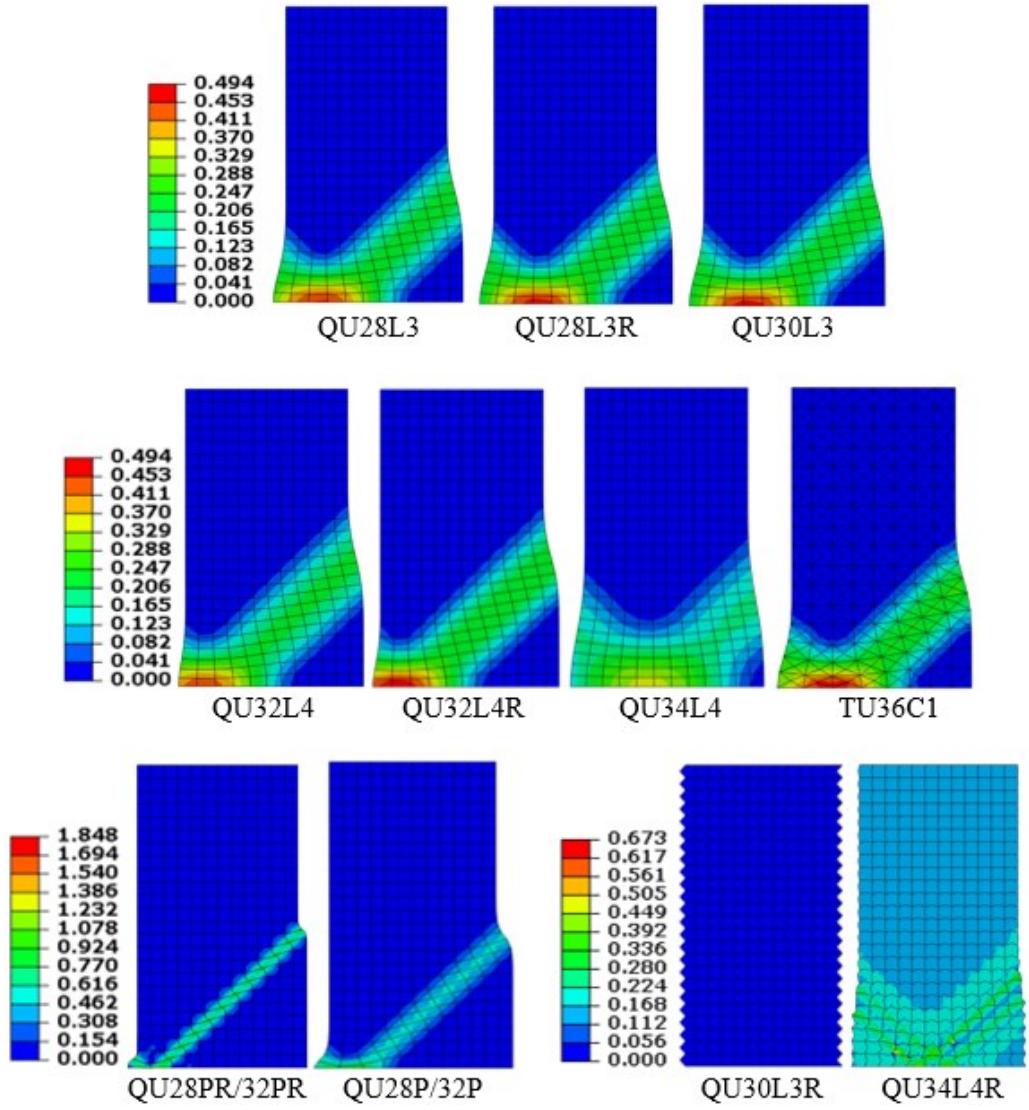

Figure 4.34 Deformed meshes and contour of the equivalent plastic strain for the elements with CCMDP model at the end of the simulation.

The load-displacement curve for the elements with FHDP model is shown in Figure 4.35. The deformed meshes and contour of the equivalent plastic strain for the elements with FHDP model are shown in Figure 4.36. All the mixed-type and penalty elements with full (quintic, 3x3) integration and triangular C^1 element predict acceptable (i.e. no significant numerical issues such as locking or hourglass deformation modes) numerical results. Among full integration elements, QU28L3 predicts the stiffest load-displacement curve. The numerical finite element solution of QU30L3R and QU34L4R does not converge at the later stages of plasticity, also suffers from hourglassing as shown in Figure 4.36 while penalty method reduced and

full integration elements are overly soft. All quadrilaterals elements with reduced (cubic, 2x2) integration show some numerical issues with FHDP model except QU28L3R and QU32L4R elements.

The element QU34L4 has been tested in elastic problems and shown to satisfy the stability condition and have been found to work well for both compressible and incompressible solids (Shu, King, & Fleck, 1999). The element QU34L4 have shown no numerical issue with plasticity models which support the work of Sku, King and Fleck (1999). However, no results are available for the element QU34L4R which gives hourglassing problem. The element QU30L3R which also gives hourglassing problem has been tested for the very first time in this thesis. The penalty method reduced integration elements are very soft compared to the rest of the elements using the same discretisation. Also, from our mesh refinement studies, we found that penalty method elements are in fact predicting pathologically mesh dependent results which is a problem that needs to be tacked by re-computing the penalty parameter in each increment instead of using a constant value for the penalty parameter. The elements with stiffer load-displacement curve predict wider plastic zone at the bottom of the specimen and a more substantial SBW as shown in Figure 4.36.

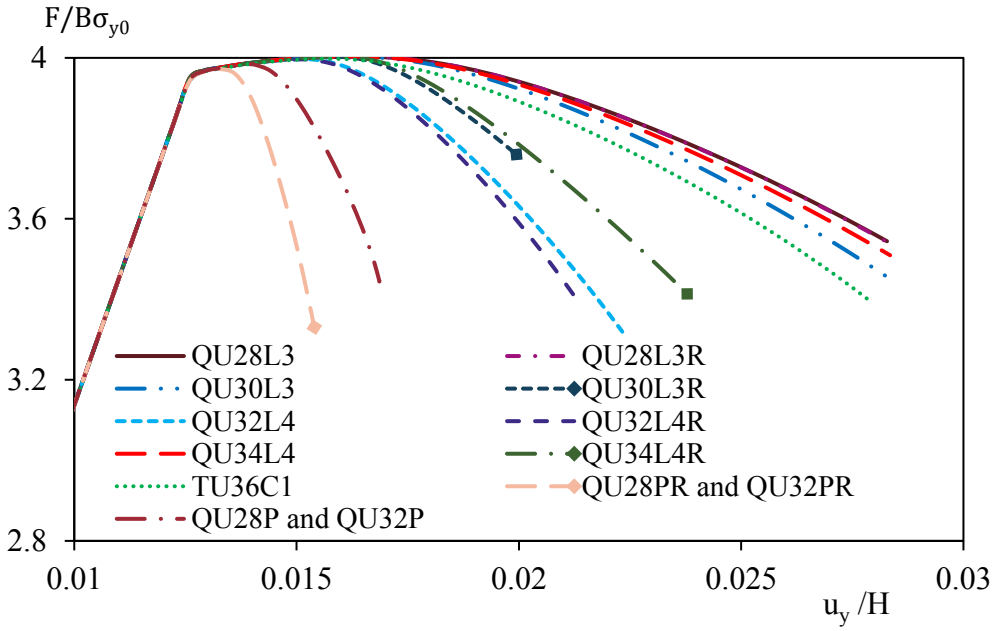

Figure 4.35 Load-displacement curves for the elements with the FHDP model.

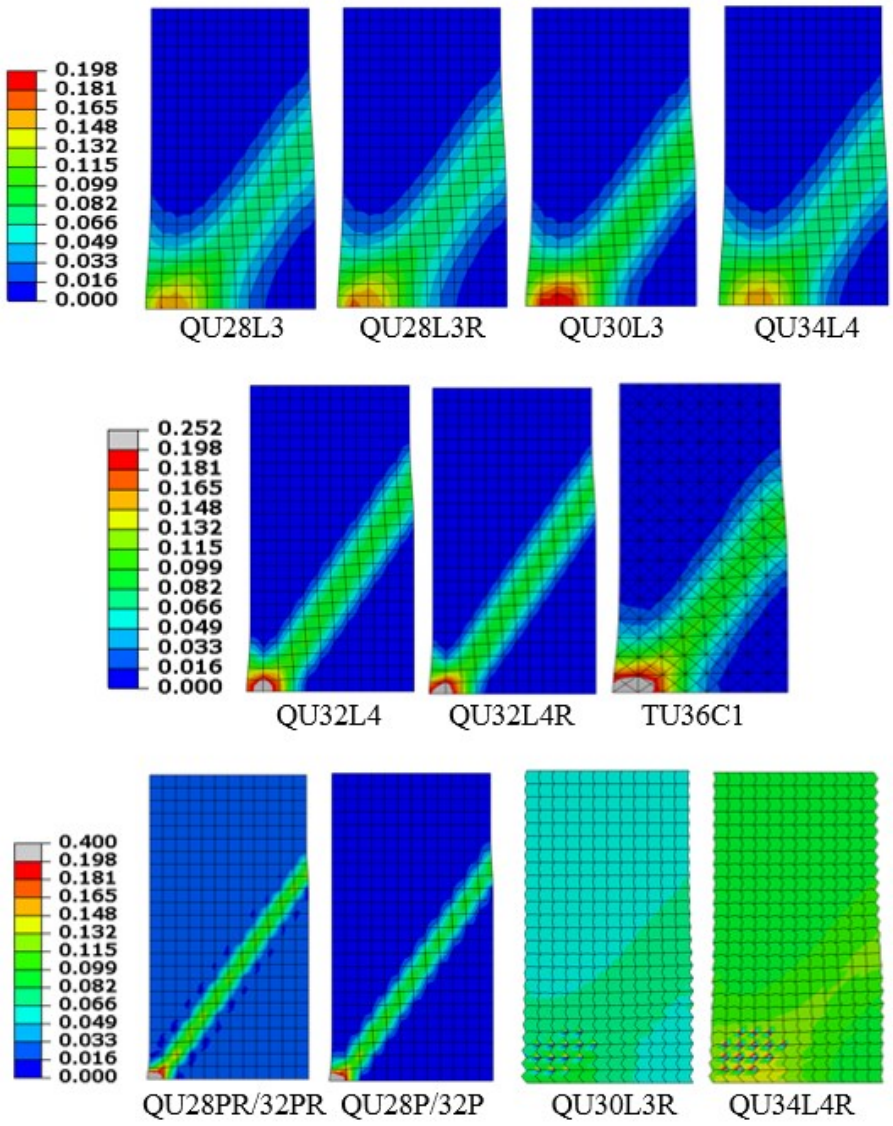

Figure 4.36 Deformed meshes and contour of the equivalent plastic strain for the elements with the FHDP model at the end of the simulation.

4.3 Conclusions

(i) Finite elements for Cosserat models:

The elements in the shear layer test show consistency in their numerical behaviour regardless of the plasticity models. All the elements predict acceptable results (i.e. no significant numerical issues such as locking or hourglass deformation modes) in the shear layer (1D) problem. Therefore, the computationally cheapest element COS4R is sufficient for the shear layer test, which undergoes pure shear. However, the shear

layer test is more restricted since many DOF are set to zero. Therefore, the shear layer test can be used for an initial benchmark test for the plasticity models and not for the elements. The shear layer test is a 1D problem simulated using the 2D elements. The simulation of the real physical behaviour of the plasticity models in 2D (and 3D), the volumetric part of the strain is activated, and intense shearing occurs within the localised deformation zone which is not the case in 1D shear layer problem. As a result, any major numerical issues such as volumetric locking or spurious hourglass deformation modes cannot be predicted for the 2D elements from the shear layer test.

The biaxial tests provide a more meaningful insight into the physical behaviour of the plasticity models. Therefore, not all elements perform well. The elements COS4F and COS4R are not recommended as they give stiff (locking) behaviour and hourglassing, respectively. The element COS3G1 does not predict consistent results with respect to the other elements in different plasticity models. Therefore, the element behaviour is suspicious although no significant numerical issues are found. Further investigation is required to determine the reasons for the variation of the results of COS3G1 concerning other elements in different plasticity models. Therefore a cheaper element than quadratic/linear ones can be obtained by reformulating COS3G1 element.

The quadratic/quadratic and quadratic/linear elements provide comparable results with no indication of numerical issues. The elements recommended for quadratic/quadratic and quadratic/linear elements are COS8(4)R or COS6(3)G3 as being computationally less expensive. The even less expensive linear/linear selective reduced integration element COS4SR shows good numerical behaviour. However, the deviation of the results of COS4SR from other elements varies in different plasticity models. Therefore, the element COS4SR requires further investigation to determine the cause of this variation and obtain cheaper quadrilateral element than quadratic/linear by reformulating.

(ii) Finite elements for strain gradient models:

The numerical behaviour of the existing and new mixed-type based on Lagrange multiplier and penalty elements with full integration scheme predicts acceptable results (i.e. no significant numerical issues such as locking or hourglass deformation modes) in the post-peak regime except for QU28L3. Among mixed-type Lagrange

multiplier with full integration elements, the new QU30L3 element is recommended. The element QU30L3 shows satisfactory result without any numerical issues concerning all the plasticity models tested. Also, the element QU30L3 is more straightforward, easier to implement and computationally less expensive compared to the existing ones.

All the mixed-type and penalty full integration (except QU28L3) and C^1 elements predict different numerical results in the post-peak regime. Among mixed-type reduced integration elements, only QU32L4R predicts acceptable results without any numerical issues with all the plasticity models. The elements QU30L3R and QU34L4R gives spurious deformation hourglass modes and therefore should not be used. Even though penalty formulation elements are easier to implement and computationally cheaper, one should be careful about the overly soft behaviour compared to the rest of the elements. The penalty elements with full and reduced integration give equivalent results. However, penalty method elements predicts pathologically mesh dependent result.

The triangular C^1 element predicts acceptable numerical results, however, the element is difficult to implement, computationally expensive and are slightly less stiff compared to the existing and new mixed-type full integration elements in the post-peak regime. The triangular C^1 elements are computationally expensive due to a large number of DOF, higher order interpolation and require computation of both the first and second derivatives of the higher order displacement shape functions. On the other hand, the triangular C^1 element predicts higher order interpolation and requires only the displacement field to be discretised where the Lagrange multiplier and penalty elements require multiple fields to be discretised. Also, the penalty elements require a suitable penalty parameters to be determined.

The numerical behaviour of the elements mainly from the Drucker-Prager plasticity models lead to the conclusions that there are three main features which affect the numerical behaviour of the elements in the plastic regime: (a) the displacement DOF at the 9^{th} node, (b) the Integration scheme and (c) the Lagrange multipliers.

The elements without the displacement DOF at the 9^{th} node (e.g. QU32L4, QU32L4R, QU28P/32P, QUQU28PR/QU32P9) predicts less stiff load-displacement

curve in the post-peak regime compared to the ones with displacement DOF (e.g. QU30L3, QU34L4) at the 9^{th} node. Secondly, the reduced integration elements are softer than the full integration elements (e.g. QU32L4 and QU32L4 elements predicts stiffer load-displacement curve than QU32L4R and QU34L4R respectively). The penalty elements with no Lagrange multipliers predicts overly soft behaviour and even softer with reduced integration scheme. The way these three main features of the elements affect the numerical solutions is discussed briefly.

Based on the numerical results obtained from strain-gradient plasticity models, in general, it can be concluded that the elements with stiffer load-displacement curve predict broader plastic zone at the bottom of the specimen and a larger SBW.

5 Finite element analysis of Cosserat plasticity models

In this chapter, the numerical behaviour and the essential features of the new Cosserat plasticity model VM5 are shown in details. A numerical comparison of Cosserat elastoplastic models VM1…VM5 from chapter 2 is provided considering biaxial compression test. The effect of different formulation for the plastic multiplier (and consistent elastoplastic modulus) and the Cosserat parameters are investigated. Finally, the effect of Cosserat parameters in the plastic regime is investigated to determine the sensitivity of the parameters regarding load-displacement curves and the localised plastic zone.

The computationally less expensive element COS8(4)R is used for all the simulations. A weak element is introduced at the bottom left of the biaxial specimen with lower yield stress to trigger the localised deformation. Note that SBW is not measured directly but considered the projected SBW which is the vertical length, l_s measured by considering the equivalent plastic strain $\bar{\varepsilon}^p$ such that $\left|\partial\bar{\varepsilon}^p/\partial H\right| > 0$ on the vertical side of the shear band where H is the height of the specimen.

5.1 Elastoplastic analysis of the model VM5

In this section, the effect of internal length l and the mesh density on the numerical solutions is investigated to determine the essential features of the proposed plasticity model VM5. The geometry, loading, boundary conditions and material parameters used for the biaxial test are same as the second tests in the previous chapter, section 4.1.2.

The effect of internal length, l on the numerical result is considered by increasing l from 1.0 mm to 3.0 mm. The discretisation used for the model VM5 is 8x12, 12x24 and 20x40-mesh. The load-displacement curves for the model VM5 with different

internal length are shown in Figure 5.1. Increasing the internal length the model predicts stiffer load-displacement curve in the post-peak regime. The model VM5 predicts same load-displacement curve for different discretisations as shown in Figure 5.1. The deformed meshes and contour of the equivalent plastic strain for the model VM5 using different discretisations for $l = 2$ mm are shown in Figure 5.4. The projected SBW and the plastic zone for VM5 remain constant for different discretisation as shown in Figure 5.4.

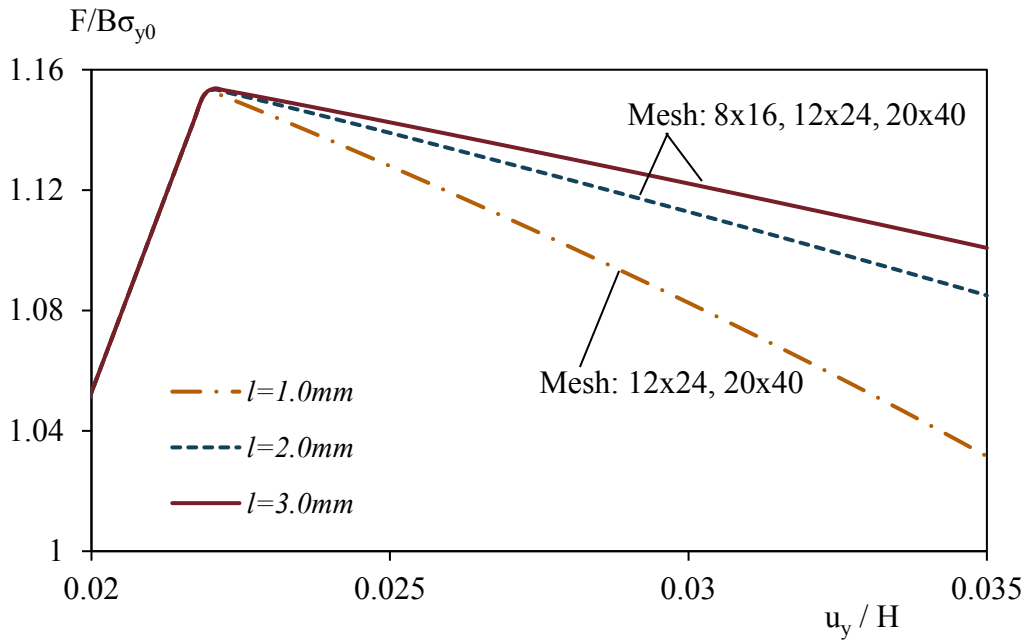

Figure 5.1 Load-displacement curves for the model VM5 with different internal length and mesh density.

The equivalent plastic strain along y-axis on the right side from the bottom of the specimen for the model VM5 with different internal length at the end of the simulation is shown in Figure 5.2. Increasing the internal length the projected SBW increases as shown in Table 5.1 and the maximum equivalent plastic strain decreases within the plastic zone as shown in Figure 5.3.

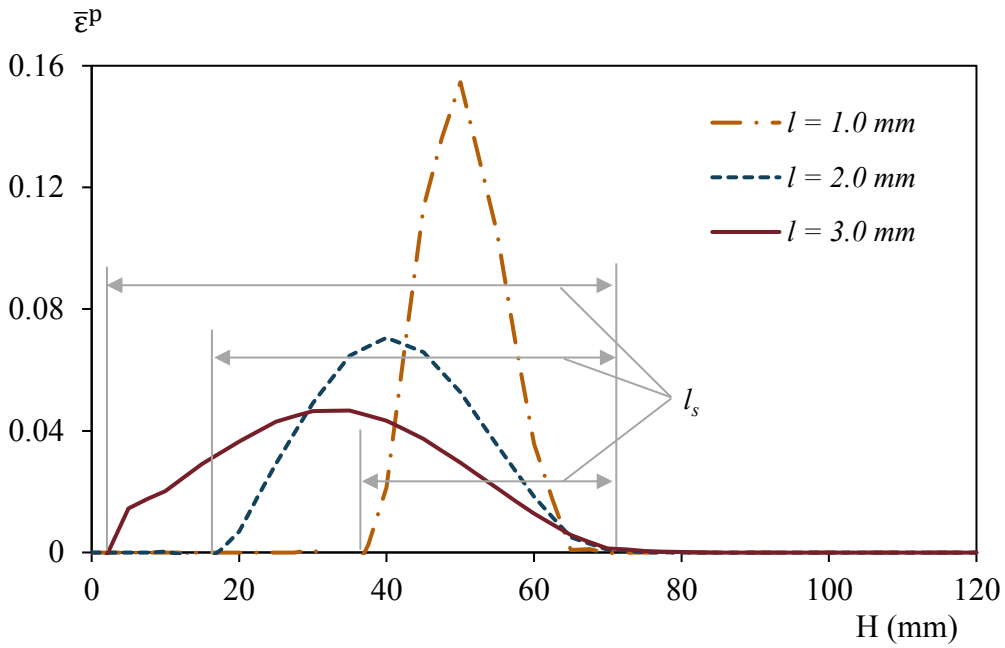

Figure 5.2 Equivalent plastic strain along y-axis on the right side from the bottom of the specimen with different internal length at $u_y = 4.2\text{mm}$.

Table 5.1 Ratio of the projected SBW to internal length for different values of internal length.

Internal length, l (mm)	1.0	2.0	3.0
Projected SBW, l_s (mm)	35	62	69
The ratio of the projected SWB to internal length, l_s/l	17.5	31	34.5

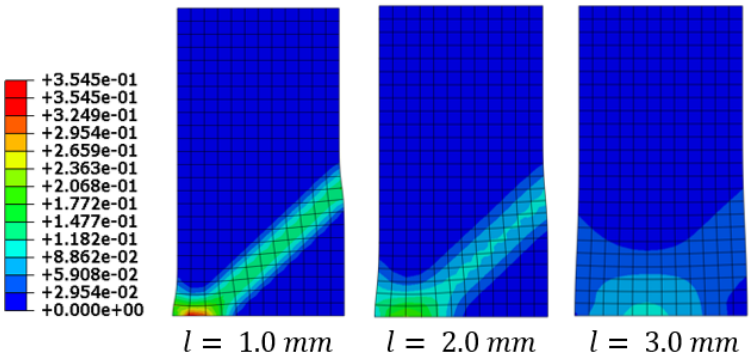

Figure 5.3 Deformed meshes and the contour of the equivalent plastic strain for the VM5 model with different internal length.

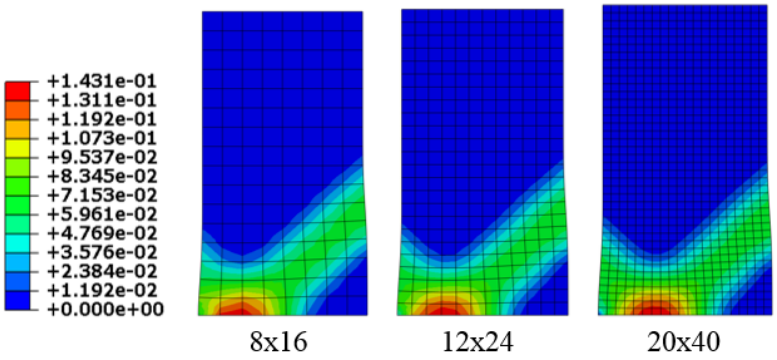

Figure 5.4 Deformed meshes and the contour of the equivalent plastic strain for the VM5 model with different discretisations (internal length, $l = 2$ mm) at $u_y = 4.2\text{mm}$.

The proposed Cosserat model VM5 holds all the essential features of the existing Cosserat plasticity models such as same load-displacement curve and finite SBW regardless of the mesh density. Another advantage of model VM5 is that it requires only three additional Cosserat parameters (l, a and b) and therefore more straightforward to implement. The effect of internal length on the numerical results has been investigated above. The effect of Cosserat parameter, a has a negligible effect on the numerical solutions (Sharbati & Naghdabadi, 2006). The effect of Cosserat parameter, b is considered by increasing the value of b from 1.0 to 4.0.

The load-displacement curves for the model VM5 with different values of the parameter, b is shown in Figure 5.5. Increasing the value of b the model VM5 predicts

stiffer load-displacement curve. Figure 5.6 shows that increasing the value of b the projected SBW increases. The deformed meshes and contour of the equivalent plastic strain for different values of the parameter b at the end of the simulation are shown in Figure 5.7. The results show that increasing the value of b the model VM5 predicts larger SBW and the equivalent plastic strain spreads at the bottom of the specimen.

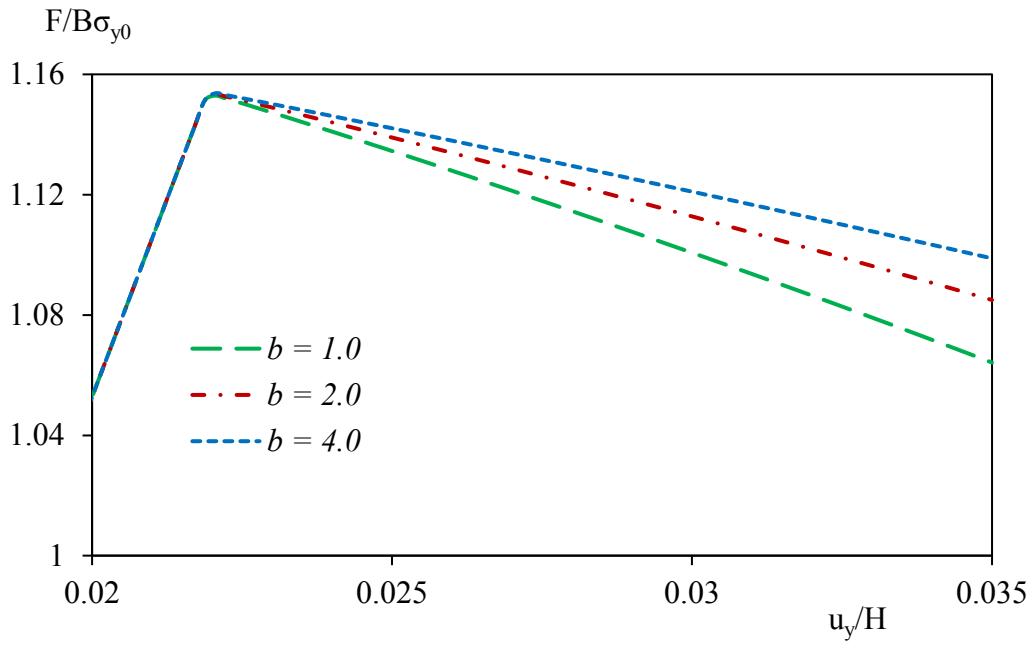

Figure 5.5 Load-displacement curves of the model VM5 with different values of the parameter, b.

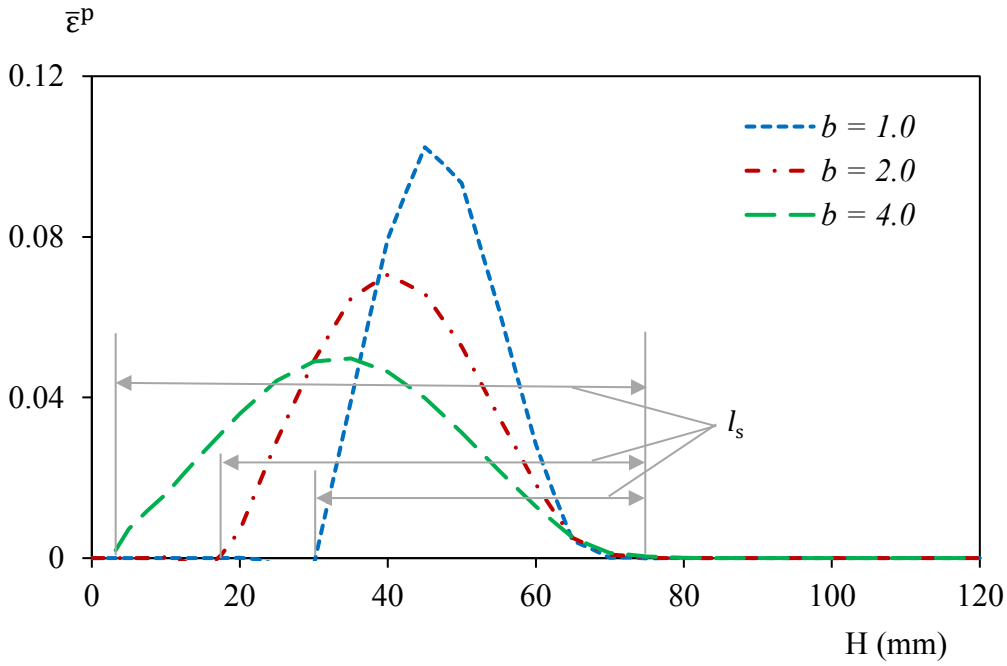

Figure 5.6 Equivalent plastic strain along y-axis on the right side from the bottom of the specimen for different values of the parameter b at the end of the simulation.

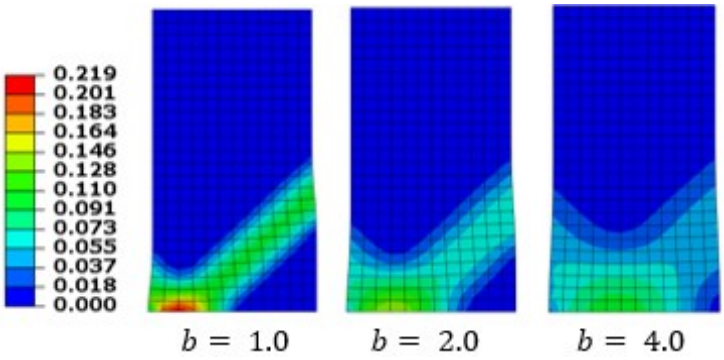

Figure 5.7 Deformed meshes and contour of the equivalent plastic strain for different values of the parameter b at the end of the simulation.

5.2 Comparisons of the Cosserat plasticity models

In this section a numerical comparison of the five different Cosserat elastoplastic models VM1…VM5 (from Chapter 2) in the plastic regime are presented.

The biaxial geometry, loading, boundary conditions and material parameters of the specimen for the tests remain same as previous section 5.1 and $l = 2\text{mm}$. The discretisation used for the models is 12x24-mesh.

The load-displacement curves for the models VM1…VM5 is shown in Figure 5.8. The models VM1 and VM3 give equivalent numerical results. Although VM1 and VM3 proposed a slightly different formulation for plastic multiplier and consistent elastoplastic modulus, all the Cosserat parameters are same for both the models. Therefore the formulations do not affect the numerical solutions of VM1 and VM3. The load-displacement curves of VM2 are in excellent agreement with the results obtained from Sharbati & Naghdabadi (2006). The model VM4 is same as model VM1 regarding the elastoplastic formulations but differs in Cosserat parameters. The numerical result of VM4 suggests that Cosserat parameters play a significant role in the numerical simulations. The model VM5 predicts the stiffest load-displacement curve.

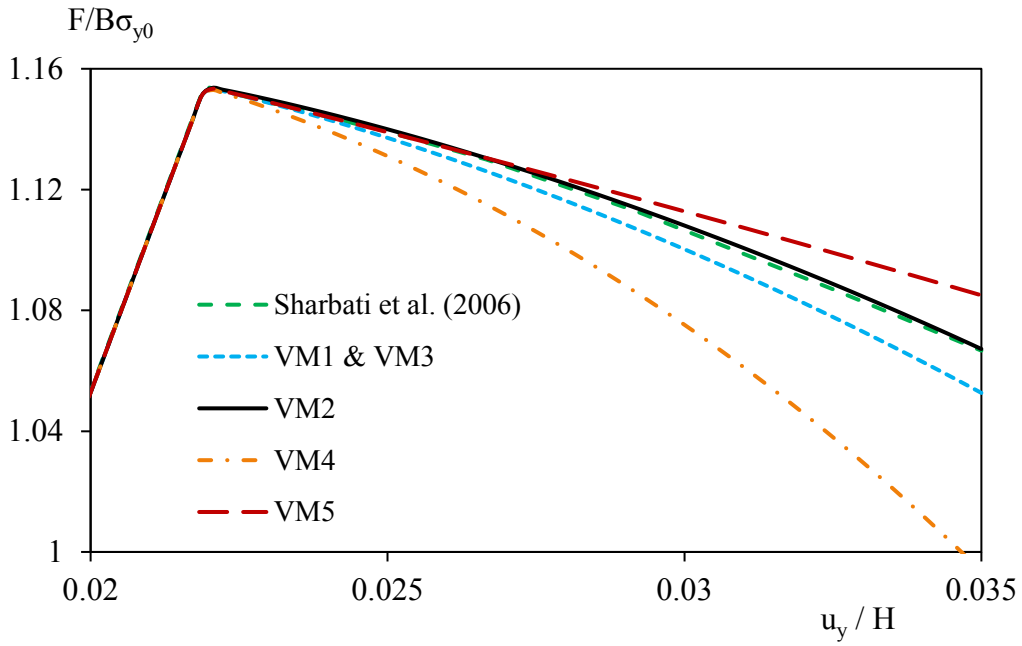

Figure 5.8 Load-displacement curves for Cosserat plasticity models VM1…VM5.

The equivalent plastic strain along y-axis on the right side from the bottom of the specimen for Cosserat models VM1…VM5 is shown in Figure 5.9. Although the

proposed model VM5 predicts stiffer load-displacement curve than VM2, their SBW remains the same as shown in Figure 5.9 and Table 5.2. Therefore, not necessarily the stiffer load-displacement curve predicts a broader SBW which is usually the case when the internal length is increased.

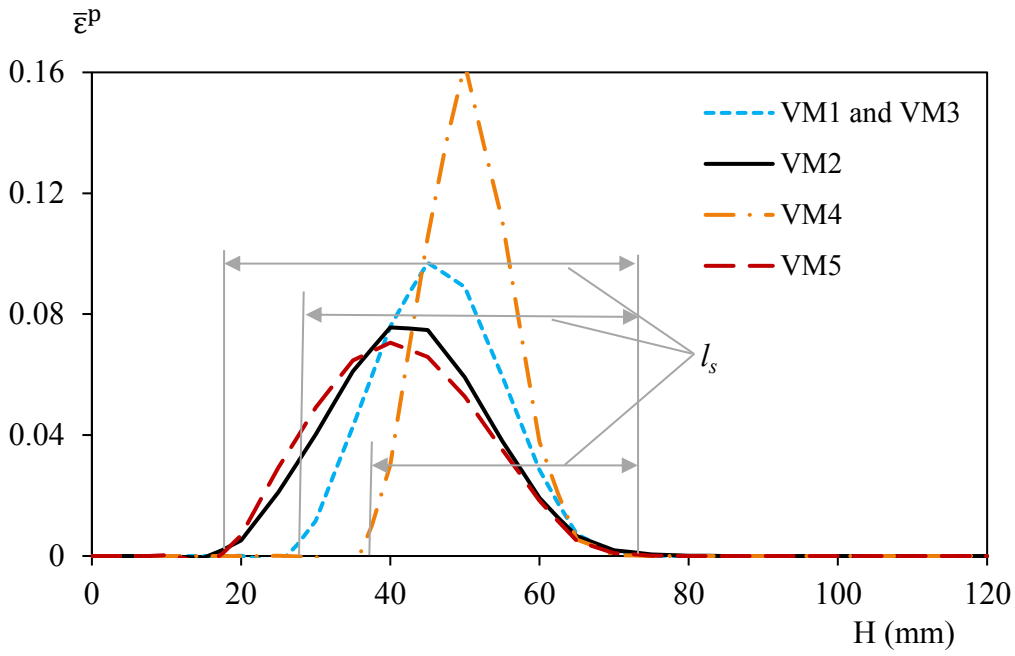

Figure 5.9 Equivalent plastic strain along y-axis on the right side from the bottom of the specimen for the models VM1…VM5 at $u_y = 4.2\text{mm}$.

Table 5.2 Ratio of the projected SBW to internal length for the models VM1…VM5.

Model	VM1	VM2	VM3	VM4	VM5
Projected SBW, l_s (mm)	46	55	46	32	55
Ratio of the projected SBW to internal length, l_s/l	23	27.5	23	16	27.5

The deformed meshes and contour of the equivalent plastic strain for the models VM1…VM5 are shown in Figure 5.10. Model VM4 predicts smaller projected SBW and higher equivalent plastic strain as shown in Table 5.2 and Figure 5.9 respectively. All the models predict strain localisation and shear band formation from the bottom left to the right side of the specimen as shown in Figure 5.10.

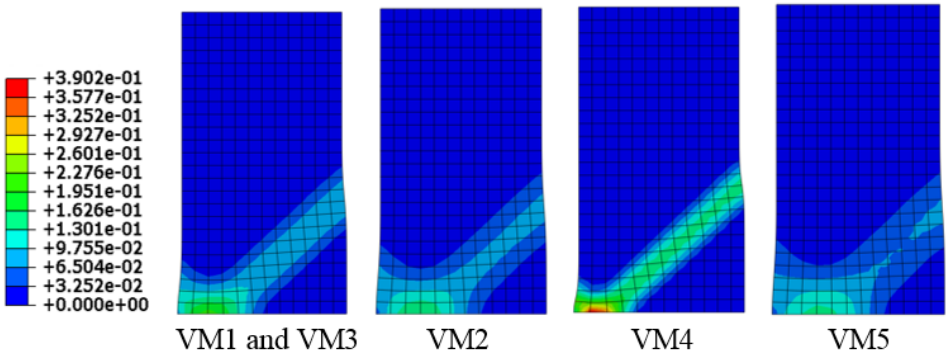

Figure 5.10 Deformed meshes and contour of the equivalent plastic strain for the models VM1…VM5 at $u_y = 4.2\text{mm}$.

Although the models (except VM1 and VM3) are not equivalent numerically, all predict localised deformation and the solutions are independent of discretisation. Therefore, the proposed Cosserat model VM5 can be used to showcase the ability to capture the localised deformation phenomena more efficiently as it requires less number of parameters and holds all the essential features of the existing Cosserat elastoplastic models.

5.3 Effect of Cosserat parameters on numerical simulation

5.3.1 Parameters a_1-a_3

In this section, the effect of Cosserat parameters $a_1 \ldots a_3$ used to compute J_2 on the numerical results has been investigated. The biaxial geometry, loading, boundary conditions and material parameters of the specimen remain same as section 5.1 and $l = 2\text{mm}$. The discretisation used for the model is 12x24-mesh.

Model VM1 is simulated with different values of a_1 (such that $a_1 + a_2 = 0.5$). The load-displacement curves for different values of a_1 are shown in Figure 5.11. Increasing the value of a_1, the model predicts less stiff load-displacement curve at the later stages in the plastic regime. The equivalent plastic strains along y-axis on the right side from the bottom of the specimen for different values of a_1 are shown in Figure 5.12. The prediction of the projected SBW (l_s=45mm) and the ratio of the projected SBW to the internal length (l/ l_s=22.5) remain same for different values of a_1. Therefore, the projected SBW is independent of the Cosserat parameter a_1 (such that $a_1 + a_2 = 0.5$). The deformed meshes and contour of the equivalent plastic strain for different values of a_1 are shown in Figure 5.13. Increasing the value of a_1, the maximum equivalent plastic strain increases within the plastic zone.

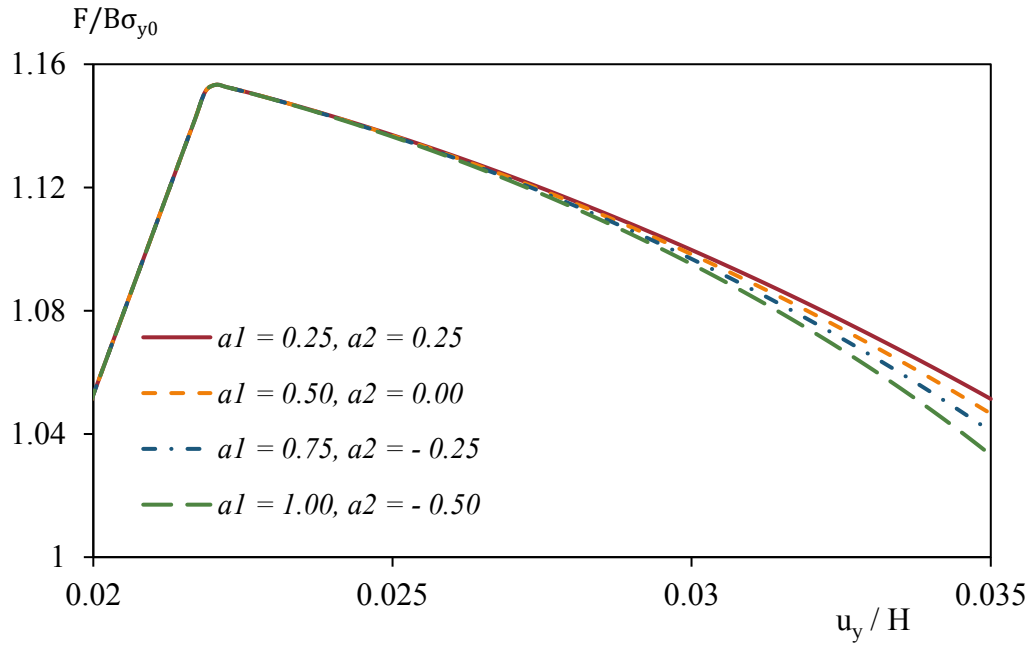

Figure 5.11 Load-displacement curves for different values of the parameter a_1.

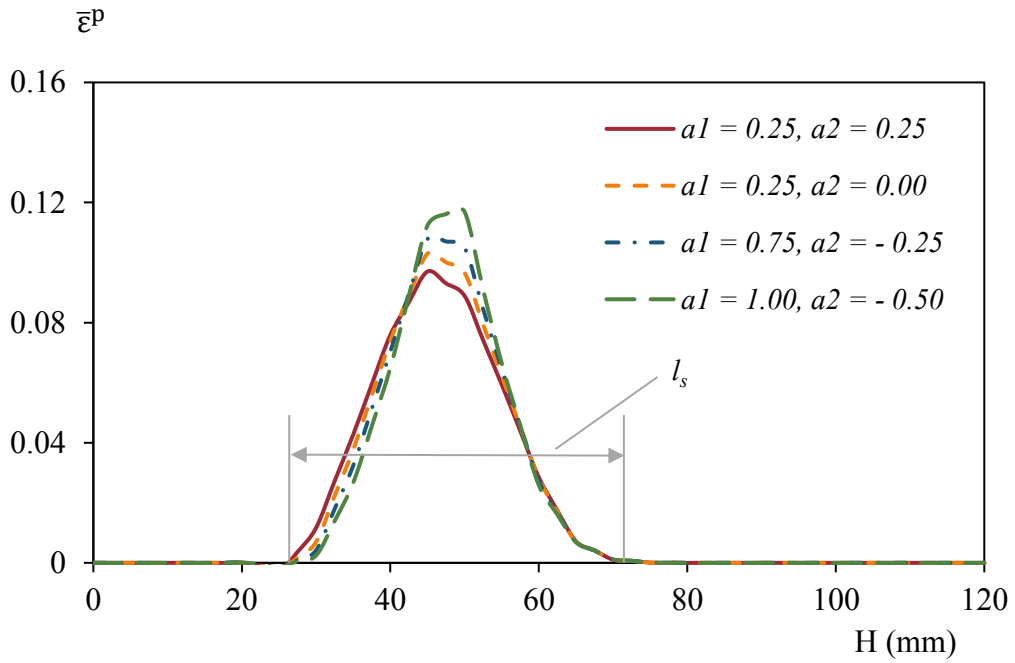

Figure 5.12 Equivalent plastic strain along y-axis on the right side from the bottom of the specimen for different values of the parameter a_1 at $u_y = 4.2\text{mm}$.

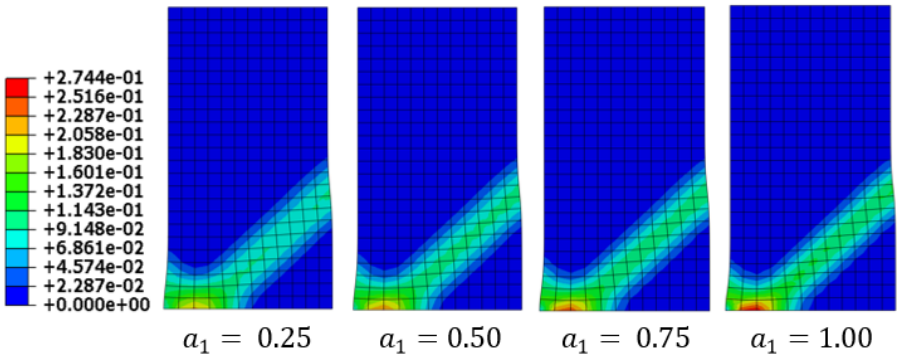

Figure 5.13 Deformed meshes and contours of the equivalent plastic strain for different values of the parameter a_1 at $u_y = 4.2\text{mm}$.

To investigate the effect of the parameter a_3 on the numerical results the model VM1 is simulated with different values of a_3. Increasing the value of a_3 the model predicts loss of load carrying capacity in the plastic regime. The equivalent plastic strain along y-axis on the right side from the bottom of the specimen for different values of a_3 is shown in Figure 5.15. Increasing the value of a_3 the ratio of the

projected SBW to internal length increases as shown in Table 5.3. Increasing the value of a_3 the maximum equivalent plastic strain increases with the decrease in the plastic zone as shown in Figure 5.16.

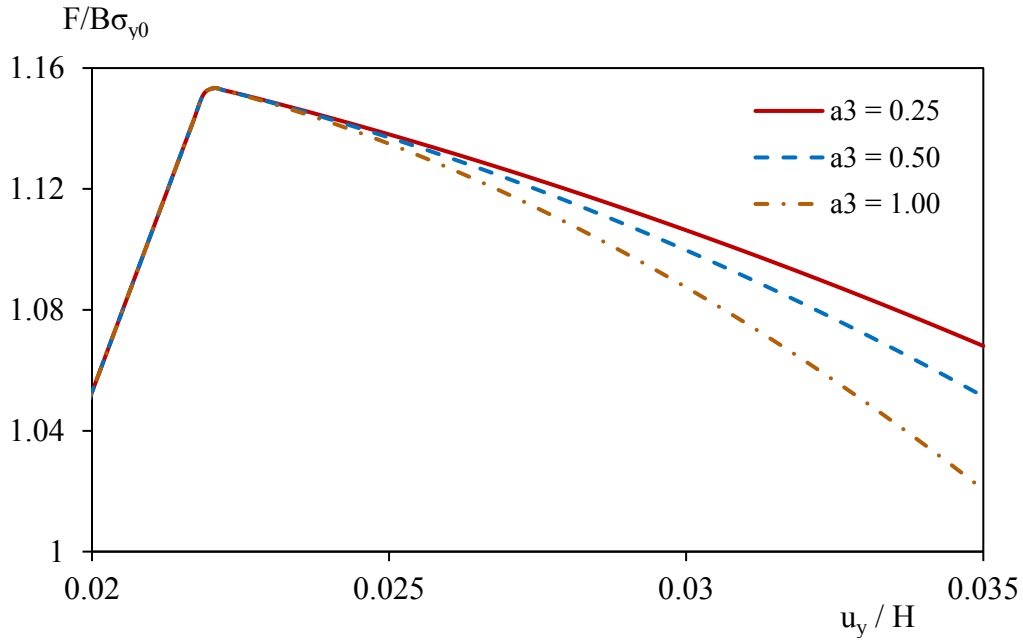

Figure 5.14 Load-displacement curves for different values of the parameter a_3

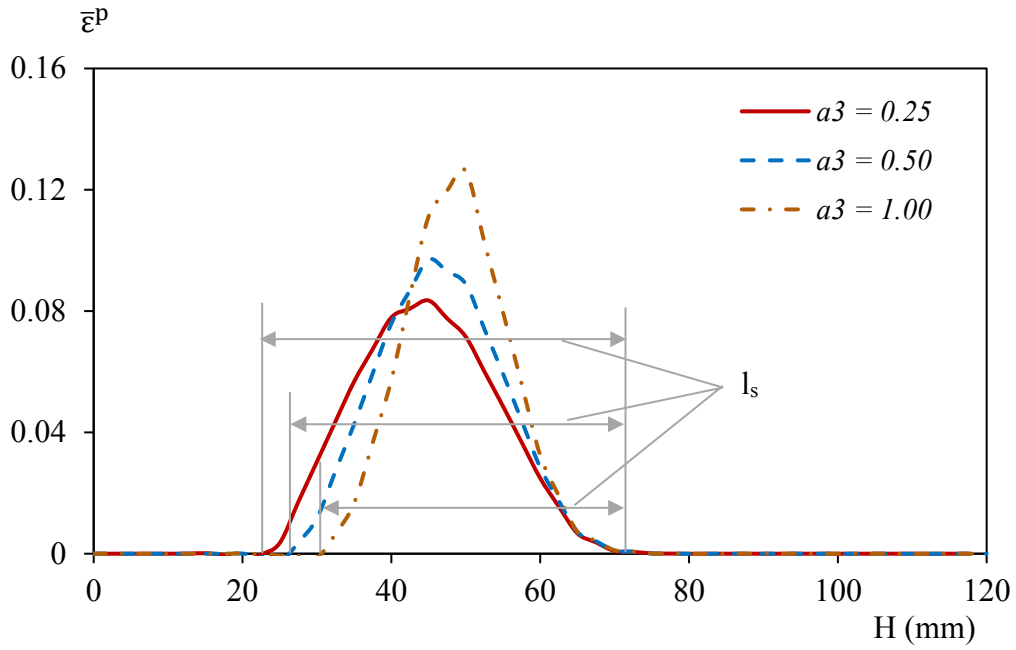

Figure 5.15 Equivalent plastic strain along y-axis on the right side from the bottom of the specimen for different values of the parameter a_3 at $u_y = 4.2\text{mm}$.

Table 5.3 Ratio of the projected SBW to internal length for different values of the parameter a_3.

a_3	0.25	0.50	1.00
Projected SBW, l_s (mm)	41	45	49
The ratio of the projected SBW to internal length, l_s/l	20.5	22.5	24.5

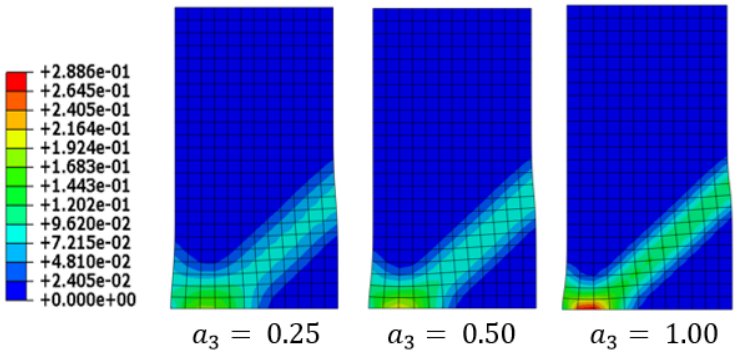

Figure 5.16 Deformed meshes and contour of the equivalent plastic strain for different values of the parameter a_3 at $u_y = 4.2\text{mm}$.

5.3.2 Parameters b_1-b_3

In this section, the effect of Cosserat parameters $b_1 \ldots b_3$ on the numerical results has been investigated. The material parameters, biaxial geometry, loading and boundary conditions are the same as the previous section. Model VM1 is simulated with different values of $b_1 \ldots b_3$.

At first, the material parameter b_1 is varied from 0.10 to 0.5 (such that $b_1 + b_2 = 2/3$) and from 1.00 to 3.00 (such that $b_1 + b_2 = 2$) as Table 2.4 shows that researchers have used various combination of $b_1 + b_2$ giving a maximum and minimum value of 2 and 2/3 respectively. Secondly, the material parameter b_3 is varied from 0.25 to 4.0. In both the cases, there are no changes in the load-displacement curves as shown in Figure 5.17 and the predicted plastic zone (not shown). Therefore, the Cosserat parameters $b_1 \ldots b_3$ have no effects on the numerical results considering the range of values $b_1 \ldots b_3$ used.

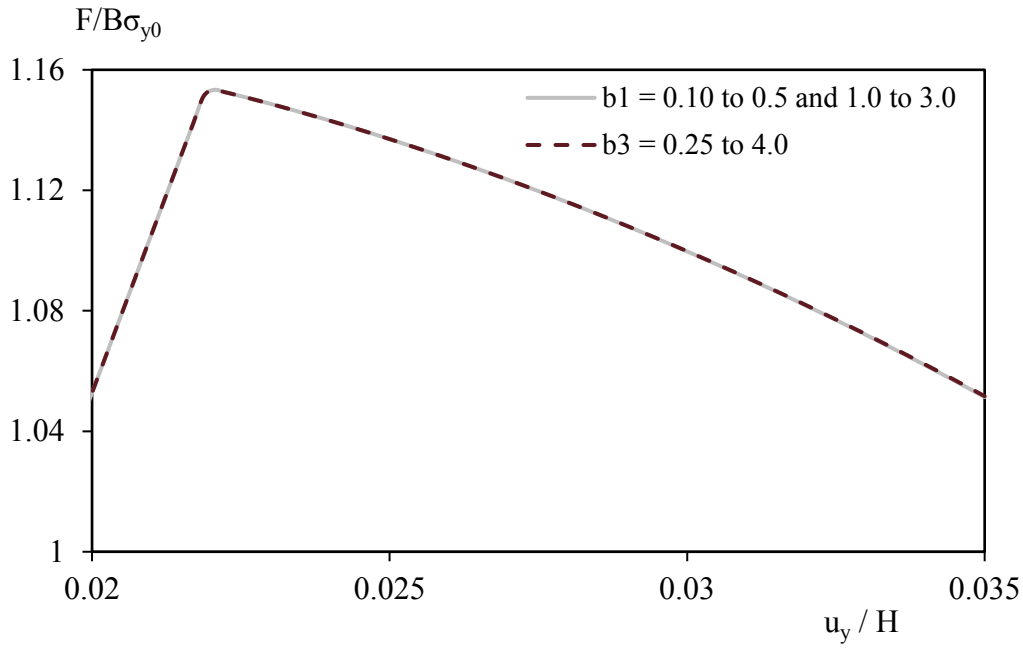

Figure 5.17 Load-displacement curves for different values of the parameters $b_1 \ldots b_3$.

5.3.3 Parameter *b*

In this section, the effect of Cosserat parameter b on the numerical results has been investigated. Different authors have used or proposed different values of b in their Cosserat models as shown in chapter 2, Table 2.6. The material parameters, biaxial geometry, loading and boundary conditions remain the same as the previous section. The model VM1 is simulated with different values of b.

The load-displacement curves for the model VM1 with different values of b are shown in Figure 5.18. As b increases, the model predicts a stiffer load-displacement curve. The load-displacement curve of the model VM1 coincides with VM2 when $b = 4$. Although VM1 and VM2 have proposed a slightly different formulation for the plastic multiplier and consistent elastoplastic modulus, the Cosserat parameters remain same except for the parameter b. This shows that the Cosserat parameter affects the numerical solutions of VM1 and VM2 and not the formulations. Therefore, the model VM1 and VM2 predict equivalent numerical results if all the Cosserat parameters are same.

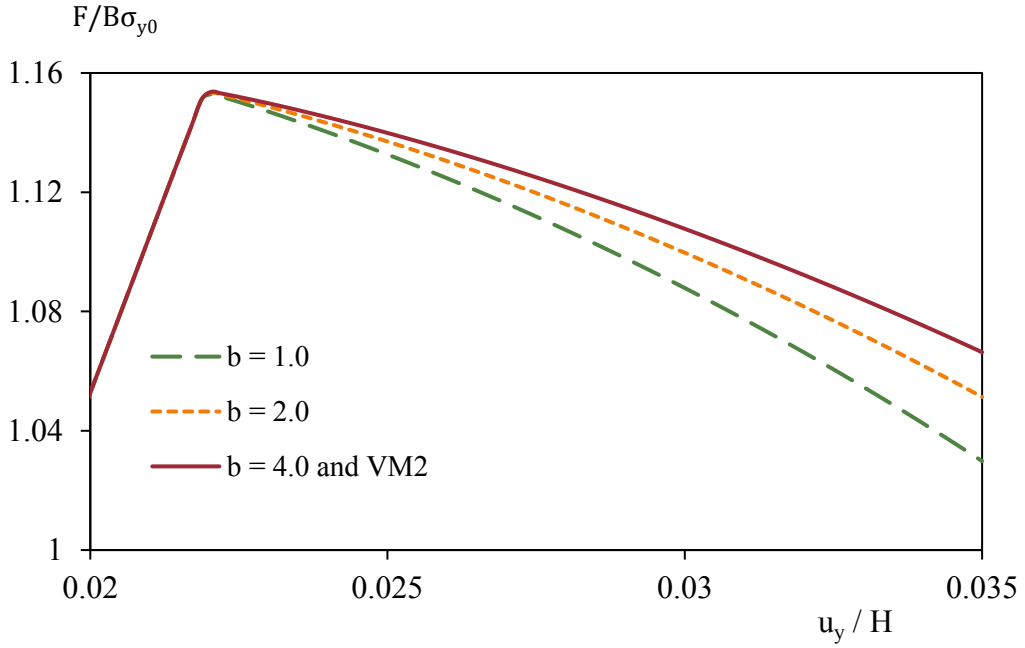

Figure 5.18 Load-displacement curves for values of the parameter b.

The equivalent plastic strain along y-axis on the right side from the bottom of the specimen for different values of b are shown in Figure 5.19. Increasing the value of b, the ratio of the projected SBW to internal length increases as shown in Table 5.4. The deformed meshes and contour of the equivalent plastic strain for different values of the parameter b are shown in Figure 5.20. Increasing the value of b not only the SBW increases but also the plastic zone at the bottom of the specimen as shown in Figure 5.20. However, increasing the value of b the maximum equivalent plastic strain decreases.

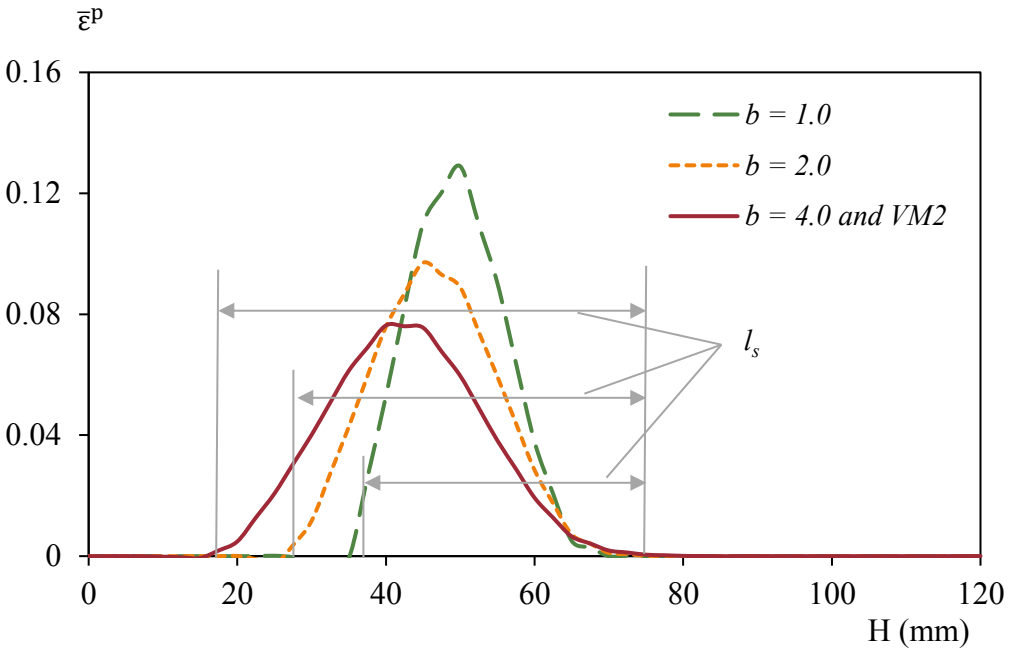

Figure 5.19 Equivalent plastic strain along y-axis on the right side from the bottom of the specimen for different values of the parameter b at the end of the simulation.

Table 5.4 Ratio of the projected SBW to internal length for different values of the parameter b.

b	1.0	2.0	4.0
Projected SBW, l_s (mm)	41	47	57
The ratio of the projected SBW to internal length, l_s/l	20.5	23.5	28.5

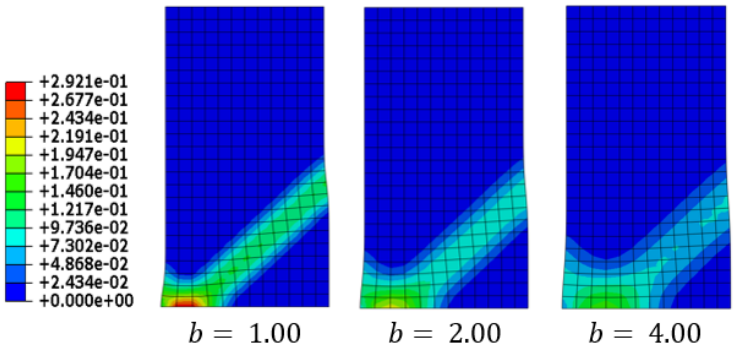

Figure 5.20 Deformed meshes and contour of the equivalent plastic strain for different values of the parameter b at the end of the simulation.

5.4 Conclusions

The proposed model VM5 holds all the essential features of the existing Cosserat models (VM1…VM4) such as unique load-displacement curves, finite SBW, and constant plastic zone for different discretisations. Another advantage of model VM5 is that it requires only three additional material parameters (*a, b* and *l*) whereas VM1…VM4 requires ten additional material parameters (*a, b, l,* $a_1 \ldots a_4$ and $b_1 \ldots b_3$) compared to classical plasticity.

The Cosserat model VM1 and VM3 are numerically equivalent since all the Cosserat parameters are the same for the models. The elastoplastic formulation of both the models VM1 and VM4 are same but differs in the value of the parameters used. The model VM1 and VM2 gives equivalent numerical results when the parameter b becomes equal in both the models. Therefore, the different formulation of the plastic multiplier and the consistent elastoplastic modulus do not affect the simulation result for the models VM1…VM4. The choice of Cosserat parameters affect the numerical results significantly. Cosserat models VM1…VM4 predicts equivalent numerical results if all the Cosserat parameters are same. Therefore, it does not matter which model (VM1…VM4) one uses as long as the models are calibrated to the data available.

Increasing the value of the parameters a_1 (such that $a_1 + a_2 = 0.5$) and a_3 the model predicts less stiff load-displacement curves in the post-peak regime. The effect

of the parameter a_3 is more significant than a_1 on the numerical results. However, the projected SBW is independent of the parameter a_1 (such that $a_1 + a_2 = 0.5$). Cosserat parameters $b_1 \ldots b_3$ do not affect the numerical solutions. Increasing the value of the parameter *b* the model predicts stiffer load-displacement curves in the post-peak regime. Therefore the numerical solutions of the models are affected significantly by choice of Cosserat parameters (except *a* and $b_1 \ldots b_3$).

6 Numerical comparison of Cosserat and strain-gradient plasticity models

In this chapter numerical comparisons of the Cosserat and strain gradient plasticity models are presented based on both the von Mises and Drucker-Prager yield criterion from chapter 2. Initially, the numerical solutions of the plasticity models are compared using the same material parameters. The evolution of the intense shearing development into the narrow band (shear band) from the early to the later stages of the plastic deformation is investigated. The effect of changing the internal length on the reduction of the load carrying capacity in the post-peak regime and the thickness of the shear band (SBW) is investigated. The Cosserat and strain gradient Drucker-Prager plasticity models with non-associated flow rule are assumed to compare the numerical solutions of localised deformation using the same material parameters. Finally, numerical experimentation is carried out to predict an equivalent projected SBW for the models by changing the internal length only.

The elements used for the Cosserat and strain gradient plasticity models are COS8(4)R and QU30L3 respectively. To obtain mesh independent numerical results as mentioned in Chapter 4 for Cosserat and strain gradient models, the discretisation used such that $l/e \geq 0.2$ and $l/e \geq 0.1$ respectively. The projected SBW, l_s is considered similar to that of chapter 5.

6.1 Evolution of shear band

In this section, we first compare the numerical results of the Cosserat (VM1) and strain gradient (CCM and FH) von Mises type plasticity models from chapter 2 using the same material parameters. We then investigate the evolution of the shear band

formation from the early to the later stages of the plastic deformation and any changes in the projected SBW.

Numerical finite element simulation is carried out considering biaxial compression test. The geometry, loading, boundary conditions and material parameters remain the same as in the second test in section 4.1.2, except for the plastic modulus and the internal length. For all the plasticity models $h_p = -40\,\mathrm{MPa}$ and internal length $l = 0.6$ mm is used. The discretisation used for the strain-gradient and Cosserat model is 12x24-mesh and 40x80-mesh respectively. For the Cosserat model, a higher mesh density is required to achieve $l/e \geq 0.2$. In this case for the model VM1, $l/e = 0.4$ is used which satisfy the requirement of predicting mesh independent solution.

The load-displacement curves for the Cosserat and strain gradient plasticity models are shown in Figure 6.1. All the plasticity models predict a reduction in the load carrying capacity in the post-peak regime. However, the load-displacement curves for the models are not the same in the plastic regime. The model CCM and VM1 predict the most and the least stiff load-displacement curve respectively for the same material parameters.

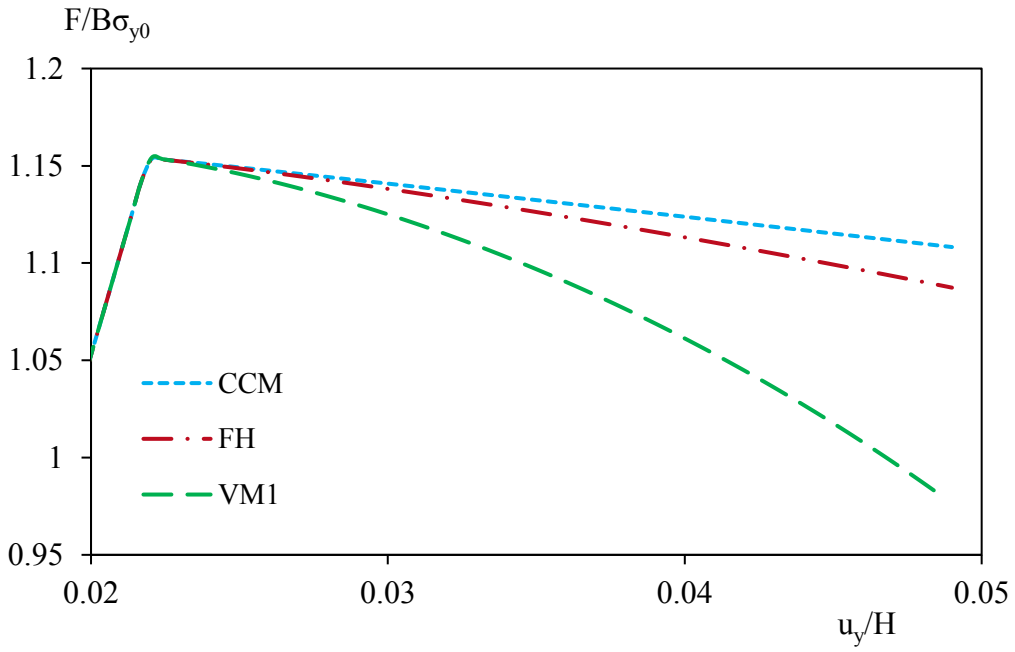

Figure 6.1 Load-displacement curves for the Cosserat (VM1) and strain gradient (CCM and FH) plasticity models.

The contour of the equivalent plastic strain and deformed meshes for Cosserat and strain gradient plasticity models at u_y = 5.85 mm are shown in Figure 6.2. All the models predict the maximum equivalent plastic strain at the bottom of the specimen. VM1 model predicts the highest equivalent plastic strain. The model CCM predicts wider plastic zone and a more substantial SBW compared to the FH and VM1 models.

The equivalent plastic strain along y-axis on the right side from the bottom of the specimen for Cosserat and strain gradient plasticity models are shown in Figure 6.3. The higher the equivalent plastic strain, the smaller the projected SBW predicted by the models. The stiffer CCM model predicts the largest projected SBW which is approximately double to that of VM1 model as shown in Table 6.1.

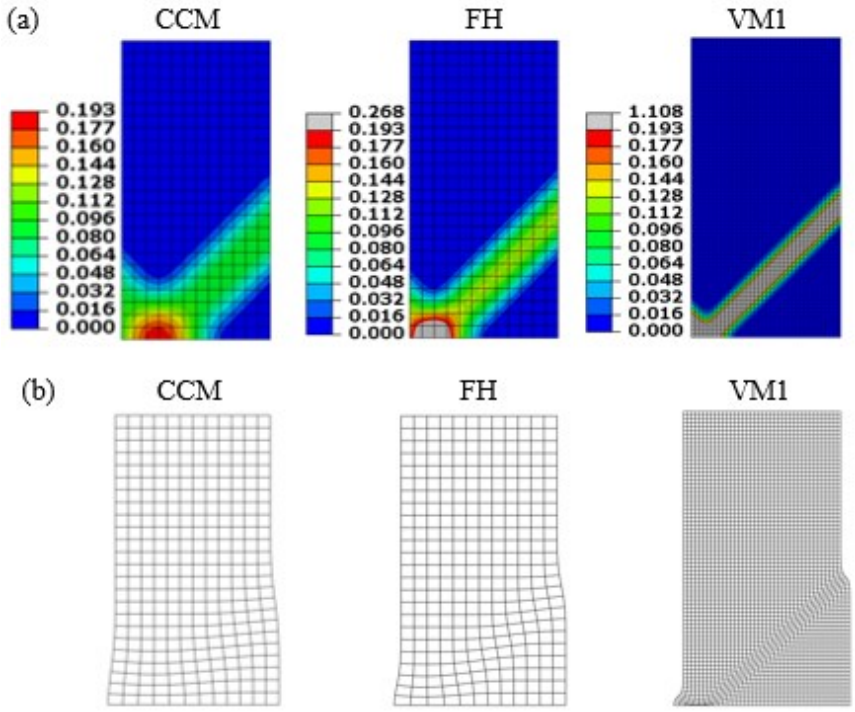

Figure 6.2 Cosserat (VM1) and strain gradient (CCM and FH) plasticity models at u_y = 5.85 mm displacement: (a) undeformed meshes with the contour of the equivalent plastic strain and (b) deformed meshes.

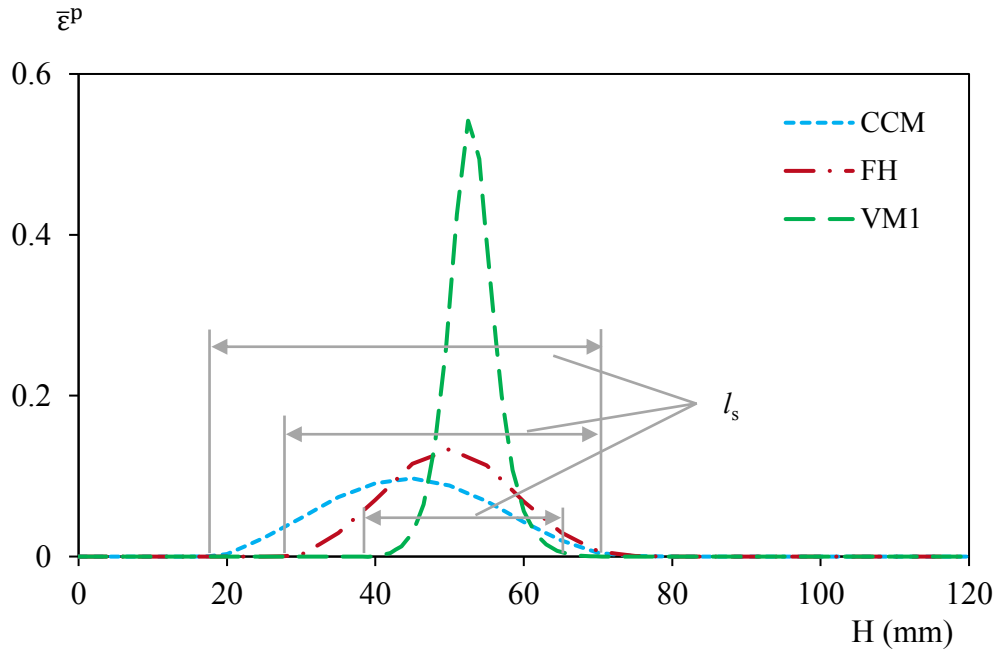

Figure 6.3 The equivalent plastic strain distribution along y-axis on the right side from the bottom of the specimen for Cosserat (VM1) and strain gradient (CCM and FH) plasticity models at u_y = 5.85 mm displacement.

Table 6.1 Ratio of the projected SBW to internal length for Cosserat (VM1) and strain gradient (CCM and FH) plasticity models

Model	CCM	FH	VM1
Projected SBW, l_s (mm)	49.6	42.4	27.2
The ratio of the projected SBW to internal length, l_s/l	83	71	45

The evolution of the SBW and the plastic zone is investigated for Cosserat (VM1) and strain gradient (CCM and FH) plasticity models with increasing prescribed vertical downward displacement u_y (in mm) from the top of the specimen.

The contour of the equivalent plastic strain on undeformed meshes for the plasticity models is shown in Figure 6.4. The inclusion of the weak element at the bottom left of the specimen triggers the localisation deformation which then extends towards the

upper right side of the specimen. The maximum equivalent plastic strain starts near the weak element and then starts to move towards the bottom right as vertical with increasing plastic deformation. Note that the plastic zone remains unchanged for all the models as deformation increases. Although the maximum equivalent plastic strain increases with plastic deformation, the projected SBW is predicted at a very early stage of plastic deformation and remains unchanged with increasing vertical displacement at the top as shown in Figure 6.5.

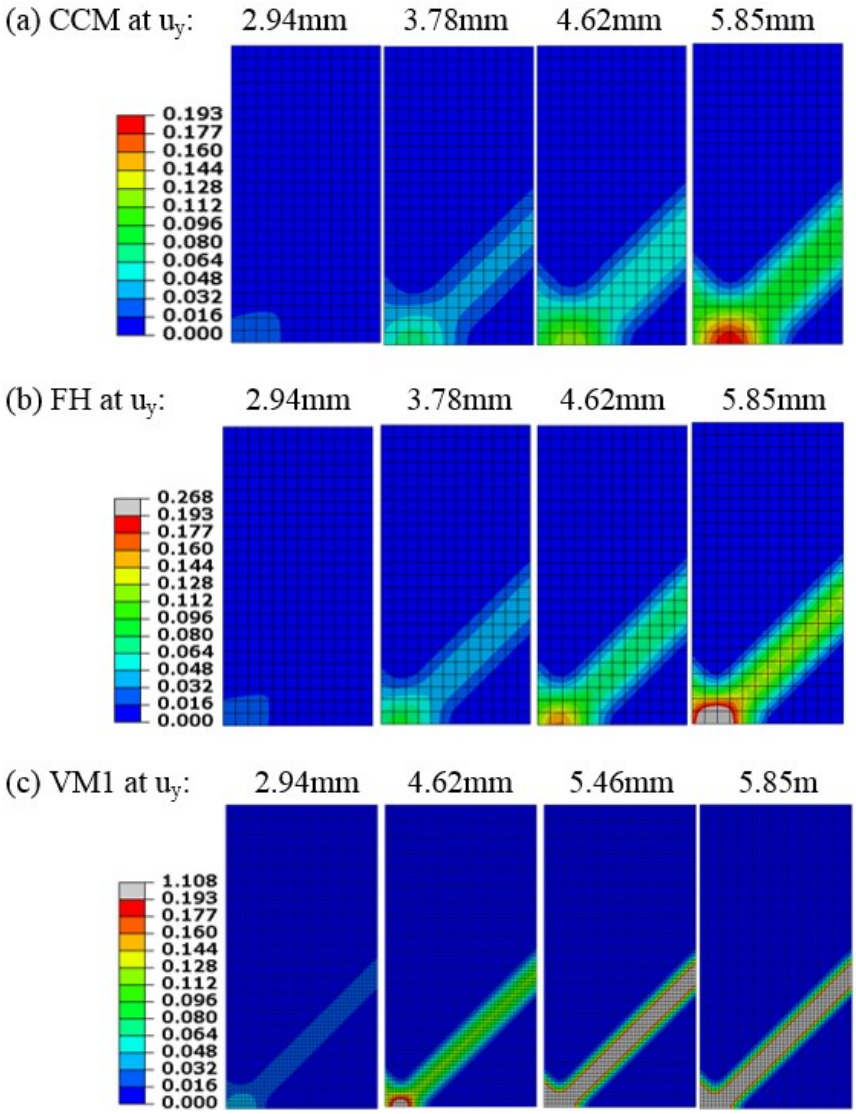

Figure 6.4 The contour of the equivalent plastic strain on undeformed meshes with increasing prescribed vertical downward displacement u_y (in mm) at the top of the specimen for the plasticity models: (a) CCM, (b) FH and (c) VM1.

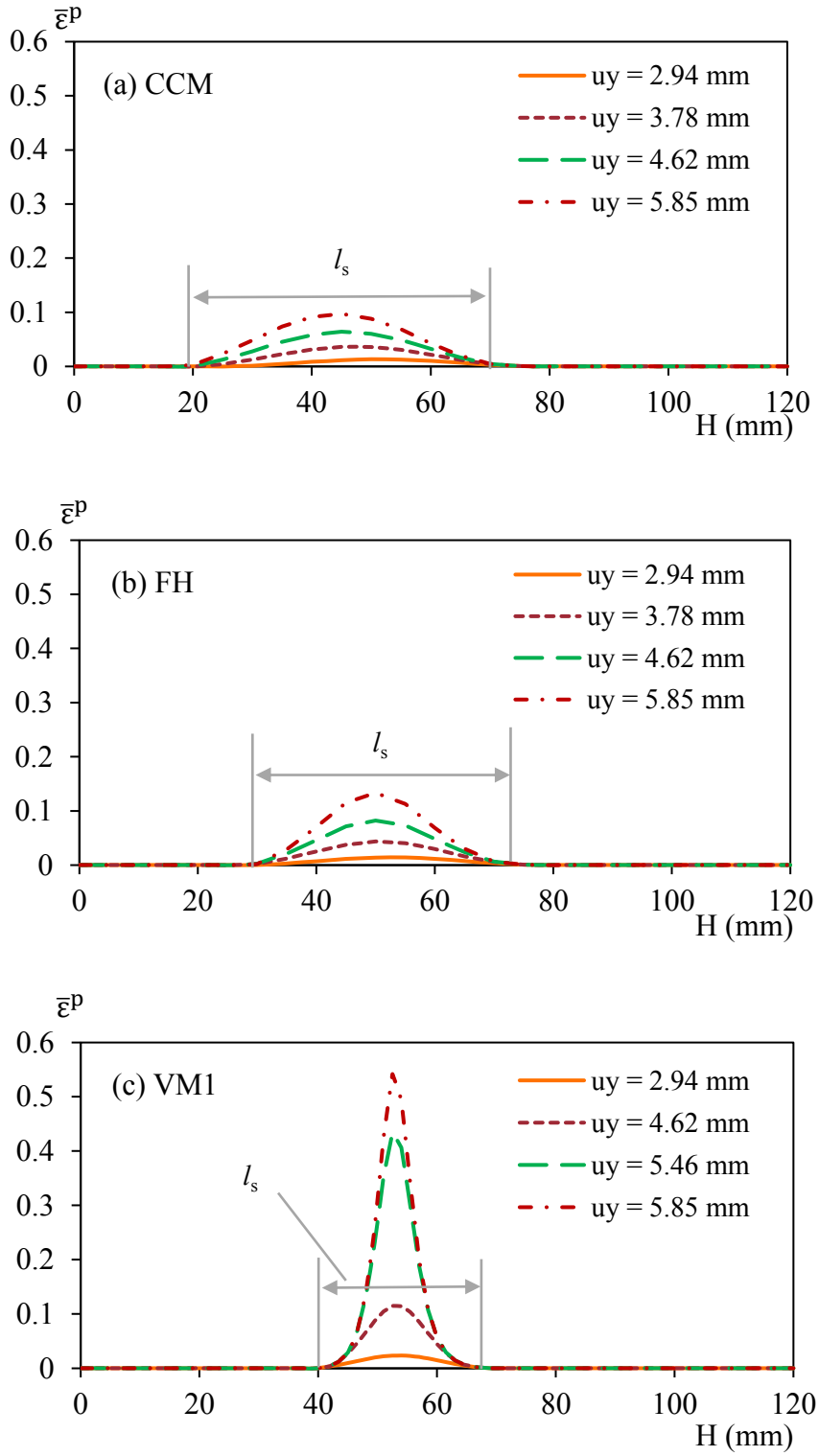

Figure 6.5 Evolution of the equivalent plastic strain along y-axis on the right side from the bottom of the specimen with increasing prescribed vertical downward displacement u_y (in mm) from the top: (a) CCM, (b) FH and (c) VM1 plasticity models.

6.2 Effect of the internal length

In this section, we compare the numerical solutions for Cosserat (VM1) and strain gradient (CCM and FH) plasticity models from chapter 2 by changing the internal length only. The load-displacement curves and the projected SBW is compared by increasing the internal length. We then investigate the change in projected SBW by increasing the internal length.

Numerical finite element simulation is carried out considering biaxial compression test. The geometry, loading, boundary conditions and material parameters remain same as the previous section. The internal length is varied from 0.5 to 0.7 mm.

The load-displacement curves with different internal length for the plasticity models are shown in Figure 6.6. All the models predict less stiff load-displacement curves in the post-peak regime with increasing internal length. However, the change in load-displacement curves with respect to the internal length of strain gradient plasticity (CCM and FH) models are negligible compared to the Cosserat (VM1) model.

The contour of the equivalent plastic strain on undeformed meshes for the plasticity models with different internal length is shown in Figure 6.7. All the models predicted larger plastic zone and projected SBW with increasing internal length. The internal length controls the plastic zone and the projected SBW.

The numerical results show that the change in the ratio of the projected SBW, l_s to l decreases if $l > 0.6\text{mm}$ as shown in Figure 6.8. However, decreasing the internal length below 0.6mm the ratio of the projected SBW, l_s to l increases for the models.

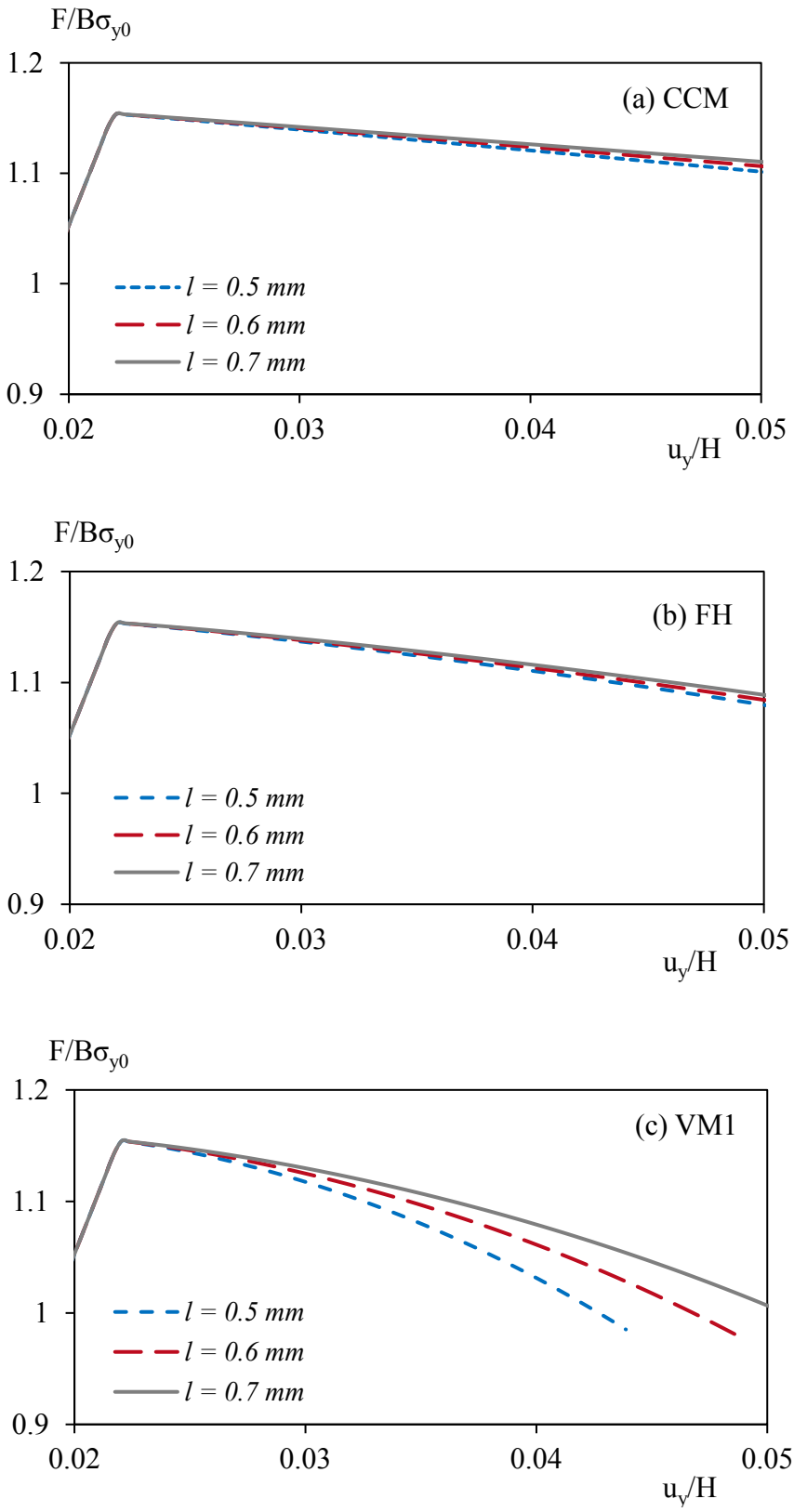

Figure 6.6 Load-displacement curves with different internal length for the plasticity models: (a) CCM (b) FH and (c) VM1.

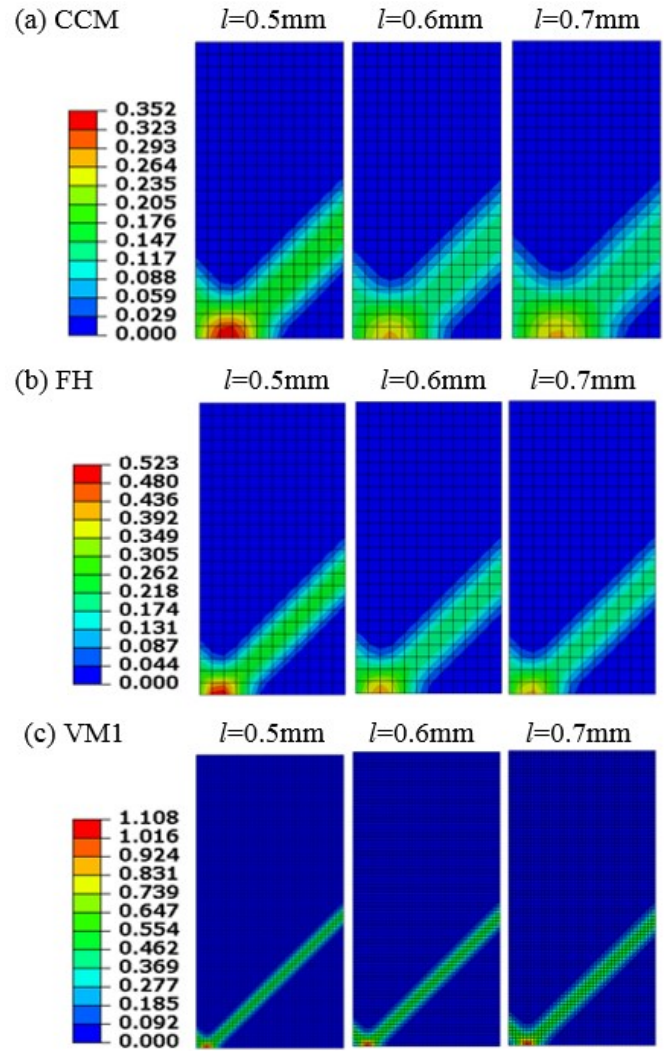

Figure 6.7 The contour of the equivalent plastic strain on undeformed meshes for the plasticity models with different internal length at the end of the simulation: (a) CCM, (b) FH and (c) VM1

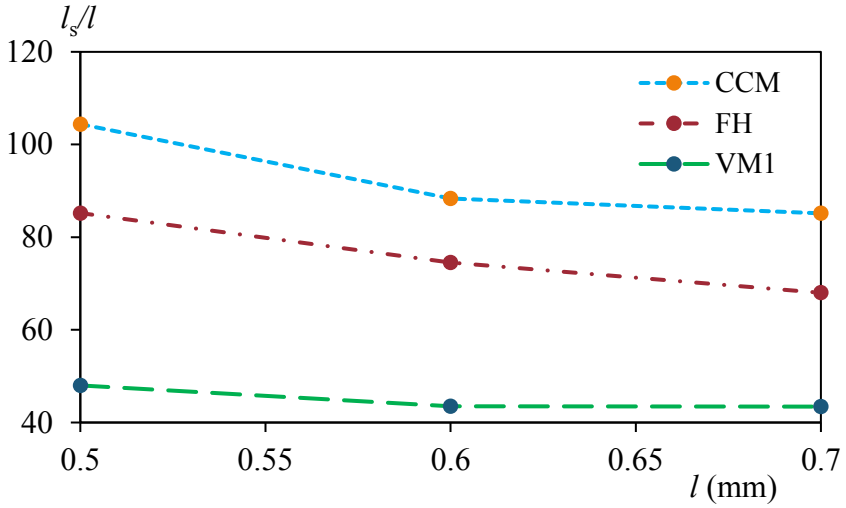

Figure 6.8 The ratio of the projected SBW, l_s to l with increasing l for the plasticity models

6.3 Drucker-Prager (Non-associative)

In this section numerical comparison is carried out for Cosserat (DP1) and strain gradient (CCMDP and FHDP) pressure dependent Drucker-Prager plasticity models from chapter 2 using the same material parameters for the models. The load-displacement curves and the projected SBW is compared, and the numerical stability of the models during plastic deformation are discussed.

Numerical finite element simulation is carried out considering biaxial compression test. The geometry, loading, boundary conditions remain same as the previous section. The material parameters used are: $E = 50\text{MPa}$, $\nu = 0.3$, $\text{h}_\text{p} = -0.15\text{MPa}$, $c_0 = 0.15\text{MPa}$, the initial cohesion of the weak element $c_{\text{w0}} = 0.14\text{MPa}$ and $l = 0.6\text{mm}$. Non-associative flow rule is assumed with $\phi = 35^\text{o}$ and $\psi = 0^\text{o}$.

The load-displacement curves for the Cosserat and strain gradient Drucker-Prager plasticity models are shown in Figure 6.9. At the initial stages of the plastic deformation (hardening), the load-displacement remains equal for all the models. However, at the later stages of the plastic deformation (softening) the load-displacement curves diverge from one another. Therefore using the same material

parameters Cosserat and strain gradient Drucker-Prager plasticity models predict different numerical solutions in the post-peak regime. The model CCMDP and DP1 predict the most and least stiff load-displacement curves in the post-peak regime. The model FHDP starts softening earlier than the other models during plastic deformation.

The numerical finite element solutions of the FHDP model becomes unstable and does not converge after specific plastic deformation in the post-peak regime. The CCMDP models being the stiffest is numerically most stable than FHDP and DP1 model.

The deformed meshes and the contour of the equivalent plastic strain for the Drucker-Prager plasticity models are shown in Figure 6.10. The model CCM predicts diffuse deformation with a wider SBW and the plastic zone spreads at the entire bottom of the specimen. Both FHDP and DP1 models predict clear shear band formation. However, the SBW for CCMDP > FHDP > DP1 model. Note that the minimum equivalent plastic strain is not zero which means the entire structure is going through plastic deformation only the localised deformation zone undergoes softening.

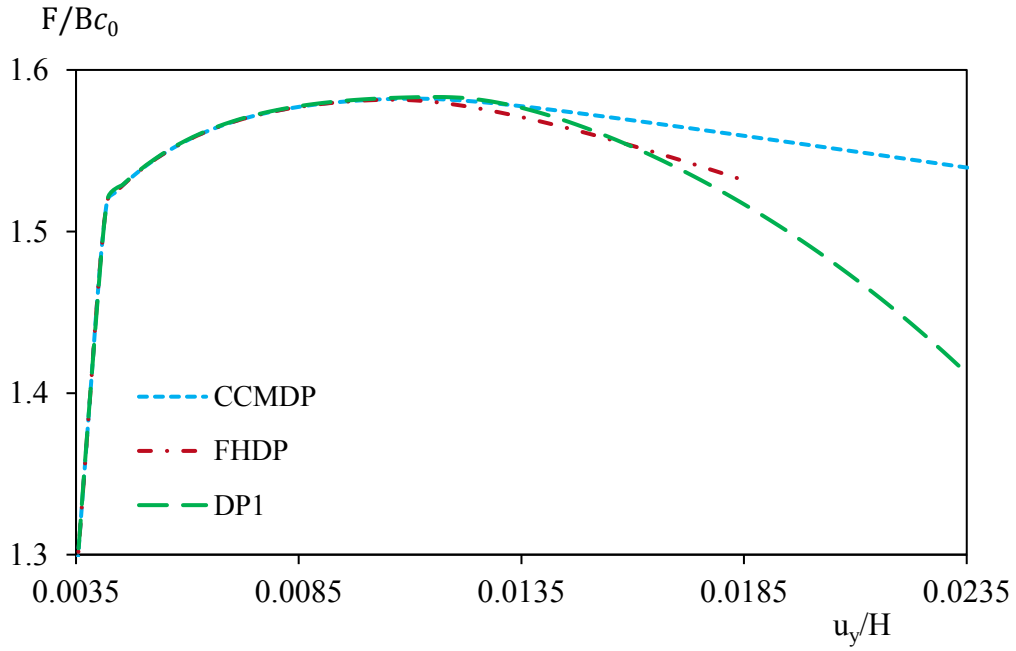

Figure 6.9 Load-displacement curves for the Cosserat (DP1) and strain gradient (CCMDP and FHDP) Drucker-Prager plasticity models.

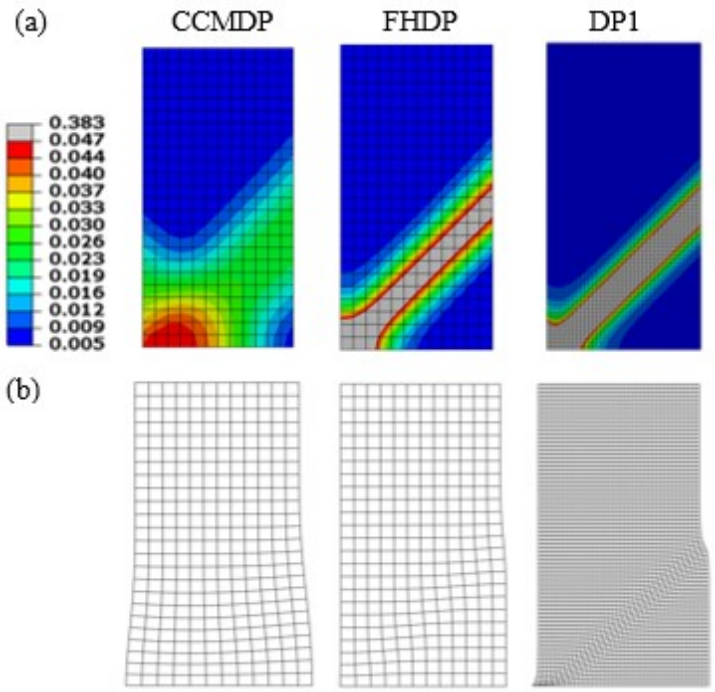

Figure 6.10 Cosserat (DP1) and strain gradient (CCMDP and FHDP) Drucker-Prager plasticity models at the end of the simulation: (a) undeformed meshes with the contour of the equivalent plastic strain and (b) deformed meshes (scale factor = 2).

The equivalent plastic strain distribution along y-axis on the right side from the bottom of the specimen for the Drucker-Prager plasticity models are shown in Figure 6.11. Although the DP1 model predicts higher equivalent plastic strain than FHDP, the model DP1 and FHDP predict an almost equivalent projected SBW. The model CCMDP predicts a much more extensive projected SBW compared to other models. Therefore, the stiffer models predict a more substantial projected SBW and the plastic zone with smaller equivalent plastic strain.

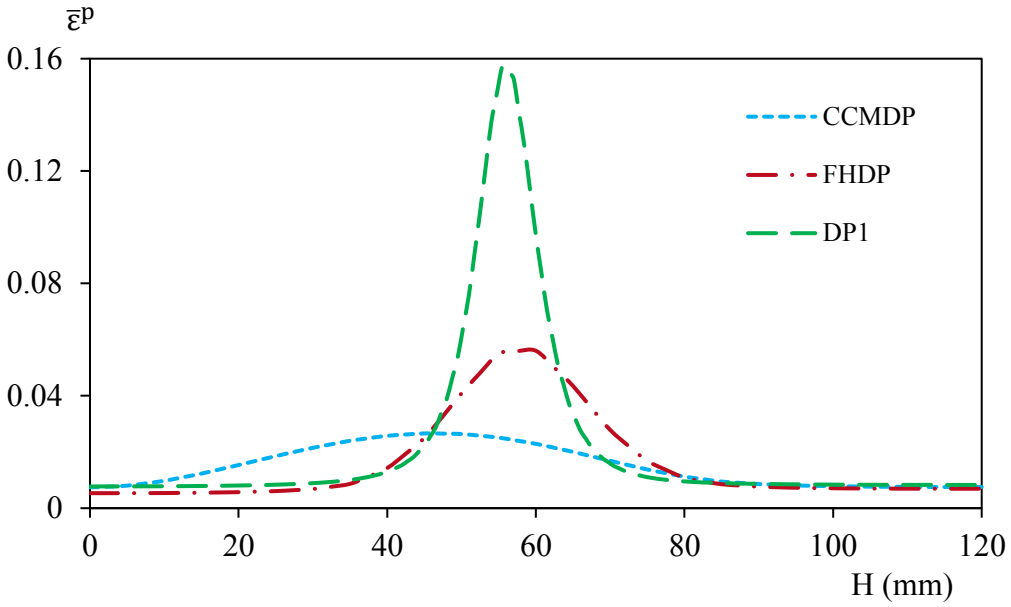

Figure 6.11 The equivalent plastic strain distribution along y-axis on the right side from the bottom of the specimen for Cosserat (DP1) and strain gradient (CCMDP and FHDP) Drucker-Prager plasticity models at the end of the simulation.

6.4 Equivalent SBW

6.4.1 Von Mises

In this section, we compare the numerical solutions of Cosserat (VM1) and strain gradient (CCM and FH) plasticity models from chapter 2. Attention is focused on predicting an equivalent projected SBW for the models.

At first, we plot the SBW against the internal length for different models as shown in Figure 6.12 using the results from section 6.2. The model CCM is considered with an internal length of 0.6mm, and a horizontal straight line (dotted) is plotted. The best fit straight (linear) lines for the plasticity models FH and VM1 are plotted. The point of intersection of the best fit straight lines with the horizontal dotted line gives the internal length for FH and VM1 models for which the projected SBW is equal to CCM models (with 0.6mm). The internal length determined from Figure 6.12 for FH and VM1 models is 0.91mm and 0.41mm respectively. Numerical finite element simulation is carried out considering biaxial compression test. The geometry, loading,

boundary conditions and material parameters remain same as Section 6.1. The internal length used for the model CCM, FH and VM1 are 0.6mm, 0.91mm and 1.41mm respectively.

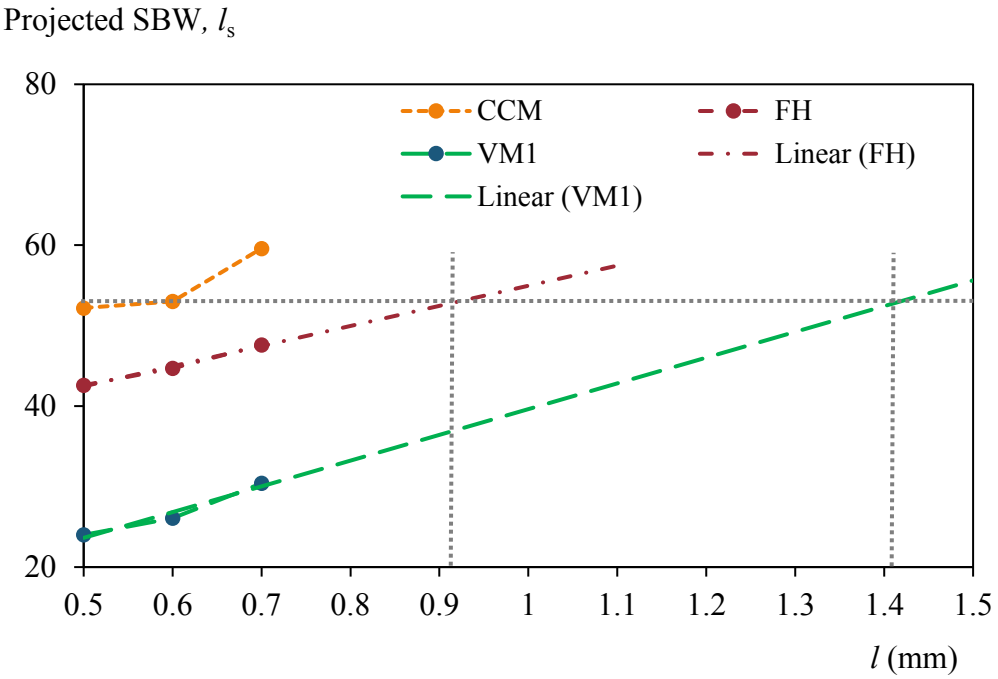

Figure 6.12 Projected SBW for the plasticity models (CCM, FH and VM1) for increasing internal length.

The contour of the equivalent plastic strain and the deformed configuration for the plasticity models are shown in Figure 6.13. All the models predict equivalent plastic zone and SBW. The maximum equivalent plastic stain occurs at the bottom of the specimen for all the models. All the model predicts a localised deformation configuration.

The equivalent plastic strain distribution along y-axis on the right side from the bottom of the specimen for the plasticity models are shown in Figure 6.14. All the models predict approximately equal projected SBW of 57 mm. The ratio of the projected SBW to the internal length for CCM, FH and VM1 models are approximately 95, 63 and 40 respectively. Therefore CCM model would require a much smaller internal length compared to FH and VM1 to predict equal projected SBW.

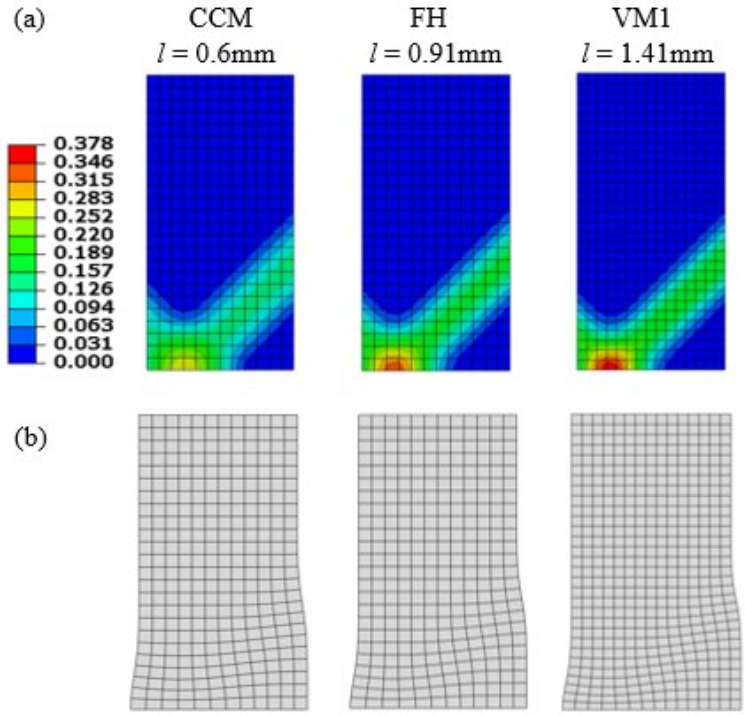

Figure 6.13 Cosserat (VM1) and strain gradient (CCM and FH) plasticity models at the end of the simulation: (a) undeformed meshes with the contour of the equivalent plastic strain and (b) deformed meshes.

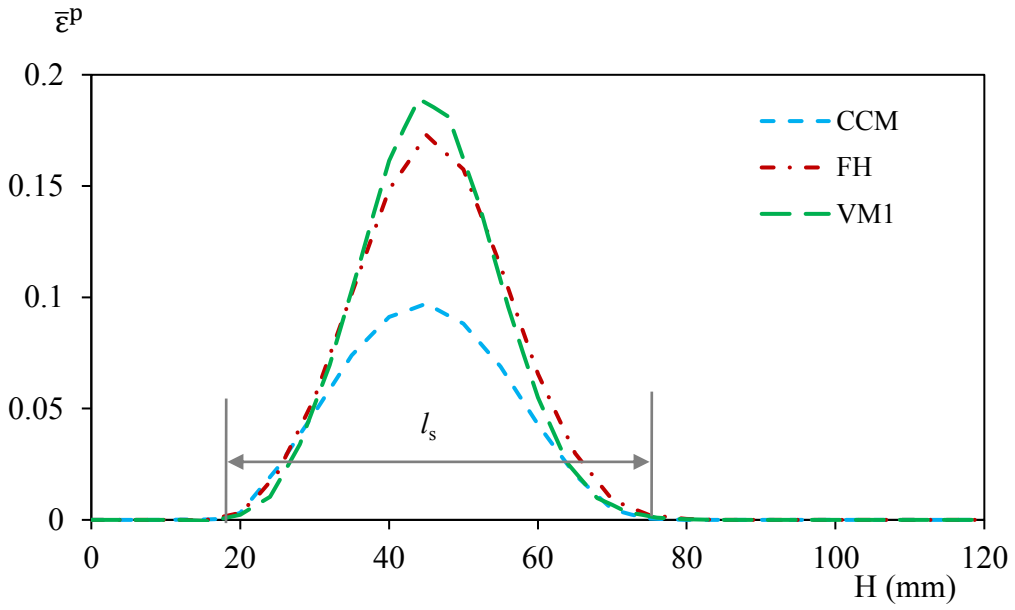

Figure 6.14 The equivalent plastic strain distribution along y-axis on the right side from the bottom of the specimen for Cosserat (VM1) and strain gradient (CCM and FH) plasticity models at the end of the simulation.

The load-displacement curves for the Cosserat and strain gradient plasticity models are shown in Figure 6.15. All the models predict almost equivalent load-displacement curves in the post-peak regime. The CCM models are slightly stiffer than the others at the later stages of the plastic deformation. Note that although the models predict an equivalent projected SBW, the load-displacement curves are very close but not equal. Therefore equalising the projected SBW for the models by changing the internal will not predict an equal load-displacement curve.

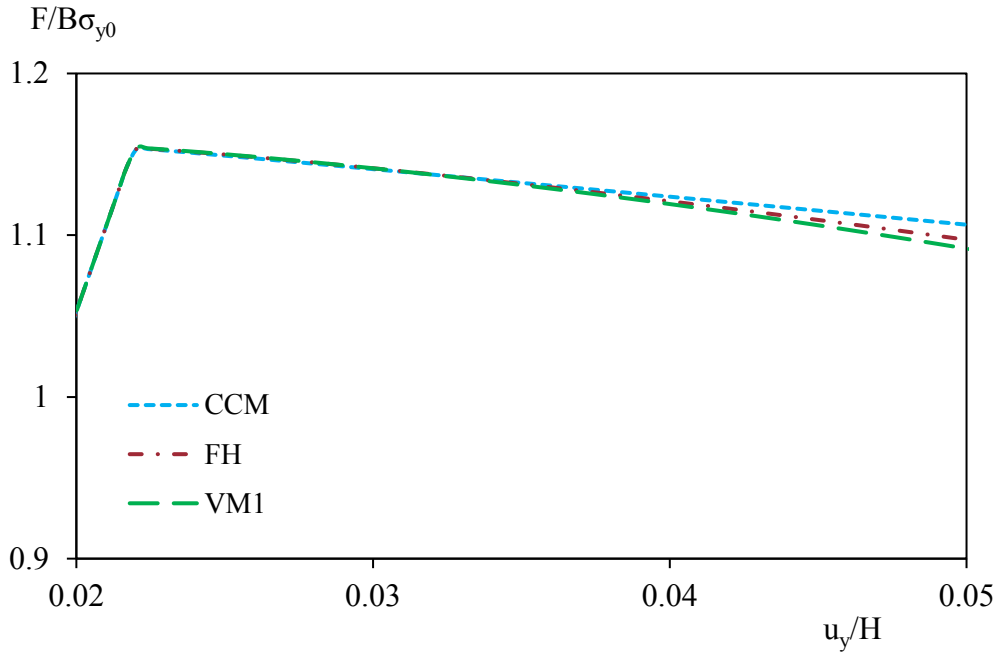

Figure 6.15 Load-displacement curves for the Cosserat (VM1) and strain gradient (CCM and FH) plasticity models with equivalent internal length.

6.4.2 Drucker-Prager

In this section numerical comparison is carried out for Cosserat (DP1) and strain gradient (CCMDP and FHDP) Drucker-Prager plasticity models from Chapter 2. Attention is focused on predicting an equivalent SBW for the models. We first consider the dilatancy angle equal to zero. Later we consider dilatancy angle greater than zero but considerably smaller compared to the friction angle.

Numerical finite element simulation is carried out considering biaxial compression test. The geometry, loading, boundary conditions remain same as section 6.1. The

material parameters remain the same as section 6.3. The numerical experimentation shows that considering the projected SBW for DP1 model with l=0.2mm a much smaller internal length for CCMDP model is required to equalise the projected SBW. Smaller internal length means higher mesh density is required to obtain acceptable numerical solutions. Therefore the dimension of the specimen is reduced: H=40mm and B=20mm which decreases the computational cost significantly.

The first set of results are obtained with zero dilatancy angle. The numerical experimentation shows that the internal length of CCMDP and FHDP models for which the projected SBW is equal to DP1 models with an internal length of 0.2mm are 0.06mm and 0.1mm respectively.

The equivalent plastic strain and the deformed meshes for the Cosserat and strain gradient Drucker-Prager plasticity models are shown in Figure 6.16. All the models predict finite SBW which appears from the bottom left and ends at the upper right side of the specimen. Note that the minimum equivalent plastic strain is not zero which means the entire structure is going through plastic deformation while the localised deformation zone undergoes softening. All the models predict localised deformation as shown in the deformed meshes in Figure 6.16.

All the model predicts equivalent projected SBW, l_s which are approximately 11.5 mm as shown in Figure 6.17. The ratio of the projected SBW to the internal length for the models CCMDP, FHDP and DP1 are approximately 192, 115 and 57.5 respectively. Therefore, the model CCMDP requires a much smaller internal length compared to FHDP and DP1 to predict an equal projected SBW.

The load-displacement curves for the Cosserat and strain gradient plasticity models with zero dilatancy angle for which the SBW becomes equal for the models are shown in Figure 6.18. Although the models predict an equivalent projected SBW by changing the internal length, the load-displacement curves diverge from one another in the post-peak regime. The model CCMDP predicts the stiffest load-displacement curve. The model FHDP predicts a reduction in load carrying capacity significantly than the other models in the post-peak regime. As a result, numerical instabilities develop for FHDP model, and the finite element solutions do not converge after specific plastic deformation.

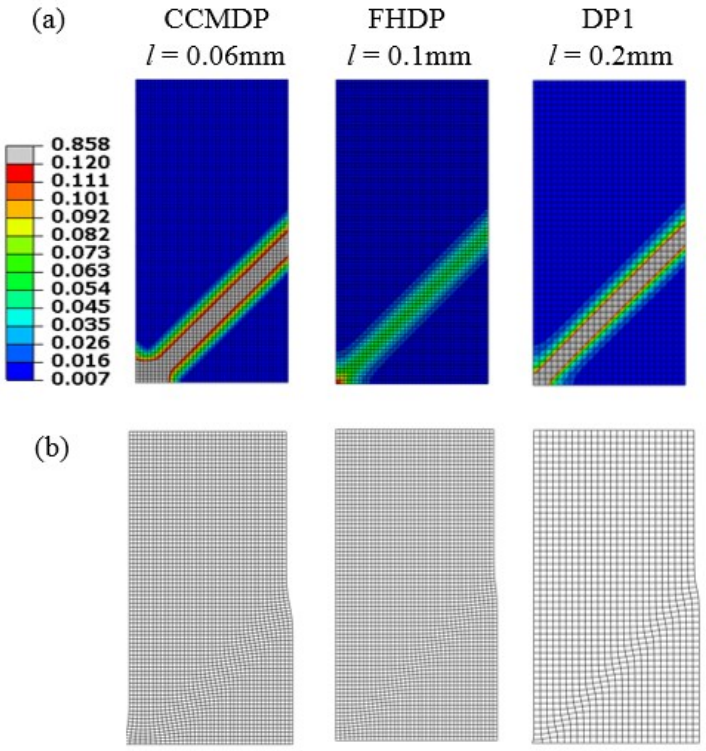

Figure 6.16 Cosserat (DP1) and strain gradient (CCMDP and FHDP) Drucker-Prager plasticity models with zero dilatancy angle at the end of the simulation: (a) undeformed meshes with the contour of the equivalent plastic strain and (b) deformed meshes.

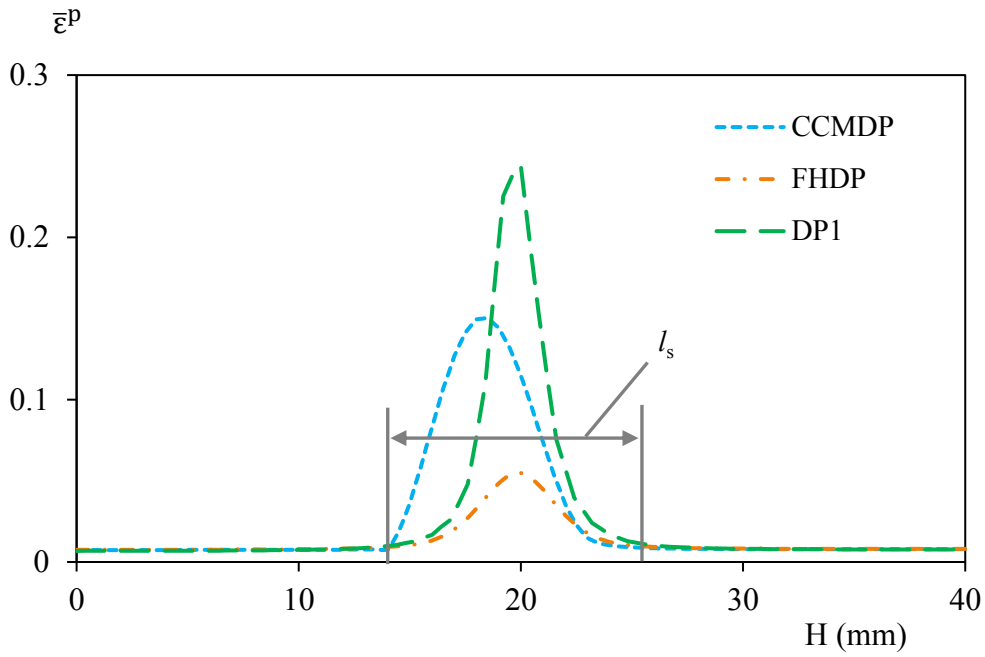

Figure 6.17 The equivalent plastic strain distribution along y-axis on the right side from the bottom of the specimen for Cosserat (DP1) and strain gradient (CCMDP and FHDP) Drucker-Prager plasticity models with zero dilatancy angle.

The numerical experimentation at the beginning shows that for Cosserat and strain gradient plasticity models using COS8(4)R and QU30L3 elements respectively predict mesh independent result if the ratio of the internal length to the size of the element is greater than equal to 0.2 and 0.1 respectively. As a result, to predict an equivalent projected SBW of 11.5mm as the above case with Cosserat and strain gradient Drucker-Prager plasticity models the required minimum size of the elements for DP1, CCMDP and FHDP models are 1mm, 0.6mm and 1mm respectively. Therefore CCMDP model requires a higher mesh density which increases the computational cost.

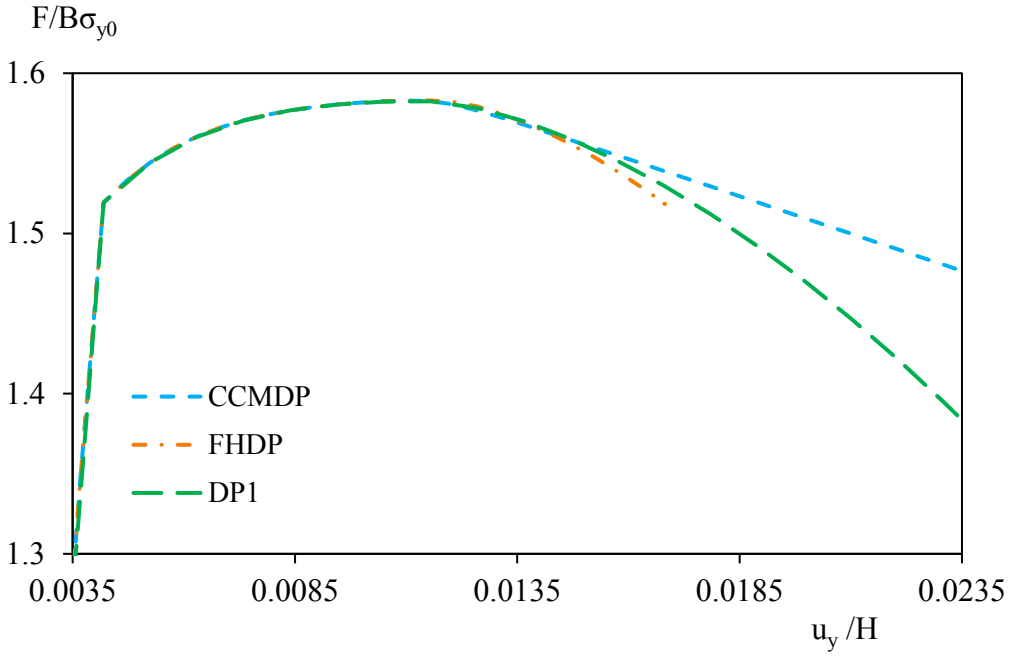

Figure 6.18 Load-displacement curves for the Cosserat (DP1) and strain gradient (CCMDP and FHDP) Drucker-Prager plasticity models with zero dilatancy angle.

The second set of results are obtained with dilatancy angle $\psi = 5^{o}$. Everything else is the same as the above case with Cosserat (DP1) and strain gradient (CCMDP and FHDP) Drucker-Prager plasticity models.

The numerical experimentation shows that the internal length of CCMDP and FHDP models for which the projected SBW is equal to DP1 models (with an internal length of 0.2mm) are 0.06mm and 0.15mm respectively as shown in Figure 6.19. All the model predicts equivalent projected SBW, l_s which are approximately 12 mm. The ratio of the SBW to the internal length for CCMDP, FHDP and DP1 models are approximately 200, 80 and 60 respectively. Therefore, the model CCMDP requires a much smaller internal length compared to FHDP and DP1 to predict an equivalent projected SBW.

The load-displacement curves for the Cosserat and strain gradient Drucker-Prager plasticity which predicts an equivalent projected SBW is shown in Figure 6.20. The CCMDP model predicts the stiffest load-displacement curve while DP1 predicts a significant reduction in the load carrying capacity in the post-peak regime. Once again

numerical instabilities develop for FHDP model, and the finite element solutions do not converge in the post-peak regime after specific plastic deformation.

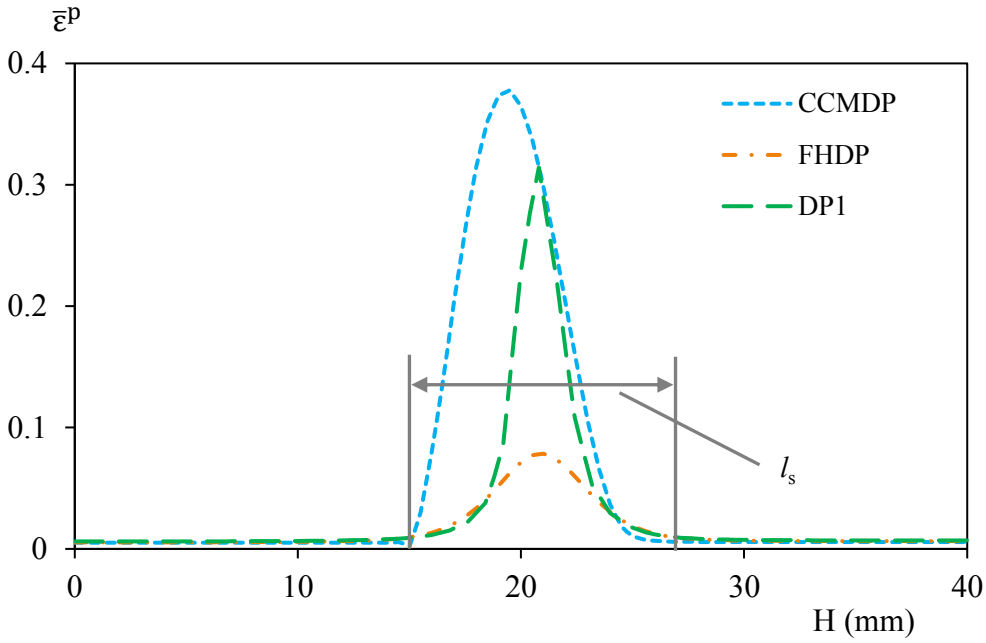

Figure 6.19 The equivalent plastic strain distribution along y-axis on the right side from the bottom of the specimen for Cosserat (DP1) and strain gradient (CCMDP and FHDP) plasticity models.

The minimum equivalent plastic strain is not entirely zero as shown in Figure 6.21 which mean the entire structure is going through plastic deformation. However, most of the structure is going through hardening phase of the plastic deformation except the localised deformation zone which undergoes softening. All the models predict shear band formation and localised deformation.

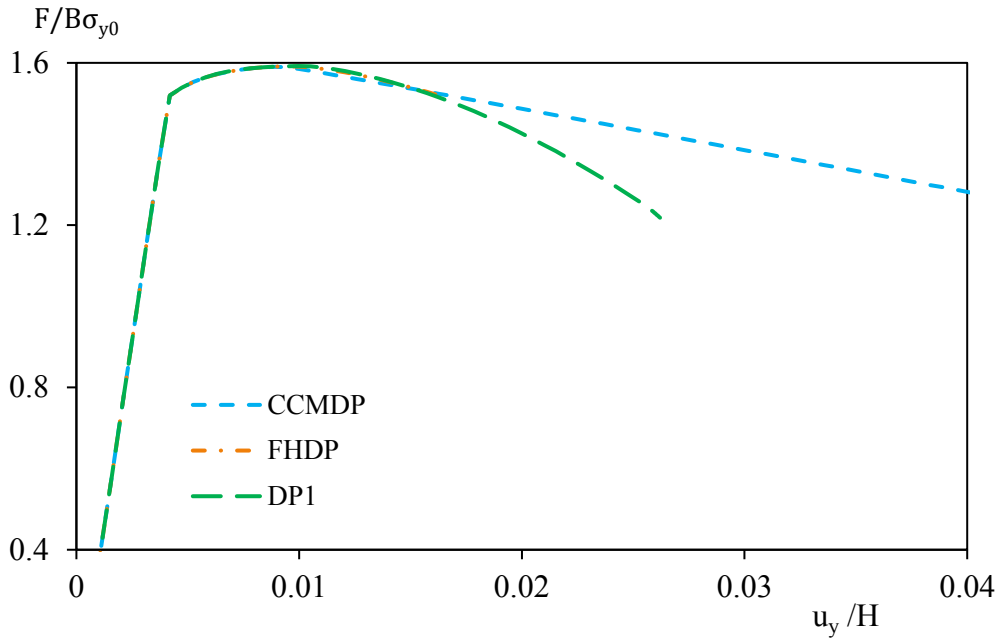

Figure 6.20 Load-displacement curves for the Cosserat (DP1) and strain gradient (CCMDP and FHDP) Drucker-Prager plasticity models for equivalent SBW.

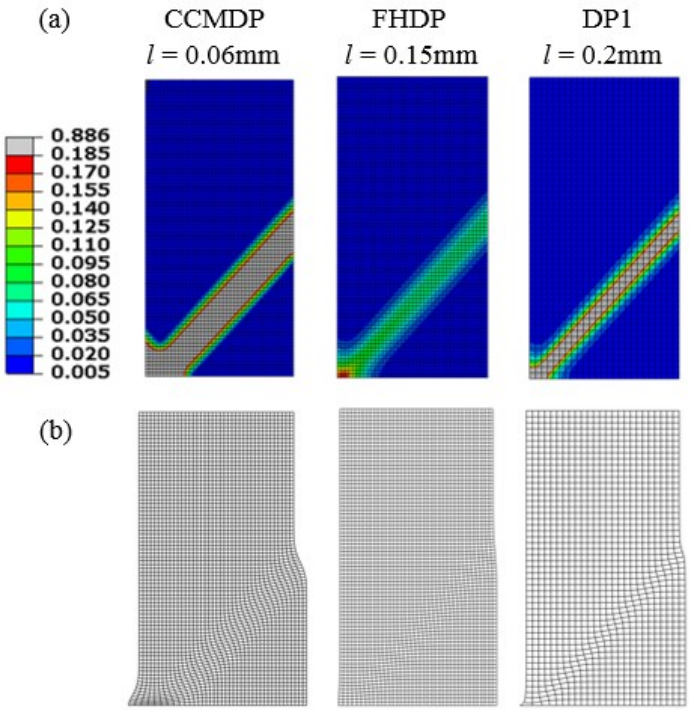

Figure 6.21 Cosserat (DP1) and strain gradient (CCMDP and FHDP) Drucker-Prager plasticity models at the end of the simulation: (a) undeformed meshes with the contour of the equivalent plastic strain and (b) deformed meshes

6.5 Conclusions

The numerical solutions of both the Cosserat and strain gradient von Mises (CCM, FH, VM1) and Drucker-Prager (CCMDP, FHDP and DP1) plasticity models are different for the same material parameters. The CCM (and CCMDP) and VM1 (and DP1) models predict the most and the least stiff load-displacement curve respectively for the same material parameters. The stiffer the model, the larger the SBW predicted. The formation of the SBW appears at an early stage of the plastic deformation and remains unchanged as plastic deformation increases.

Increasing the internal length, all the plasticity models (CCM, FH and VM1) predict less stiff load-displacement curves in the post-peak regime with a larger SBW. However, the load-displacement curves of Cosserat (VM1) plasticity model are more sensitive to the change in internal length compared to the strain gradient (CCM and FH) models.

Predicting an equivalent projected SBW for the von Mises plasticity models (CCM, FH and VM1) by changing the internal length only, the models predict almost equal load-displacement curves with CCM model slightly stiffer at the later stages of the plastic deformation. However, this is not the case for Drucker-Prager (CCMDP, FHDP and DP1) plasticity models. The load-displacement curve diverges significantly from one another during the softening stage of the plastic deformation. Numerical instabilities develop for FHDP model and even worse when the dilatancy angle is greater than zero. In a paper by Jirasek and Rolshoven (2009) obtained a similar behaviour of FH model considering one-dimensional setting and strain-softening material that at the later stage of softening FH model develop instabilities. Therefore equalising the projected SBW by changing the internal length is not realistic for Drucker-Prager plasticity models to predict equal load-displacement. If we try to predict equal load-displacement curves for the Drucker-Prager models by changing the internal length, the projected SBW will no longer be equal.

7 Example problems of soil instability

In this chapter strain localisation phenomena due to strain softening are simulated using Cosserat (DP1) and strain gradient (CCMDP and FHDP) pressure dependent Drucker-Prager plasticity models from chapter 2 considering vertical and inclined soil slope stability problems.

To obtain mesh-independent results, discretisation used for Cosserat and strain gradient models is such that the ratio of the internal length to the size of the element is greater than equal to 0.2 and 0.1 respectively. The elements used for Cosserat and strain gradient models are COS8(4)R and QU30L3 respectively which performed well and predicts acceptable results (i.e. no significant numerical issues such as locking or spurious deformation hourglass modes) in the plastic regime based on the results obtained in chapter 4.

7.1 Vertical slope stability

In this section vertical soil slope stability problem is simulated for 2D plain strain case to compare the numerical solutions of the Cosserat (DP1), strain gradient (CCMDP and FHDP) and classical (CLA) Drucker-Prager plasticity models.

In Chapter 6 it was observed that calibrating the internal length only in the biaxial test to equalise the projected SBW, the load-displacement curves of Cosserat and strain-gradient plasticity models diverge in the softening stage of the plastic deformation. This suggests that some other parameters need to be calibrated along with the internal length to reproduce the same behaviour (regarding the load-displacement curve and the projected SBW). However, in this chapter some example problems of soil instability are simulated by calibrating only the internal length to equalise the projected SBW since calibrating multiple parameters would require further

investigation which we recommend for future work to reproduce the same behaviour in all aspect of the numerical solutions.

The geometry, loading and boundary conditions for the vertical slope are shown in Figure 7.1. The soil slope is loaded by a footing resting on its crest. The contact between the footing and the soil is assumed to be perfectly adhesive. The increasing load is applied to the soil by increasing the vertical downward displacement prescribed to the nodal points on top of the footing elements. The material parameters for the Drucker-Prager models remain the same as the first part of Section 6.4.2 in the previous chapter with zero dilatancy angle.

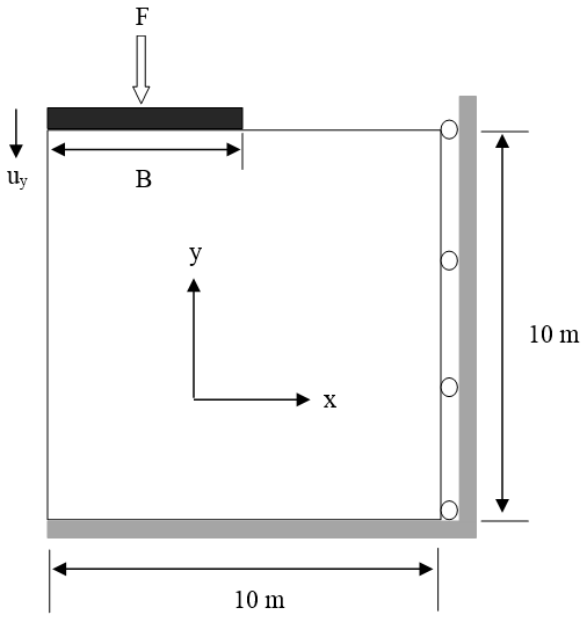

Figure 7.1 The geometry, loading and boundary conditions for the vertical slope

The equivalent plastic strain distribution and the deformed configuration for the vertical slope with Cosserat, strain gradient and classical (CLA) Drucker-Prager plasticity models are shown in Figure 7.2. The shear band formation develops from the middle of the crest towards the bottom left. The deformed meshes of all the models show localised deformation into a shear band formation. The FHDP models undergo numerical instabilities, and the finite element solution does not converge at the initial stages of the plastic deformation. As a result, the FHDP model undergoes minimal deformation compared to the other models in the plastic regime.

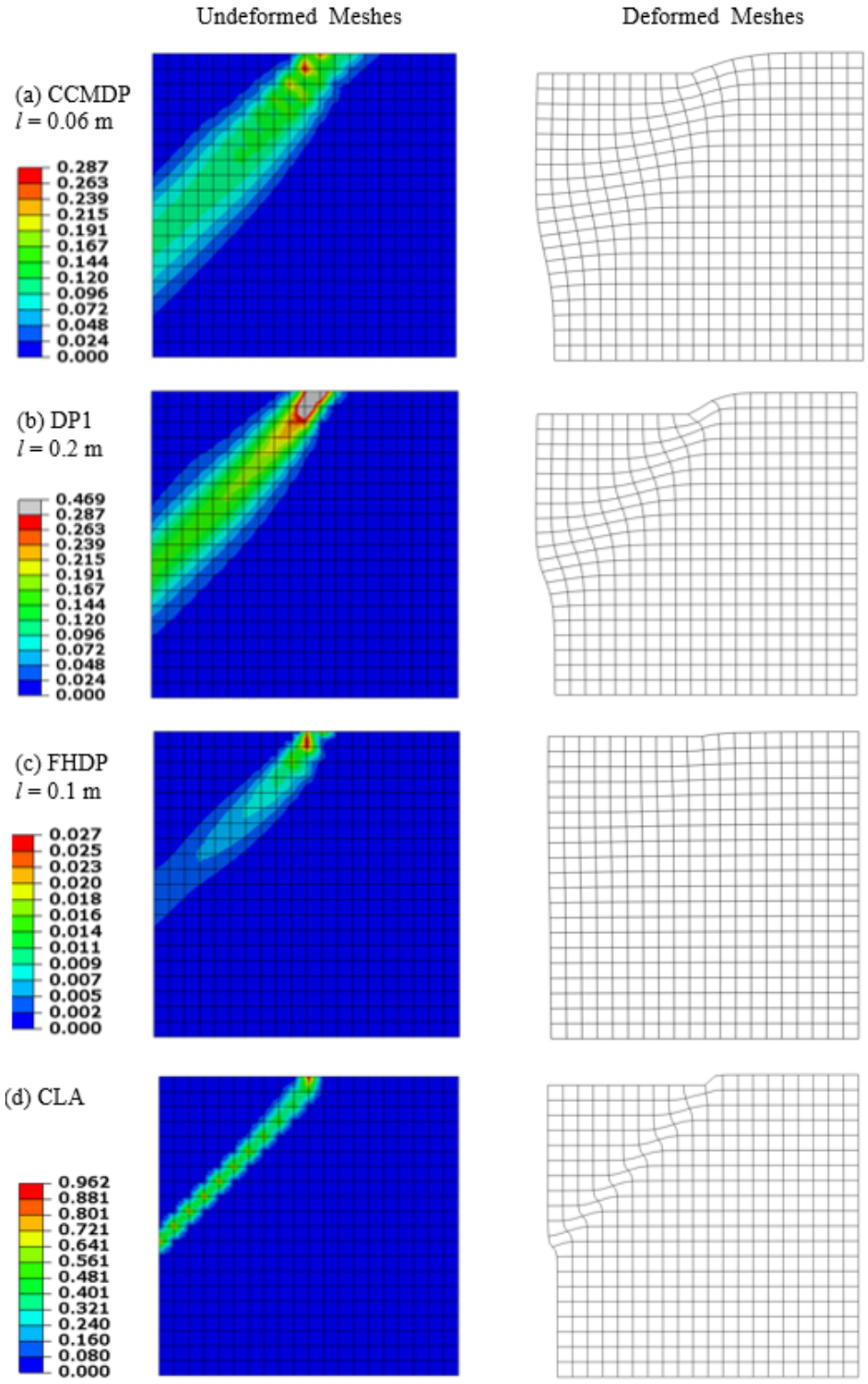

Figure 7.2 The contour of the equivalent plastic strain on undeformed meshes and deformed meshes (scale factor = 2) for the vertical slope with the Drucker-Prager plasticity models: (a) CCMDP, (b) DP1, (c) FHDP and (d) CLA.

The equivalent plastic strain distribution along y-axis on the left side from the bottom of the soil for the Drucker-Prager plasticity models are shown in Figure 7.3. The ratio of the projected SBW to internal length are shown in Table 7.1. Although, CCMDP uses the smallest internal length the projected SBW for CCMDP is much larger than the other models.

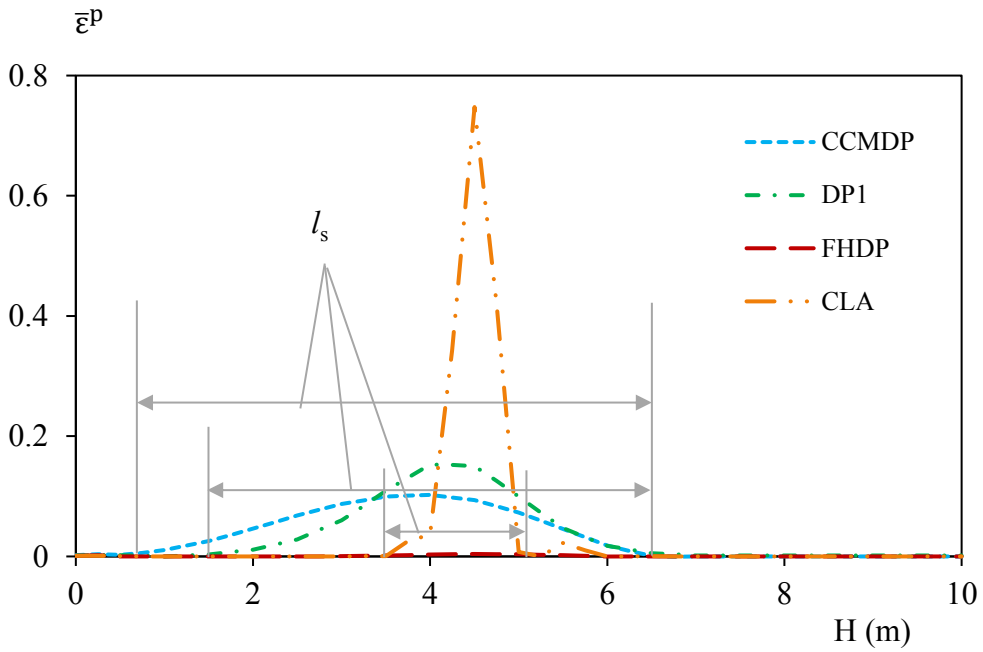

Figure 7.3 The equivalent plastic strain distribution along y-axis on the left side from the bottom of the soil for Cosserat (DP1), strain-gradient (CCMDP and FHDP) and classical (CLA) Drucker-Prager plasticity models at the end of the simulations.

Table 7.1 The ratio of the projected SBW to internal length for the vertical slope with the Cosserat, strain-gradient and classical (CLA) Drucker-Prager plasticity models.

Model	CCMDP	FHDP	DP1	CLA
Projected SBW, l_s (m)	5.9	2.8	5	1.6
The ratio of the projected SBW to internal length, l_s/l	98	28	25	N/A

The load-displacement curves for vertical slope with the Cosserat, strain-gradient and classical Drucker-Prager plasticity models are shown in Figure 7.4. The load-displacement curves are different for the plasticity models in the plastic regime as shown in the previous chapter using biaxial compression test. The CCMDP model predicts a much stiffer load-displacement curve than DP1. Therefore, equalising the projected SBW do not make the models equal regarding the load-displacement curves as mentioned in the previous chapter. The model FHDP suffer numerical instabilities, and the finite element solutions do not converge at the initial stage of the plastic deformation.

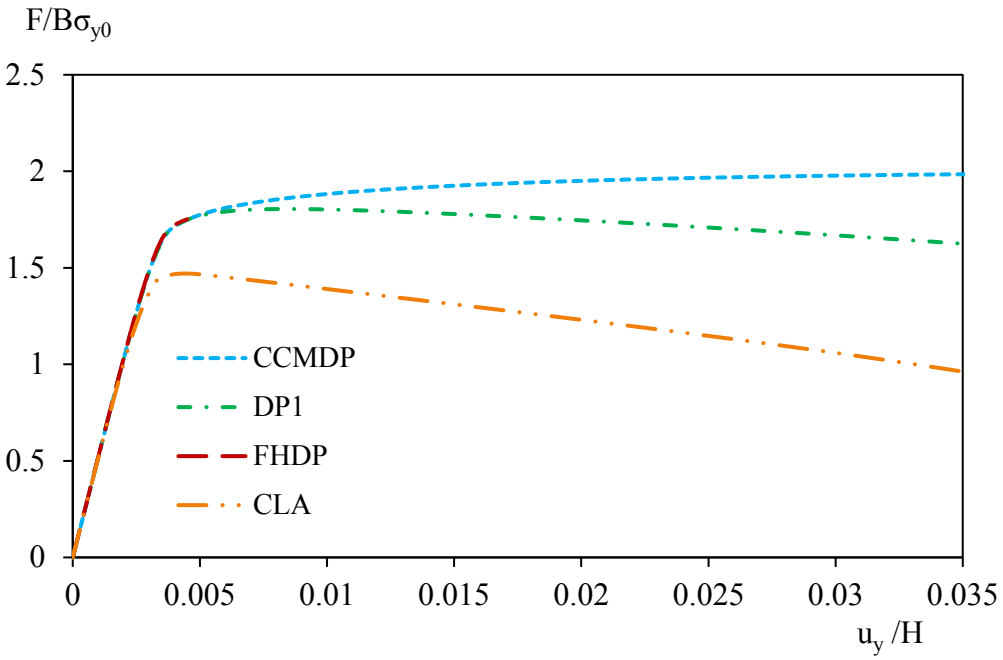

Figure 7.4 Load-displacement curves for the vertical slope with Cosserat (DP1), strain-gradient (CCMDP and FHDP) and classical (CLA) Drucker-Prager plasticity models.

7.2 Inclined slope stability

In this section inclined slope stability problem is simulated for 2D plain strain case to compare the numerical solutions of the Cosserat (DP1), strain gradient (CCMDP and FHDP) and classical (CLA) Drucker-Prager plasticity models.

The geometry, loading and boundary conditions are shown in Figure 7.5. The soil slope is loaded by a footing resting on its crest. The contact between the footing and the soil slope is assumed to be perfectly adhesive. The increasing load is applied to the soil slope by increasing the vertical displacement prescribed to the nodal point A so that the footing is allowed to rotate around the point A.

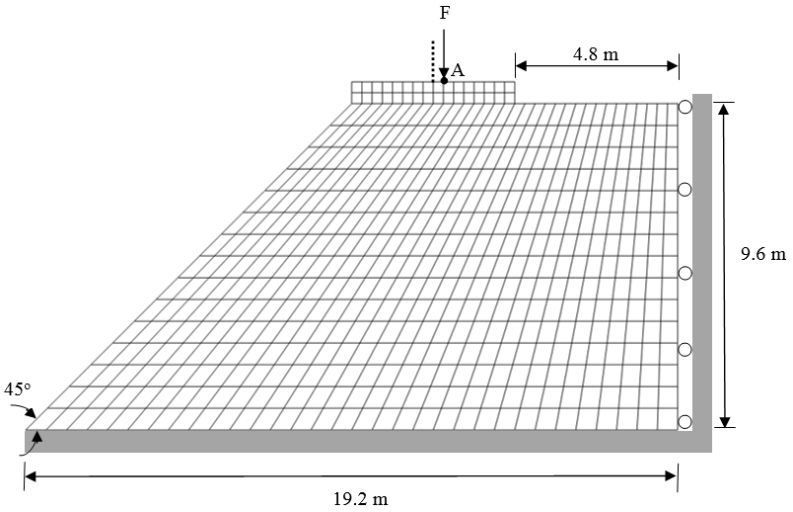

Figure 7.5 The geometry, loading and boundary conditions for the inclined slope

The footing is modelled by 32 elements with the quasi-rigid material properties: $E = 50000\text{MPa},\ c_0 = 5000\text{MPa},\ h_p = -0.02\text{MPa}$ and all other material parameters remains the same as the slope region. The slope is discretised into a finite element mesh with 480 elements. The material parameters for the Drucker-Prager models remain same as in the second part of Section 6.4.2 in the previous chapter with dilatancy angle $\psi = 5^o$.

The deformed configuration of the slope is shown in Figure 7.6. The deformed meshes of CCMDP, DP1 and CLA Drucker-Prager plasticity models show localised deformation into a shear band formation. The contour of the equivalent plastic strain for the Drucker-Prager plasticity models is shown in Figure 7.7. The localised shear band formation for CCMDP, DP1 and CLA starts from the middle of the crest and extend towards the centre of the slope. The model FHDP undergoes numerical instabilities, and the finite element solutions do not converge at plasticity. As a result, minimal deformation is predicted for the FHDP model.

The equivalent plastic strain distribution along the slope length is shown in Figure 7.8. The length d_a is approximately equal to d_b which mean the projected SBW on the slope for CCMDP and DP1 models are about equal. Therefore, we have successfully predicted equivalent projected SBW on the slope for CCMDP and DP1 models.

However, the CLA plasticity models predict a much smaller projected SBW. The CLA plasticity model predicts a high plastic staining at the top of the inclined slope which is not the case for Cosserat and strain-gradient plasticity models. The ratio of projected SBW to internal length for the CCMDP model is much higher than the DP1 model as shown in Table 7.2.

The load-displacement curves for the inclined slope with the Cosserat, strain gradient and classical Drucker-Prager plasticity models are shown in Figure 7.9. Although CCMDP and DP1 models predict equivalent projected SBW, the load-displacement curves are not equal. The model CCMDP predicts an overly stiff load-displacement curve in the plastic regime compared to the DP1 model for the slope stability problem. Once again predicting equivalent projected SBW do not make the load-displacement curve equal or even close for the models. Therefore, further investigation is needed to make the Drucker-Prager models comparable in terms of predicting both the projected SBW and the load-displacement curves.

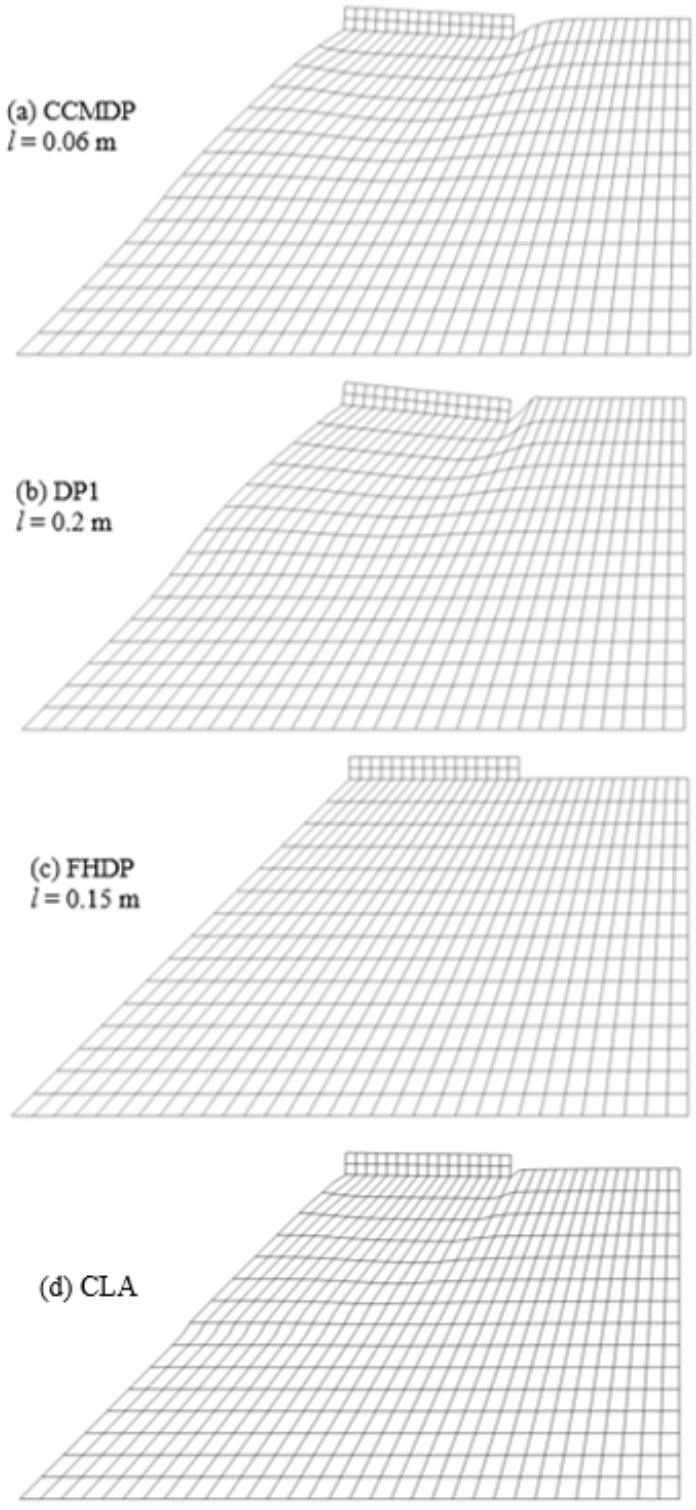

Figure 7.6 Deformed configuration (scale factor = 2) of the inclined slope subjected to a vertical displacement $u_y = 0.24\text{m}$ prescribed at the nodal point A for the Drucker-Prager plasticity models: (a) CCMDP, (b) DP1, (c) FHDP and (d) CLA.

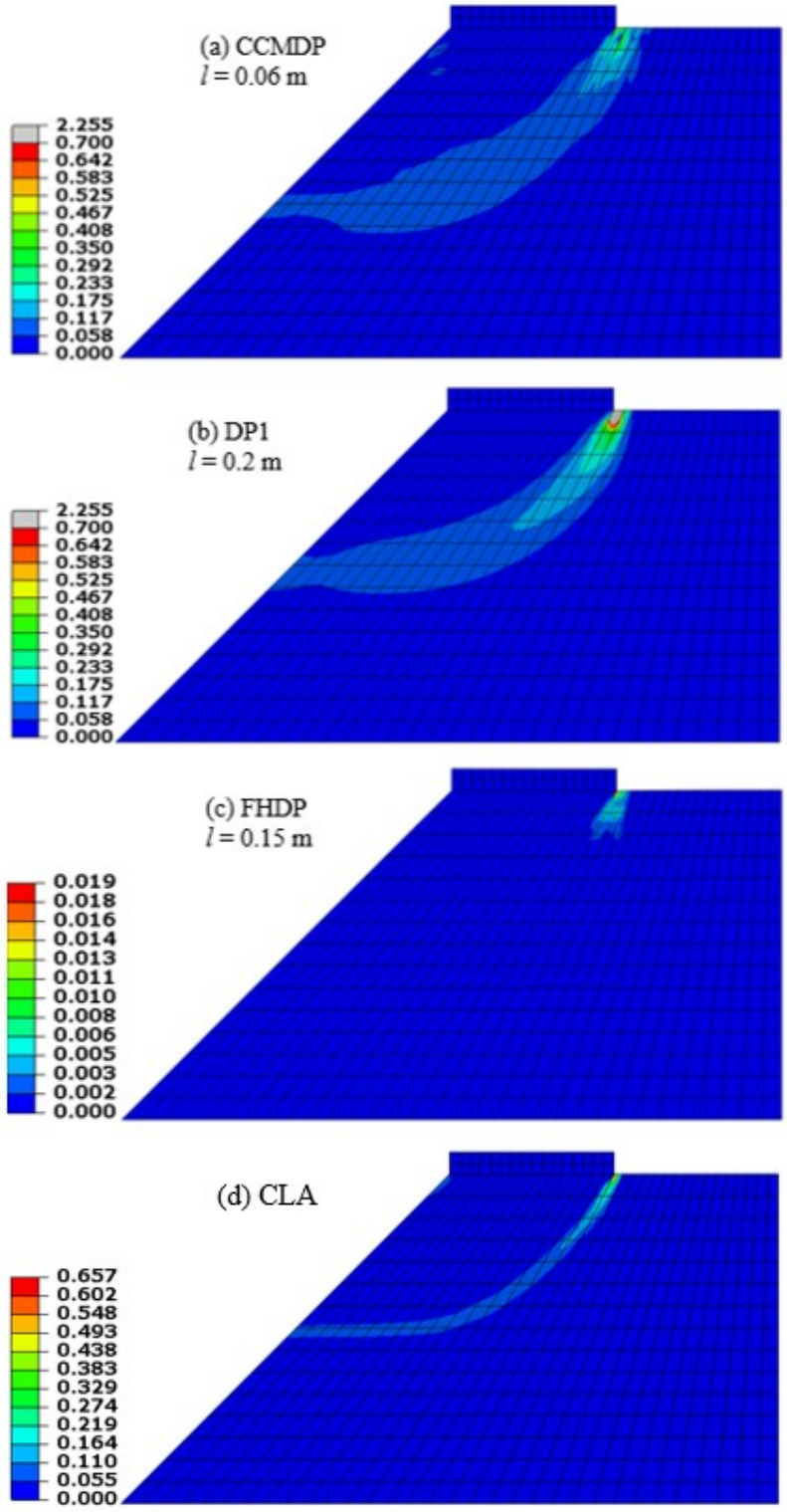

Figure 7.7 The contour of the equivalent plastic strain on undeformed for the inclined slope with the Drucker-Prager plasticity models: (a) CCMDP, (b) DP1, (c) FHDP and (d) CLA

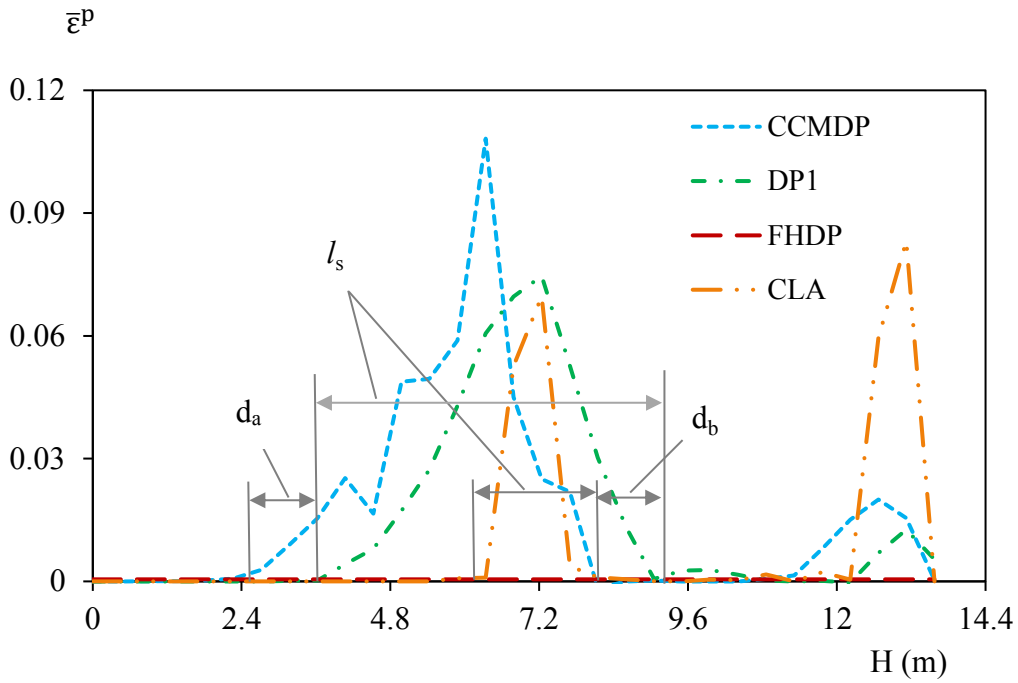

Figure 7.8 The equivalent plastic strain distribution along the inclined slope from the bottom at the end of the simulations for Cosserat (DP1), strain-gradient (CCMDP and FHDP) and classical (CLA) Drucker-Prager plasticity models.

Table 7.2 The ratio of projected SBW to internal length for the inclined slope with the Cosserat (DP1), strain-gradient (CCMDP and FHDP) and classical (CLA) Drucker-Prager plasticity models.

Model	CCMDP	FHDP	DP1	CLA
Projected SBW, l_s (m)	5.38	0	5.38	1.95
Ratio of projected SBW to internal length, l_s/l	90	0	27	N/A

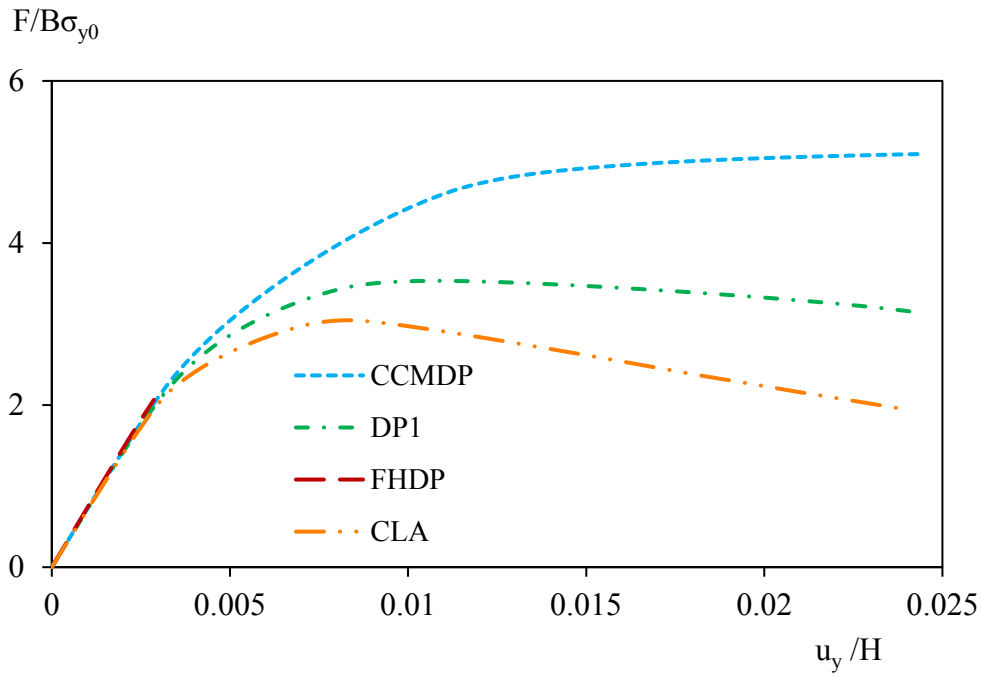

Figure 7.9 Load-displacement curves for the inclined slope with the Cosserat (DP1) and strain gradient (CCMDP and FHDP) Drucker-Prager plasticity models.

7.3 Conclusions

In the case of vertical slope stability problem, the projected SBW for DP1 and CCMDP models are not equal. However, in the inclined slope stability problem DP1 and CCMDP models predict equivalent projected SBW. All the models predicted localised deformation for vertical slope stability problem. However, in inclined slope stability problem FHDP model failed to predict a complete shear band formation due to numerical instabilities. Equalising the projected SBW by using different internal length, the models do not predict equivalent load-displacement curves.

8 Conclusions and final remarks

8.1 Concluding remarks

In this thesis, a detailed theoretical and numerical comparisons of the existing and proposed generalised plasticity (Cosserat and strain gradient) models are provided. An essential aspect of numerical finite element analysis is the use of appropriate elements in 2D (and 3D) elastoplastic problems. In this thesis, a detailed comparison of different existing and proposed 2D elements for Cosserat and strain gradient models are provided considering different formulations, ease of numerical implementations and their numerical behaviour (especially in the plastic regime). Therefore, encouraging the use of generalised plasticity models in practical applications by providing both the theoretical basis and appropriate numerical tools.

In the existing Cosserat von Mises and Drucker-Prager type plasticity models different formulations are derived for the plastic multiplier and consistent elastoplastic modulus. Also, the value of the Cosserat parameters used is different which make it difficult to understand the differences in the numerical behaviour from the formulatios. However, all the existing von Mises plasticity models show same numerical behaviour when the models use the same Cosserat parameters. The different formulation of the plastic multiplier and consistent elastoplastic modulus does not affect the numerical results. Any Cosserat plasticity models can be used to obtain the same result as long as the parameters are calibrated to the data available.

A new Cosserat von Mises (VM5) and Drucker-Prager (DP5) plasticity model is proposed considering classical plasticity and requires only three additional material parameters compared to classical plasticity. The proposed model VM5 shows all the essential features of the existing models such as same load-displacement curves and finite SBW for different discretisations. All the Cosserat parameters affect the numerical results (except parameter a and $b_1 \ldots b_3$) in the plastic regime.

In strain-gradient von Mises and Drucker-Prager type plasticity models, the yield function is dependent on different quantities, and the formulation of the plastic multiplier is different. Therefore, the strain-gradient models are entirely different and expected to predict different numerical solutions.

The elements recommended to use with Cosserat plasticity models are COS8(4)R and COS6(3)G3 for elastoplastic analysis. The element COS8(4)R and COS6(3)G3 are computationally cheaper than quadratic/quadratic elements. The even less expensive element COS4SR shows acceptable numerical results. However, the deviation of the COS4SR in different plasticity models require further investigation.

The new penalty method and Lagrange multiplier elements are easier to implement and computationally cheaper compared to the existing ones. Among the existing and new elements, the most and the least computationally expensive elements are C^1 (TU36C1) and new penalty method (QU28PR) respectively. Although the mixed-type Lagrange multiplier and penalty elements are computationally cheaper, the elements require multiple fields to be discretised. Among mixed-type full integration elements, the new QU30L3 element is recommended. The penalty elements are not recommended as it requires a suitable penalty parameter to be determined and predict pathologically mesh dependent results.

The numerical solutions of both the Cosserat and strain gradient von Mises (CCM, FH, VM1) and Drucker-Prager (CCMDP, FHDP and DP1) plasticity models are different for the same material parameters. The formation of the SBW appears at an early stage of the plastic deformation and remains unchanged as plastic deformation increases for both the Cosserat and strain gradient plasticity models. The load-displacement curves of Cosserat (VM1) plasticity model are more sensitive to the change in internal length compared to the strain gradient (CCM and FH) models.

Predicting an equivalent projected SBW for Drucker-Prager (CCMDP, FHDP and DP1) plasticity models by changing the internal length only, the load-displacement curves diverge from one another significantly during the softening stage of the plastic deformation. Numerical instabilities are developed for the FHDP model and even worse when the dilatancy angle is greater than zero. We conclude that if we change

the internal length so that that load-displacement curves are equal for the Drucker-Prager models, then the SBW will no longer be equal to the models.

In both the vertical and inclined slope stability problems the Cosserat and strain-gradient Drucker-Prager models predict different load-displacement curves for the same SBW. All the models predicted localised deformation in vertical slope stability problem. However, for an inclined slope stability problem FHDP model fails to predict a complete shear band formation due to the development of numerical instabilities in plasticity.

8.2 Recommendation for future work

The thesis was focused on small strain theory. However, the localised deformation usually leads to large deformation. Cosserat and strain gradient equations can be formulated and compared for large deformation analysis. Also, the 2D models can be expanded to three dimensional (3D) for realistic comparisons to understand the localisation mechanism better. The new mixed-type element QU30L3 can be formulated into a 3D element and compared with the existing ones regarding numerical behaviour, ease of numerical implementations and the computational cost. The cheapest possible elements with no major numerical issues (such as locking or hourglassing) for Cosserat and strain-gradient models are COS4SR and the new penalty QU28PR element respectively. However, further investigation is required to determine the reasons for the inconsistency in the numerical behaviour regarding different plasticity models and overly soft behaviour for COS4SR and QU28PR element respectively. Therefore, a slight modification of the elements (COS4SR and QU28PR) is required so that they work correctly while still being cheap computationally.

References

Adhikary, D., & Dyskin, A. (2007). Modelling of progressive and instantaneous failures of foliated. *Rock Mech Rock Eng, 40*(4), 349-362.

Adhikary, D., Mühlhaus, H., & Dyskin, A. (1999). Modelling the large deformations in stratified media—the Cosserat continuum approach. *Mech Cohes-Frict Mater, 4*(3), 195-213.

Aero, E., & Kuvshinskii, E. (1961). Fundamental equations of the theory of elastic media with rotationally interacting particles. *Translated in Soviet Physics Solid State 2*, 1272-1281.

Aifantis, E. (1984). On the microstructural origin of certain inelastic models. *J. Eng. Mater. Technol. (Trans.ASME), 106*, 326–330.

Aifantis, E. (1987). The physics of plastic deformation. *Int. J. Plast., 3*(3), 211–247.

Aifantis, E. (1992). On the role of gradients in the localization of deformation and fracture. *Int. J. Engng Sci, 30*, 1279–1299.

Alsaleh, M. (2004). Numerical modeling of strain localization in granular materials using Cosserat theory enhanced with microfabric properties. *PhD thesis, Louisiana State University and Agricultural and Mechanical College*.

Alshibli, K., & Sture, S. (2000). Shear band formation in plane strain experiments of sand. *J. Geotech. Geoenviron. Engng. ASCE, 126*(6), 495–503.

Amanatidou, E., & Aravas, N. (2002). Mixed finite element formulations of strain-gradient elasticity problems. *Comput. Methods Appl. Mech. Eng., 191*, 1723–1751.

Amanatidou, E., & Aravas, N. (2002). Mixed finite element formulations of strain-gradient elasticity problems. *Comput. Methods Appl. Mech. Eng, 191*, 1723–1751.

Andò, E., Salvatore, E., Desrues, J., Charrier, P., Toni, J.-B., & Modoni, G. (2017). Strain Localisation in Sand in Cycles of Triaxial Compression and Extension: Continuum and Grain-Scale Analysis. *Springer Series in Geomechanics and Geoengineering*.

Argyris, J., Fried, I., & Scharpf, D. (1968). The TUBA family of plate elements for the matrix displacement method. *Aeronaut. J. R. Aeronaut. Soc, 72,*, 701–709.

Arsenlis, A., & Parks, D. (1999). Crystallographic aspects of geometrically-necessary and statistically-stored dislocation density. *Acta Mater, 47*, 1597–1611.

Arslan, H., & Sture, S. (2008). Finite element analysis of localization and micro–macro structure relationin granular materials. part ii: Implementation and simulations. *Acta Mech, 197*(3), 153.

Ashby, M. (1970). The deformation of plastically non-homogeneous alloys. *Phil. Mag, 21*, 399–424.

Askes, H., & Aifantis, E. (2002). Numerical modelling of size effects with gradient elasticity-formulation, meshless discretization and examples. *Int. J. Fract, 117*(4), 347–358.

Askes, H., & Gutiérrez, M. (2006). Implicit gradient elasticity. *Int. J. Numer. Methods Eng., 67*(3), 400–416.

Askes, H., & Gutiérrez, M. (2006). Implicit gradient elasticity. *Int. J. Numer. Methods Eng, 67*(3), 400–416.

Atkins, A. G., & Tabour, D. (1965). Plastic indentation in metals with cones. *Journal of the Mechanics and Physics of Solids, 13*, 149-164.

Atkinson, R. (1993). *Hardness tests for rock characterisation* (Vol. 1). Pergamon Press: Hudson J, editor. Comprehensive rock engineering.

Bazant, Z., & Jirásek, M. (2002). Nonlocal integral formulations of plasticity and damage: survey of progress. *J. Eng. Mech., 128*, 1119–1149.

Bazant, Z., & Pijaudier-Cabot, G. (1988). Nonlocal continuum damage, localization instability and convergence. *J. Appl. Mech., 55*, 287–293.

Begley, M., & Hutchinson, J. W. (1998). The mechanics of size-dependent indentation. *J. Mech. Phys. Solids, 46*(10), 2049-2068.

Beltyschko, T., Krongauz, Y., Organ, D., Fleming, M., & Krysl, P. (1996). Meshless methods: an overview and recent developments. *Comp. Meth. Appl. Mech. Engrg, 139*, 3–47.

Biot, M. A. (1967). Rheological stability with couple stresses and its application to geological folding. *Proc. Roy. Soc. A, 298*, 402-423.

Brace, W. (1961). Dependence of fracture strength of rocks on grain size. *76*, 99–103.

Casolo, S. (2006). Macroscopic modelling of structured materials: Relationship between orthotropic Cosserat continuum and rigid elements. *International Journal of Solids and Structures, 43*, 475–496.

Cauchy, A.-L. (1851). Note sur l'équilibre et les mouvements vibratoires des corps solides. *Comptes Rendus Acad. Sci., 32*, 323-326.

Chambon, E., Caillerie, D., & Matsuchima, T. (2001). Plastic continuum with microstructure, local second gradient theories for geomaterials: localisation studies. *International Journal of Solids and Structures, 38*, 8503-8527.

Cosserat, E., & Cosserat, F. (1909). *Theorie des Corps Deformables.* Paris: Herman et fils.

Cosserat, E., & Cosserat, F. (1909). *Théorie des corps deformables.* Paris: Hermann.

Cottrell, A. (1964). *The Mechanical Properties of Materials.* New York: J. Willey.

Dasgupta, S., & Sengupta, D. (1990). A higher-order triangular plate bending element revisited. *Int. J. Numer. Methods Eng, 30*, 419–430.

de Borst, R. (1991). Simulation of strain localization: a reappraisal of the Cosserat continuum. *Eng Comp, 8*(4), 317-332.

de Borst, R. (1993). A generalisation of J2-flow theory for polar continua. *Comput Methods Appl Mech Eng, 103*(3), 347-362.

de Borst, R., & Sluys, L. (1991). Localisation in a Cosserat continuum under static and dynamic loading conditions. *Comput Methods Appl Mech Eng, 20*(1), 805-827.

Desreues, J., & Viggiani, G. (2004). Strain localization in sand: overview of the experiments in Grenoble using stereo photogrammetry. *Int. J. Numer. Anal. Meth. Geomech, 28*(4), 279–321.

Desrues, J., & Hammad, W. (1989). Shear banding dependency on mean pressure level in sand. (pp. 57–67). Gdansk, Poland: Proc. Int. Workshop on Numerical Methods for Localization and Bifurcation of Granular Bodies.

Desrues, J., Chambon, R., Mokni, M., & Mazerolle, F. (1996). Void ratio evolution inside shear bands in triaxial sand specimens studied by computed tomography. *Géotechnique, 46*(3), 529–546.

Doerner, M. F., & Nix, W. D. (1986). A method for interpreting the data from depth sensing indentation measurements. *J. Mater. Res, 1*, 601-609.

Ebrahimian, J., Noorzad, A., & Alsaleh, M. (2011). Modeling shear localization along granular soil–structure interfaces using elasto-plastic Cosserat continuum. *International Journal of Solids and Structures, 49*(2012), 257-278.

Edelen, D. (1976). *Non Local Field Theories.* New York: Academic Press.

Ehlers, W., & Volk, W. (1998). On theoretical and numerical methods in the theory of porous media based on polar and non-polar elasto-plastic solid materials. *Int. J. Solids Structures, 35*, 4597–4616.

Eringen, A. (1966). Linear theory of micropolar elasticity. *J Math Mech, 15*, 909–923.

Eringen, A. (1999). Microcontinuum Field Theories I: Foundations and Solids. New York: Springer-Verlag.

Eringen, A. C., & Suhubi, E. S. (1964). Nonlinear Theory of Simple Micro-elastic Solid-I,. *Int. J. Engng. Sci, 2*, 189-203.

Fleck, N. A., & Hutchinson, J. W. (1993). A phenomenological theory for strain gradient effects in plasticity. *J. Mech. Phys. Solids, 41*(12), 1825–1857.

Fleck, N. A., Muller, G. M., Ashby, M. F., & Hutchinson, J. W. (1994). Strain gradient plasticity: theory and experiment. *Acta Metall. Mater, 42*(2), 475–487.

Fleck, N., & Hutchinson, J. (1997). Strain Gradient Plasticity. *Advanced in applied mechanics, 33*, 295-362.

Gane, N., & Cox, J. M. (1970). The microhardness of metals at very low loads. *Philos. Mag., 22*, 881-891.

Gao, H., Huang, Y., Nix, W., & Hutchinson, J. (1999). Mechanism-based strain gradient plasticity-I. Theory. *Journal of the Mechanics and Physics of Solids, 47*.

Germain, P. (1973). The method of virtual power in continuum mechanics. Part 2: microstructure. *SIAM J. Appl. Math, 25*(3), 556-575.

Gitman, I. (2006). Representative volumes and multi-scale modeling of quasi-brittle materials. University of Delft.

Godio, M., Stefanou, I., Sab, K., & Sulem, J. (2015). Dynamic finite element formulation for Cosserat elastic plates. *Int J Numer Methods Eng, 101*(13), 992-1018.

Gurtin, M. (2000). On the plasticity of single crystals: free energy, microforces, plastic-strain gradients. *J. Mech. Phys. Solids, 48*, 989–1036.

Han, C., & Vardoulakis, I. (1991). Plane strain compression experiments on water saturated fine-grained sand. *Geotechnique, 41*, 49–78.

Harris, W., Viggiani, G., Mooney, M., & Finno, R. (1995). Use of stereo photogrammetry to analyze the development of shear bands in sand. *Geotech. Test. J., 18*(4), 405–420.

Huang, Y., Gao, H., Nix, W., & Hutchinson, J. (2000). Mechanism-based strain gradient plasticity-II. Analysis. *Journal of the Mechanics and Physics of Solids, 48*, 99±128.

Huang, Y., Qu, S., Hwang, K., Li, M., & Gao, H. (2004). A conventional theory of mechanism-based strain gradient plasticity. *International Journal of Plasticity, 20*, 753–782.

Huang, Y., Xue, Z., Gao, H., Nix, W., & Xia, Z. (2000). A study of microindentation hardness tests by mechanism-based strain gradient plasticity. *J. Mater. Res, 15*(8), 1786-1796.

Iordache, M., & Willam, K. (1998). Localized failure analysis in elastoplastic Cosserat continua. *Comput Methods Appl Mech Eng, 151*(3-4), 559-586.

Ivancevic, V. G. (2009). New mechanics of spinal injury. *International Journal of Applied, 1*, 387–401.

Jaeger, J. (1967). Brittle failure of rocks. In: Failure and breakage of rocks. *Proc. 8th US Symposium on Rock Mechanics*, (pp. 3–57).

Jirásek, M., & Rolshoven, S. (2009). Localization properties of strain-softening gradient plasticity models.Part I: strain-gradient theories. *Int J Solids Struct, 46*(11-12), 2225-2238.

Kanatani, K. (1979). A continuum theory for the flow of granular materials. *Theoretical and Applied Mechanics, 27*, 571-578.

Khoei, A. R., Gharehbaghi, S. A., & and Tabarraie, A. R. (2007). Error estimation, adaptivity and data transfer in enriched plasticity continua to analysis of shear band localization. *Applied Mathematical Modelling, 31*, 983-1000.

Khoei, A., Yadegari, S., & Anahid, M. (2006). Three-dimensional modeling of strain localization in Cosserat continuum theory. *International Journal of Civil Engineerng., 4*(3), 176-191.

Koiter, W. (1964). Couple stresses in the theory of elasticity, I and II. *Proc. Ned. Akad. Wet. (B), 67*(1), 17-44.

Kröner, E. (1967). Elasticity theory of materials with long-range cohesive forces. *Int. J. Solids Struct, 3*, 731–742.

Kuvshinskii, R., & Aero, E. (1964). Continuum theory of asymmetric. *Sov Phys-Solid State, 5*, 1892–7.

Lade, P. (2002). Instability, shear banding and failure in granular materials. *I. J. Solids Structures, 39*, 3337–3357.

Lai, T., Borja, R., Duvernay, B., & Meehan, R. (2003). Capturing strain localization behind a geosynthetic-reinforced soil wall. *I. J. Num. Anal. Meths. Geomech., 27*, 425–451.

Larsson, J., & Larsson, R. (2000). Finite-element analysis of localization of deformation and fluid pressure in elastoplastic porous medium. *Int. J. Solids Structures, 37*, 7231–7257.

Li, X., & Tang, H. (2005). A consistent return mapping algorithm for pressure-dependent elastoplastic Cosserat continua and modelling of strain localisation. *Computers and Structures, 83*, 1-10.

Liu, D. C., & Rosing, R. (2007). Finite element formulation of slender structures with shear deformation based on the Cosserat theory. *International Journal of Solids and Structures, 44*, 7785–7802.

Löffelmann, F. (1989). Theoretische und experimentelle Untersuchungen zur Schüttgut-Wand-Wechselwirkung und zum Mischen und Entmischen von Granulaten. Universität Karlsruhe.

Manzari, M. (2004). Application of micropolar plasticity to post failure analysis in geomechanics. *Int J Numer Anal Methods Geomech, 28*(10), 1011-1032.

Martínez-Pañeda, E., & Betegón, C. (2015). Modeling damage and fracture within strain-gradient plasticity. *International Journal of Solids and Structures, 59*, 208-215.

Matsushima, T., Chambon, R., & Caillerie, D. (2002). Large strain finite element analysis of a local second gradient model: application to localization. *Int. J. Numer. Meth. Engng, 54*, 499–521.

Mindlin, R. (1964). Micro-structure in linear elasticity. *Arch. Ration. Mech. Anal, 16*(1), 51–78.

Mindlin, R. (1965). Stress functions for a Cosserat continuum. *Int J Solids Struct, 1*, 265–271.

Mindlin, R., & Eshel, N. (1968). On first strain-gradient theories in linear elasticity. *Int. J. Solids Struct, 4*, 109–124.

Mindline, R. D., & Tiersten, H. F. (1962). Effects of Couplestress in linear Elasticity. *Arch. Rat. Mech. Anal., 11*, 415-448.

Muhlhaus, H. (1991). Continuum models for layered and blocky rock. In J. A. Hudson, *Comprehensive rock engineering* (Hudson, J.A ed., Vol. 2). Oxford: Oxford: Pergamon Press.

Muhlhaus, H., & Vardoulakis, I. (1987). The thickness of shear bands in granular materials. *Géotechnique, 37*(3), 271-283.

Muhlhaus, H., Vardoulakis, I., & Tejchman, J. (1987). A generalized flow theory for granular materials. *Lecture. Inst. Soil Mechanics and Rock Mechanics*.

Nakamura, S., & Lakes, R. (1988). Finite element analysis of stress concentration around a blunt crack in a Cosserat elastic solid. *Comput Methods Appl Mech Eng, 66*(3), 257-266.

Nakamura, S., Benedict, R., & Lakes, R. (1984). Finite element method for orthotropic micropolar elasticity. *Int J Eng Sci, 22*(3), 319-330.

Nguyen, G., Korsunsky, A., & Belnoue, J. P.-H. (2015). A nonlocal coupled damage-plasticity model for the analysis of ductile failure. *International Journal of Plasticity, 64*, 56–75.

Nix, W. D., & Gao, H. (1998). Indentation size effects in crystalline materials: a law for strain gradient plasticity. *J. Mech. Phys. Solids, 46*(3), 411–425.

Nix, W., & Gao, H. (1998). Indentation size effects in crystalline materials: a law for strain gradient plasticity. *Journal of the Mechanics and Physics of Solids, 46*, 411–425.

Nye, J. (1953). Some geometrical relations in dislocated crystals. *Acta Metall. Mater, 1*, 153–162.

Oda, M., & Iwashita, K. (1999). *Mechanics of granular materials: an introduction.* Rotterdam: A.A.Balkema.

Oda, M., & Iwashita, K. (2000). Study on couple stresses and shear band development in granular media based on numerical simulation analyses. *Int. J. of Enging. Science, 38*, 1713–1740.

Oda, M., & Kazama, H. (1998). Microstructure of shear bands and its relation to the mechanisms of dilatancy and failure of dense granular soils. *Geotechnique, 48*, 465–481.

Oda, M., Konishi, J., & Nemat-Nasser, S. (1982). Experimental micromechanical evaluation of strength of granular materials, effects of particle rolling. *Mech. Mater, 1*, 269–283.

Pamin, J., Askes, H., & de Borst, R. (2003). Two gradient plasticity theories discretized with the element-free Galerkin method. *Comp. Meth. Appl. Mech. Enging, 192*, 2377–2403.

Pan, K., & Fang, J. (1994). Nonlocal interaction of a dislocation with a crack. *Arch. Appl. Mech., 64*, 44–51.

Papamichos, E. (2010). Borehole failure analysis in a sandstone under anisotropic stresses. *Int J Numer Anal Methods Geomech, 34*(6), 581-603.

Papanastasiou, P., & Vardoulakis, I. (1992). Numerical treatment of progressive localization in relation to borehole stability. *Int J Numer Anal Methods Geomech, 16*(6), 389-424.

Papanicolopulos, S., & Zervos, A. (2009). Numerical solution of crack problems in gradient elasticity. *Eng. Comput. Mech*.

Papanicolopulos, S., & Zervos, A. (2010). Continua with microstructure: second-gradient theory. *European Journal of Environmental and Civil Engineering, 14*(8-9), 1031-1050.

Papanicolopulos, S., Zervos, A., & Vardoulakis, I. (2009). A three dimensional C1 finite element for gradient elasticity. *Int. J. Numer. Methods Eng., 77*(10), 1396–1415.

Papanicolopulos, S.-A., Zervos, A., & Vardoulakis, I. (2010). Discretization of Gradient Elasticity Problems Using C1 Finite Elements. In G. Maugin, & A. Metrikine, *Mechanics of Generalized Continua* (Vol. 21, pp. 269-277). New York: Springer.

Park, H., & Lakes, R. (1986). Cosserat micromechanics of human bone: strain redistribution by a hydration sensitive constituent. *J. Biomech., 19*, 385–397.

Pastor, M., & Peraire, J. (1989). Capturing shear bands via adaptive remeshing techniques. *Euromech*, 248.

Peng, C., Kong, X., & Xu, C. (2011). Numerical implementation of pressure-dependent elasto-plastic cosserat continuum model in abaqus. *Second International Conference*, (pp. 6621-6624).

Providas, E., & Kattis, M. (2002). Finite element method in plane cosserat elasticity. *Computers & Structures, 80*(27-30), 2059-2069.

Qiu, X., Huang, Y., Wei, Y., Gao, H., & Hwang, K. (2003). The flow theory of mechanism-based strain gradient plasticity. *Mechanics of Materials*, 245–258 .

Regueiro, R. (2009). Finite Strain Micromorphic Pressure-Sensitive Plasticity. *J. Eng. Mech., 135*, 178-191.

Regueiro, R. (2010). On finite strain micromorphic elastoplasticity. *International Journal of Solids and Structures, 47*, 786–800.

Regueiro, R., & Borja, R. (2001). Plane strain finite element analysis of pressure sensitive plasticity with strong discontinuity. *Int. J. Solids Structures, 38*(21), 3647–3672.

Regueiro, R., & Isbuga, V. (2011). Length scale effects in finite strain micromorphic linear isotropic elasticity: finite element analysis of three-dimensional cubical microindentation. *Proc. IMechE, 224*(Part N: J. Nanoengineering and Nanosystems), 101-122.

Riahi, A., & Curran, J. H. (2009). Full 3D finite element Cosserat formulation with application in layered structures. *Applied Mathematical Modelling, 33*, 3450–3464.

Riahi, A., Curran, J. H., & Bidhendi, H. (2009). Buckling analysis of 3D layered structures using a Cosserat continuum approach. *Computers and Geotechnics, 36*, 1101–1112.

Ristinmaa, M., & Vecchi, M. (1996). Use of couple-stress theory in elasto-plasticity. *Comput. Methods Appl. Mech. Engrg, 136*, 205-224.

Rubin, M. B. (2005). Numerical solution of axisymmetric nonlinear elastic problems including shells using the theory of a Cosserat point. *Computational Mechanics, 36*, 266–288.

Rudnicki, J. W., & Rice, J. R. (1975). Conditions for the localization of the deformation in pressure-sensitive materials. *J. Mech. Phys. Solids, 23*, 371-394.

Sansour, C., Skatulla, S., & Zbib, H. (2010). A formulation for the micromorphic continuum at finite inelastic strains. *International Journal of Solids and Structures, 47*(11-12), 1546–1554.

Sharbati, E., & Naghdabadi, R. (2006). Computational aspects of the cosserat finite element analysis of localization phenomena. *Computational Materials Science, 38*(2), 303-315.

Shu, J., & Fleck, N. (1999). Strain gradient crystal plasticity: size-dependent deformation of bicrystals. *J. Mech. Phys. Solids, 47*, 292–324.

Shu, J., King, W., & Fleck, N. (1999). Finite elements for materials with strain gradient effects. *Int. J. Numer. Methods Eng, 44*(3), 373–391.

Specht, B. (1988). Modified shape functions for the three-node plate bending element passing the patch test. *Int. J. Numer. Methods Eng, 26*(3), 705–715 .

Stolken, J., & Evans, A. G. (1998). A microbend test method for measuring the plasticity length scale.

Sulem, J., & Cerrolaza, M. (2002). Finite element analysis of the indentation test on rocks with microstructure. *Comput Geotech, 29*(2), 95-117.

Sulem, J., & Vardoulakis, I. (1990). Bifurcation analysis of the triaxial test on rock specimens. A theoretical model for shape and size effect. *Acta ~echanica, 83*, 195-212.

Tejchman, J. (1989). Scherzonenbildung und Verspannungseffekte in Granulaten unter Berücksichtigung von Korndrehungen. *Publication Series of the Institute of Soil and Rock Mechanics, 117*, 1-236.

Tejchman, J. (2008). Shear Localization in Granular Bodies with Micro-Polar Hypoplasticity. Verlag Berlin Heidelberg: Springer.

Tejchman, J., & Wu, W. (1993). Numerical study on patterning of shear bands in a Cosserat continuum. *Acta Mech, 99*(1), 61-74.

Thornton, C. Z. (2003). Numerical simulations of the direct shear test. *Chem. Eng. Technol., 26*(2), 1-4.

Toupin, R. (1962). Elastic materials with couple stresses. *Arch. Ration. Mech. Anal, 11*(1), 385–414.

Tsagrakis, I., & Aifantis, E. C. (2002). Recent developments in gradient plasticity. Part I: formulation and size effects. *J. Eng. Mater. Technol. (Trans. ASME), 124*(3), 352–357.

Uesugi, M., Kishida, H., & Tsubakihara, Y. (1988). Behaviour of sand particles in sand-steel friction. *Soils Found, 28*(1), 107–118.

Vardoulakis, I. (1980). Shear band inclination and shear modulus in biaxial tests. *Int. J. Num. Anal. Meth. Geomech, 4*, 103–119.

Vardoulakis, I., & Graf, B. (1985). Calibration of constitutive models for granular materials using data from biaxial experiments. *Géotechnique, 35*, 299–317.

Vardoulakis, I., & Sulem, J. (1995). *Bifurcation Analysis in Geomechanics.* London: Blackie Academic and Professional.

Vardoulakis, I., & Sulem, J. (1995). *Bifurcation Analysis in Geomechanics.* Glasgow: Blackie Academic and Professional.

Voigt, W. (1887). Theoretische Studien fiber die Elastizitatsverhiltnisse der Kristalle. *Abh. Gesch. Wissenschaften*, 34.

Wei, Y., & Hutchinson, J. (1997). Steady-State Crack Growth and Work of Fracture for Solids Characterized by Strain Gradient Plasticity. *J. Mech. Phys. Solids, 45*(8), 1253-1273,.

Wijk, G. (1989). The stamp test for rock drillability classification. *Int J Rock Mech and Min Sci, 26*(1), 37–44.

Yang, J., & Lakes, R. (1982). Experimental study of micropolar and couple stress elasticity in compact bone in bending. *J. Biomech., 15*, 91–98.

Zbib, H. M., & Aifantis, E. C. (1988). On the localization and post-localization behavior of plastic deformation, I-III. *Res Mech, 23*, 261–305.

Zbib, H. M., & Aifantis, E. C. (1988). On the structure and width of shear bands. *Scripta Metall, 22*(5), 703–708.

Zervos, A. (2008). Finite elements for elasticity with microstructure and gradient elasticity. *Int. J. Numer. Methods Eng, 73*(4), 564–595.

Zervos, A., Papanastasiou, P., & Vardoulakis, I. (2001). A finite element displacement formulation for gradient elastoplasticity. *Int. J. Numer. Methods Eng., 50*(6), 1369–1388.

Zervos, A., Papanastasiou, P., & Vardoulakis, I. (2001). Modelling of localisation and scale effect in thick-walled cylinders with gradient elastoplasticity. *Int. J. Solids Struct, 30*(30-31), 5081–5095.

Zervos, A., Papanicolopulos, S., & Vardoulakis, I. (2009). Two finite element discretizations for gradient elasticity. *J. Eng. Mech., 135*(3), 203–213.

Zhang, H., Wang, H., & Liu, G. (2005). Quadrilateral isoparametric finite elements for plane elastic. *Acta Mech Sin, 21*(4), 388-394.

Zybell, L., Mühlich, U., Kuna, M., & Zhang, Z. (2012). A three-dimensional finite element for gradient elasticity based on a mixed-type formulation. *Computational Materials Science, 52*, 268–273.

References

Appendix 1

The elastic bulk modulus

$$\mathrm{K} = \frac{E}{3(1-2v)} \tag{A1.1}$$

The formulation of $\mathbf{P}^*$, α, $\mathbf{c}_\lambda$ and $\mathbf{C}_\alpha$ are given by

$$\mathbf{P}^* = \begin{bmatrix} 2/3 & -1/3 & -1/3 & 0 & 0 & 0 & 0 \\ -1/3 & 2/3 & -1/3 & 0 & 0 & 0 & 0 \\ -1/3 & -1/3 & 2/3 & 0 & 0 & 0 & 0 \\ 0 & 0 & 0 & 1 & 0 & 0 & 0 \\ 0 & 0 & 0 & 0 & 1 & 0 & 0 \\ 0 & 0 & 0 & 0 & 0 & 1 & 0 \\ 0 & 0 & 0 & 0 & 0 & 0 & 1 \end{bmatrix} \tag{A1.2}$$

$$\mathbf{C}_\alpha = \begin{bmatrix} \alpha & 0 & 0 & 0 & 0 & 0 & 0 \\ 0 & \alpha & 0 & 0 & 0 & 0 & 0 \\ 0 & 0 & \alpha & 0 & 0 & 0 & 0 \\ 0 & 0 & 0 & (\alpha+1)/2 & (\alpha+1)/2 & 0 & 0 \\ 0 & 0 & 0 & (\alpha+1)/2 & (\alpha+1)/2 & 0 & 0 \\ 0 & 0 & 0 & 0 & 0 & \alpha & 0 \\ 0 & 0 & 0 & 0 & 0 & 0 & \alpha \end{bmatrix} \tag{A1.3}$$

$$\alpha = \frac{\bar{\sigma}}{\bar{\sigma}^{\mathrm{trial}}} \tag{A1.4}$$

$$\mathbf{c}_\lambda = \mathbf{a}_{\mathrm{qe}}\mathbf{c}_\varepsilon \,, \quad \mathbf{c}_\varepsilon = (\mathbf{b}_{\mathrm{qe}} - \mathbf{a}_{\mathrm{qe}})^{-1} \tag{A1.5}$$

$$\mathrm{b}_{\mathrm{qe}} = -3K\alpha_1\alpha_2 \frac{\partial \mathrm{f}/\partial \bar{\varepsilon}^{\mathrm{p}}}{\partial \mathrm{f}/\partial \dot{\gamma}} - \frac{\partial c}{\partial \bar{\varepsilon}^{\mathrm{p}}} \,, \quad \mathrm{a}_{\mathrm{qe}} = 3\mu \frac{\partial \mathrm{f}/\partial \bar{\varepsilon}^{\mathrm{p}}}{\partial \mathrm{f}/\partial \dot{\gamma}} \tag{A1.6}$$

Appendix 1